Evidence for Excitonic Superfluidity in a Bilayer Two-Dimensional Electron System

Thesis by

Melinda Jane Kellogg

In Partial Fulfillment of the Requirements for the

degree of

Doctor of Philosophy

CALIFORNIA INSTITUTE OF TECHNOLOGY

Pasadena, California

2005

(Defended July 15, 2004)

© 2005

Melinda Kellogg

All Rights Reserved

ACKNOWLEDGEMENTS

I am forever indebted to my advisor, Jim Eisenstein. If not for Jim, I would not be a scientist now. Especially because of Jim, I might even become a good scientist. Thank you Jim for taking me into your wonderful lab, and allowing me to learn and grow and sometimes even play a little in your world of two-dimensional electrons. You were generous with your time and your knowledge; and I have benefited greatly from both. You have modeled for me integrity and maturity, and I hope I can carry these things with me into my life. You have a zest for life and a charisma that I will greatly miss. You helped me out when I needed it most, and I will always see you as a knight in shining armor, which I know will amuse you terribly.

Thanks also to my first two friends in the lab, Mike Lilly and Steve Stryker. To find two such kind souls in the subbasement of Sloan Labs was the last thing I expected. Mike took it upon himself to personally ensure that everyone in the lab felt warm and welcomed – this made my transition into the lab very easy. And Steve is the Zen philosopher of the machine shop, who was always available for listening whenever I wanted to talk. They shared their knowledge and their many skills with me, and I am grateful to them both.

To Ken Cooper and Ian Spielman, thank you for setting the bar so high. I spent the first two years in awe of your prowess in the lab, and your facile understanding of the complex physics. I did not imagine that I would ever be on the same level as the two of you. When the years passed, and I found myself becoming your peer, I knew I had done well. You are two of the most honorable young men I have met, and I am glad to have known you.

Finally, thanks to the Caltech physics department, specifically Tom Tombrello, Ken Libbrecht, Frank Porter, Alan Weinstein, Kip Thorne, David Goodstein and Mike Cross. Thank you for taking a chance on me and supporting me. You are all my knights.

ABSTRACT

The discovery of the integer quantum Hall effect (QHE) and the fractional quantum Hall effect (FQHE) revealed that unexpected physics could be found in a seemingly very simple system: free electrons constrained to move in only two dimensions. Adding a degree of complexity to this system by bringing *two* of these layers of two-dimensional electrons into close proximity, multiplies the exciting physical phenomena available for study and discovery. This thesis is a report on electrical transport studies of bilayer two-dimensional electron systems (2DES) found in GaAs/AlGaAs double quantum well semiconductor heterostructures. Through studies at zero magnetic field using a fairly new transport measurement called "Coulomb drag" pure electron-electron scattering is measured with unprecedented accuracy and clarity. In large magnetic fields applied perpendicular to the electron layers, at the right combination of magnetic field strength, electron density and layer separation, a new, uniquely bilayer, many-body quantum ground state exists that can be described alternately as an itinerant pseudospin ferromagnet or as a Bose-Einstein condensate (BEC) of interlayer excitons. This bilayer quantum state was first predicted theoretically fifteen years ago, and its discovery and exploration is the basis of this thesis. In this thesis, transport measurements allow for the direct detection of the BEC of excitons by their ability to flow with vanishing resistance and vanishing influence from the large external magnetic field. Excitonic BEC has been pursued experimentally for almost 40 years, but this thesis likely represents the first detection of the elusive state. Coulomb drag is found to be an excellent probe of the phase transition out of the bilayer quantum state and is used to extend the mapping of the phase diagram into the temperature and layer density imbalance planes.

TABLE OF CONTENTS

Acknowledgements iii
Abstract iv
Table of Contents v
List of Figures vii
List of Symbols and Abbreviations x

Introduction 1

Chapter 1: Sample & Processing 6
    1.1 Double Quantum Wells 6
        1.1.1 Crystal Specifications 8
            1.1.1.a Layer Separation 9
            1.1.1.b Tunneling 10
            1.1.1.c Well Width and Interface Roughness 12
    1.2 Sample Processing 12

Chapter 2: Coulomb Drag 18
    2.1 Definition 18
    2.2 Free Electron Model of Coulomb Drag 19
    2.3 Electron-Electron Scattering in Metals 22
    2.4 Boltzmann Model of Drag Scattering 24
        2.4.1 A Limiting Case 33
    2.5 History of Coulomb Drag 35

Chapter 3: Coulomb Drag at B=0 39
    3.1 Sample: 'K' 39
    3.2 Longitudinal Drag versus Temperature 41
        3.2.1 Search for Phonon-Mediated Drag 43
    3.3 Longitudinal Drag versus Density 45
    3.4 Longitudinal Drag versus Density Imbalance 51
        3.4.1 Numerical Modeling 54
    3.5 Spin Polarization ($B_{\perp}=0$, $B_{\parallel}\neq 0$) 58

Chapter 4: 2D Electrons in a Perpendicular Magnetic Field 68
4.1 Quantum Hall Effect 68
4.2 Fractional Quantum Hall Effect 75
4.3 Composite Fermions, ν=½ 78
4.4 Bilayer Quantum Hall Phase Diagram 80
4.5 The (111) State 84
4.6 Pseudospin Ferromagnet 86
4.7 Excitonic Condensate 90

Chapter 5: Coulomb Drag at $\nu_T = 1$ 95
5.1 Samples: 'N' and 'R' 95
5.2 Hall and Longitudinal Drag versus Magnetic Field 96
5.3 Temperature Dependence 103
5.4 Dependence of Hall Coefficients on Effective Layer Separation ...106

Chapter 6: Phase Boundary 109
6.1 Coulomb Drag across the Phase Boundary 110
6.2 Effect of Density Imbalance on Phase Boundary 120
6.3 Longitudinal Coulomb Drag at High d/ℓ 123
6.4 Density Imbalance at High d/ℓ 129

Chapter 7: Counterflow Superfluidity 134
7.1 Sample: 'Y' 136
7.2 Counterflow and Parallel Definitions 137
7.3 Hall and Longitudinal Resistance versus Magnetic Field 140
7.4 Temperature Dependence at $\nu_T = 1$ 142
7.5 Dependence on Effective Layer Separation 145
7.6 Discussion 146

Appendix A: Detailed Sample Processing Steps 152
Appendix B: Mask Design 159
Appendix C: Coulomb Drag Setup 164
Appendix D: Counterflow Measurement Setup 173
Appendix E: Modeling Current Flow with PDEtool in MATLAB 175
Appendix F: How to Take Gate Characteristics 178
Appendix G: Layer Density Balancing by Coulomb Drag 181
Appendix H: How to Determine Density and Mobility 184
Appendix I: How to Determine Density Imbalance 188
Appendix J: Chronological List of 2D-2D Experimental Drag Papers 191
Appendix K: Boltzmann Integration Fortran Code 194

LIST OF FIGURES

Number *Page*

1.1 Energy levels in single quantum well 7
1.2 Double quantum wells 8
1.3 Sample processing steps 13
1.4 Photo of sample 'Y' 15

2.1 Coulomb drag measurement schematic 19
2.2 Simple model of Coulomb drag 21
2.3 Diagram of a scattering event 25
2.4 Rotated momentum axes for Boltzmann integration 28

3.1 Sample 'K' photo 40
3.2 Longitudinal drag resistivity vs. temperature 41
3.3 Longitudinal drag resistivity divided by T^2 vs. temperature 44
3.4 Density dependence of longitudinal drag vs. temperature 46
3.5 Longitudinal drag resistivity vs. density 48
3.6 Theoretical models compared to our data 50
3.7 Longitudinal drag resistivity vs. density imbalance 53
3.8 Computed drag resistivity vs. temperature and density imbalance 55
3.9 Computed drag intensity vs. wavevector q 56
3.10 Longitudinal drag resistivity vs. density imbalance for $B_{\|} = 0$ 60
3.11 Longitudinal drag resistivity vs. density imbalance for $B_{\|} \neq 0$ 62

4.1 Density of states diagram for 2D electrons 72
4.2 Quantum Hall effect in conventional transport 74
4.3 Fractional quantum Hall effect in conventional transport 75
4.4 Effective layer separation schematic 81
4.5 Bilayer quantum Hall effect phase diagram 83
4.6 Merons 89

5.1 Sample 'N' photo 96
5.2 Quantized Hall drag 97
5.3 Quantized Hall drag wih $B_{||} \neq 0$ and with interlayer bias 101
5.4 Temperature dependence of quantized Hall drag 103
5.5 Temperature dependence of longitudinal Coulomb drag near $\nu_T = 1$ 104
5.6 Arrhenius plot of drag and conventional resistances at $\nu_T = 1$ 105
5.7 Effective layer separation dependence of Hall resistances at $\nu_T = 1$ 106

6.1 Longitudinal and Hall drag across the phase boundary 111
6.2 Longitudinal and Hall drag vs. effective layer separation d/ℓ 113
6.3 Temperature dependence of longitudinal and Hall drag vs. d/ℓ 114
6.4 Power law behavior of longitudinal drag away from peak 115
6.5 Temperature dependence of longitudinal Coulomb drag at $\nu_T = 1$ .. 116
6.6 Hall drag at $\nu_T = 1$ vs. d/ℓ with density imbalance 121
6.7 New phase diagram showing $d/\ell - \Delta n/n_T$ plane 122
6.8 Longitudinal drag resistivity at high d/ℓ 125
6.9 Layer separation dependence of longitudinal drag at high d/ℓ 126
6.10 Temperature dependence of longitudinal drag at high 127
6.11 Temperature dependence of longitudinal drag at $\nu_T = 1$ 128
6.12 Density imbalance dependence of longitudinal drag at high d/ℓ . 130

7.1 Parallel mode minus counterflow mode equals Coulomb drag 135
7.2 Photo of sample ‘Y’ 137
7.3 Counterflow measurement schematic 138
7.4 Parallel measurement schematic 139
7.5 Counterflow Hall and longitudinal resistance goes to zero at $\nu_T = 1$ 141
7.6 Arrhenius plots of counterflow and parallel transport at $\nu_T = 1$ 143
7.7 Layer separation dependence of counterflow Hall at $\nu_T = 1$ 145
7.8 Schematic of interlayer excitons producing counterflow current 147
7.9 Meron-antimeron pair bound by tunneling “domain string” 149

B.1 Sample ‘Y’ map 160
B.2 Numerical simulation of current flow in mesa 161
C.1 Sample ‘Y’ map 166
C.2 Coulomb drag circuit with interlayer bias 167
C.3 Sample ‘K’ map 168
C.4 Out-of-phase common mode voltage vs. ratio standard setting 169
D.1 Sample ‘Y’ map 174
E.1 Numerical simulation of current flow in mesa 176
F.1 Typical gate characteristics 179
F.2 Gate characteristic measurement circuit and resistances 180
G.1 Longitudinal Coulomb drag for density balancing 182
H.1 Conventional longitudinal resistance in high Landau levels 185
H.2 Determining density with B_ν vs. $1/\nu$ 186
I.1 Longitudinal Coulomb drag vs. interlayer bias 190

LIST OF SYMBOLS AND ABBREVIATIONS

2D two-dimensional

2DEG two-dimensional electron gas

2DES two-dimensional electron system

ac alternating current

AlGaAs Aluminum Gallium Arsenide

AuNiGe Gold Nickel Germanium

Å Angstrom

a mean inter-electron spacing in one layer $(\pi n)^{-1/2}$

a_B effective Bohr radius $\varepsilon\hbar^2 / m^* e^2$

A_{ee} electron-electron scattering constant

BEC Bose-Einstein condensate

B magnetic field

B_{eff} effective magnetic field seen by composite fermions

$B_{\perp(\parallel)}$ component of magnetic field perpendicular (parallel) to 2DEG

C capacitance

C Coulomb

dc direct current

DIP header dual in-line package header

DOS density of states

DQW double quantum well

drag layer the open electron layer in a Coulomb drag measurement

drive layer the electron layer carrying the current in a Coulomb drag measurement

d center-to-center well separation

d/ℓ effective layer separation

D Landau level degeneracy

∇ gradient operator

Δ_{SAS} energy splitting between symmetric and antisymmetric dqw eigenstates

e electron charge

ε single particle energy

ε dielectric constant

ε_0 permittivity of free space

E electric field

E_D electric field in drag layer

FWHM full width at half maximum

FQH(E) fractional quantum Hall (effect)

f fraction of sample occupied by interlayer coherent puddles

f Fermi-Dirac distribution function

f^0 equilibrium Fermi-Dirac distribution function

GaAs Gallium Arsenide

g g-factor

g^* effective g-factor, for GaAs $g^* = -0.44$

h Planck's constant

$h(q)$ drag intensity

$\hbar$ Planck's constant divided by 2π

HLL high Landau level

Hz hertz

I current

I_x current flowing in the x direction

J, J_{2D} two-dimensional current density

K Kelvin

KE kinetic energy

k single particle momentum state wavevector

k_B Boltzmann constant

k_F Fermi wavevector

κ dielectric constant

L well width

L length measured along

ℓ magnetic length $\sqrt{\hbar / eB}$

l_{tr} transport mean free path

Ω ohm

meV milli-electronvolt

mK milliKelvin

mm millimeter

mV millivolt

MOSFET metal-oxide-semiconductor field effect transistor

m_e electron mass

m^* effective mass, for GaAs $m^* = 0.067 m_e$

µm micron

μ electron mobility

μ_B Bohr magneton $e\hbar / 2m_e$

nA nanoamp

n, n_{2D} 2D electron density per layer

n_T total 2D electron density in both layers

N number of electrons or composite fermions

$N(E)$ 2D density of states

nF nanoFarad

ν single layer filling factor

ν_T filling factor of both layers

ξ spin polarization

pA picoamp

PE potential energy

pF picofarad

ρ resistivity

ρ_{ee} resistivity due to electron-electron scattering events

$\rho_{xx(,D)}$ longitudinal (drag) resistivity

$\rho_{xy(,D)}$ Hall (drag) resistivity

Φ electrostatic potential

Φ_0 magnetic flux quantum h/e

Ψ_m Laughlin wavefunction

QHE quantum Hall effect

q momentum transfer wavevector

q_{TF} Thomas-Fermi screening wavevector

RMS root mean square

RPA random-phase approximation

r_s dimensionless inter-electron coupling constant a/a_B

R resistance

$R_{xx(,D)}$ longitudinal (drag) resistance

$R_{xy(,D)}$ Hall (drag) resistance

R_{xy}^{*} Hall resistance measured only in one layer

SAW surface acoustic wave

□ square (length/width)

s sound velocity

σ single particle spin

$\sigma_{xx}^{CF(\parallel)}$ longitudinal conductivity in counterflow (parallel) channel

T Tesla

TF Thomas-Fermi

τ_D interlayer momentum relaxation time

T temperature

T_c crossover temperature

T_F Fermi temperature

T_{KT} Kosterlitz-Thouless temperature

V volt

$V_{x(y),D}$ drag voltage in the x (y) direction

$V(q)$ potential in fourier space

υ_{drift} drift velocity

W sample width

ω energy transferred in scattering event

$w(1,2;1',2'), w(q,\omega)$ collision probability

$\chi(q,\omega)$ susceptibility function

Introduction

Condensed matter physics is the study of a tremendously large number of particles crowded (condensed) together so that the effects they have on one another cannot be ignored. It is an exciting field of physics because even though all the particles obey known physical laws, solving the physical equations for such a large number of particles is not always feasible. So it is not always known what will happen in a condensed matter system and there are still some surprises to be found.

The condensed matter system studied in this thesis is a system of electrons that have been confined so that they can only move in two dimensions – a two-dimensional electron system (2DES). Roughly 10^{10} electrons are crowded into one square centimeter, all repelling each other electrically. Although an equation can be written describing all the electrons' interactions with one another, with 10^{10} electrons, it is too difficult to solve. So it was a surprise when it was found that under certain conditions, involving the application of a perpendicular magnetic field, the electrons will specially arrange themselves in accord with the magnetic flux quanta passing through the layer in such a way as to lower the energy of the entire system. This surprise was called the fractional quantum Hall effect (FQHE) and was discovered in 1982 [1].

In this thesis, we study a system in which two layers of these two-dimensional electrons are brought very close together in parallel (a bilayer 2DES). We show that when the layers are sufficiently close together and subjected to a specific value of perpendicular magnetic field, a new, uniquely bilayer, state is formed that is mathematically similar to the FQHE state. In this state, the system achieves a lower energy when the electrons in one layer become highly correlated with the electrons in the other layer.

This correlated state can be portrayed as one where the electrons lose track of which layer they are in (this view is discussed in **Section 4.6**), or as one where the electrons in one of the layers line up with the vacancies between the electrons in the other layer. These vacancies are called “holes” and behave much like positively charged electrons. The holes in one layer are electrically attracted to the electrons in the other layer, and the two bind together to form composite particles called excitons. Excitons are a type of boson and can undergo a process called Bose-Einstein condensation (BEC); thus the excitons all condense into the same quantum state. This view of the state as a BEC of excitons is covered in **Section 4.7**.

The main goal of this thesis is to detect this excitonic BEC. We aim to detect it by probing the bilayer 2DES using electrical transport measurements. Wires are electrically contacted to the electron layers, and currents are sent through one or both of the layers. The voltages measured in response to these currents yield a great deal of information on the state of the bilayer electron system.

The excitonic BEC can be detected through electrical transport if a flow of the BEC is set up through the layers. Electrical transport due to such a flow will be vastly different from the usual currents carried by electrons. BECs exhibit superfluid properties that we can detect as a vanishing of the current's dissipation when the system enters the excitonic BEC state. Additionally, transport due to the flow of excitons will be unaffected by the magnetic field since excitons are charge-neutral. This will show itself as a vanishing of the Hall resistance when the system is in this state. Both of these indicators were detected and are discussed in **Chapter 7**.

This state was first detected more indirectly, using an electrical transport measurement called "Coulomb drag." In this measurement, interlayer electron scattering processes are directly detected when current is sent through one of the layers, and voltages are probed in the non-current-carrying layer. The first-ever observation of "quantized Hall drag," the remarkable spectacle in which a quantized Hall voltage appears in a layer that has no net current flow, is an indirect display of the likely excitonic superfluid, and is shown in **Chapter 5**.

Coulomb drag, although only an indirect method for detecting the excitonic superfluidity, is an excellent probe of the phase transition out of the BEC state as the (effective) layer separation is increased. Studies of this phase transition are covered in **Chapter 6**, including the interesting result that the BEC state becomes more robust when the electron densities in the two layers are not equal.

The theoretical framework for understanding this special state is covered in **Chapter 4**. Readers interested only in the theory and experiments on the correlated bilayer excitonic state should proceed directly to this chapter.

Chapter 3 shows early Coulomb drag work done in zero magnetic field. It precedes the other chapters mainly because the work was done chronologically earlier, although it also lays the foundation for understanding the Coulomb drag measurements performed in the exciton BEC state shown in later chapters. Coulomb drag experiments in zero magnetic field are used to study electron-electron scattering processes – Coulomb drag is the first measurement technique to detect these processes directly. Our experiments have led to a better understanding of the nature of these interactions.

The Coulomb drag measurement itself is discussed extensively in **Chapter 2**, including the theory and history of electron-electron scattering and Coulomb drag in zero magnetic field. A detailed equation for zero field electron-electron Coulomb drag scattering derived by Jauho and Smith [2] is extended theoretically, and a Fortran program that numerically solves this equation for a variety of experimental conditions can be found in **Appendix K**.

In **Chapter 1**, the double quantum wells that are used to confine the electrons to two dimensions are discussed, with special focus on the parameters that affect the ability to achieve and perform electrical measurements on the exciton BEC state. Also included is a basic description of the crystal processing, which allows for experimental access to the electron layers.

For those who wish to perform these types of experiments, there are eleven **Appendices** that contain detailed information on the experimental procedures.

* * *

---

1 D.C. Tsui, H.L. Störmer and A.C. Gossard, Phys. Rev. Lett. **48**, 1559 (1982).

2 A.P. Jauho and H. Smith, Phys. Rev. B **47**, 4420 (1993).

Chapter 1: Sample & Processing

1.1 DOUBLE QUANTUM WELLS

The exciting physics presented in the thesis would not exist but for the skill of our collaborators at Bell Labs, Loren Pfeiffer and Ken West, who design and grow the ultra-clean, ultra-high mobility GaAs/AlGaAs heterostructures needed to see the subtle quantum effects reported here.

These crystals are grown by a technique called Molecular Beam Epitaxy, in which crystals are grown one atomic layer at a time, with control over the composition of each layer. The semiconductors Gallium Arsenide (GaAs) and Aluminum Gallium Arsenide (AlGaAs) have very similar lattice constants and can be grown together in layers to create a very clean, high quality crystal with few defects. But, since the two materials have different conduction band energies, layers of GaAs and AlGaAs will form wells in the conduction band profile in the dimension perpendicular to the layers (see Fig. 1.1). Conduction band electrons can fall into these wells and become trapped.

These bound state electrons have discrete energy levels – the wavefunctions for the first two levels are depicted in Fig. 1.1. For a GaAs well 180 Å wide, the energy difference between the first two levels is ~37 meV, approximately 400 K in temperature units. Even at room temperature (~ 300 K), many of the electrons will be in the lowest energy state; but at the cryogenic temperatures that we work (d 1 K), *all* of the electrons will be confined to the lowest energy state. This will preclude any electron motion in this dimension and the electrons will only be free to move in the remaining two dimensions, in the plane of the GaAs layer. Electrons constrained to only move in two dimensions are called "two-dimensional electrons."

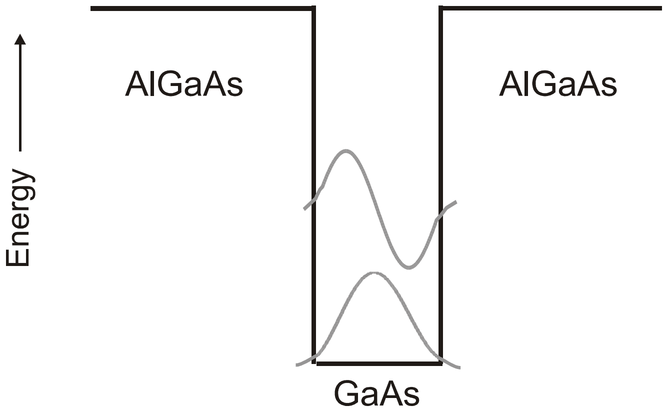

Figure 1.1: Quantum well formed in the conduction band profile from a layer of GaAs sandwiched between layers of AlGaAs. Schematics of the first two wavefunction solutions for a conduction band electron trapped in this "box" are shown in grey.

In these two dimensions, the electrons will behave as regular GaAs conduction band electrons, moving through the crystal as free electrons with an effective mass $m^* = 0.067 m_e$, where m_e is the conventional electron mass.

A single quantum well provides a single layer of two-dimensional electrons. For the experiments shown in this thesis, two layers of two-dimensional electrons are needed, spaced very close together and in parallel – but well isolated electrically. For this, *double* quantum well structures are grown. For double quantum wells, two layers of GaAs are grown into the crystal, separated by a thin AlGaAs barrier.

1.1.1 CRYSTAL SPECIFICATIONS

The crystal used for these experiments is a GaAs/AlGaAs modulation doped [1] double quantum well structure grown on the (100) surface. The conduction band is populated by symmetrical silicon delta-doped layers setback approximately 2000 Å from the double quantum well structure. The wells are 180 Å layers of GaAs, separated by a 100 Å wide $Al_{0.9}Ga_{0.1}As$ barrier; there are $Al_{0.3}Ga_{0.7}As$ cladding layers on the outer sides of the wells. Figure 1.2 shows a schematic of this double quantum well structure.

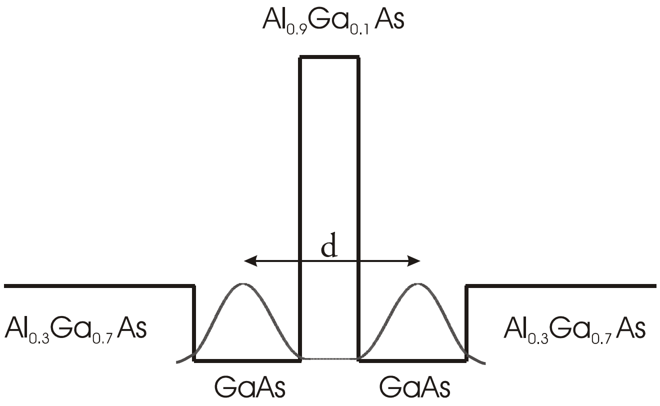

Figure 1.2: Γ-minimum conduction band energy diagram of the double quantum well structure with the calculated electron density shown in grey.

The barrier and cladding heights in the figure reflect the energy difference between the conduction bands of the pure GaAs and the AlGaAs alloys. The $Al_{0.3}Ga_{0.7}As$ conduction band is 232 meV higher than the GaAs conduction band and $Al_{0.9}Ga_{0.1}As$ is approximately 928 meV higher (in this case even though the X-band minimum is lower in energy than the Γ-band, in-plane momentum conservation and energy considerations inhibit Γ–X–Γ transport, so it is the Γ-minimum that is relevant here [2]). The especially high barrier between the wells is critical to our experiments. This keeps the tunneling negligibly low, even though the wells are only 100 Å apart.

To estimate the charge distribution in the wells, Schrödinger's equation is solved numerically for this double quantum well configuration. Since the electron distribution will bend the conduction bands (this is not shown in the figure), Schrödinger's equation must be solved iteratively with Poisson's equation in order to calculate the electron wavefunction for an accurate representation of the double quantum well potential [3]. The calculated electron density, $\psi^*\psi$, for the lowest energy state is shown in grey in Figure 1.2

1.1.1.a LAYER SEPARATION

A parameter of crucial importance in double layer transport experiments is the separation between the electrons in the two layers. Since the breadth of the electron distribution is larger than the AlGaAs barrier, this is not really adequately described by a single number. Although in some of the numerical work in later chapters the finite extent of the wavefunction is included in the calculations, for the experimental work we usually just refer to the distance between the peaks of the electron distributions, which we approximate as the distance between the centers of the two wells and refer to as "d." The Coulomb interactions between the two layers are strongly dependent on this interlayer distance. Because of the inverse dependence on distance of the Coulomb force, the closer together the layers are, the stronger will be the interlayer Coulomb interactions. Since our experiments are meant to probe the effects of interlayer Coulomb interactions, it behooves us to make d as small as possible.

1.1.1.b TUNNELING

We are limited in how narrow we can make the barrier because the amount of tunneling between the two wells is exponentially dependent on the width of the barrier [4] and for our experiments extremely low tunneling is crucial. For our 100 Å $Al_{0.9}Ga_{0.1}As$ barrier, we can calculate the strength of this tunneling, which we assess in terms of the energy splitting Δ_{SAS} between the lowest energy symmetric and antisymmetric eigenstate solutions for the double quantum well system. This splitting is calculated to be about $\Delta_{SAS} \approx 90\mu K$ for this system. This is done by solving the Schrödinger equation iteratively with Poisson's equation, taking into account Hartree and exchange effects, for the double quantum well parameters (using the Γ valley energy for the barrier), and finding the energy difference between the symmetric and antisymmetric solutions. The electron effective mass was kept at the GaAs value $m^* = 0.067m_e$ throughout the structure, even though the mass is higher in the AlAs barrier. Using a higher effective mass in the barrier would reduce the calculated Δ_{SAS} even further, so $\Delta_{\mathrm{SAS}} \approx 90\mu\mathrm{K}$ is an upper limit.

Empirically, we evaluate this tunneling in terms of the amount of interlayer resistance it offers under resonance conditions. The typical value of this resistance for the results shown in this thesis is $R_{tunneling} \sim 100\mathrm{M}\Omega$. We find this to be a satisfactorily small value of tunneling for our experiments. When the barrier width is reduced, even by the small amount that occurs in the same GaAs/AlGaAs wafer due to the difference in beam flux during the molecular beam epitaxy growth process between the center of the wafer and the edges, the tunneling becomes dramatically larger, so much so that we have been restricted to using only sample pieces, for this thesis, that come from or near the center of this wafer.

The barrier height could be increased by about 10% (and the tunneling current reduced by roughly the same factor [4]) if the barrier were made of pure AlAs, however samples grown with pure AlAs barriers, prior to my time in the research group, could not be successfully contacted electrically. This is believed to be due to the high reactivity of aluminum with oxygen; oxygen burrows into the AlAs layer from an exposed edge and the entire layer can become oxidized [5]. This prevents the diffused ohmic contact from penetrating the barrier to reach the bottom electron layer. The small amount of gallium in the $\mathrm{Al_{0.9}Ga_{0.1}As}$ barrier, however, seems sufficient to arrest this process, and we are able to successfully contact both the electron layers in these samples.

1.1.1.c WELL WIDTH AND INTERFACE ROUGHNESS

Another way to reduce the mean electron separation, without reducing the barrier width, would be to reduce the widths of the quantum wells – this would move the peaks in the electron density distribution closer together. But there is a strong dependence of the electron mobility on the well width, and since high electron mobility is also very important to our experiments, we are limited in how narrow we can make our wells. This dependence arises from interface roughness scattering. The "GaAs-on-AlGaAs" interface is the predominant source of this scattering, as it tends to be rougher than the "AlGaAs-on-GaAs" interface [6]. This roughness gives a spatial dependence to the well width, which creates a spatial dependence to the energies of the eigenstate solutions for the electron in the quantum well and these become strong scattering centers. Empirically, and theoretically, the mobility is observed to depend on the sixth power of the well width [7]. The mobility of our electrons in the 180 Å wide wells is roughly $\mu = 5 \times 10^5$ cm^2/V s in the regime of our ν_T=1 work, this appears to be near the limit of tolerable mobilities.

Thus our double quantum well parameters are likely the current state-of-the-art for bilayer electron transport studies in the limit of zero interlayer tunneling.

1.2 SAMPLE PROCESSING

Our processing is done on a 5 mm x 5 mm square cleaved from the parent crystal wafer. We use standard photolithographic techniques, depicted in Fig. 1.3, to shape the region that

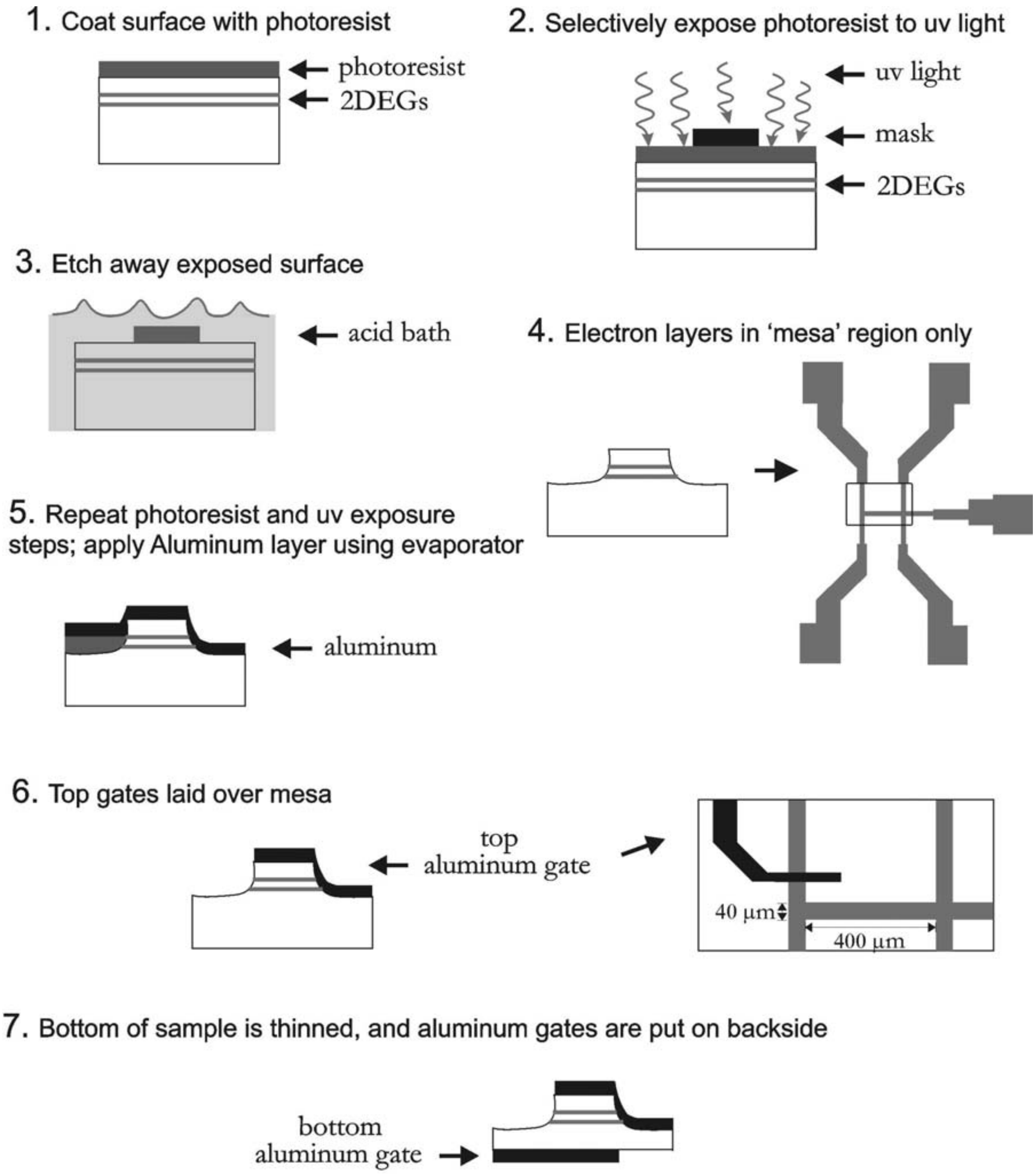
1. Coat surface with photoresist
photoresist
2DEGs
2. Selectively expose photoresist to uv light
uv light
mask
2DEGs
3. Etch away exposed surface
acid bath
4. Electron layers in 'mesa' region only
5. Repeat photoresist and uv exposure steps; apply Aluminum layer using evaporator
aluminum
6. Top gates laid over mesa
top aluminum gate
40 μm
400 μm
7. Bottom of sample is thinned, and aluminum gates are put on backside
bottom aluminum gate

Figure 1.3: Sample processing steps. 1. Sample is coated with photoresist. 2. A mask is put over the surface and ultraviolet light is shined on it. 3. The exposed crystal surfaces are etched away in an acid bath. 4. Only the unexposed surfaces still contain the electron layers, the picture on the right is the top view of the mesa pattern used for sample 'K'. 5. Photoresist, mask and ultraviolet exposure are repeated for gate pattern, and a thin layer of aluminum is evaporated onto the surface. 6. These make "top gates". 7. The sample is thinned and "bottom gates" are lithographed onto the backside.

the two-dimensional electrons occupy, and to lay down metallic structures on the surfaces to control the electrons by electrostatic gating.

The top side of the sample is processed first. The top side of the crystal is coated with photoresist as shown in step 1, Fig.1.3. Photoresist is an organic polymer which forms a tough acid-resistant barrier, but will break down when exposed to ultraviolet light. A glass mask with the desired electron region geometry patterned on it in ultraviolet-opaque iron oxide is placed on top of the photoresist, and then the whole ensemble is exposed to ultraviolet light (step 2, Fig. 1.3). This breaks down the photoresist everywhere except in the location of the mask pattern. Then by etching the crystal in an acid solution (step 3), the two-dimensional electron layers (2DEGs), located approximately 0.5 μm below the surface, are removed everywhere except in the patterned area. This creates a raised "mesa" on the crystal that contains the electron layers (step 4).

To lay down metallic gates on the top side, photoresist is again applied and covered with a glass mask with the desired gate pattern – this time transparent in the iron oxide background. Ultraviolet light exposure removes the photoresist where the gates will be. The sample is put in a thermal evaporator, and ~0.1 μm of aluminum are evaporated over the entire sample (step 5). When the residual photoresist is removed, only the metal in the patterned regions will remain on the sample (step 6).

The sample is then thinned. Originally ~500 μm thick, it is thinned to ~50 μm using a bromine-methanol etch. We thin the sample in order to bring the back gates, which will be processed onto the back surface, as close to the electron layers as possible. We are limited in how much we can reduce the distance between the electron layers and the bottom side of the crystal, as the sample becomes excessively brittle when it is thinned much below 50μm, and can not be handled without breaking.

The bottom side of the thinned sample is then lithographed with the pattern for the back gates and aluminum is evaporated into this pattern (step 7).

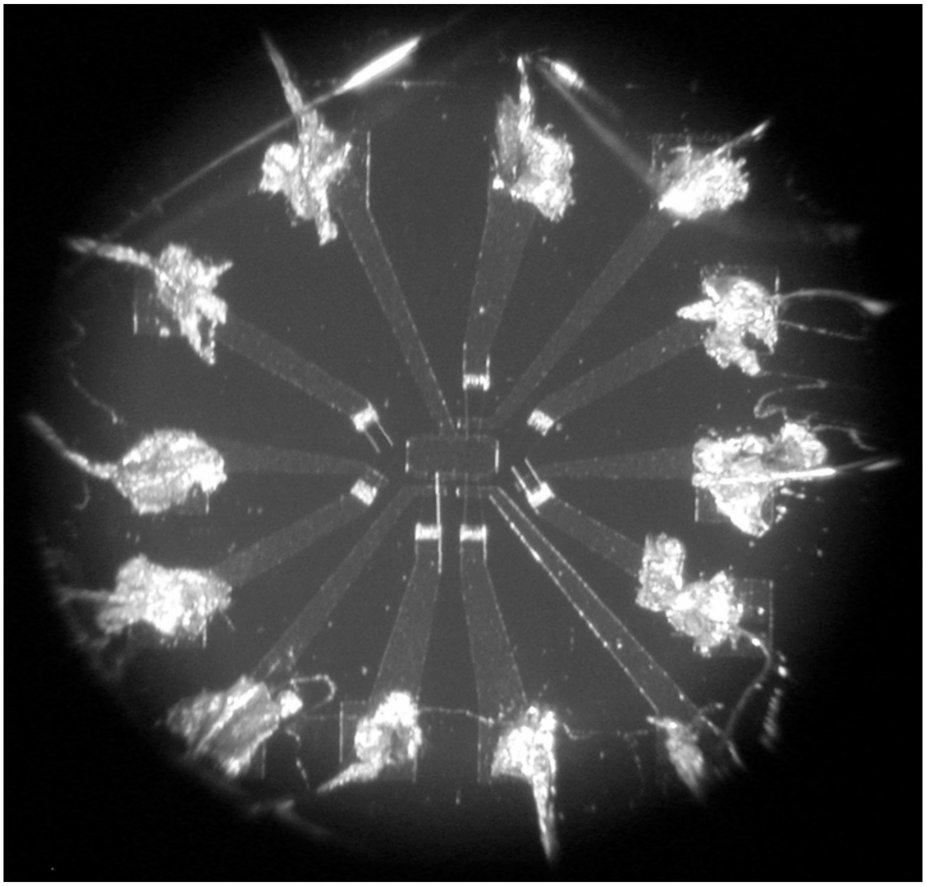

Figure 1.4: Top side of crystal after processing is complete. Small bright rectangles near center of photo are AuNiGe contacts. The larger bright shapes at the perimeter are Indium solder connections where thin gold wires are connected to the aluminum gates. The field of view is ~4 mm in diameter. Sample 'Y'.

Electrical contact is made to the electron layers by applying either indium [8] (with a soldering iron) or gold-nickel-germanium [9] (by thermal evaporation) in appropriate locations on the electron mesa. The metals are then diffused into the crystal by annealing and will come into contact with the electron layers. The diffused metal will interact with the conduction band profiles of the wells in such a way as to allow electronic access to the electron layers [8, 9]. The contacts and metal gates are then wired up to a standard DIP header for easy handling of the sample. Figure 1.4 shows the top surface of one of the crystals after it has been processed and wired up.

Detailed information on the sample processing can be found in Appendix A.

* * *

---

1 H.L. Stormer, R. Dingle, A.C. Gossard, W. Wiegmann and M.D. Sturge, Solid State Commun. **29**, 705 (1979).

2 J.J. Finley, *et al*., Phys. Rev. B **58**, 10619 (1998).

3 See Appendix K, program "dqwbiasandform".

4 J.H. Davies, *The Physics of Low-Dimensional Semiconductors* (Cambridge University Press, Cambridge 1998).

5 Loren Pfeiffer, personal communication.

6 Z. Liliental-Weber, H. Sohn and J. Washburn, *Imperfections in III/V Materials*, ed. E.R. Weber (Academic Press, Inc., Boston 1993).

7 H. Sakaki, T. Noda, K. Hirakawa, M. Tanaka and T. Matsusue, Appl. Phys. Lett. **51**, 1934 (1987).

8 J.M. Woodall, J.L. Freeouf, G.D. Pettit, T. Jackson and P. Kirchner, J. Vac. Sci. Technol. **19**, 626 & 794 (1981); A.A. Lakhani, J. Appl. Phys. **56**, 1888 (1984).

9 N. Braslau, J.B. Gunn and J.L. Staples, Solid State Electron. **10**, 381 (1967).

Chapter 2: Coulomb Drag

2.1 DEFINITION

In the Coulomb drag measurement a current I_x is driven into just one of the layers (called the "drive" layer) and the voltage, either longitudinal $V_{x,D}$ or Hall $V_{y,D}$ is measured in the other layer (the "drag" layer), which is kept electrically open (see Fig. 2.1). Since under usual conditions the longitudinal voltage $V_{x,D}$ will be negative, the longitudinal drag resistivity $\rho_{xx,D}$ is defined by convention as:

$$\rho_{xx,D} = \frac{-V_{x,D}}{I_x \cdot L/W} \tag{2.1}$$

so that the drag resistivity is usually a positive number. L/W is the length of sample L that the voltage is measured along divided by the width W of the sample, also referred to as a "square".

The convention for the Hall drag measurement $\rho_{xy,D}$ is to define the Hall drag voltage $V_{y,D}$ as positive if it has the same sign as the Hall voltage in the drive layer. Then the Hall drag resistivity will be:

$$\rho_{xy,D} = \frac{V_{y,D}}{I_x}. \tag{2.2}$$

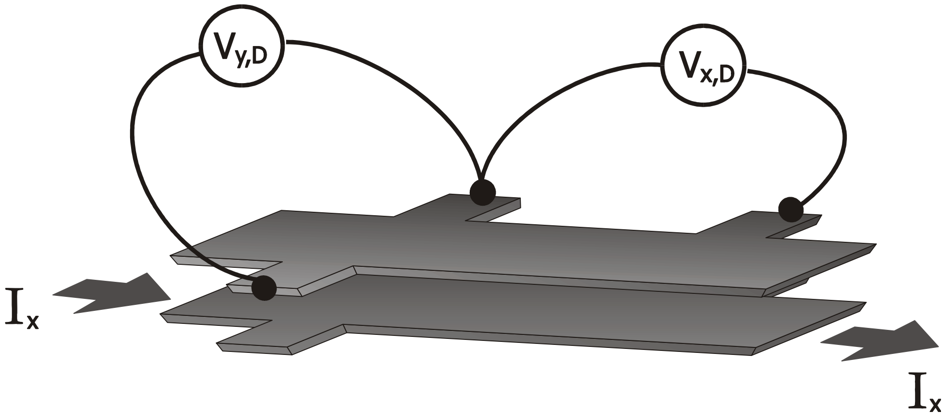

Figure 2.1: In the Coulomb drag measurement, current is sent through just one of the layers (the drive layer). The other layer (the drag layer) is kept open, and voltages are measured in this layer in response to current in the drive layer.

2.2 FREE ELECTRON MODEL OF COULOMB DRAG

Coulomb drag is a unique transport measurement in that it directly measures electron-electron scattering rates – independent of other electron scattering processes (such as phonon, impurity, and defect scattering) in the individual layers. Measurements at zero magnetic field are especially useful because the electron systems are relatively simple to model theoretically.

A simple Drude model [1] of the drag at zero magnetic field can give a nice elementary-level understanding of the physical mechanism for the drag resistivity and so is worth going through here. In the Drude picture, current is modeled as free electrons moving under the influence of an electric field, but frustrated in their motions by scattering events with phonons, impurities and defects, and as a result move at a steady state velocity called the drift velocity υ_{drift}. The two-dimensional current density J_{2D} in the drive layer can then be given by:

$$J_{2D} = n_{2D} e\, \upsilon_{drift} \tag{2.3}$$

where n_{2D} is the two-dimensional electron density in the layer and e is the charge of the electron.

Although the electrons remain in their respective layers, because of the long range Coulomb force they will affect one another's motion by scattering off each other. Some of the momentum of the current in the drive layer can be transferred to the drag layer by these scattering events. The time it takes to transfer the full momentum of a drive layer electron $m^* \upsilon_{drift}$ (where m^* is the effective mass of the electron) to a drag layer electron defines the mean interlayer momentum relaxation time τ_D. This momentum will push the drag layer electrons to one end, causing a voltage to build up in that layer (see Fig. 2.2). Notice that this will be a longitudinal voltage. The force from this electric field E_D in the drag layer will balance the momentum transfer rate due to the scattering:

$$eE_D = \frac{m^* \upsilon_{drift}}{\tau_D}. \tag{2.4}$$

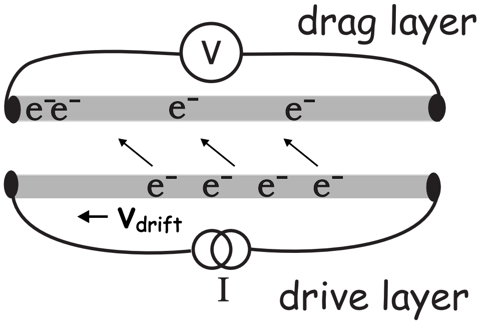

Figure 2.2: In the free electron model of Coulomb drag, electrons in the drive layer transfer their momentum to electrons in the drag layer through long-distance scattering events that cause a voltage to build up along the drag layer.

So, the electric field in the drag layer is a direct measure of the interlayer momentum relaxation time τ_D. To express this in terms of the longitudinal drag resistivity $\rho_{xx,D}$, we define the longitudinal drag resistivity:

$$\rho_{xx,D} = \frac{E_D}{J_{2D}}. \tag{2.5}$$

Combining equations (2.3), (2.4), and (2.5), an expression for the drag resistivity can be derived:

$$\rho_{xx,D} = \frac{m^*}{n_{2D} e^2 \tau_D} \tag{2.6}$$

Thus the longitudinal drag, for a known electron density and effective mass, directly measures the interlayer momentum relaxation time due to electron-electron scattering.

2.3 ELECTRON-ELECTRON SCATTERING IN METALS

The theory of electron-electron scattering (in metals) was first addressed by Landau and Pomeranchuk in 1936 [2]. They found that the contribution of electron-electron scattering to the resistivity would go as $\rho_{ee} = A_{ee}T^2$ (for $T \ll T_F$ where T_F is the Fermi temperature; true for all metals at room temperature), where A_{ee} is constant for a given material and tends to be very small relative to the electron-phonon/impurity/defect scattering contributions.

The T^2 dependence arises from Pauli restrictions on the phase space available for scattering. In order for a scattering event to take place, there must be a vacant state available for an electron to scatter into. And any gain in energy in one layer must have a corresponding loss of energy in the other layer. The largest loss of energy possible will be on the order of k_BT, where k_B is the Boltzmann constant, because there will be a "fuzziness" in the occupancy statistics at the edge of the Fermi disk of that order, as per the Fermi-Dirac distribution function:

$$f = \frac{1}{\exp\left(\frac{E-\mu}{k_BT}\right)+1}. \tag{2.7}$$

The vast majority of electrons, those occupying *k*-states in the bulk of the Fermi disk, won't be able to scatter, as all the states up to k_BT away are occupied. Roughly speaking, only the electrons in the region of width $\sim k_BT$ at the edge of the Fermi disk are able to participate in scattering events. Since the number of electrons in each layer available for scattering increases linearly with T; the number of scattering events will go up as T^2.

A_{ee} is very small because normal electron-electron collisions conserve total electron momentum (in a translationally invariant system), and so do not effect the net charge flow; but umklapp processes [3], which involve the reciprocal lattice vector, do not conserve the total electron momentum and although these processes are rare, they are the main contributor to A_{ee} [4].

There have been clever schemes over the years for detecting ρ_{ee} amidst the much larger contributions to the total resistivity from the other scattering processes. Since electron-impurity scattering is temperature independent, it can be distinguished from the temperature dependent $\rho_{ee}(T)$ provided the temperature is sufficiently low to suppress the most dominant temperature dependent scattering process: electron-phonon scattering. The first reported measurements of ρ_{ee} were obtained in the metals Indium and Aluminum by this method [5, 6].

Comparisons between the thermal and electrical conductivities in alkali metals were the next method used to infer the electron-electron scattering rate [7]. The normal scattering processes while not affecting charge flow, do impede heat flow, causing detectable deviations in the Wiedemann-Franz law at high temperatures [8].

Much later, electron-electron scattering was probed in two-dimensional systems via their dephasing effect [9, 10] – the destruction of quantum interference effects studied on length scales shorter than the mean free path – and by their resistivity contributions in translationally non-invariant systems [11]. However Coulomb drag is the only technique that directly measures electron-electron scattering.

2.4 BOLTZMANN MODEL OF DRAG SCATTERING

Jauho and Smith (JS) [12] were the first to publish an explicit equation to predict the drag as a function of temperature, layer separation, well width and electron density. (Allan MacDonald was the first to derive it, but only published the end result [24].) Their equation is constructed primarily from linearized Boltzmann transport theory, but incorporates quantum mechanics for the formulation of the scattering term. Purely quantum formulations of Coulomb drag reduce to Boltzmann theory in the long mean free path limit [13-15], and for near equilibrium situations (one where low drive currents are used), the linearized theory is sufficiently accurate. Since we use very low drive currents (0.5 to 20 nA) and since our samples have very high mobility ($\mu \sim 10^6 cm^2 / V \cdot s$), their equation should suit our system very well.

Their equation is based on the basic scattering event depicted in Fig. 2.3. An electron in the drive layer is scattered from initial momentum state $\mathbf{k}_2$ to final momentum state $\mathbf{k}_{2'}$ in an interaction with an electron in the drag layer scattered from initial state $\mathbf{k}_1$ to final state $\mathbf{k}_{1'}$. The momentum transferred in the interaction is $\mathbf{q} = \mathbf{k}_{1'} - \mathbf{k}_1$.

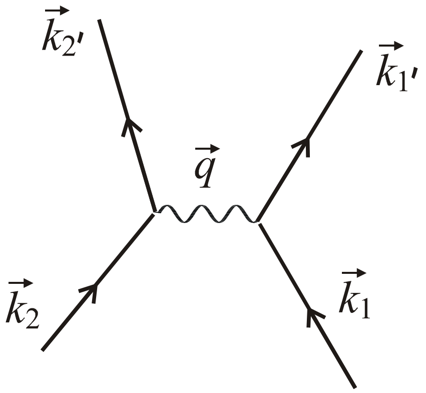

Figure 2.3: Scattering event between an electron in the drive layer (subscript 2) and an electron in the drag layer (subscript 1). Initial momentum states are unprimed, final states are primed. q is the wavevector characterizing the momentum transferred in the scattering event.

I start with their most basic derived equation (eqns. 13 and 16 in ref. 12):

$$\frac{eE_1 n_1}{\hbar} = -\frac{e\hbar E_2 \tau_2}{4m^* k_b T} \sum_{\sigma_1,\sigma_2,\sigma_{1'},\sigma_{2'}} \int \frac{d\mathbf{k}_1}{(2\pi)^2} \int \frac{d\mathbf{k}_2}{(2\pi)^2} \int \frac{d\mathbf{k}_{1'}}{(2\pi)^2} w(1,2;1',2') q^2 f_1^0 f_2^0 (1-f_{1'}^0)(1-f_{2'}^0)$$
$$\times \delta(\varepsilon_1 + \varepsilon_2 - \varepsilon_{1'} - \varepsilon_{2'}) \tag{2.8}$$

The subscripts i = (1, 2) refer to the (drag, drive) layer; E_i, n_i, τ_i are to the electric field, electron density and momentum relaxation time in layer i; m^* is the effective mass of the electron; f_i^0 is the equilibrium Fermi distribution function in layer i; $\mathbf{k}_i, \varepsilon_i$, σ_i are the wavevector, energy, and spin of a specific electron in layer i, (primed indices represent final states, unprimed are initial states); and $w(1,2;1',2')$ is the probability that two electrons in states $\mathbf{k}_1 \sigma_1$ and $\mathbf{k}_2 \sigma_2$ will scatter to $\mathbf{k}_{1'} \sigma_{1'}$ and $\mathbf{k}_{2'} \sigma_{2'}$.

This equation simply integrates over all possible scattering events from every possible initial and final momentum state in each of the layers. Momentum conservation fixes the final momentum state of the drive layer electron if the three other initial and final states are known, so there is no integration over $\mathbf{k}_{2'}$. Energy conservation is ensured by the delta function in the integrand. Phase space availability is monitored in the four Fermi distribution function terms. The q^2 term weights the scattering events – large q scattering is more efficient at transferring net momentum to the drag layer, and so large q events get more heavily weighted (see Section 3.3). $w(1,2;1',2')$ tells the likelihood of a given scattering event regardless of phase space availability – this is the term that incorporates the Coulomb interactions between the electrons that cause them to scatter in the first place.

Combining eqn. 2.6 with the identity offered in (JS): $\frac{E_1}{E_2}=\frac{\tau_2}{\tau_D}$, equation 2.8 can be written as:

$$\rho_{xx,D} = -\frac{\hbar^2}{4n_2n_1e^2k_BT}\sum_{\sigma_1,\sigma_2,\sigma_{1'},\sigma_{2'}}\int\frac{d\mathbf{k}_1}{(2\pi)^2}\int\frac{d\mathbf{k}_2}{(2\pi)^2}\int\frac{d\mathbf{k}_{1'}}{(2\pi)^2}w(1,2;1',2')q^2 \times f_1^0 f_2^0(1-f_{1'}^0)(1-f_{2'}^0)\delta(\varepsilon_1+\varepsilon_2-\varepsilon_{1'}-\varepsilon_{2'}), \tag{2.9}$$

where the integration in each dimension goes from -∞ to ∞.

Some of these integrals have even symmetry, for those $\int_{-\infty}^{\infty} dx$ will be replaced by $2\int_0^{\infty} dx$.

One of the integration variables can be dropped by taking advantage of the symmetry of the integral to rotation of the $\mathbf{k}_1$ axes, and so I can rewrite that integral as:

$$\int_{-\infty}^{\infty} \frac{d\mathbf{k}_1}{(2\pi)^2} = \frac{1}{2\pi}\int_{0}^{\infty} k_{1y} dk_{1y} \tag{2.10}$$

setting $k_{1x} = 0$.

By again invoking rotational symmetry and by integrating over the delta function, I can remove still another integration variable. Unlike JS, I do not dispatch the delta function by bringing in the susceptibility function $\chi(q,\omega)$. These susceptibility functions are difficult to evaluate for $T \neq 0$ and JS simply use the $T = 0$ expression throughout their paper. Although using the susceptibility function removes two more integration variables than my method does, my method remains accurate for all temperatures.

To illustrate my method, I will address just the parts of the equation which depend on $\mathbf{k}_2$ (it is reasonable to assume that $w(1,2;1',2') = w(q,\omega)$ and does not explicitly depend on $\mathbf{k}_2$ [12]):

$$\int \frac{d\mathbf{k}_2}{(2\pi)^2} f^0(\varepsilon_2)\left[1 - f^0(\varepsilon_{2'})\right]\delta(\varepsilon_2 - \varepsilon_{2'} + \varepsilon_1 - \varepsilon_{1'}) \,. \tag{2.11}$$

Because of the symmetry of the distribution function, I can rotate my axes of integration so that they run parallel and perpendicular to the **q** determined by k_{1y}, $k_{1'x}$ and $k_{1'y}$. And rather than integrate over k_{2x} and k_{2y}, I instead integrate over $k_{2\parallel}$ and $k_{2\perp}$ (see Fig. 2.4). This greatly simplifies the integration.

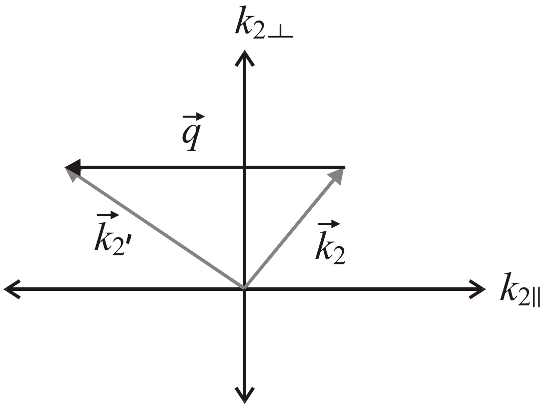

Figure 2.4: Novel integration axes for initial momentum states in drive layer. By rotating the axes parallel $k_{\|}$ and perpendicular $k_{\perp}$ to q the integral can be simplified.

Recalling the electronic energy dispersion relations:

$$\varepsilon_2 = \frac{\hbar^2}{2m^*}\left(k_{2\|}^2 + k_{2\perp}^2\right) \tag{2.12}$$

$$\varepsilon_{2'} = \frac{\hbar^2}{2m^*}\left(k_{2'\|}^2 + k_{2'\perp}^2\right) \tag{2.13}$$

and using $k_{2\perp} = k_{2'\perp}$, I get the following relation:

$$\varepsilon_2 - \varepsilon_{2'} = \frac{\hbar^2}{2m^*}\left(k_{2\|}^2 - k_{2'\|}^2\right) \tag{2.14}$$

Then using the identity $k_{2'\|} = k_{2\|} - q$:

$$k_{2'\|}^2 = k_{2\|}^2 - 2qk_{2\|} + q^2 , \tag{2.15}$$

which leads to

$$\varepsilon_2 - \varepsilon_{2'} = \frac{\hbar^2}{2m^*}\left(2qk_{2\|} - q^2\right), \tag{2.16}$$

and so
$$d(\varepsilon_2 - \varepsilon_{2'}) = \frac{\hbar^2 q}{m^*} dk_{2\parallel} \qquad (2.17)$$

Making this substitution, the $d\mathbf{k}_2$ part of the integral reduces to:

$$\frac{m^*}{2\pi\hbar^2 q}\int \frac{dk_{2\perp}}{2\pi}\int d(\varepsilon_2 - \varepsilon_{2'}) f^0(\varepsilon_2)\left[1 - f^0(\varepsilon_{2'})\right]\delta(\varepsilon_2 - \varepsilon_{2'} + \varepsilon_1 - \varepsilon_{1'})$$

$$= \frac{m^*}{4\pi^2\hbar^2 q}\int dk_{2\perp}\{f^0(\varepsilon_2)\left[1 - f^0(\varepsilon_{2'})\right]\}_{evaluated\, at\, \varepsilon_2 - \varepsilon_{2'} + \varepsilon_1 - \varepsilon_{1'} = 0} \qquad (2.18)$$

This conservation of energy requires that:

$$\varepsilon_2 = \frac{\hbar^2}{2m^*}\left[k_{2\perp}^2 + \frac{q^2}{4} + \frac{\omega^2}{4q^2} - \frac{\omega}{2}\right] \qquad (2.19)$$

$$\varepsilon_{2'} = \frac{\hbar^2}{2m^*}\left[k_{2\perp}^2 + \frac{q^2}{4} + \frac{\omega^2}{4q^2} + \frac{\omega}{2}\right] \qquad (2.20)$$

where

$$q^2 = (k_{1'x})^2 + \ (k_{1'y} - k_{1y})^2 \qquad (2.21)$$

and
$$\omega \equiv \left(k_{1y}^2 - k_{1'x}^2 - k_{1'y}^2\right) \qquad (2.22)$$

The integral is now:

$$\rho_{xx,D} = \frac{-m^*}{32\pi^5 n_2 n_1 e^2 k_B T}\sum_{\substack{\sigma_1,\sigma_2,\\ \sigma_{1'},\sigma_{2'}}}\int_0^\infty dk_{1y}\int_0^\infty dk_{1'x}\int_{-\infty}^\infty dk_{1'y} w(q,\omega) k_{1y} q \int_0^\infty dk_{2\perp} f_1^0 f_2^0 (1 - f_{1'}^0)(1 - f_{2'}^0).$$

(2.23)

As is, this equation should be a very accurate model of our system. But in order to evaluate this integral, an expression must be chosen for the collision probability $w(q,\omega)$. Here is where the equation becomes less exact. Assumptions and simplifications must be made in order to evaluate this term.

As a starting point, JS invoke Fermi's golden rule:

$$w(q,\omega)=\frac{2\pi}{\hbar}\left|V(q)\right|^2 \tag{2.24}$$

to evaluate the collision probability. Here the assumption is that the scattering potential is weak: the Born approximation. This approximation is good in the same long mean free path limit for which Boltzmann theory holds, however it is good to keep in mind that there are higher order terms that are being neglected and that this approximation does not account for interference effects such as weak localization. There is also an implicit assumption in this method that the conductivity of a single layer is linearly dependent on the density [16], which is not what we observe. However, at zero magnetic field, this should not be too important [16]. So I have followed JS' lead and use the Born approximation in my version of their integral.

The next set of assumptions comes in evaluating the potential $V(q)$. JS use a screened Coulomb potential; the bare potential of a single electron is being screened by the electrons both within the same layer and those in the other layer. The choice of screening theory affects the difficulty and the accuracy of the equation.

The simplest theory (and the one JS use) is the static screening Thomas-Fermi (TF) approximation. This approximation excludes dynamical screening effects such as coupled plasmon modes, which are a sort of anti-screening which enhances the drag. This mode becomes important when $T \gtrsim 0.2T_F$ [17]. Also excluded are electron correlation effects [18, 19] , multi-particle excitations [20], enhanced disorder effects[13, 18], and phonon-mediated electron-electron scattering [21]. The latter is not an important process in our samples (see Section 3.2.1), but inclusion of the other effects would likely improve the quantitative agreement of the integral with the data. However, for understanding qualitative effects, such as the peak in the drag at balanced densities below some critical temperature observed in Section 3.4, which is fundamentally a phase space effect, it is sufficient to use the simpler TF screening model for the potential $V(q)$, and so I do.

TF screening is identical to static Random Phase Approximation (RPA) screening (in the zero temperature limit) for $q \leq 2k_F$, where $k_F = \left(2\pi n\right)^{1/2}$ is the Fermi momentum and begins to deviate from static RPA for $q > 2k_F$. RPA screening can be approximated for $q > 2k_F$ by adding a simple function to the TF formulation that should mimic static RPA; this function can be found in reference 22. For the Coulomb drag parameters explored in this thesis (primarily in Chapter 3), this additional function made very little difference in the results, so I have just kept to the TF approximation used in the paper.

In the TF approximation the collision term is given by (see eqns. 22 and 25 in JS):

$$\sum_{\substack{\sigma_1,\sigma_2,\\ \sigma_{1'},\sigma_{2'}}} w(q,\omega) = \frac{2\pi}{\hbar} 4 \left| \frac{2\pi e^2}{4\pi\varepsilon_0 \kappa q_{TF}} \frac{q/q_{TF}}{A^{-1}(B+q/q_{TF})^2 - A} \right|^2 \tag{2.25}$$

Where κ is the dielectric constant (~12.8 for GaAs) and q_{TF} is the TF screening wavevector:

$$q_{TF} = \frac{2m^* e^2}{4\pi\varepsilon_0 \kappa \hbar^2} \approx 1.977\times10^8\,\mathrm{m}^{-1} \text{ (for GaAs electrons)}, \tag{2.26}$$

while A and B contain information on the form factors associated with the shape of the wavefunction of the electrons confined in the wells. It is sufficient to assume that the wavefunction takes on a half-cosine shape inside the well and is zero outside of the well, then (see eqns. A16 and A17 in JS):

$$A = e^{-qd}\left(\sinh\frac{qL}{2}\right)^2 \left(\frac{8\pi^2}{qL(4\pi^2+q^2L^2)}\right)^2; \tag{2.27}$$

$$B = \frac{2}{qL} + \frac{qL}{4\pi^2+q^2L^2} - e^{-qL/2}\sinh\frac{qL}{2}\left(\frac{8\pi^2}{qL(4\pi^2+q^2L^2)}\right)^2 \tag{2.28}$$

where d is the center-to-center separation between the wells and L is the well width. Alternately, the form factors can be computed from a more realistic wavefunction that itself is computed from a program, such as one that Jim Eisenstein wrote [23], which calculates the wavefunction for a specified conduction band profile and electron density. This exercise mainly shows that it is sufficient to use the cosine approximation. To calculate the form factor coefficients from a more realistic wavefunction, use equation (A8) in JS.

Now including the expression for the collision probability, and summing over spins, the integral I use for calculating Coulomb drag reaches its final form:

$$\rho_{xx,D} = \frac{m^* e^2}{\pi^2 k_B T \hbar \kappa^2 q_{TF}^4 n_2 n_1 \left(4\pi\varepsilon_0\right)^2} \int_0^\infty dk_{1y} \int_{-\infty}^\infty dk_{1'y} \int_0^\infty dk_{1'x} \left\{ \frac{k_{1y} q^3 f(E_1)\left[1 - f(E_{1'})\right]}{\left[A^{-1}\left(B + \frac{q}{q_{TF}}\right)^2 - A\right]^2} \int_0^\infty dk_{2\perp} f(E_2)\left[1 - f(E_{2'})\right] \right\} \tag{2.29}$$

This integral assumes: low drive current, high mobility, the Born approximation and Thomas-Fermi screening. There are Fortran programs in Appendix K that numerically solve this integral for a range of T, n_1, n_2, m^*, d, and L.

2.4.1 A LIMITING CASE

A simplified version of this equation can be derived analytically, as was done first by Gramila *et al.* [24] and then by Jauho and Smith [12]. This requires certain assumptions to be made about the conditions in actual drag experiments. In addition to the simplifications used above, Thomas-Fermi screening and the Born approximation, the assumptions that $T / T_F \ll 1$ and $k_F d \gg 1$ reduce the drag integral to:

$$\rho_{xx,D} = \frac{m^* \pi \zeta(3) k_B T^2}{16\, e^2 n \hbar T_F (q_{TF} d)^2 (k_F d)^2} . \tag{2.30}$$

At the time, $T/T_F \ll 1$ was a reasonable assumption, as the lowest electron density per well of the samples studied at the time was $n \approx 1.5\times10^{11}\,\mathrm{cm}^{-2}$ [24], which has a Fermi temperature of $T_F \approx 60\,\mathrm{K}$, much larger than the cryogenic temperatures probed at the time (as low as $T \approx 0.3\,\mathrm{K}$).

The assumption $k_F d \gg 1$, was somewhat reasonable: $k_F \approx 10^8\,\mathrm{m}^{-1}$ for the above density and $d \approx 375\times10^{-10}\,\mathrm{m}$ was the smallest layer separation used. When $k_F d \gg 1$ only small-angle scattering makes an important contribution to the drag. Large-angle scattering is suppressed when the layers are relatively far apart (relative to ${k_F}^{-1}$), because the small wavelength (large q) components of the Fourier transform of the Coulomb potential of one layer, can not be resolved by the other layer a distance d away. The Fourier transform of the bare Coulomb interaction contains a factor e^{-qd}; by Fermi's Golden Rule (eqn. 2.24) this inhibits scattering events with large momentum transfer q by the same factor squared. Large-angle scattering means large momentum transfer scattering and corresponds to $q \to 2k_F$.

Equation 2.30 predicts the temperature $\rho_{xx,D} \propto T^2$, density $\rho_{xx,D} \propto n^{-3}$ $\left(T_F, k_F^2 \propto n\right)$ and layer separation $\rho_{xx,D} \propto d^{-4}$ dependence of the Coulomb drag under (at the time) likely experimental conditions.

2.5 HISTORY OF COULOMB DRAG

Drag experiments were first performed in 1960 by Hubner and Shockley between two thin (but not two-dimensional) layers of electrons in a semiconductor-insulator-semiconductor structure fashioned from a boron-doped silicon wafer [25]. Because their layers were relatively far apart (~100 μm), they were for the most part measuring phonon-assisted electron-electron scattering. In phonon-assisted scattering, an electron in one layer scatters with a phonon, which then travels to the other layer and scatters an electron there, and so their measurements do not give information on direct electron-electron interactions.

Coulomb drag was first considered theoretically, again for two thin films of electrons in a semiconductor-insulator-semiconductor structure, in 1977 by the Russian theorist M. B. Pogrebinskii [26]; and later for two-dimensional electron layers in GaAs/AlGaAs heterostructures by Peter Price in 1983 at IBM [27].

But Coulomb drag experiments would not be attempted again until technical advances in molecular beam epitaxy allowed for the precision construction of GaAs/AlGaAs heterostructures with layer thicknesses a thousand times smaller than Hubner and Shockley's samples – engendering much stronger electron-electron interactions. In 1989, IBM scientist Solomon *et al.* made the first drag measurements between a 2D layer and a 100 nm thick 3D layer [28]. The first drag measurements between two 2D layers were made soon after by Gramila *et al.* at Bell Labs [24]. Then there were Coulomb drag measurements between a 2D layer of electrons and a 2D layer of holes, also at IBM [29].

Currently, 2D-2D Coulomb drag measurements continue to be performed in labs around the world [30].

* * *

---

1 N.W. Ashcroft and N.D. Mermin, *Solid State Physics* (Saunders College, Philadelphia 1976).

2 L.D. Landau and I. Pomeranchuk, Phys. Z. Sowjet **10**, 649 (1936).

3 C. Kittel, *Introduction to Solid State Physics* (John Wiley & Sons, Inc., New York 1996).

4 Jack Bass, William P. Pratt, Jr. and Peter A. Schroeder, Rev. Mod. Phys. **62**, 645 (1990).

5 J.C. Garland and R. Bowers, Phys. Rev. Lett. **21**, 1007 (1968).

6 J.H.J.M. Ribot, J. Bass, H. van Kempen and P. Wyder, J. Phys. F. Met. Phys. **9** (6), L117 (1979).

7 J.G. Cook, M.P. Van der Meer and M. J. Laubitz, Can. J. Phys. **50** (12), 1386 (1972); J.G. Cook, Can. J. Phys. **57** (8), 1216 (1979).

8 M.J. Laubitz, Phys. Rev. B **2**, 2252 (1970).

9 G. Bergmann, Phys. Rep. **107**, 1 (1984).

10 A. Yacoby, U. Sivan, C.P. Umbach and J.M. Hong, Phys. Rev. Lett. **66**, 1938 (1991).

11 A. Messica, A. Soibel, U. Meirav, Ady Stern, Hadas Shtrikman, V. Umansky and D. Mahalu, Phys. Rev. Lett. **78**, 705 (1997).

12 A.P. Jauho and H. Smith, Phys. Rev. B **47**, 4420 (1993).

13 L. Zheng and A.H. MacDonald, Phys. Rev. B **48**, 8203 (1993).

14 M. C. Bonsager, K. Flensberg, B. Y. K. Hu and A. H. MacDonald, Phys. Rev. B **57**, 7085 (1998).

15 K. Flensberg, B.Y. K. Hu, A. P. Jauho and J. M. Kinaret, Phys. Rev. B **52**, 14761 (1995).

16 F. von Oppen, S. H. Simon and A. Stern, Phys. Rev. Lett. **87**, 106803 (2001).

17 K. Flensberg and B. Y. K. Hu, Phys. Rev. Lett. **73**, 3572 (1994).

18 E. H. Hwang, S. Das Sarma, V. Braude and A. Stern, Phys. Rev. Lett. **90**, 086801 (2003).

19 A. Yurtsever, V. Moldoveanu and B. Tanatar, Solid State Comm. **125**, 575 (2003).

20 H. Noh, et al., Phys. Rev. B **58**, 12621 (1998).

21 H. Noh, S. Zelakiewicz, T. J. Gramila, L. N. Pfeiffer and K. W. West, Phys. Rev. B **59**, 13114 (1999).

22 T. Ando, A. B. Fowler and F. Stern, Rev. Mod. Phys. **54**, 437 (1982). See especially p. 450.

23 See Appendix K, program "dqwbiasandform".

24 T.J. Gramila, J.P. Eisenstein, A.H. MacDonald, L.N. Pfeiffer and K.W. West, Phys. Rev. Lett. **66**, 1216 (1991).

25 Kurt Hubner and William Shockley, Phys. Rev. Lett. **4**, 504 (1960); Science **132**, 1494 (1960).

26 M.B. Pogrebinskii, Sov. Phys. Semicond. **11**, 372 (1977).

27 P.J. Price, Physica B & C, **117**, 750 (1983).

28 P.M. Solomon, P.J. Price, D.J. Frank and D.C. La Tulipe, Phys. Rev. Lett. **63**, 2508 (1989).

29 U. Sivan, P.M. Solomon and H. Shtrikman, Phys. Rev. Lett. **68**, 1196 (1992).

30 M. Kellogg, J.P. Eisenstein, L.N. Pfeiffer and K.W. West, Phys. Rev. Lett. **90**, 246801 (2003); R. Pillarisetty, H. Noh, D.C. Tsui, E.P. de Poortere, E. Tutuc and M. Shayegan, Phys. Rev. Lett. **89**, 016805 (2002); C. Jorger, S.J. Cheng, W. Dietsche, R. Gerhardts, P. Specht, K. Eberl and K. von Klitzing, Physica E **6** (1-4), 598 (2000); N.P.R. Hill, J.T. Nicholls, E.H. Linfield, M. Pepper, D.A. Ritchie, B.Y.K. Hu and K. Flensberg, Physica B **251**, 868 (1998); S. Zelakiewicz, H. Noh, T.J. Gramila, L.N. Pfeiffer and K.W. West, Phys. Rev. Lett. **85**, 1942 (2000).

Chapter 3: Coulomb Drag at B=0

Coulomb drag measurements in zero magnetic field give information on basic electron-electron scattering processes with unprecedented clarity; and with a wide range of parameter space to explore. Not only can we measure the temperature dependence of the scattering, but we can also vary the electron density, as well as create a density imbalance between the two layers by establishing different densities in each layer.

3.1 SAMPLE: 'K'

The data shown in this chapter (and thesis) was obtained from a single wafer. This wafer was used for the experiments because of its very low tunneling. It is discussed in detail in Chapter 1. To reiterate here: the wells are 180 Å wide GaAs, separated by a 100 Å wide $Al_{0.9}Ga_{0.1}As$ barrier and embedded in thick $Al_{0.3}Ga_{0.7}As$ cladding layers. It has been symmetrically silicon δ-doped, setback approximately 2000 Å from the wells on each side.

This data is from a 5 mm x 5 mm piece taken from the center of the wafer and is called sample 'K'. The central region of the mesa is a 40 μm x 400 μm bar with 5 arms extending out of it for electrical contact (see Fig. C.3 for sample map and Fig. 3.1 for a photo of this

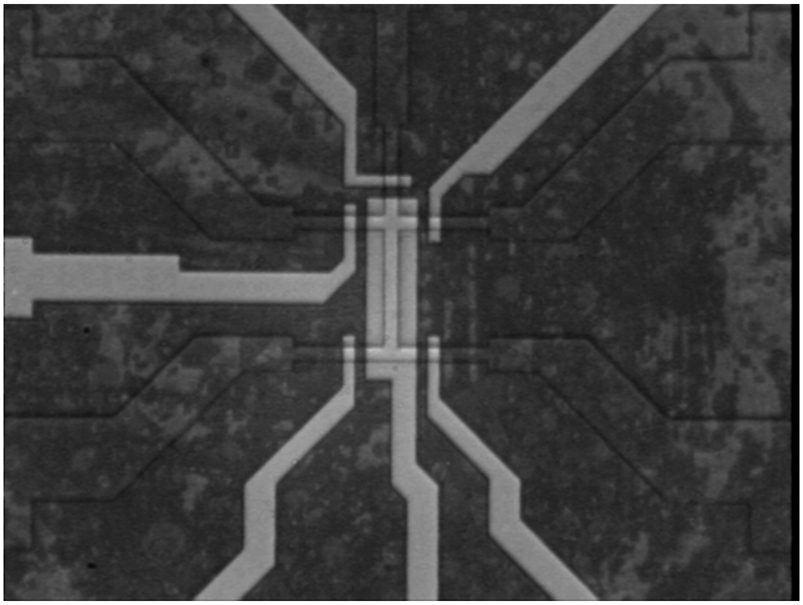

Figure 3.1: Picture of top side of sample 'K' showing the mesa structure in faint outline with its central 40 μm x 400 μm bar. The lighter regions are the top side aluminum gates. Field is ~2mm across.

sample). For this sample, contact was made by putting indium [2] at the ends of the arms, on the large "contact pads" located there, using a miniature soldering iron. Then the sample was annealed at 440°C for 10 minutes in a 15% H_2, 85% N_2 environment and wired up as usual. The nominal density in each well was 5.3 x 10^{10} cm^{-2}, the mobility 1 x 10^6 cm^2/Vs [3] and the tunneling resistance at resonance $R \approx 500\ \text{M}\Omega$. The density in the central mesa region was controlled by electrostatic gates above and below the central bar. We could achieve densities as low as 1.7 x 10^{10} cm^{-2} and as high as 8.8 x 10^{10} cm^{-2} per layer by applying voltages to these gates. The densities in the two layers were matched by finding the gate voltages that maintained a positive drag signal in the high Landau levels [4].

3.2 LONGITUDINAL DRAG VERSUS TEMPERATURE

Figure 3.2 shows the temperature dependence of the longitudinal Coulomb drag at nominal density with a 20 nA, 13 Hz drive current. This data represents the largest nominal density electron-electron Coulomb drag signal measured at zero magnetic field, at this time. This is because interlayer electron-electron scattering is strongly dependent on the inverse of the electron density and layer separation (see Section 2.4.1), and the as-grown densities of our quantum wells are less than half that of the quantum wells used in the previously published Coulomb drag experiments [5]. The center-to-center well separation of 280 Å is also smaller than the prior experiments (of those done in the low-tunneling regime, and consequently our nominal density drag signal is two orders of magnitude larger than any other electron-electron drag published at zero magnetic field.

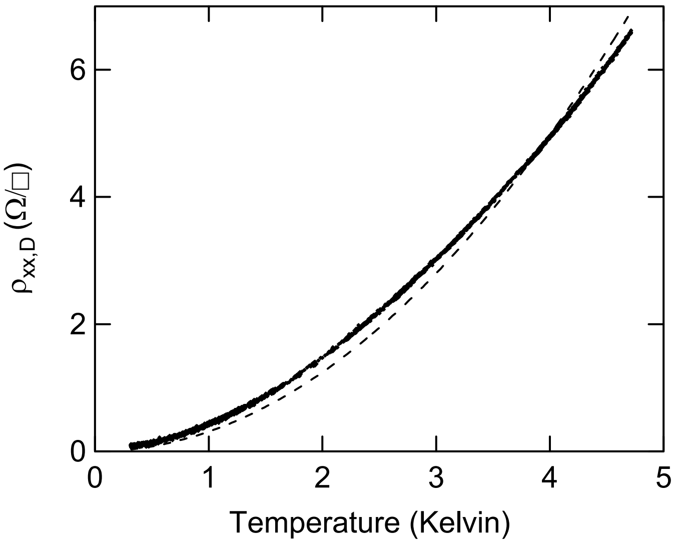

Figure 3.2: Longitudinal drag resistance vs. temperature taken at nominal density $n = 5.3 \times 10^{10} cm^{-2}$, dashed line shows a simple parabolic fit.

The significance of this, beyond the convenience of the larger signal-to-noise ratio, is that our drag is likely dominated by direct electron-electron scattering events, rather than phonon-mediated electron-electron scattering, which dominates much of the previously published drag. This means our data is directly probing the interlayer electron interactions.

Notice the nearly T^2 dependence as originally predicted by Landau and Pomeranchuk for electron-electron scattering in metals [6]. The dashed line corresponds to the equation $\rho_{xx,D}[\Omega/\square] = 0.372 \times T^2[K]$. This quadratic dependence on the temperature is evidence that we are indeed predominately measuring direct electron-electron scattering.

Although the T^2 dependence was calculated for electrons free to move in three dimensions, it holds roughly true for two-dimensional electrons as well. The two-dimensional nature of our electrons does necessitate a change of the shape of the Fermi surface used in Landau and Pomeranchuk's calculations from a sphere to a disk (or rather a cylinder), which creates $T^2 lnT$ corrections in the temperature dependence [7]. This is due to divergences in the phase space at low T for scattering processes with momentum changes $q \sim 0, 2k_F$, where k_F is the Fermi momentum – this is a uniquely two-dimensional phenomenon [8]. But as this term is expected to be very small, and the coefficient is unknown, there is little point in including this term in our fit as there are easily many two-parameter functions that would fit our data nicely, but for the curious:

$$\rho_{xx,D}[\Omega/\square] = 0.165 \times T^2[K] - 0.080 \times T^2[K]\ln(T/T_F), \qquad (3.1)$$

where the Fermi temperature is $T_F = 22.1K$, would fit the data nearly perfectly. This is a two-parameter fit to the data shown in Fig. 3.2 which includes the expected $T^2 lnT$ term.

Parenthetically, Zheng and MacDonald [9] also predict $T^2 lnT$ corrections in the drag scattering but for entirely different reasons. They say disorder in the sample will also create this correction term, but only at inaccessibly low temperatures; so we ignore this effect here.

3.2.1 SEARCH FOR PHONON-MEDIATED DRAG

We can look for subtle deviations from the T^2 behavior by dividing the drag resistivity by T^2 and then plotting $\rho_{xx,D}/T^2$ (see Fig. 3.3). In particular we can look for non-monotonic behavior in the temperature dependence, which is the hallmark of phonon-mediated Coulomb drag [10].

Phonon-mediated Coulomb drag hinges on electron-phonon scattering processes, which have a different temperature dependence than electron-electron scattering, mainly because phonons are bosons. Electron-phonon scattering is linear in T at high T because in this regime, large-angle scattering dominates the momentum transfer. The population of these efficacious $q = 2k_F$ phonons is given by the Bose-Einstein distribution function

$$n[\omega(2k_F)] = \frac{1}{\exp\left(\frac{\hbar\omega(2k_F)}{k_B T}\right) - 1} \tag{3.2}$$

which reduces to $n[\omega(2k_F)] \sim \frac{k_B T}{\hbar\omega(2k_F)}$ when $\hbar\omega(2k_F) \ll k_B T$. The scattering rate merely reflects this linear temperature dependence of the number of phonons available for scattering.

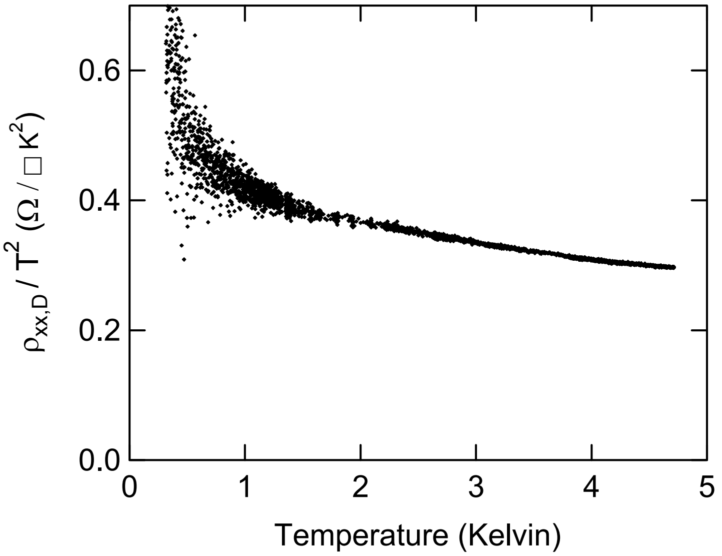

Figure 3.3: Longitudinal drag resistance divided by the temperature squared vs. temperature at nominal density (5.3×10^{10} cm^{-2}). Phonon-mediated processes exhibit a bump near the Bloch-Grüneisen temperature when the data is plotted in this manner; no bump is seen in our data.

But at low T, $q = 2k_F$ phonons become scarce and for more complicated reasons the scattering dependence will have T^5 and/or T^7 terms [11]; the scattering will drop dramatically as the temperature drops (this is called the Bloch-Grüneisen regime). The transition temperature between these two different behaviors is given by the Bloch-Grüneisen temperature $T_0 = \frac{\hbar s k_F}{k_B}$, where s is the sound velocity. In the data shown in

Fig. 3.3 this crossover would occur at approximately 1 K. With the data plotted as $\rho_{xx,D}/T^2$ this would be seen as a peak in the data near this transition temperature; but clearly there is no peak observed, indicating that phonon-mediated scattering is not a significant contributor to our drag resistivity.

This is consistent with earlier drag measurements, in which the largely d independent phonon-mediated drag was measured to be very small, in the range of $\rho_{xx,D}/T^2 \sim 1\ m\Omega/\Box K^2$, and showed little density dependence [12]. If our data includes a phonon-mediated drag signal of that order (which it presumably must), then it will be of negligible importance.

3.3 LONGITUDINAL DRAG VERSUS DENSITY

Figure 3.4 shows the longitudinal drag resistivity versus temperature at six different matched densities (the same density in each layer). The drag is observed to increase significantly with decreasing density – as was expected. The physical reasons for this are threefold: When the density in the drive layer is reduced, the drift velocity must increase to maintain the same current density ($J_{2D} = n_{2D} e\, \upsilon_{drift}$). A larger drift velocity yields a larger net momentum transfer per scattering event. But as the number of electrons available for scattering is independent of the density (the two-dimensional density of states is constant, and the number of electrons available for scattering is proportional to $k_B T$ times the density of states), the total net momentum transferred via scattering is increased. There is a competing effect in that the smaller momentum at the edge of the Fermi disk means more time between scattering events, but this goes as the square root of the density $k_F = \sqrt{2\pi n_{2D}}$ and so it is a weaker effect.

Likewise, a reduction of density in the drag layer increases the ratio of electrons participating in scattering events relative to the total number of electrons in the layer. Since the drag voltage is determined by the momentum transferred per electron – regardless of whether it is at the edge of the Fermi disk participating in scattering or deep in the middle – this rate will go up, even if the total momentum transferred stays the same. So this is another mechanism by which reducing the electron density will increase the drag resistivity.

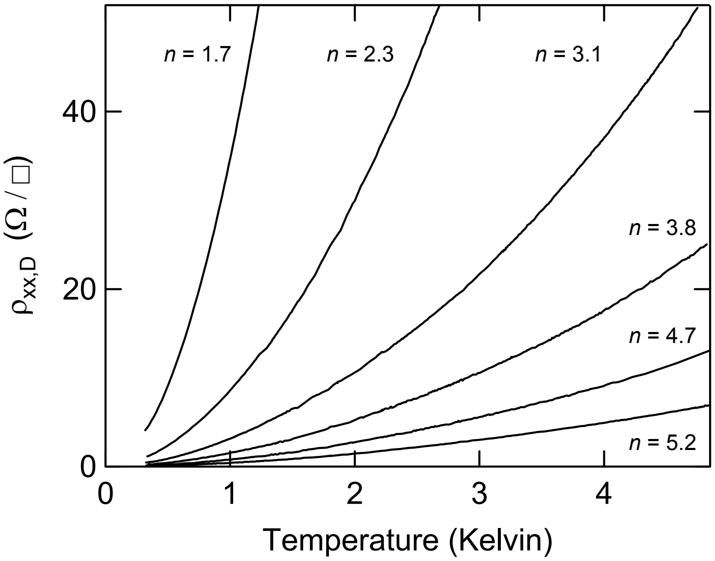

Figure 3.4: Drag resistivity vs. temperature for six different densities *n*. Densities are in units of 10^{10} cm^{-2}.

And lastly, reducing the size of the Fermi disks means that a scattering event of momentum q will be a larger-angle scattering event than the same q in a larger Fermi disk. Momentum is transferred more efficiently by large-angle scattering events and is maximized when $q = 2k_F$; pure backscattering. To account for this effect, scattering events are weighted by a factor of $1 - \cos\theta$ where θ is the angle between the initial and final momentum states in one of the layers. Simple geometry can show that this term is proportional to $\frac{q^2}{k_F^2}$ [13], and so scattering events of momentum q will be weighted more strongly as k_F is made smaller.

What was not expected was the rate at which the longitudinal drag is observed to increase as the density is lowered. Theoretical calculations of the drag resistivity based on Boltzmann transport theory predict an n^{-3} dependence as discussed in Section 2.4.1. But our data, the first to probe the density dependence of direct electron-electron drag scattering, indicates that the dependence on density is even stronger, going roughly as n^{-4}. Figure 3.5 shows the longitudinal drag resistivity versus density at three different temperatures T = 1, 2 and 4K plotted in a log-log fashion. The roughly straight line behavior over three decades of resistivity indicates that there is indeed a power-law dependence on density. But rather than the expected n^{-3} slope, shown as a dashed line, the data is better matched to the n^{-4} solid lines.

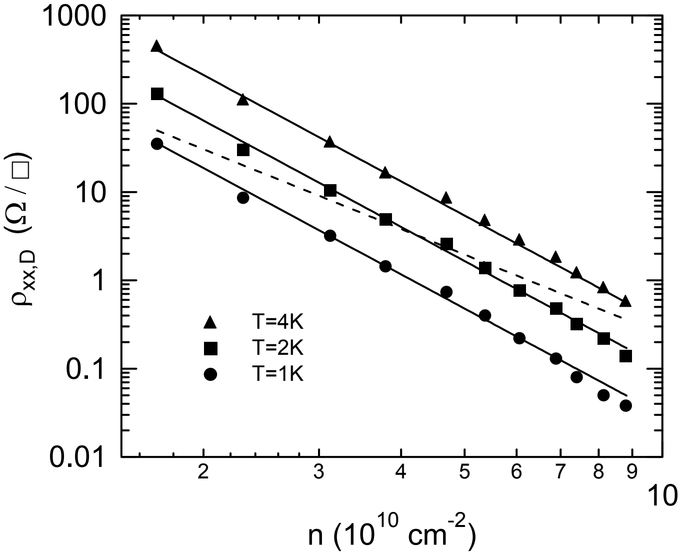

Figure 3.5: Drag resistivity vs. density at three temperatures: T = 4K, 2K and 1K. Solid lines are proportional to n^{-4}; dashed line proportional to n^{-3}.

The theoretical model predicting the n^{-3} dependence includes many simplifying assumptions in order to derive such a nice analytical result. Among them are that $T/T_F \ll 1$, which, especially for our lowest density $n = 1.7\times10^{10}\text{cm}^{-2}$ with its $T_F = 7K$, does not hold for much of our data. Also assumed is that the layer separation d is large compared to the inverse of the Fermi wavevector k_F, thus $k_F d \gg 1$. This assumes that only small-angle scattering is important. The greater the layer separation, the greater the scattering impact parameter and the less prevalent the large-angle scattering events. Large-angle scattering is suppressed by a factor e^{-qd} because the Fourier transform of the bare Coulomb interaction contains such a factor, and the probability for a scattering event to occur, by Fermi's golden rule, goes as the square of this. The requirement $k_F d \gg 1$ means that large-angle scattering is neglected. For our data $k_F d$ ranges from 0.9 to 2.1; clearly large-angle scattering cannot be neglected in our results.

The model also uses Thomas-Fermi screening, which is likely an over-simplification of the actual interaction potential [16]. These simplifications lead to the following analytic form for the longitudinal drag resistivity:

$$\rho_{xx,D} = \frac{m^* \pi \zeta(3) k_B T^2}{16\, e^2 n \hbar T_F (q_{TF} d)^2 (k_F d)^2} \tag{3.3}$$

where q_{TF} is the Thomas-Fermi screening wavevector, k_B is the Boltzmann constant and $\zeta(3)$ is a Riemann zeta function. All the data shown in Figure 3.5 exceed the model's predictions. Even the highest density data shown, $n = 8.8 \times 10^{10}\,\text{cm}^{-2}$, exceeds the value of equation (3.3) by a factor of 2. This discord between theory and experiment increases as n is lowered because of the anomalous experimental density dependence n^{-4}; so it's off by a factor of 10 by $n = 1.7 \times 10^{10}\,\text{cm}^{-2}$.

Theoretical work done after these results were published sought to reconcile these discrepancies by including many-body effects in the interaction Hamiltonian. Yurtsever, Moldoveanu and Tanatar [17] noted that random-phase approximation (RPA) breaks down for $r_s > 1$, where $r_s = a / a_B$ is a dimensionless coupling parameter relating the average inter-electron separation $a = (\pi n)^{-1/2}$ within one of the layers to the effective Bohr radius $a_B = \varepsilon \hbar^2 / m^* e^2$, where ε is the dielectric constant for GaAs. Because of the low density of our sample, especially when gated to our lowest density $n = 1.7 \times 10^{10}\,\mathrm{cm}^{-2}$, we were the first group to work in the regime where $r_s > 1$; with $r_s = 4.3$ at our lowest density.

The Thomas-Fermi model used to derive eqn. 3.3, is similar to the RPA with static screening and so should not be expected to be valid in the regime that our sample surveys. And indeed they show that the formulation of Coulomb drag using RPA both with static and dynamical screening, greatly underestimate our Coulomb drag data (see the dotted and long-dashed lines in Fig. 3.6).

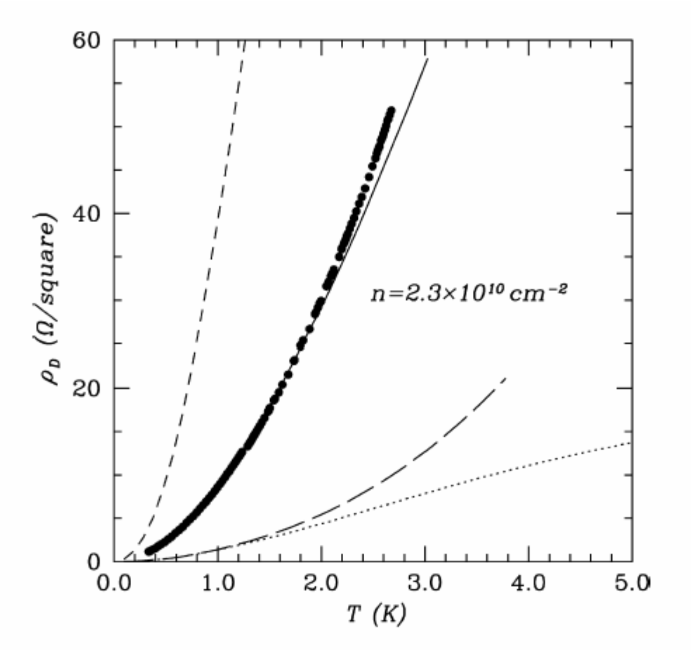

Figure 3.6: Theoretical models from Yurtsever *et al.* are compared to our data at $n = 2.3 \times 10^{10}\,cm^{-2}$, as also shown in Fig. 3.4. The dotted line corresponds to static screening RPA, much like the model we use in Sec. 3.4.1, and underestimates the actual data, shown as filled circles. The long-dashed line is for RPA with dynamical screening, a slight improvement over the static screening case. The short-dashed line is for a 1968 theory from Singwi *et al.* [18] which overestimates the correlation effects. The solid line is the Yurtsever *et al.* original formulation, which matches our data nicely. Taken from Ref. 17.

To account for the correlation effects expected to be important at these low densities, Yurtsever *et al.* first apply a 1968 theoretical model from Singwi *et al*. [18] which includes corrections due to exchange and correlation effects associated with charge fluctuations. They find that this model overestimates the correlation effects (see the short-dashed line in Fig. 3.6).

Finally, they derive a new model, built from an approach from Kukkonen and Overhauser [19] which takes into account the background semiconductor lattice into the screening term, and then Yurtsever *et al.* build on this model to include exchange interactions for charge and spin fluctuations. Not only does their new model agree nicely with the magnitude and temperature dependence of our published $n = 2.3\times10^{10}\,\text{cm}^{-2}$ data (our data is shown as filled circles in Fig. 3.6 and their model is the solid line), but it also reproduces the n^{-4} dependence that we observed (Fig. 3.5).

3.4 LONGITUDINAL DRAG VERSUS DENSITY IMBALANCE

Aside from the dependence of the drag on matched densities, we can also look at the drag's response to having different densities in the two layers. The parameter we will use to denote this is $\dfrac{\Delta n}{n_T}$, where $\Delta n \equiv n_1 - n_2$ (n_i is the density in the i^{th} layer), and $n_T \equiv n_1 + n_2$ is the total density in both the layers. We can change Δn while keeping n_T constant quite simply by applying a bias voltage between the two layers (see Appendix I).

The observed relationship $\rho_{xx,D} \sim n^{-4}$, carries within it a prediction for the behavior we expect to see when we imbalance the layer densities. By symmetry this relationship implies $\rho_{xx,D} \sim n_1^{-2} n_2^{-2}$, which can also be written as:

$$\rho_{xx,D} \sim \frac{1}{[\frac{1}{2}(n_T + \Delta n)]^2 [\frac{1}{2}(n_T - \Delta n)]^2} \sim \frac{1}{16 n_T^4 (1 + \frac{\Delta n}{n_T})^2 (1 - \frac{\Delta n}{n_T})^2} \tag{3.4}$$

Focusing just on the terms containing Δn, as n_T is constant, and applying the binomial expansion:

$$\rho_{xx,D} \sim \left[1 - \left(\frac{\Delta n}{n_T}\right)^2\right]^{-2} \sim \; 1 + 2\left(\frac{\Delta n}{n_T}\right)^2 \tag{3.5}$$

And so it can be seen that, aside from an offset, there will be a quadratic increase in the drag with layer imbalance $\dfrac{\Delta n}{n_T}$. Note that any inverse dependence on density, $\rho_{xx,D} \sim n^{-x}$ where x is a positive number, will lead to a quadratic increase in the drag with layer imbalance, the exponent x will only affect the coefficient of the $\left(\dfrac{\Delta n}{n_T}\right)^2$ term.

Figure 3.7 shows the longitudinal drag resistivity as a function of density imbalance at two different densities and two different temperatures. Panels a and b show this quadratic increase in the drag with increasing density imbalance for $n = 3.7 \times 10^{10} cm^{-2}$ and $n = 5.2 \times 10^{10} cm^{-2}$ when taken at $T \sim 4.4K$. Both data sets are well fit by the curve:

$\rho_{xx,D} = \rho_{xx,D}\left(\text{at } \frac{\Delta n}{n_T}=0\right)\times\left[1+1.6\left(\frac{\Delta n}{n_T}\right)^2\right]$. This is very close to the equation we just derived (eqn. 3.5). But as the temperature is lowered to $T = 1.4K$ for these same densities (panels c and d), we see quite different behavior; here the drag is seen to decrease with increasing density imbalance. The data evolve smoothly from one regime to the other as the temperature is varied. The temperature at which the curvature is roughly zero is defined to be the cross-over temperature T_c. The inset in Fig. 3.7 shows that T_c is linear in density, and thus linear in the Fermi temperature T_F, with the relation: $T_c \sim 0.12\times T_F$.

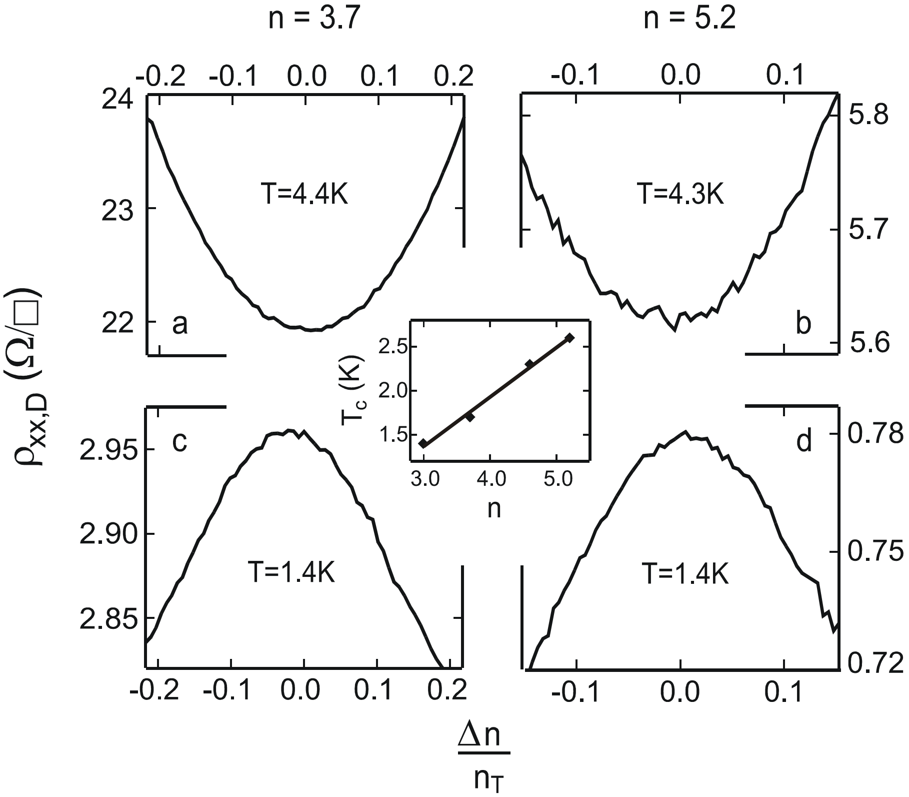

Figure 3.7: Drag resistivity vs. density imbalance at (roughly) two temperatures: $T = 1.4K$ and $\sim 4.4K$, and two densities (at $\Delta n = 0$): $n = 3.7$ and 5.2 ($\times 10^{10} cm^{-2}$) per layer. The central inset shows the density dependence of the cross-over temperature T_c.

A peak in the drag at matched density is typically seen in phonon-mediated drag. The importance of $q = 2k_F$ scattering in phonon-mediated drag means that the drag will be maximized when both the layers have the same Fermi wavevector k_F (and thus the same density). This peak was observed in prior work in the phonon-dominated drag regime [10, 12]. But as discussed in Section 3.2.1, phonon-mediated drag makes a negligible contribution to our data. So the origin of this peak was quite mysterious at the time.

3.4.1 NUMERICAL MODELING

Because prior theoretical work [14, 15] on direct electron-electron drag presumed that only small-angle scattering contributed significantly to the drag, it was very surprising to see this peak at matched densities in our data. But we will show that because our sample parameters do not fall within the prescribed $k_F d \gg 1$ used in all that prior theoretical work, what we are actually seeing are the first observations of significant $2k_F$ scattering in direct Coulomb drag.

To investigate the effects of our small $k_F d$ on our drag measurements, we performed the first theoretical investigation of Coulomb drag for differing densities in the layers. Following the approach of Jauho and Smith [15], we solve their drag scattering integral for the case where $n_1 \neq n_2$. We take a slightly different approach in calculating the imaginary part of the susceptibility, as discussed in Section 2.4. Our approach gives the full temperature dependence of the susceptibility, whereas Jauho and Smith use the zero-temperature susceptibility in their calculations. The full calculation can be found in Section 2.4, and the Fortran programs used to solve the integral are in Appendix K.

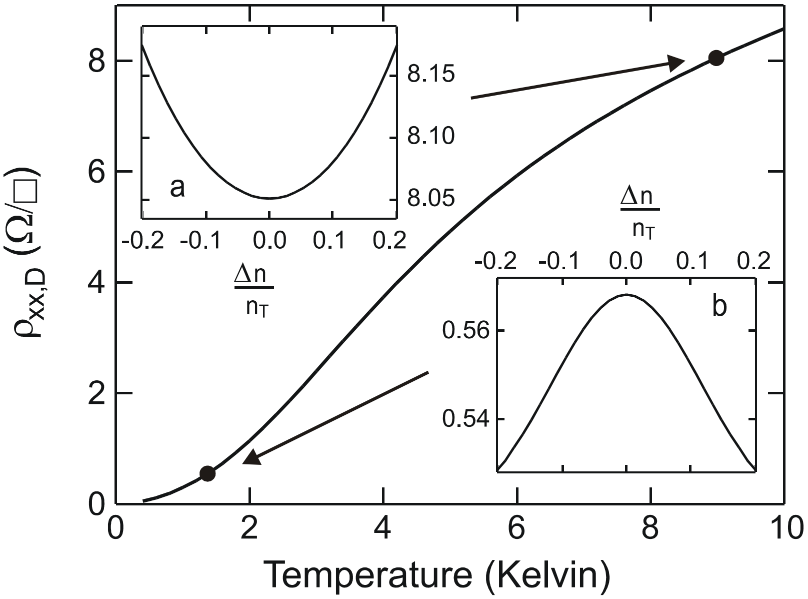

Figure 3.8: Computed drag resistivity vs. temperature for $n = 3.7 \times 10^{10} cm^{-2}$. The insets show the dependence of the drag resistivity on density imbalance at two different temperatures.

Figure 3.8 shows the result of this calculation done with our sample's parameters: layer separation $d = 280$ Å, well width $L = 180$ Å and density $n = 3.7 \times 10^{10} cm^{-2}$. The main figure shows the temperature dependence at matched densities and the insets show the dependence on density imbalance at low temperature (inset b) and at high temperature (inset a). Inset a, computed for $T = 9K$, shows a quadratic increase in the drag with increasing density imbalance, and inset b at $T = 1.4K$ shows the drag decreasing with imbalance. So our theoretical calculations show the same qualitative behavior that we observe in the data in Figure 3.7.

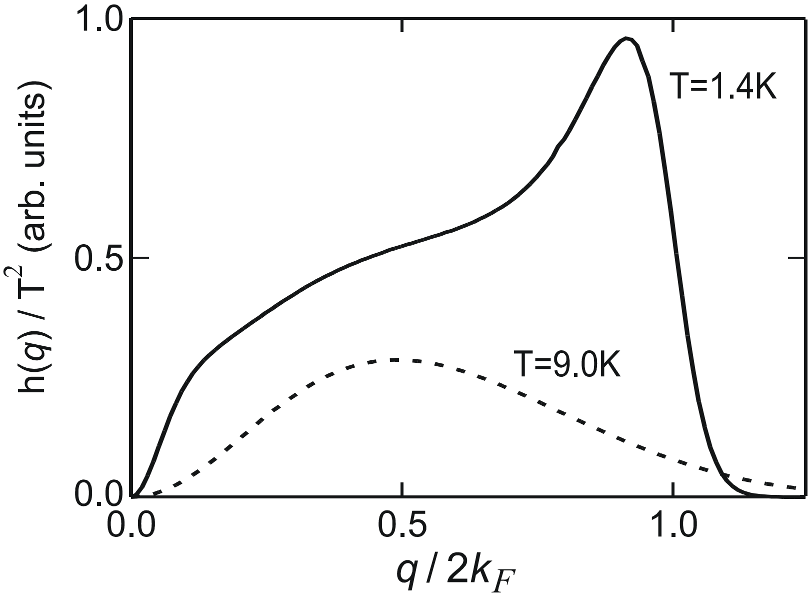

Figure 3.9: Drag intensity $h(q)$, divided by T^2, vs. scattering wavevector q in units of $2k_F$. Calculated for $n = 3.7 \times 10^{10} cm^{-2}$ at two different temperatures. The drag resistivity is the area under the curves.

Closer inspection of the theoretical model, specifically looking at the q dependence of the computed drag resistivity (Figure 3.9), reveals the cause of this anomalous peak at matched density at low temperature. The figure shows the drag intensity

$$h(q) \equiv \frac{d(\rho_{xx,D})}{dq}, \tag{3.6}$$

divided by T^2 to facilitate comparison between the two different temperatures shown $T = 1.4K$ and $9K$. At the low temperature, there is a peak in the drag intensity near $q = 2k_F$, indicating that $2k_F$ scattering processes are indeed important in samples with our parameters. When $2k_F$ processes are significant, the drag becomes sensitive to the matching of the Fermi wavevectors in each layer (by matching their densities). When $k_{F,1} = k_{F,2}$ ($k_{F,i}$ is the Fermi momentum in layer i), $2k_F$ processes are resonant between the layers and the drag will be maximized. Imbalancing the layers means a favored $q = 2k_{F,1}$ scattering event in layer 1 will not be the favored scattering wavevector in layer 2 and the drag will decrease relative to the matched density condition.

At higher temperatures, the edge of the Fermi disk, where all the scattering occurs, becomes thermally broadened and the $2k_F$ feature dissipates, then disappears, as shown in the $T = 9K$ calculation in Figure 3.9. The broader the edge of the Fermi disk, the less relative phase space is available for large angle scattering events. At some critical temperature T_c the $2k_F$ scattering becomes relatively unimportant and the simple $\rho_{xx,D} \sim 1 + 2\left(\frac{\Delta n}{n_T}\right)^2$ behavior wins out, leading to increasing drag with density imbalance.

Although our calculation mirrors our data qualitatively and shows unambiguously that the peak in matched density at low temperature is due to the enhanced phase space available for scattering at $2k_F$, it does not correctly predict the critical temperature. The cross-over occurs at a higher temperature, $T_c = 6.3K$ in the calculated figure compared to the $T_c = 1.7K$ observed in Figure 3.7. This may be due to the inadequacy of the simple electron-electron interaction potential used in our theoretical model. As previously discussed in Section 3.3, this simple potential underestimates the drag resistivity for all the data shown and predicts a n^{-3} dependence on density rather than the n^{-4} observed. Both of these discrepancies were resolved by including the more theoretically complicated many-body effects into the interaction potential [17], and inclusion of them in our calculation may be expected to do the same. However, as the cross-over behavior that we observe in Figure 3.7 is purely a phase space phenomenon, the simpler interaction potential proves sufficient to ratify this fact.

3.5 SPIN POLARIZATION ($B_{\perp}=0$, $B_{\parallel}\neq 0$)

This resonance at $2k_F$ in the longitudinal drag resistivity at low temperatures makes the drag measurement versus density imbalance a good probe of the relative sizes of the Fermi disks in each layer. There are in reality two Fermi disks in each layer; one populated by spin-up electrons and another populated by spin-down electrons. In zero magnetic field, the two populations are identical and thus so are the two Fermi disks. But the application of a magnetic field parallel to the plane of the electron layers will change the relative populations of the spin states – due to the Zeeman interaction; and the two Fermi disks in each layer will then have different radii. This change should be detectable in the longitudinal drag versus density imbalance.

This change in relative population is characterized by the spin polarization ξ. The difference between the spin-up population density $n_{\uparrow}$ and the spin-down population $n_{\downarrow}$ is just the Zeeman energy times the density of states (which in two dimensions is merely a constant):

$$n_\uparrow - n_\downarrow = g^* \mu_B B \times \frac{m^*}{2\pi\hbar^2} = \frac{g^* m^* eB}{2hm_e} \tag{3.7}$$

where g^* is the effective g-factor ($g^* = -0.44$ for GaAs at B$_{||}$=0), $\mu_B = e\hbar / 2m_e$ is the Bohr magneton and the two-dimensional electronic density of states is $n(E) = m^* / 2\pi\hbar^2$. Then the spin polarization ξ is defined as:

$$\xi \equiv \frac{n_\uparrow - n_\downarrow}{n_\uparrow + n_\downarrow} = \frac{g^* m^* eB}{2hnm_e} \tag{3.8}$$

At low densities it is expected that Coulomb exchange effects will lead to an enhancement of this splitting beyond the Zeeman value [20]. This can be characterized as a variation of the product $g^* m^*$ with density. This variation in $g^* m^*$ has been studied in Silicon MOSFETs [19] and in GaAs heterostructures both with electrons [22, 23] and holes [24] under the application of an in-plane magnetic field. Usually, though not always [23], $g^* m^*$ is found to increase with decreasing density as expected.

These other studies relied on features in the magnetoresistance to infer the spin polarization. Coulomb drag offers a novel way to detect the spin polarization. In the regime where $2k_F$ scattering is important, matching Fermi momenta in the two layers corresponds to a peak in the drag resistivity. When an in-plane magnetic field is applied, there are two different Fermi momenta in each layer and four different combinations of Fermi momenta that are contributing to the drag: $(k_{F,1\uparrow}, k_{F,2\uparrow})$, $(k_{F,1\uparrow}, k_{F,2\downarrow})$, $(k_{F,1\downarrow}, k_{F,2\uparrow})$ and $(k_{F,1\downarrow}, k_{F,2\downarrow})$ where $k_{F,i\uparrow(\downarrow)}$ is the Fermi momentum in the i^{th} layer of the spin-up (spin-down) electron population. It seems reasonable to assume that the resulting drag resistivity will be a linear combination of the contributions of the four Fermi disk pairs, with the behavior of which we are already empirically familiar.

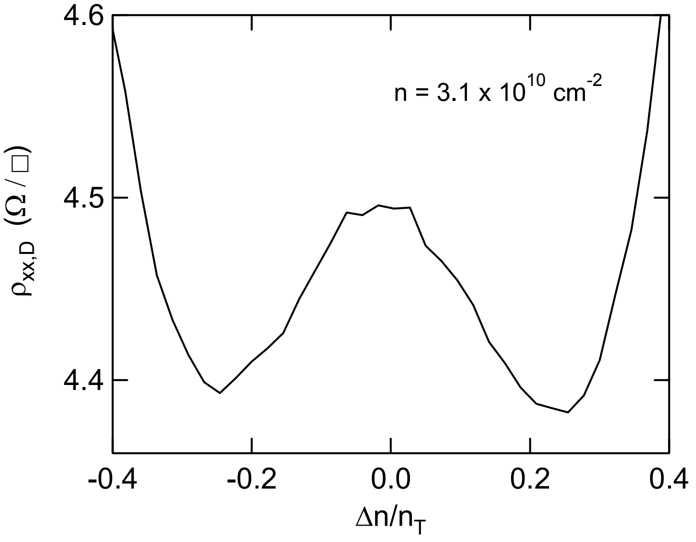

Figure 3.10: Longitudinal drag resistivity vs. density imbalance at zero magnetic field for $n = 3.1\times10^{10} cm^{-2}$ taken at $T = 1.3K < T_c$ shows that at sufficiently large density imbalance (at $\Delta n / n_T \sim \pm 0.25$ in this case) the drag will eventually increase with increasing density imbalance.

At this point I should reveal that the peak at matched density for $T < T_c$ as observed in Figure 3.7 only occurs near $\Delta n / n_T = 0$. At sufficiently large density imbalance the drag begins to rise with increasing density imbalance as shown in Figure 3.10. Since the two opposite spin pairs $(k_{F,1\uparrow}, k_{F,2\downarrow})$ and $(k_{F,1\downarrow}, k_{F,2\uparrow})$ will have a combined density n, which is equal to the single layer density, the drag contribution from these two terms, should look just like the $B_{\parallel} = 0$ drag, but offset by

$$\frac{\Delta n}{n_T} = \frac{g^* m^* e B_{\parallel}}{2 m_e h n_T}. \tag{3.9}$$

The two matching spin pairs $(k_{F,1\uparrow}, k_{F,2\uparrow})$ and $(k_{F,1\downarrow}, k_{F,2\downarrow})$ will have combined densities that are less than ($\uparrow$) and greater than ($\downarrow$) the single layer density by some $\pm\Delta n$. Their contributions should be similar to $B_{\parallel} = 0$ drag taken at $(n \pm \Delta n)$.

Figure 3.11 shows the longitudinal drag resistivity versus density imbalance with four different values of in-plane magnetic field, ranging from $B_{\parallel} = 0T$ to $B_{\parallel} = 9T$. The per layer density is $n = 2.3 \times 10^{10} cm^{-2}$ and the temperature is $T = 0.3K$. The $B_{\parallel} = 0T$ curve shows the expected peak at matched densities as observed and discussed in the previous section. The application of an in-plane magnetic field reduces the value of the drag at $\Delta n / n_T = 0$ and causes the peak to become squattier, until it disappears (at $B_{\parallel} = 6T$ in Fig. 3.11) and ultimately turns over to a roughly quadratic increase in drag with density imbalance typically seen at $T > T_c$.

The contributions of the $(k_{F,1\uparrow}, k_{F,2\downarrow})$ and $(k_{F,1\downarrow}, k_{F,2\uparrow})$ pairs alone would be expected to produce such a progression from a peak to a minimum at matched densities. The minima on either side of the central peak shown in Fig. 3.10 can be seen to be developing at $\Delta n / n_T \sim \pm 0.3$ from the central peak in the $B_{\parallel} = 0T$ data in Fig. 3.11. If the minimum in the $B_{\parallel} = 9T$ data corresponds to these side minima being shifted over by $\Delta n / n_T \sim \pm 0.3$, then this would be consistent with a spin polarization of $\xi \sim 0.60$, corresponding to a more than four-fold enhancement in $g^* m^*$ over its zero field value.

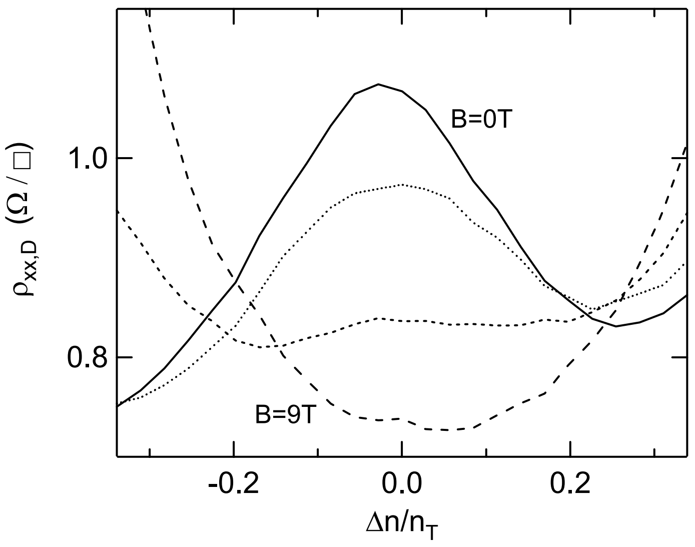

Figure 3.11: Drag resistivity vs. density imbalance for different in-plane magnetic field strengths. The solid, dotted, short-dashed and long-dashed lines shows $B_{||} = 0, 3, 6$ and $9T$ respectively for $n = 2.3\times10^{10} cm^{-2}$ and $T = 0.3K$.

The contribution of the matched pairs, $(k_{F,1\uparrow}, k_{F,2\uparrow})$ and $(k_{F,1\downarrow}, k_{F,2\downarrow})$ would be dominated by the lower density pair. Drag is observed to be inversely proportional to the fourth power of the density. In this case, it also must be taken into consideration that the current in the drive layer is being carried by two different Fermi disks. Given the same drive voltage for both disks, the smaller Fermi disk will be carrying a smaller portion of the current, as given by the following equation

$$J = neE\mu \tag{3.10}$$

where μ is the mobility. Not only is the current directly dependent on n but it also depends on the mobility μ, which is observed to be roughly linearly dependent on n. So the drag contribution from the smaller Fermi disks will still dominate, but only as $\sim n^{-2}$ not n^{-4}. However, this contribution will also cause a progression from a peak to a minimum at matched density, because lowering the density of the one spin population lowers the Fermi temperature and thus the critical temperature: $T_c \sim 0.12 \times T_F$. Even though the temperature is not changing, T can rise above T_c just by reducing the density, and the drag will enter the regime where it displays a minimum at matched density.

Much harder to reckon are the effects of the in-plane magnetic field on the electronic wavefunction in the confining potential and how this will impact the drag. Even in the ideal case of zero-width electron layers, the in-plane field distorts the Fermi surface, which alters the effective mass of the electrons. Smrčka and Jungwirth predict a greater than 20% increase in the electron mass at $B_{\|} = 9T$ [25]. This corresponds to a 20% decrease in the Fermi temperature ($T_F = h^2 n / 4\pi k_B m^*$) and thus the critical temperature. Again, this will push the system closer to the cross-over point, and could enhance the effects enumerated above.

Even more complications arise when the finite thickness of the confined electron wavefunction is taken into account. Again Smrčka and Jungwirth addressed this issue, this time specifically for double layers (though in a single wide quantum well) and found that in addition to the distortion of the Fermi surface, there was a k-dependent displacement of the centroids of the wavefunctions [26]. This creates a small, but noticeable, change in the charge distribution in the well, which they calculated for a heterojunction confining potential. However, it's likely that in a square potential, this charge redistribution will be less significant.

Das Sarma and Hwang were the first to note that at high parallel magnetic field, the magnetic length ℓ was smaller than the widths of most of the wavefunctions confined in these quasi-2D quantum wells used in published experiments, and that orbital motion would be significant in the confining direction [27]. This would lead to considerable intersubband scattering, which they were able to show was responsible for some anomalously high longitudinal resistivity observed in single layers with an applied in-plane magnetic field [28]. It is not known how this effect will manifest in the drag resistivity. We did observe the same phenomena in the conventional longitudinal resistivity however.

In some experimental (plus numerical) work on this issue, Tutuc et al. found that both g^* and m^* increased with increasing in-plane magnetic field in a way that was dependent on the electron layer thickness [29]. Given all these factors and the uncertainty in how they will affect the drag resistivity, at this point it seems premature to make definitive claims on the interpretation of the data. It is, however, interesting to note that there has been one published study of Coulomb drag with an in-plane magnetic field [30] and their observations were uniformly in opposition to ours. They were lookinat hole-hole scattering in the same $k_F d \sim 1$ regime as we were, but at $T > T_c$. Also of interest to note is that their drive current ran parallel to the in-plane magnetic field, while ours ran perpendicular (and it seems that future work ought to look at both cases in the same sample). They found that the longitudinal drag resistivity increased at matched density with increasing in-plane magnetic field, and that the curvature of the density imbalance curves, which always exhibited a minimum at balanced density in their data, became squattier as the in-plane magnetic field increased.

* * *

---

1 See Appendix A for detailed processing steps, however note that for this sample Indium contacts were used, not the AuNiGe contacts described in the Appendix.

2 J.M. Woodall, J.L. Freeouf, G.D. Pettit, T. Jackson and P. Kirchner, J. Vac. Sci. Technol. **19**, 626 & 794 (1981); A.A. Lakhani, J. Appl. Phys. **56**, 1888 (1984).

3 See Appendix H for detailed information on how to determine these quantities.

4 See Appendix G for detailed information on how to balance the layers using the Coulomb drag measurement.

5 See Appendix J for a complete list of all experimental 2D-2D Coulomb drag papers.

6 See Chapter 2, section 2.3.

7 C. Hodges, H. Smith and J.W. Wilkins, Phys. Rev. B **4**, 302 (1971).

8 S. Fujimoto, J. Phys. Soc. Jpn. **59**, 2316 (1990).

9 L. Zheng and A.H. MacDonald, Phys. Rev. B **48**, 8203 (1993).

10 T.J. Gramila, J.P. Eisenstein, A.H. MacDonald, L.N. Pfeiffer and K.W. West, Phys. Rev. B **47**, 12957 (1993).

11 P.J. Price, Solid State Commun. **51**, 607 (1984).

12 H. Rubel, E.H. Linfield, D.A. Ritchie, K.M. Brown, M. Pepper and G.A.C. Jones, Semicond. Sci. Technol. **10**, 1229 (1995); H. Noh, S. Zelakiewicz, T.J. Gramila, L.N. Pfeiffer and K.W. West, Phys. Rev. B **59**, 13114 (1999).

13 J.H. Davies, *The Physics of Low-Dimensional Semiconductors* (Cambridge University Press, Cambridge 1998). See section 8.2.

14 T.J. Gramila, J.P. Eisenstein, A.H. MacDonald, L.N. Pfeiffer and K.W. West, Phys. Rev. Lett. **66**, 1216 (1991).

15 A.P. Jauho and H. Smith, Phys. Rev. B **47**, 4420 (1993).

16 See Chapter 2, section 2.4 for an in depth discussion of the theoretical model.

17 A. Yurtsever, V. Moldoveanu and B. Tanatar, Solid State Commun. **125**, 575 (2003).

18 K.S. Singwi, M.P. Tosi, R.H. Land and A. Sjölander, Phys. Rev. **176**, 589 (1968).

19 C.A. Kukkonen and A.W. Overhauser, Phys. Rev. B **20**, 550 (1979).

20 B. Tanatar and D.M. Ceperley, Phys. Rev. B **39**, 5005 (1989).

21 T. Okamoto, K. Hosoya, S. Kawaji and A. Yagi, Phys. Rev. Lett. **82**, 3875 (1999); V.M. Pudalov, M.E. Gershenson, H. Kojima, N. Butch, E.M. Dizhur, G. Brunthaler, A. Prinz and G. Bauer, Phys. Rev. Lett **88**, 196404 (2002).

22 J. Zhu, H.L. Stormer, L.N. Pfeiffer, K.W. Baldwin and K.W. West, Phys. Rev. Lett. 90, 056805 (2003).

23 E. Tutuc, S. Melinte and M. Shayegan, Phys. Rev. Lett. **88**, 036805 (2002).

24 E. Tutuc, E.P. De Poortere, S.J. Papadakis and M. Shayegan, Phys. Rev. Lett. **86**, 2858 (2001).

25 L. Smrčka and T. Jungwirth, J. Phys.: Condens. Matter **6**, 55 (1994).

26 L. Smrčka and T. Jungwirth, Superlattices and Microstructures **13**, 499 (1993).

27 S. Das Sarma and E.H. Hwang, Phys. Rev. Lett. **84**, 5596 (2000).

28 D. Simonian, S.V Kravchenko, M.P. Sarachik and V.M. Pudalov, Phys. Rev. Lett. **79**, 2304 (1997).

29 E. Tutuc, S. Melinte, E.P. De Poortere, M. Shayegan and R. Winkler, Phys. Rev. B **67**, 241309 (2003).

30 R. Pillarisetty, H. Noh, E. Tutuc, E.P. De Poortere, D.C. Tsui and M. Shayegan, Phys. Rev. Lett. 90, 226801 (2003).

Chapter 4: 2D Electrons in a Perpendicular Magnetic Field

The physics of two-dimensional electrons gets much more interesting when a perpendicular magnetic field is applied. Classical cyclotron orbits become quantized in sufficiently clean systems, and with the high electron densities found in the solid state, the system organizes itself into a highly regular array, filling up discrete energy levels each with a strict occupancy limit. The energy gaps between these levels are responsible for the phenomena observed in the quantum Hall effect (QHE). However, the fractional quantum Hall effect and most of the QHE in bilayers are more complex many-body states that engender even more fascinating physics, giving us such things as the highly ordered (111) state with its fractionally charged ($\pm e/2$) excitations and its superfluid mode.

4.1 QUANTUM HALL EFFECT

In nonrelativistic quantum mechanics, the Hamiltonian for a charged particle in a magnetic field, ignoring spin, has the form:

$$H = \frac{1}{2m}\left(\mathbf{p} - e\mathbf{A}\right)^2 \tag{4.1}$$

where $\mathbf{p} = -i\hbar\nabla$ is the generalized momentum of the particle, and $\mathbf{A}$ the vector potential, such that $\mathbf{B} = \nabla \times \mathbf{A}$. Defining the plane of the electron motion as the x-y plane, the magnetic field will be perpendicular to that plane, $\mathbf{B} = B\hat{\mathbf{z}}$. Then using the Landau gauge, the vector potential can be written $\mathbf{A} = -yB\hat{\mathbf{x}}$.

The time-independent Schrödinger equation for this Hamiltonian is

$$\left[\frac{1}{2m}\left(-i\hbar\frac{\partial}{\partial x} + eyB\right)^2 - \frac{\hbar^2}{2m}\frac{\partial^2}{\partial y^2}\right]\psi(\mathbf{R}) = E\psi(\mathbf{R}), \tag{4.2}$$

where $\psi(\mathbf{R})$ is the wavefunction in the x-y plane only. In the z direction the electrons are confined in the quantum well potential; this can be treated separately and will not affect the solution to the equation in the x-y plane.

Since the Hamiltonian is independent of the coordinate x, then $[p_x, H] = 0$ (p_x is the momentum operator in the x-direction). This suggests that $\psi(\mathbf{R}) = U(y)e^{ikx}$, where e^{ikx} is a plane wave state with momentum k. Expanding out equation 4.2 and making this substitution yields:

$$\left[\frac{1}{2m}\left(-\hbar^2\frac{\partial^2}{\partial x^2} - i2\hbar eyB\frac{\partial}{\partial x} + e^2y^2B^2\right) - \frac{\hbar^2}{2m}\frac{\partial^2}{\partial y^2}\right]U(y)e^{ikx} = EU(y)e^{ikx}; \tag{4.3}$$

then operating on e^{ikx},

$$\left[\frac{1}{2m}\left(\hbar^2k^2e^{ikx} + 2\hbar keyBe^{ikx} + e^2y^2B^2e^{ikx}\right) - \frac{\hbar^2}{2m}e^{ikx}\frac{\partial^2}{\partial y^2}\right]U(y) = EU(y)e^{ikx}. \tag{4.4}$$

The e^{ikx} term cancels from both sides, and the equation simplifies to:

$$\left[-\frac{\hbar^2}{2m}\frac{\partial^2}{\partial y^2}+\frac{1}{2}m\omega_c^2\left(y+\frac{\hbar k}{eB}\right)^2\right]U(y)=EU(y)\,, \tag{4.5}$$

where $\omega_c = eB/m$ is the cyclotron frequency. This is just the Schrödinger equation for a one-dimensional harmonic oscillator, oscillating about the point $y=-\hbar k/eB$, with frequency ω_c. The eigenvalues for this equation are

$$E_n=\left(n+\frac{1}{2}\right)\hbar\omega_c\,, \tag{4.6}$$

where $n=0,1,2,\ldots$, which are thus also the eigenvalues to equation 4.2. These energy levels are called "Landau levels," as it was Landau who first solved this problem [1].

The eigenfunctions for eqn. 4.2 are plane waves in the x-direction, and one-dimensional harmonic oscillator eigenfunctions in the y-direction – for the lowest energy, these are just Gaussians, centered about

$$y=-\hbar k/eB\,. \tag{4.7}$$

As the energy E_n is independent of k, there is a degeneracy to the Landau levels. The degeneracy is equivalent to the density of electrons that can fit in each Landau level. Considering the system as a rectangle with dimensions $L_x \times L_y$, periodic boundary conditions on the plane wave portion of the wavefunction in the x-direction require that

$k = (2\pi / L_x) j$, where $j = 0, \pm 1, \pm 2, \ldots$. Then the spacing between adjacent k-states in the y-direction will be (from eqn. 4.7) $y_j - y_{j-1} = h/(eBL_x)$. The number N of k-states that can fit along $0 < y < L_y$ will then be:

$$N = \frac{L_y}{y_j - y_{j-1}} = \frac{L_y L_x eB}{h}, \tag{4.8}$$

and the density $n = N / L_y L_x$ of electrons in each Landau level, which defines the degeneracy D, is equal to eB/h.

The number of Landau levels filled in a system is called the "filling factor" ν and is given by

$$\nu \equiv \frac{n}{D} = \frac{nh}{eB}, \tag{4.9}$$

where n is the 2D density of electrons in the system. When $\nu = 1$, exactly one Landau level is filled. When $\nu = \frac{1}{2}$, exactly one-half of a Landau level is filled.

Ideally, this energy degeneracy leads to a density of states (DOS) composed of a ladder of delta functions spaced $\hbar\omega_c$ apart. But in real systems, inhomogeneities in the sample spread out the energy of the Landau levels, and the DOS resembles more the curve shown in Figure 4.1. Inclusion of the electron spin (not shown), splits each of these Landau levels into two levels, offset by a Zeeman energy gap $\Delta_z = g\mu_B B$, where μ_B is the Bohr magneton, and g is the g-factor (which does not equal the free electron value, but rather is

$g = -0.44$ for electrons in GaAs).

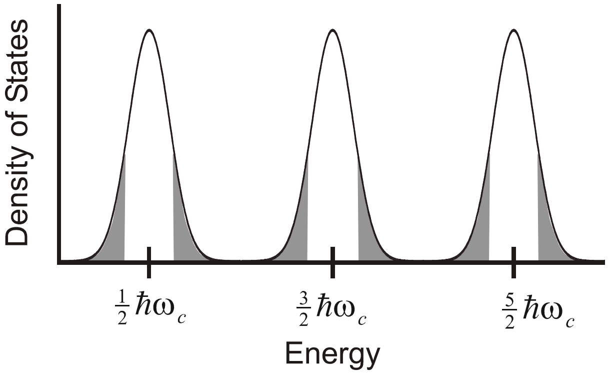
Density of States
$\frac{1}{2}\hbar\omega_c$
$\frac{3}{2}\hbar\omega_c$
$\frac{5}{2}\hbar\omega_c$
Energy

Figure 4.1: Density of states diagram for the first three Landau levels in an inhomogeneous system. Each Landau level can accommodate eB/h electrons. Shaded areas at edges of each Landau level represent localized states. Electrons in these states cannot participate in current flow.

The shaded regions at the edges of the Landau levels represent localized states: dips and peaks in the potential energy that trap ("localize") electrons and prevent them from participating in current flow across the sample. It is the combination of the gaps in energy between adjacent Landau levels and the existence of the localized states that leads to an effect in the transport properties called the "quantum Hall effect".

Discovered in 1980 by von Klitzing [2], the quantum Hall effect (QHE) consists of perfectly quantized plateaus in the Hall resistivity – so perfect that they are used as resistance standards at the National Institute of Standards ($\rho_{xy} = \frac{1}{j}(h/e^2)$ where j is an integer) – accompanied by zeros in the longitudinal resistivity, in the vicinity of integral filling factors (see Figure 4.2). The observation of the QHE requires low temperatures

($k_B T \ll \hbar\omega_c$), so that the Landau level energy gaps ($\hbar\omega_c \approx 1$ K at $B = 1$ Tesla for GaAs) are not being breached thermally, and high electron mobility, so that the electrons can complete multiple orbits before being scattered, such that they can interfere with themselves and allow quantization to set in. High electron mobility depends on low disorder in the system, however, disorder is necessary for the existence of localized states, which are imperative for the QHE.

The precision of the Hall resistance in the plateau regions is a direct consequence of the precision of the electron density in the conducting states in the plateau regions. When the filling factor in the conducting areas of the sample is integral ($\nu = j$, where j is an integer), the electron density in that area is extremely precise, exactly $n = jD = jeB/h$. The Hall resistivity is inversely proportional to the electron density, $\rho_{xy} = B/ne$, and at integral filling factor:

$$\rho_{xy} = (h/jeB)\times(B/e) = \tfrac{1}{j}(h/e^2)\,, \qquad (4.10)$$

just the values observed in the QHE plateaus. If there were no localized states, the conducting areas would be at a precise integral filling only at a very precise value of the magnetic field B, and the Hall resistivity would show no plateaus. But because of the localized states, the conducting areas can remain at integral filling factor over broad ranges of the total filling factor of the sample as a whole. This is because when the Fermi level moves through the localized states, the filling factor in the localized states will change, but the filling factor in the conducting regions won't. Samples in which a large fraction of the states are localized states, will have very broad plateaus, like those shown in Figure 4.2.

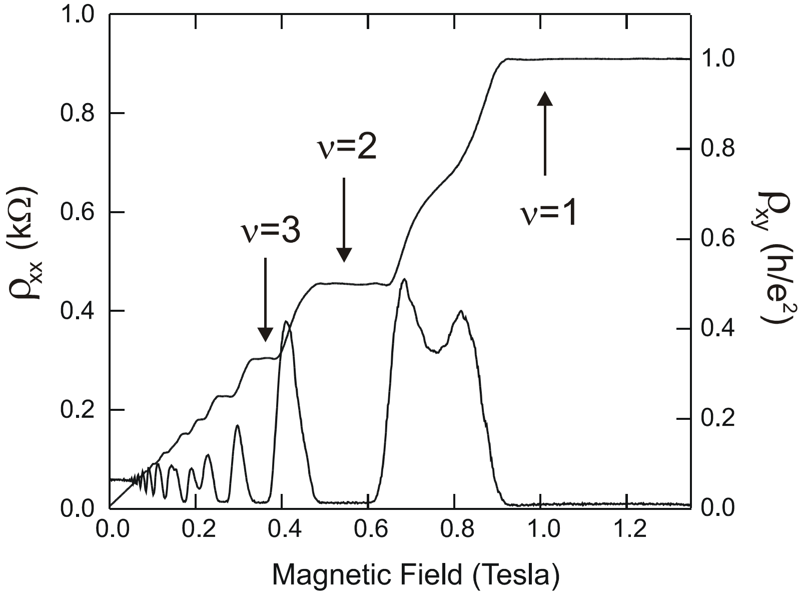

Figure 4.2: Plateaus in the Hall resistivity ρ_{xy} and broad zeroes in the longitudinal resistivity ρ_{xx}, as a function of the magnetic field, characterize the quantum Hall effect. Data from sample 'N'.

The longitudinal resistivity ρ_{xx} goes to zero over the same range that the Hall resistivity plateaus. This also reflects that an integral number of Landau levels are filled in the conducting areas. When all the occupied Landau levels are filled, the only available states for an electron to be scattered into are in the next vacant Landau level up. These will be too far away, energywise, so scattering will not occur and the longitudinal resistivity will drop to zero.

4.2 FRACTIONAL QUANTUM HALL EFFECT

It is the energy gap in the single particle DOS that leads to the QHE, but the fractional quantum Hall effect (FQHE) discovered in 1982 by Tsui *et al.* [3] cannot be explained by single-particle physics.

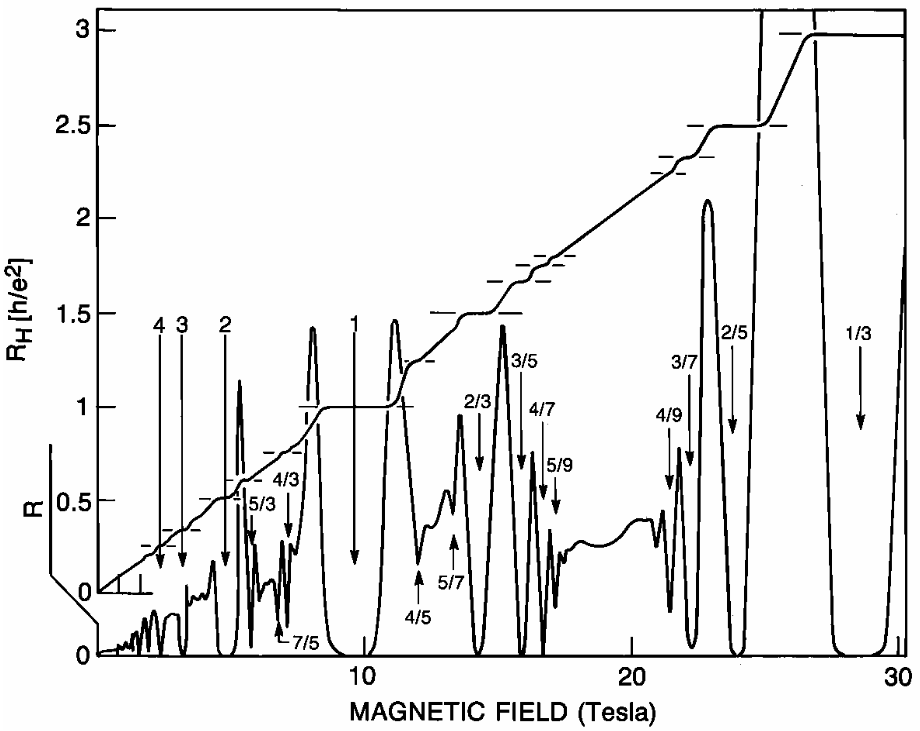

Figure 4.3: In addition to plateaus in the Hall resistance R_H and zeroes in the longitudinal resistance R at integral values of filling factor, the fractional quantum Hall effect shows these also at filling factors $\nu = p/q$, where p, q are integers, q usually odd. Figure from Ref. 4.

In the FQHE, the plateaus in ρ_{xy} and the zeroes (or minima) in ρ_{xx} appear at fractional values of the filling factor: $\nu = p/q$, where p, q are integers, q is generally odd (see Fig. 4.3). Like the original QHE, these also arise because of energy gaps in the DOS; but the cause of these energy gaps was not understood until Laughlin [5] formulated a wavefunction that could correctly account for the fractional quantum Hall (FQH) state at $\nu = 1/3$ (the first FQHE observed), and predicted additional FQH states at $\nu = 1/q$, q being an odd integer, which were later observed.

The Laughlin wavefunction shows that it is many-body effects between the electrons that lead to new energy gaps in the system. The Laughlin wavefunction for the FQH state at $\nu = 1/3$ is:

$$\Psi_3 \equiv \prod_{i<j} (z_i - z_j)^3 \prod_i \exp(-|z_i|^2 / 4), \tag{4.11}$$

where $z_i = x_i - iy_i$ is the location of the i^{th} electron in the 2D plane with coordinates (x_i, y_i).

At $\nu = 1/3$ there is a 3:1 ratio between the number of magnetic flux quanta piercing the 2DEG ($\Phi_0 = h/e$ is the quantum of magnetic flux) and the number of electrons. The system can collect into a lower energy state when three magnetic flux quanta attach themselves to each electron. Each flux quanta increases the order of the zeroes of the wavefunction Ψ_3 by one. With three flux quanta attached to each electron, Ψ_3 vanishes as $z_i \to z_j$, and it does so to the third power. This $(z_i - z_j)^3$ term keeps the electrons well separated and greatly reduces the Coulomb repulsive energy of the system. This is the ground state that the system condenses into at this filling factor. The excitations of this state are fractionally charged ($-e/3$), with an energy gap to their creation, and thus there is a QHE at $\nu = 1/3$.

Laughlin explained the FQHE for filling factors $\nu = 1/q$, where q is an odd integer. A simple particle-hole transformation can be used to then account for FQH states observed at $\nu = (q-1)/q$. The remaining odd-denominator fractional states require analogous condensations of the fractionally charged quasiparticle excitations of the Laughlin states; this is called the "hierarchy model" [6]. But the even-denominator FQH states (and there have only been two of them observed; at $\nu = 5/2$ [7] and $\nu = 7/2$ [8]) are not well understood. It had been thought that they were a result of the electrons in the topmost Landau level not being spin-polarized (in general it is thought that the Zeeman energy from the external magnetic field aligns all the spins), and that they were forming opposite spin pairs and behaving like bosons. Bosons can condense into a symmetric version of Laughlin's wavefunction, and create even-denominator FQH states [9], but later investigations of these even-denominator states indicated that they were spin-polarized after all [10], and so the nature of these states remains uncertain.

Laughlin's wavefunction, along with the hierarchy model, provided a basis for understanding all the observed odd-denominator FQH states, and a possible explanation for the two observed even-denominator FQH states; but it could not describe the state of the system in between the FQH states, and it could not describe the system at $\nu = 1/2$, which does not display a FQHE.

4.3 COMPOSITE FERMIONS, $\nu = \frac{1}{2}$

The description of the quantum state at filling factor one-half, $\nu = 1/2$, had not been dealt with at the time. The theory that would lay the foundation for a theoretical description of the $\nu = 1/2$ state came about in 1989, when Jain [11] greatly simplified the difficult many-body problem of strongly interacting electrons in a magnetic with the idea of "composite fermions."

Jain found that by attaching two fictitious flux quanta to each electron, the system could be reduced to a much more tractable problem, that of a weakly interacting gas of these "composite fermions." The motions of these fictitious flux greatly reduce the effective magnetic field that the composite fermions experience, such that

$$B_{eff} = B(1-2\nu), \tag{4.12}$$

B_{eff} being the effective field, and B the real external field.

Jain showed that this theory can offer an alternate explanation of the FQHE – and in fact is something of a unifying theory for the integer QHE and the FQHE. In response to this effective magnetic field, the composite fermions form their own Landau levels, and each time an *integral* number of Landau levels are filled with composite fermions, the system will exhibit a QHE. From equation 4.12, the relationship between the electron filling factor ν and the composite fermion filling factor ν_{CF} is:

$$\nu = \frac{\nu_{CF}}{2\nu_{CF} \pm 1}. \tag{4.13}$$

So, an integer QHE of the composite fermions will correspond to a FQHE of the electrons (as well as the integral $\nu = 1$ state). This can account for FQH states that otherwise must be described in the hierarchical model, descending from the Laughlin wavefunction. A problem with the hierarchical model is that it predicts many fractional states that are not observed; and great-granddaughter states like $\nu = 4/9$, a fractional quantum Hall state made of the excitations of a fractional quantum Hall state made of the excitations of a fractional quantum Hall state of electrons, should not be very robust, and yet make a robust appearance in the spectrum shown in Fig. 4.3. The composite fermion model predicts only the fractions that are observed, and predicts energy gaps for these FQH states that are much more in line with observations [12].

Halperin *et al*. [13] addressed filling factor $\nu = 1/2$ in this composite fermion model in 1993, developing a seminal theory which both explained existing anomalous observations at $\nu = 1/2$ and initiated a great deal of theoretical and experimental work on this filling factor. They noted that at filling factor $\nu = 1/2$, the effective magnetic field is zero. The composite fermions should then fill up a Fermi disk of momentum states, much like electrons do at zero magnetic field, even though the external magnetic field may be quite high. As remarkable as this seems, this is the only theory that can account for anomalously high conductivities observed at $\nu = 1/2$ via surface acoustic wave (SAW) measurements that were done in the late 1980s. SAWs sent across the piezo-electric GaAs surface of a 2DEG heterostructure will interact with the buried 2DEG layer in such a way that properties of the 2DEG can be inferred. At very high frequency (~1 GHz) and large wavevector q, an unexpected enhancement in the 2DEG conductivity was seen [14]. Halperin *et al.* [13] showed that composite fermions at the Fermi surface having momentum in the direction of the SAW propagation can short the SAW field if the composite fermion can conduct without scattering (thus when $q \gg l^{-1}$ where l is the composite fermion mean free path), leaving a signature in the SAW propagation indicative of enhanced 2DEG conductivity, as seen by Willett *et al.* [14]. This is considered direct evidence of the reality of the existence of a well-defined Fermi surface at this filling factor.

4.4 BILAYER QUANTUM HALL PHASE DIAGRAM

When a single layer is at $\nu = \frac{1}{2}$, it can be well described by composite fermion theory. However, when there are two layers in parallel, each at filling factor $\nu = \frac{1}{2}$, things become more complicated. In the ideal limit of infinite separation between the layers, they are just two independent layers, each at $\nu = \frac{1}{2}$, but when the layers are brought close together, the system can enter a new state, another QHE state, but this one uniquely bilayer in nature [15, 16, 17]. The coupling between the layers arises from interlayer tunneling and Coulomb interactions. These two parameters are quantified by the symmetric-antisymmetric tunneling gap energy Δ_{SAS} and the effective layer separation d / ℓ.

Δ_{SAS} is the energy gap between the lowest energy symmetric and antisymmetric eigenstates in the double quantum well system. The bilayer QHE effect that occurs at

$\nu_T = \frac{1}{2} + \frac{1}{2} = 1$ (ν_T is the total filling factor: the sum of the two individual layer filling factors) for large Δ_{SAS} is a trivial consequence of this new bilayer energy gap forming in the density of states. All the electrons will occupy the lower energy symmetric state, and there will be one filled Landau level of symmetric state electrons. The conventional transport will show a minimum in R_{xx} and a quantized Hall plateau in R_{xy}. The temperature dependence will be activated, thus $R_{xx} = R_0 e^{-\Delta/2T}$, with $\Delta = \Delta_{SAS}$. However, even with large Δ_{SAS}, if the effective layer separation d/ℓ is also large, many-body Coulomb effects will destroy this gap [15, 18].

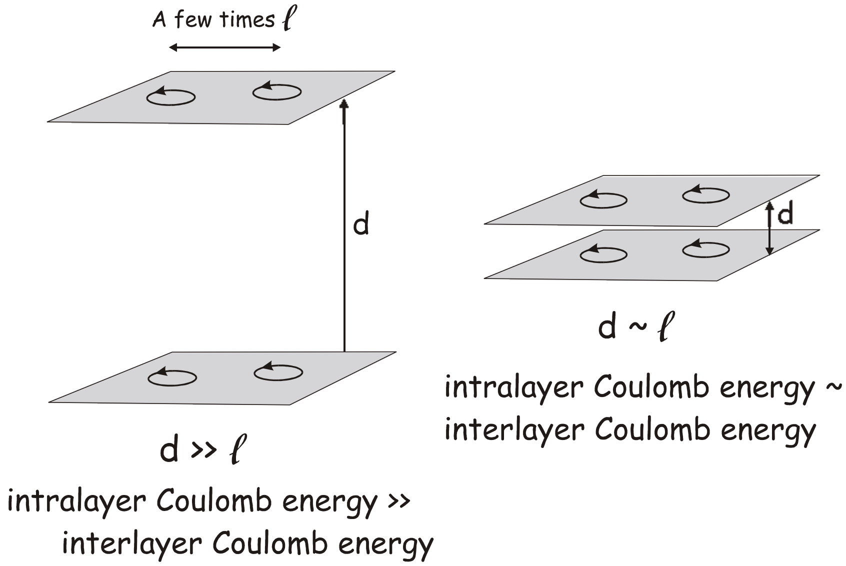
A few times ℓ
d
d >> ℓ
intralayer Coulomb energy >>
interlayer Coulomb energy
d
d ~ ℓ
intralayer Coulomb energy ~
interlayer Coulomb energy

Figure 4.4: The effective layer separation d/ℓ gives the relative importance of the interlayer and intralayer Coulomb energies. In these schematics, the electrons in each layer are represented by their semi-classical orbits and are spaced roughly a few ℓ's apart. For large d/ℓ, shown on the left, intralayer Coulomb coupling will be more important than the interlayer coupling. At small d/ℓ, shown on the right, interlayer coupling will be as significant as intralayer coupling.

The effective layer separation d/ℓ characterizes the relative importance of interlayer and intralayer Coulomb energies. d represents the center-to-center well separation and determines the Coulomb energy between electrons in the different layers $e^2/\varepsilon d$; while the magnetic length $\ell = \sqrt{\hbar/eB}$ measures the mean separation between electrons within the same layer, and so characterizes the intralayer Coulomb energy $e^2/\varepsilon\ell$. The ratio of these two energies, just d/ℓ, parameterizes the interlayer Coulomb coupling (see Figure 4.4).

At large d/ℓ, the system behaves roughly as two independent single layers each described by a Fermi liquid of composite fermions [19, 20, 21, 22]. In this case no quantum Hall state exists at $\nu_T = 1$ since there are no $\nu = \frac{1}{2}$ quantum Hall states in the single layers. By monitoring the system for the appearance of a quantum Hall state at different effective layer separations d/ℓ, and different tunneling strengths Δ_{SAS}, a phase diagram can be established.

Figure 4.5 shows this phase diagram as pioneered experimentally by Murphy *et al.* [23] (although the first phase diagram appeared in a theory paper, and it correctly predicted the non-zero y-axis intercept [18]). The main figure shows the conventional longitudinal resistivity ρ_{xx} versus magnetic field measured with the current flowing parallel through both layers and with the voltage probes also connected to both layers. The dotted curve shows a typical ρ_{xx} trace for when the system is not exhibiting a QHE at $\nu_T = 1$, and the solid curve for when it is – as indicated by a deep minimum at that filling factor.

The inset shows the results of these measurements for $T = 0.3$ K done on a number of samples with a range of different d/ℓ and Δ_{SAS} values. The x-axis represents the tunneling gap energy Δ_{SAS} in units of the intralayer Coulomb energy $e^2/\varepsilon\ell$ (evaluated at $\nu_T = 1$), and the y-axis the effective layer separation d/ℓ. Samples that showed a QHE at $\nu_T = 1$ are indicated by filled symbols, and those that did not by open symbols. An estimated boundary between the two groups is sketched as a dashed line.

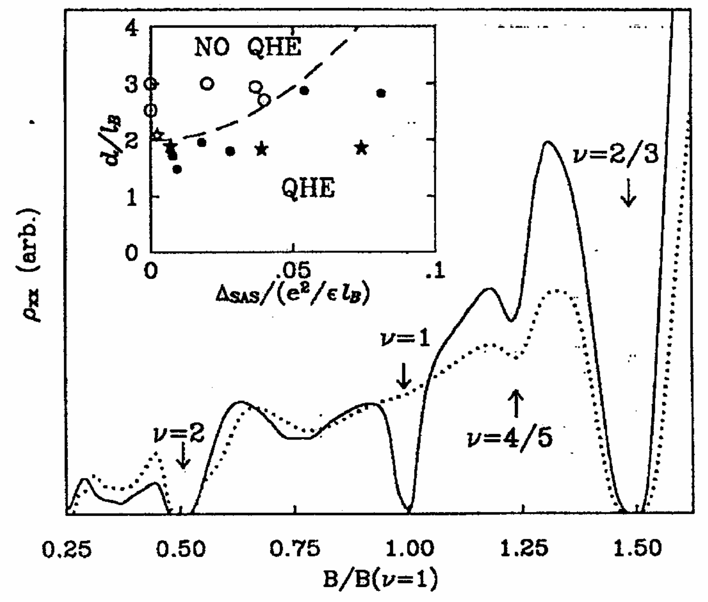

Figure 4.5: Phase diagram for bilayer QHE at $\nu_T = 1$. Main figure shows the longitudinal conventional resistivity ρ_{xx} versus magnetic field for the cases with (solid curve) and without (dotted curve) a $\nu_T = 1$ QHE. Samples that showed a QHE are plotted in the phase diagram in the inset as filled symbols, those that didn't, as open symbols. The dashed line is an estimate of the phase boundary. Taken from Ref. 23.

One of the most intriguing features of this phase diagram is that the phase boundary appears to intercept the y-axis at a finite value, thus indicating that a bilayer QHE can exist even in the absence of a tunneling energy gap; that a new kind of energy gap arising entirely from many-body Coulomb interactions between the electrons must exist.

This new phase was in fact predicted [24, 25], and it is the exploration of this novel phase that is the primary concern of the remaining chapters of this thesis.

Our sample was designed to probe the region where this new phase might exist, and so the tunneling gap energy Δ_{SAS} was kept extremely low. For this wafer $\Delta_{SAS}/(e^2/\varepsilon\ell)\approx 10^{-6}$ and so would fall effectively right on the y-axis in the phase diagram in Fig. 4.5. The nominal effective layer separation of this wafer is $d/\ell \approx 2.3$, which is above the phase boundary, but by electrostatic gating we can continuously reduce the electron densities in the layers, which has the effect of increasing ℓ, and thus probe a range of d/ℓ values down the axis in the hopes of encountering the phase barrier, and discovering a new quantum ground state.

4.5 THE (111) STATE

The ground state in the limit of small effective layer separation and zero tunneling was first studied theoretically. Its true genesis was in the seminal work by Robert Laughlin [5] who found the wavefunction that correctly described the fractional quantum Hall effect discovered the previous year [3]. The energy gaps responsible for the QHE that occur at fractional filling factors $\nu = 1/m$, where m is an odd integer, arise entirely from many-body Coulomb interactions between the electrons, and can be described by Laughlin's wavefunction:

$$\Psi_m \equiv \prod_{i<j}(z_i - z_j)^m \prod_i \exp(-|z_i|^2/4) \tag{4.14}$$

where $z_i = x_i - iy_i$ is the location of the i^{th} electron in the 2D plane with coordinates (x_i, y_i), and m is an odd integer. Notice that $\Psi_m \to 0$ when $z_i = z_j$, as would be expected for identical fermions. For the strongest fractional quantum Hall state, which occurs at $\nu = 1/3$, $m = 3$ and the electrons are repelled from each other as $(z_i - z_j)^3$.

Shortly after Laughlin's wavefunction appeared, Halperin generalized it to two-state systems, where initially the two states considered were the spin states of the electrons [26]:

$$\Psi_{(lmn)} = \prod(z_i - z_j)^l \prod(w_i - w_j)^m \prod(z_i - w_j)^n \exp\left[-\tfrac{1}{4}\left(\sum|z_i|^2 + \sum|w_i|^2\right)\right] \tag{4.15}$$

In this wavefunction, generally called the (lmn) state, z and w are the coordinates of the electrons in the first and second states respectively. Even though the z and w particles are not identical, this wavefunction nonetheless vanishes when $z_i = w_j$.

This equation would eventually be considered for bilayer electron systems at total filling factor one (and smaller), where the two states were not the electron spin states (which are expected to be aligned with the magnetic field in this case) but the electron layer index: "top layer" and "bottom layer." First considered by Yoshioka *et al.*, they found that the

$\Psi_{(111)}$ state was well matched to exact numerical solutions of the Hamiltonian of a bilayer electron system at $\nu_T = 1$ having 10 electrons – provided that the effective layer separation was below a certain critical value [27]. This $\Psi_{(111)}$, or just (111), state would come to be the accepted description of the strongly-coupled bilayer $\nu_T = 1$ state:

$$\Psi_{(111)} = \prod (z_i - z_j) \prod (w_i - w_j) \prod (z_i - w_j) \exp\left[-\tfrac{1}{4} \left(\sum |z_i|^2 + \sum |w_i|^2 \right) \right]. \quad (4.16)$$

In this state the electrons in each layer must avoid each other (the zeroes are only first-order in this case though), but most importantly, the electrons in the different layers must also avoid each other. Then each orbital state in the first Landau level will be occupied, if not by an electron in one layer, then necessarily by an electron in the other layer. The Landau level will be filled and there will be an energy gap for the addition of another electron to the system and a QHE will be observed.

4.6 PSEUDOSPIN FERROMAGNET

In 1994, Yang *et al.* showed that the (111) state can be likened to a single layer Laughlin wavefunction for $m = 1$ of spin-$\frac{1}{2}$ electrons all aligned in the XY plane [28]:

$$\Psi(z_1, z_2, ..., z_N) = \prod_{i<j}^{N} (z_i - z_j) \exp(-\tfrac{1}{4} \sum_m |z_m|^2) \left| \rightarrow \rightarrow \rightarrow \rightarrow \rightarrow ... \rightarrow \right\rangle \quad (4.17)$$

$$\text{where} \quad \left| \rightarrow \right\rangle = \frac{1}{\sqrt{2}} \left(\left| \uparrow \right\rangle + e^{i\varphi} \left| \downarrow \right\rangle \right). \quad (4.18)$$

Thus the layer degree of freedom can be mapped to a spin-$\frac{1}{2}$ particle. In this language an electron in the top layer may be called "pseudospin up" $\left|\uparrow\right\rangle$ and then an electron in the bottom layer will be "pseudospin down" $\left|\downarrow\right\rangle$. In this view the electrons go into a superposition of the two layer eigenstates and completely fill one Landau level. The pseudospins lie near the XY plane and their orientation in that plane is given by the phase φ. In the absence of tunneling, the energy is degenerate for all angles $0 \le \varphi < 2\pi$, so this is a broken symmetry state as the final state has less symmetry than the Hamiltonian. This system is equivalent to an easy-plane itinerant ferromagnet of spin-$\frac{1}{2}$ particles. The broken symmetry imparts a neutral gapless mode with a linear dispersion relation [18, 29, 30]. Finite tunneling will introduce a gap to this mode, but if it is sufficiently small it should not completely destroy the character of the state [31].

In this model, the electrons have a fundamental quantum uncertainty as to which layer they are in. Because of this, the number of electrons in each layer is not a conserved quantity, and small amounts of charge will fluctuate between the layers. This has been detected as a large peak in the tunneling conductance at zero interlayer bias [32].

These pseudospins have also been detected by their interaction with an in-plane magnetic field. Murphy *et al.* detected an unexpected change in the slope of the activation energy of the $\nu_T = 1$ state in a sample with tunneling gap energy $\Delta_{SAS} = 0.8$ K with applied in-plane magnetic field $B_{\|}$ [23]. $B_{\|}$ effects a spatially modulated phase change to the tunneling matrix element, which the pseudospins initially try to follow. The greater $B_{\|}$, the more rapid the spatial variation in the phase ($\lambda = h / eB_{\|}d$ where λ is the wavelength of the modulation). However, there is an energy cost $\sim |\nabla\varphi|^2$ associated with the twisting of the pseudospins that eventually wins out, and the pseudospins opt for a $\nabla\varphi = 0$ state and relinquish the tunneling energy [28]. The phase transition can be detected as a discontinuity in the slope of the activation energy when plotted as a function of $B_{\|}$.

By applying the current density formula from basic quantum mechanics ($J \propto \psi^*\nabla\psi - \psi\nabla\psi^*$, where J is the current density, ψ is the wavefunction and ψ^* is its conjugate) to just the pseudospin portion of the wavefunction (eqn. 4.18) It can be seen that there exists a pseudospin current $J \propto \nabla\varphi$, which is proportional to the gradient of the phase φ. This current manifests as equal but oppositely directed regular currents moving through the two layers without dissipation [33]. The kinetic energy of this dissipationless current is where the $|\nabla\varphi|^2$ energy is stored.

The easy-plane itinerant ferromagnet is mathematically equivalent to a two-dimensional superfluid or 2D dirty superconductor film or 2D Josephson junction array [34] where φ serves as the phase of the superconducting order parameter, and like those systems, our system can also support supercurrents. Detecting this supercurrent is the main goal of this thesis.

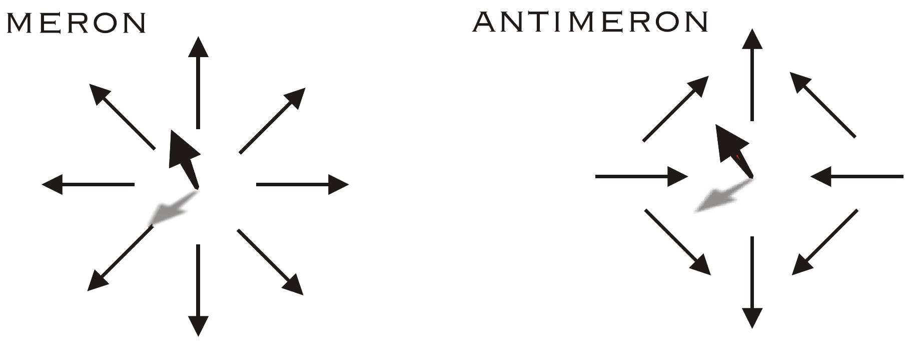

Figure 4.6: Stable topological defects with charge $\pm e/2$. Merons have positive vorticity, antimerons have negative vorticity. Merons and antimerons come in two "flavors" depending on whether the central pseudospin is pointing "up" or "down". The charge depends on a combination of the vorticity and the flavor.

In this pseudospin ferromagnet picture, the charged excitations of the ground state are stable topological defects called merons and antimerons (see Figure 4.6). They are charged excitations, carrying a charge of $\pm e/2$.

Far from the core of the meron, the pseudospins lie in the XY plane, with a phase winding of $\pm 2\pi$ corresponding to positive (meron) or negative (antimeron) vorticity, and there are corresponding superfluid vortex currents ($J \propto \nabla\varphi$). The cores of the merons consist of a pseudospin pointing completely out of the XY plane – thus corresponding to an electron entirely localized in one or the other of the layers. The pseudospins fall away from the vertical in a continuous manner as the distance from the core is increased.

Single merons are highly disruptive to the long-range pseudospin order, however oppositely charged meron-antimeron pairs are electrically neutral and together have zero vorticity, and so only create a local disturbance in the order. Below a critical temperature, the Kosterlitz-Thouless temperature T_{KT}, free energy considerations keep merons and antimerons bound in neutral, zero vorticity pairs. Above T_{KT}, the pairs unbind, and the order and thus the superfluidity is lost. This is called a Kosterlitz-Thouless phase transition [35]. T_{KT} is predicted to be in the range of 0.1 K to 0.5 K for our sample parameters [31].

Below T_{KT} the conductivity should be infinite in linear response. A current will pull on the meron-antimeron pairs imparting an energy gap to their dissociation – so this system has a critical current of zero. Below T_{KT}, the voltage-current relationship obeys [36]

$$V \propto I^p, \tag{4.19}$$

$$\text{where} \qquad p = 1 + 2\frac{T_{KT}}{T}. \tag{4.20}$$

Above T_{KT} the voltage-current relationship will be ohmic $V \propto I$, so there should be a discontinuous jump in the value of p at $T = T_{KT}$ from $p = 1$ to $p = 3$. This jump has been observed in 2D superconducting arrays [37]. Observation of this jump in our system would be an excellent confirmation of the Kosterlitz-Thouless phase transition.

4.7 EXCITONIC CONDENSATE

The (111) state can alternately be mapped to a Bose-Einstein condensate (BEC) of electron-hole pairs, electrons in one layer and holes in the other [29, 38, 39]. By a particle-hole transformation on just one of the layers, our system becomes one layer of electrons plus one layer of holes. At $\nu_T = 1$, regardless of whether or not the layers are balanced, there will always be an equal number of electrons and holes. In the (111) state each electron binds to a hole that is directly opposite to it in the other layer, this corresponds to electron-hole pairs with opposite k states, where k labels the lowest Landau level orbital states (see Section 4.1), and so the combined state has $k = 0$. All of the excitons will then be in the same $k = 0$ state, which is permitted because excitons are bosons, and the system will then be a BEC of excitons.

The BEC of electron-hole pairs (excitons) has been studied extensively since 40 years ago, when it was first considered [40, 41], and pursued experimentally almost as long [42]. But always the holes have been valence band holes, not the conduction band holes that exist in our system. Despite much effort, the BEC of excitons has never been achieved in these systems. The greatest obstacle has been the short lifetimes of the excitons and the fact that they are created by photo-excitation, which heats them above the local thermal equilibrium. Before they can cool and then Bose condense, they have usually already recombined.

Our excitons make better candidates for undergoing BEC because they do not suffer from these problems: they are not optically generated, and so remain in thermodynamic equilibrium with the local environment, and even more significantly, they have infinite lifetimes. In this picture of the (111) state, the superfluid pseudospin current of the ferromagnet view is equivalent to a superfluid flow of this exciton condensate. Since the electrons and holes will be moving together in the same direction, but with the electrons in one layer, and the holes in the other, this will correspond to equal but oppositely directed regular currents flowing through the two layers without dissipation.

This view also makes readily apparent an additional attribute to the pseudospin current: not only can two oppositely directed currents flow through the layers without dissipation, but they will also flow through the layers without producing a Hall voltage. Individual electrons and holes flowing in the same direction in the presence of a perpendicular magnetic field will be compelled in opposite directions by the Lorentz force. Since our electrons and holes are bound together, they will feel no net force due to the magnetic field, and so they will move through the layers without causing a Hall voltage to arise.

Detection of this dissipationless, charge-neutral transport is how we intend to show that our bilayer electron system has transformed itself into an excitonic BEC.

* * *

---

1 L. Landau, Z. Phys. **64**, 629 (1930).

2 K. von Klitzing, G. Dorda and M. Pepper, Phys. Rev. Lett. **45**, 494 (1980).

3 D.C. Tsui, H.L. Störmer and A.C. Gossard, Phys. Rev. Lett. **48**, 1559 (1982).

4 H.L. Störmer, Physica B **177**, 401 (1992).

5 R.B. Laughlin, Phys. Rev. Lett. **50**, 1395 (1983).

6 J.P. Eisenstein and H.L. Störmer, Science **248**, 1510 (1990).

7 R. Willett, J.P. Eisenstein, H.L. Störmer, D.C. Tsui, A.C. Gossard and J.H. English, Phys. Rev. Lett. **59**, 1776 (1987).

8 J.P. Eisenstein, K.B. Cooper, L.N. Pfeiffer and K.W. West, Phys. Rev. Lett. **88**, 076801 (2002).

9 F.D.M. Haldane and E.H. Rezayi, Phys. Rev. Lett. **60**, 956 (1988).

10 W. Pan, H.L. Störmer, D.C. Tsui, L.N. Pfeiffer, K.W. Baldwin and K.W. West, Solid State Commun. **119**, 641 (2001).

11 J.K. Jain, Phys. Rev. Lett. **63**, 199 (1989).

12 R.R. Du, H.L. Störmer, D.C. Tsui, L.N. Pfeiffer and K.W. West, Phys. Rev. Lett. **70**, 2944 (1993).

13 B.I. Halperin, P.A. Lee and N. Read, Phys. Rev. B **47**, 7312 (1993).

14 R.L. Willett, M.A. Paalanen, R.R. Ruel, K.W. West, L.N. Pfeiffer and D.J. Bishop, Phys. Rev. Lett. **65**, 112 (1990).

15 G.S. Boebinger, H.W. Jiang, L.N. Pfeiffer and K.W. West, Phys. Rev. Lett. **64**, 1793 (1990).

16 J.P. Eisenstein, G.S. Boebinger, L.N. Pfeiffer, K.W. West and S. He, Phys. Rev. Lett. **68**, 1383 (1992).

17 Y.W. Suen, L.W. Engel, M.B. Santos, M. Shayegan and D.C. Tsui, Phys. Rev. Lett. **68**, 1379 (1992).

18 A.H. MacDonald, P.M. Platzman and G.S. Boebinger, Phys. Rev. Lett. **65**, 775 (1990).

19 I. Ussishkin and A. Stern, Phys. Rev. B **56**, 4013 (1997).

20 S. Sakhi, Phys. Rev. B **56**, 4098 (1997).

21 Y.B. Kim and A.J. Millis, Physica E **4**, 171 (1999).

22 B.N Narozhny, I.L. Aleiner and A. Stern, Phys. Rev. Lett. **86**, 3610 (2001).

23 S.Q. Murphy, J.P. Eisenstein, G.S. Boebinger, L.N. Pfeiffer and K.W. West, Phys. Rev. Lett. **72**, 728 (1994).

24 T. Chakraborty and P. Pietiläinen, Phys. Rev. Lett. **59**, 2784 (1987).

25 D. Yoshioka, A.H. MacDonald and S.M. Girvin, Phys. Rev. B **39**, 1932 (1989).

26 B.I. Halperin, Helv. Phys. Acta **56**, 75 (1983).

27 D. Yoshioka, A.H. MacDonald and S.M. Girvin, Phys. Rev. B **39**, 1932 (1989).

28 K. Yang, *et al.*, Phys. Rev. Lett. **72**, 732 (1994).

29 H.A. Fertig, Phys. Rev. B **40**, 1087 (1989).

30 X.G. Wen and A. Zee, Phys. Rev. Lett. **69**, 1811 (1992).

31 S. Das Sarma and A. Pinczuk, *Perspectives in Quantum Hall Effects* (John Wiley & Sons, Inc., New York 1997). See chapter by S.M. Girvin and A.H. MacDonald.

32 I.B. Spielman, J.P. Eisenstein, L.N. Pfeiffer and K.W. West, Phys. Rev. Lett. **84**, 5808 (2000) and Phys. Rev. Lett. **87**, 036803 (2001).

33 K. Moon, *et al.,* Phys. Rev. B **51**, 5138 (1995).

34 A.M. Goldman and S.A. Wolf, *Percolation, Localization, and Superconductivity* (Plenum Press, New York 1984). See chapter by J.E. Mooij.

35 J.M. Kosterlitz and D.J. Thouless, J. Phys. C **6**, 1181 (1973).

36 S.M. Girvin, *July 2000 Boulder School on Superconductivity*, Lecture II: The Kosterlitz-Thouless Phase Transition, http://research.yale.edu/boulder/index.html.

37 D.W. Abraham, C.J. Lobb, M. Tinkham and T.M. Klapwijk, Phys. Rev. B **26**, 5268 (1982).

38 A.H. MacDonald, Physica B **298**, 129 (2001).

39 A.H. MacDonald, A.A. Burkov, Y.N. Joglekar and E. Rossi, Phys. Of Semicond. 2002, IOP Conf. Series **171**, 29 (2003). (cond-mat/0310740)

40 S.A. Moskalenko, Fiz. Tverd. Tela **4**, 276 (1962).

41 J.M. Blatt, K.W. Boer and W. Brandt, Phys. Rev. **126**, 1691 (1962).

42 For a review see: S.A. Moskalenko and D.W. Snoke, *Bose-Einstein Condensation of Excitons and Biexcitons* (Cambridge University Press, Cambridge 2000).

Chapter 5: Coulomb Drag at $\nu_T = 1$

The (111) state at $\nu_T = 1$ arises from many-body interactions in which the interlayer Coulomb interactions play a key role. As Coulomb drag is a direct measure of interlayer Coulomb interactions (Chapter 3), it should make for an excellent probe of this state, and this chapter shows that it does indeed.

5.1 SAMPLES: 'N' AND 'R'

Sample piece 'N' was taken $\sim 7\,\text{mm}$ away and sample piece 'R' $\sim 5\,\text{mm}$ from the center of the wafer. Both were processed by Ian Spielman. They both consist of a central square mesa $250\,\mu\text{m}$ on a side, with four arms extending out of each side (see Fig. 5.1). AuNiGe was diffused into the end of each arm for electrical contact. Electrostatic gates above and below each arm allow for *in situ* control over which layer(s) each arm makes contact with [1]. Similar gates above and below the main central mesa allow for individual control over the electron density in each layer. Both samples' as-grown density was $n = 5.3 \times 10^{10}\,\text{cm}^{-2}$ per layer, and the mobility was $\mu \approx 10^6\,\text{cm}^2/\text{Vs}$. For both samples the zero field tunneling resistance at resonance is $R \approx 30\,\text{M}\Omega$.

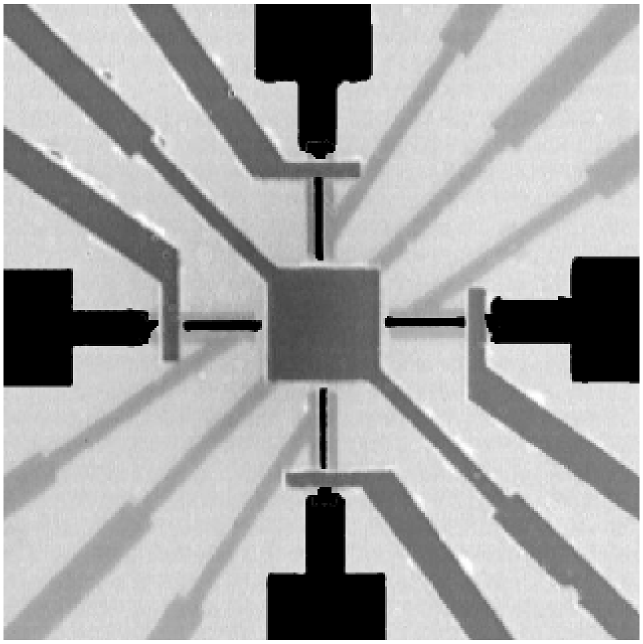

Figure 5.1: Infrared photo of sample ‘N’. Black shows mesa (central $250\,\mu\mathrm{m}\times 250\,\mu\mathrm{m}$ square is hidden below central back gate), the back gates are medium gray, and the top gates are light gray. The field of view is ~ 2 mm across. Photo courtesy of Ian Spielman.

5.2 HALL AND LONGITUDINAL DRAG VERSUS MAGNETIC FIELD

Figure 5.2 shows the main result of this chapter. In it are the conventional and the drag resistances at $n = 2.6\times 10^{10}\ \mathrm{cm}^{-2}$ per layer ($d/\ell = 1.60$ at $\nu_T = 1$) versus magnetic field. The current used was typically 2 nA at 5 Hz. All the traces were taken at $T = 20$ mK except for the longitudinal drag (curve ‘C’) which was taken at $T = 50$ mK.

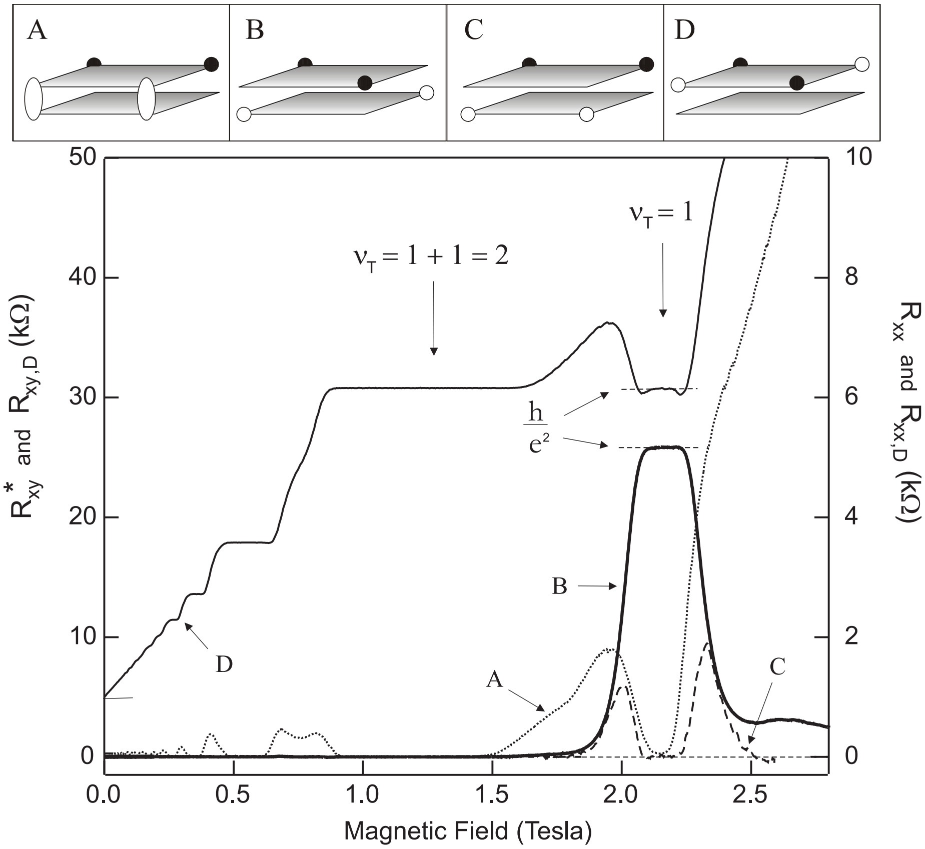

Figure 5.2: Conventional and drag resistances versus magnetic field for $n = 2.6\times10^{10}$ cm^{-2} corresponding to $d/\ell = 1.60$ at $\nu_T = 1$. Curve A shows the conventional longitudinal resistance R_{xx} for current injected in both the layers and voltage measured only in one. Curve B is the Hall drag $R_{xy,D}$, C is the longitudinal drag $R_{xx,D}$, and D is the conventional Hall resistance measured in just one layer R^*_{xy}, offset by 5 kΩ for clarity. The schematics in the top panel show the current (white dots) and voltage (black dots) contact points for the respective data curves, A-D. Curves A, B and D were taken at $T = 20$ mK, while curve C was taken at $T = 50$ mK. Sample 'N'.

Curve 'A' shows the conventional longitudinal resistance R_{xx}. For this measurement, current is sent in through both layers – the current entry points are indicated by the two white dots shown in the measurement schematic 'A' in the top panel; the longitudinal voltage is measured along the remaining two adjacent contacts, this time in just one of the layers (the two black dots).

Throughout most of the magnetic field range, curve ‘A’ simply reflects the resistance of the single layer being measured, as the layers only become strongly coupled around $\nu_T = 1$ which occurs at $B \approx 2.2\,\mathrm{T}$ for this density (in theory, they should also be strongly coupled at $\nu_T = \frac{1}{3}$ and other fractional filling factors with odd denominator [2, 3], but our samples go insulating long before we reach such a low filling factor). When the strongly coupled $\nu_T = 1$ phase sets in, the resistance instead reflects the bilayer quantum Hall state and drops towards zero, displaying the quantum Hall minimum as had already been seen in other experiments [4, 5, 6]. At fields above $\nu_T = 1$, the resistance rises steeply because the sample is going insulating.

Curve ‘D’ shows the conventional Hall resistance R_{xy}^*, but with the current flowing in, and the voltage measured in, just one of the layers. It is offset by 5 kΩ for clarity. Up to $B \approx 1.5$ Tesla the quantum Hall plateaus are reflecting the single-layer filling factor. The broad plateau centered about $B \approx 1.1$ Tesla is quantized at h/e^2 (25.8 kΩ), appropriate to the $\nu = 1$ in the each layer. When the layers become strongly coupled around $B \approx 2.2$ Tesla, R_{xy}^* *again* plateaus at h/e^2 – but this time it is in response to the *total* filling factor $\nu_T = 1$.

Curve ‘B’ shows the Hall drag $R_{xy,D}$. Current flows in the drive layer, and the Hall voltage in the drag layer is measured. Up to $B \approx 1.6$ Tesla, the Hall drag is essentially zero, some energy-dependent scattering processes can lead to a Hall drag signal [7, 8], but a very very small one, which was not detectable at these sensitivities. This essentially null signal is consistent with the basic physical fact that a Hall voltage is a response to a current flowing in a magnetic field. Since the drag layer is electrically open, no current can flow in this layer, and so there is no Hall voltage. Despite the lack of current in the drag layer, when the system enters the strongly-coupled phase near $\nu_T = 1$, remarkably, a Hall voltage does appear in the layer. And like curve ‘D’ at $\nu_T = 1$, the Hall drag also forms a $\nu_T = 1$ quantized Hall plateau: quantized at h/e^2 to within 5 parts in 10^4.

Curve ‘C’ is the longitudinal drag $R_{xx,D}$. There are features in the drag at low magnetic field arising from interlayer scattering, much like at $B = 0$ (see Appendix G for pictures of $R_{xx,D}$ at low field), they are just not visible on this scale. As the system approaches $\nu_T = 1$, the drag becomes much larger than its lower field values, as large as 2 kΩ measured along just one side of the square mesa, this corresponds to approximately $\ln 2/\pi \sim 0.22$ squares, and a drag resistivity of $\rho_{xx,D} \sim 9\,\mathrm{k}\Omega/\mathrm{square}$, assuming van der Pauw formalism [9]. This is the same order of magnitude as the single layer resistance – extraordinarily large on the scale of typical Coulomb drag due to scattering, indicating that the drag in this region is caused by a whole new mechanism altogether. At $\nu_T = 1$, $R_{xx,D}$ drops to zero.

Although the absence of Hall drag below $B \approx 1.6\,\mathrm{T}$ is proof that there is indeed no current flowing in the drag layer under the usual circumstances, it was necessary to gather more evidence to show that the Hall drag seen at $\nu_T = 1$ wasn't due to a sudden flooding of current into the layer by some unconventional means. As the $\nu_T = 1$ state shows an enhancement of the tunneling conductance around zero bias voltage, this was the obvious suspect that needed to be ruled out [10]. Although the tunneling conductance peak around zero bias voltage is dramatic; it corresponds to very little tunneling current, as the peak is only $\approx 6\,\mu\mathrm{V}$ wide, and even at resonance, the tunneling resistance is still a rather formidable $R \approx 100\,\mathrm{k}\Omega$ [11]. Direct tunneling measurements on the sample used here have shown that the maximum tunnel current that can flow between the two layers is $\approx 10\,\mathrm{pA}$. Compared to the $\approx 2\,\mathrm{nA}$ drive current used here, this amounts to at most a 0.5% current leakage.

However, to be sure there were no unforeseen effects due to this onset of tunneling at $\nu_T = 1$, the Hall drag was measured with the addition of an in-plane magnetic field, and (separately) an interlayer bias voltage, as both of these are known to dramatically suppress the tunneling conductance [12].

Figure 5.3 shows these measurements. On the left are five different Hall drag traces centered around the $\nu_T = 1$ feature, taken with five different in-plane magnetic fields, (-0.21, 0, 0.27, 0.53, 0.72) Tesla, with the same perpendicular field (which is plotted on the x-axis) for $d/\ell = 1.61$. The Hall drag is shown to be robust against the application of an in-plane magnetic field. Ref. 12 shows that the tunneling conductance peak at $d/\ell = 1.61$ is diminished steadily with the application of an in-plane magnetic field, reduced by a factor of ≈ 100 by $B_{in-plane} = 0.59$ Tesla.

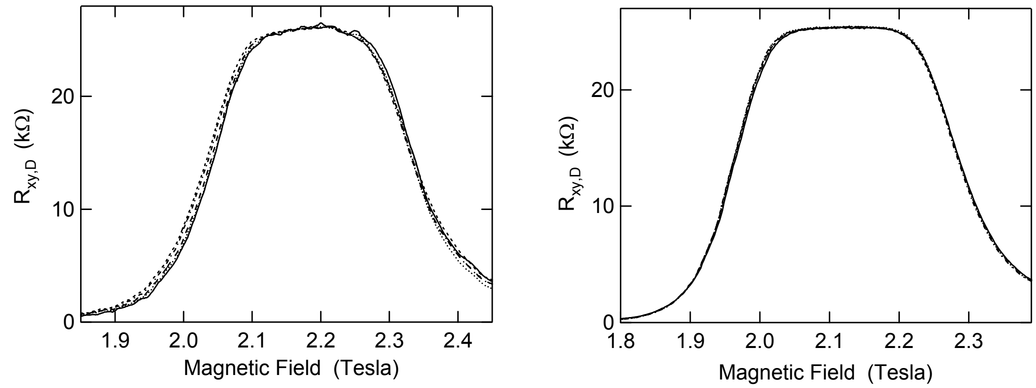

Figure 5.3: The left panel shows five Hall drag traces taken with five different in-plane magnetic fields $B_{in-plane} = (-0.21,\ 0,\ 0.27,\ 0.53,\ 0.72)$ Tesla (the perpendicular field is plotted on the x-axis) at $d/\ell = 1.61$ and $T = 30$ mK. Sample 'N'. The right panel shows five Hall drag traces taken with five different interlayer bias voltages $(-10,\ 0,\ 25,\ 75,\ 100)\ \mu\text{V}$ at $d/\ell = 1.59$ and $T = 25$ mK. Sample 'R'.

On the right are five different Hall drag traces centered around the $\nu_T = 1$ feature, taken with five different interlayer bias voltages (-10, 0, 25, 75, 100) μV at $d/\ell = 1.59$. An interlayer bias with a magnitude greater than $\approx 4\,\mu\text{V}$ suppresses the tunneling conductance by almost two orders of magnitude [11], yet this suppression of tunneling has no noticeable effect on the Hall drag, indicating that the Hall drag itself is not a byproduct of the tunneling enhancement.

Quantized Hall drag was predicted [13 – 18], and is a consequence of the interlayer phase coherence. In the pseudospin ferromagnet picture, when the system is in the $\nu_T = 1$ state the electrons are in a superposition of the two layer eigenstates – the electrons are neither localized in one layer nor the other. This makes it impossible to localize the drive current to just the drive layer, instead a symmetric current will flow through both the layers. This current will produce a Hall voltage in each layer, and since these delocalized electrons fill up one Landau level between the two layers, this Hall voltage will be quantized, relative to the drive current, at h/e^2.

But the drag layer is still electrically open and cannot support a net current flow. In order to meet the boundary requirements of this layer, there must be an equivalent antisymmetric current. In the ferromagnet picture, a gradient of the order parameter produces a superfluid antisymmetric current, which can alternately be thought of as a dissipationless flow of a Bose-Einstein condensate of excitons [19]. Because this current is being carried by charge neutral excitons, it will not be affected by the magnetic field, and it will not produce a Hall voltage. But it will oppose the current in the drag layer such that there will be no net transport of charge in that layer, and the drag layer boundary conditions will be met.

The longitudinal drag resistance is consistent with this model. $R_{xx,D}$ goes to zero across the same range of magnetic field ($2.10 \le B \le 2.22$ Tesla) for which the Hall drag is quantized, suggesting that the momentum transferred to the drag layer by the symmetric current is being compensated by the superfluid flow of the excitons. The peaks in the longitudinal drag on either side of the minimum, as the sample is transitioning into the $\nu_T = 1$ state, correspond (in this view) to isolated regions in the sample becoming interlayer coherent as the phase boundary is approached – thus setting up some symmetric current, but without yet enough phase coherence across the sample for the macroscopic phase gradient needed to induce the antisymmetric current. So in these peaks, there is a tremendous amount of momentum being transferred to the drag layer by the delocalized electrons, but there is not yet sufficient superfluid antisymmetric current to counteract it, and so the longitudinal drag becomes extraordinarily large.

5.3 TEMPERATURE DEPENDENCE

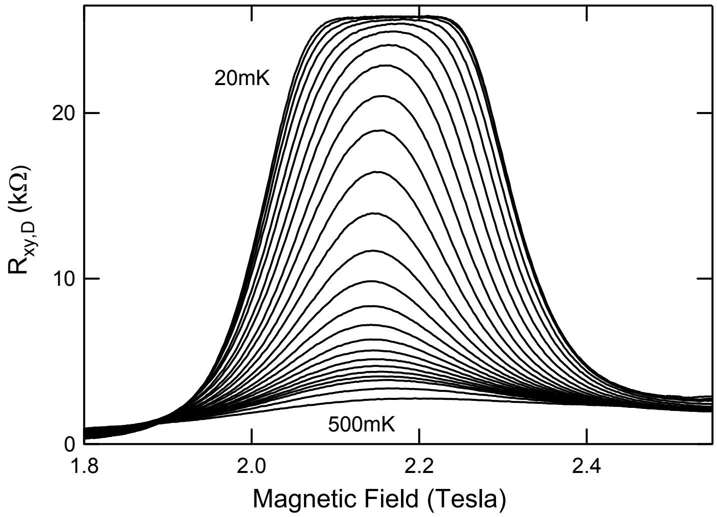

Figure 5.4: Hall drag versus magnetic field at $d/\ell = 1.60$ for $T = 20$ (topmost), 35, 50, 65, 80, 95, 110, 125, 140, 155, 170, 185, 200, 215, 230, 245, 260, 275, 290, 305, 320, 335, 350, 395, 500 (bottommost) mK. Sample 'N'.

Figure 5.4 shows the Hall drag $R_{xy,D}$ in the vicinity of $\nu_T = 1$ at a series of temperatures ranging from 20 to 500 mK, again at $d/\ell = 1.60$. At 20 mK the Hall drag rises up around $\nu_T = 1$ to form a broad plateau quantized at h/e^2. As the temperature is increased the plateau becomes less broad until it is just a peak in the drag locating $\nu_T = 1$. Further heating and the peak becomes smaller and smaller; by 500 mK it is barely discernable over the background.

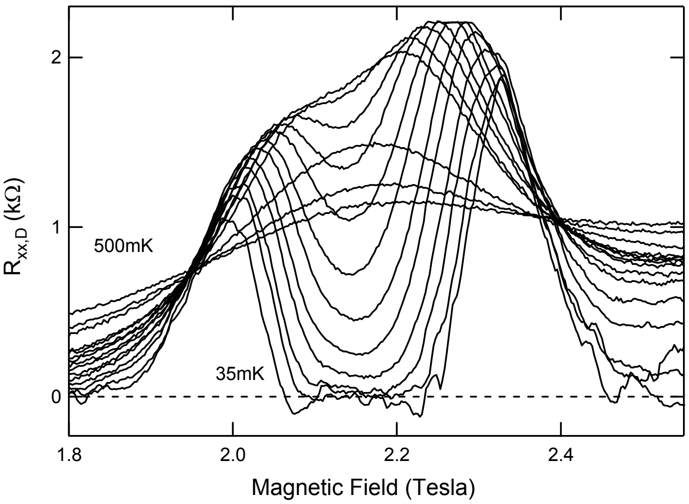

Figure 5.5: Longitudinal drag versus magnetic field at $d/\ell = 1.60$ for $T = 35$ (bottommost), $50, 65, 80, 95, 110, 125, 140, 155, 170, 185, 200, 300, 400, 500$ mK. Sample 'N'.

And Figure 5.5 shows the longitudinal drag resistance $R_{xx,D}$ at $d/\ell = 1.60$ taken over a similar temperature range. Unlike the Hall drag, the temperature dependence of the longitudinal drag at $\nu_T = 1$ is non-monotonic. On raising the temperature the broad zero around $\nu_T = 1$ becomes narrower, and then just becomes a non-zero minimum. $R_{xx,D}$ at $\nu_T = 1$ then increases steadily with increasing temperature, always maintaining a local minimum around $\nu_T = 1$ until the temperature reaches $T \approx 200$ mK. At this temperature $R_{xx,D}$ reaches its maximum height and further heating reduces its value, but now $\nu_T = 1$ is marked by a *peak* in the drag, rather than a minimum.

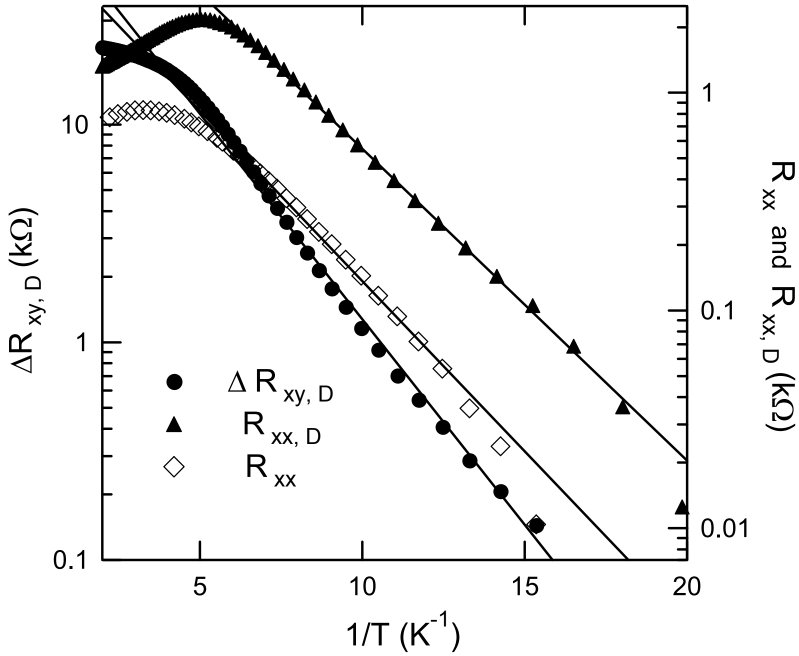

Figure 5.6: $\nu_T = 1$ values of the conventional and drag longitudinal resistances R_{xx} and $R_{xx,D}$, and the deviation in Hall drag from its quantized value $\Delta R_{xy,D} \equiv (h/e^2 - R_{xy,D})$ versus the inverse of the temperature. The lines are merely guides to the eye. $d/\ell = 1.60$. Sample 'N'.

Figure 5.6 shows the temperature dependence, at $\nu_T = 1$ only, for these different resistance measurements. Shown are R_{xx}, $R_{xx,D}$, and $\Delta R_{xy,D} \equiv (h/e^2 - R_{xy,D})$, the difference between the Hall drag and its quantized value. Both the conventional and drag longitudinal resistances show activated behavior, thus $R_{xx(,D)} = R_0 e^{-\Delta/2T}$, with the same energy gap $\Delta \approx 0.8$ K. Interestingly, the deviation in the Hall drag $\Delta R_{xy,D}$, although not as straight a line, does correspond to a similar gap energy.

5.4 DEPENDENCE OF HALL COEFFICIENTS ON EFFECTIVE LAYER SEPARATION

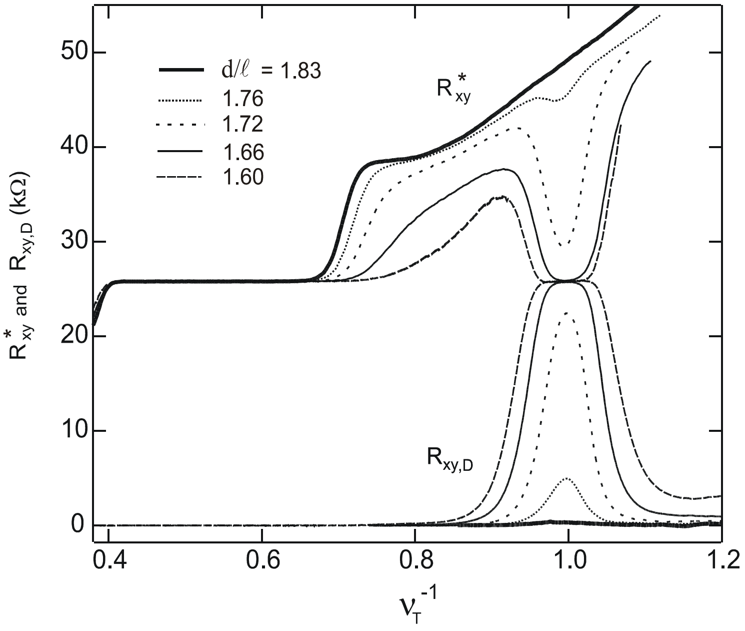

Figure 5.7: Conventional and drag Hall resistances R^*_{xy} and $R_{xy,D}$ versus ν_T^{-1} for $d/\ell = 1.60, 1.66, 1.72, 1.76, 1.83$ taken at $T = 30$ mK. The strongly coupled state at $d/\ell = 1.60$ weakens, and ultimately disappears altogether as d/ℓ is increased. Sample 'N'.

Figure 5.7 shows the Hall resistance R^*_{xy}, with the current being sent through just one of the layers and the Hall voltage measured in that same layer; and the Hall drag resistance $R_{xy,D}$, versus inverse total filling factor $\nu_T^{-1} = eB/hn_T$ (we held n_T constant and changed *B*), at five different effective layer separations $d/\ell = 1.60, 1.66, 1.72, 1.76, 1.83$. This shows the progression from the strongly coupled phase at low d/ℓ, with the Hall drag showing a broad quantized plateau and the conventional Hall resistance R_{xy}^* showing the same plateau, to the weakly coupled phase at high d/ℓ, in which the Hall drag is near zero and the conventional Hall resistance shows no feature at $\nu_T = 1$. There appears to be a smooth progression between the two extreme cases, with the midway point between the two apparently located at $d/\ell \approx 1.74$. This phase transition will be explored in more detail in the next chapter.

* * *

---

1 J.P. Eisenstein, L.N. Pfeiffer and K.W. West, Appl. Phys. Lett. **57**, 2324 (1990).

2 X.G. Wen and A. Zee, Phys. Rev. Lett. **69**, 1811 (1992).

3 K. Yang, *et al.*, Phys. Rev. Lett. **72**, 732 (1994).

4 G.S. Boebinger, H.W. Jiang, L.N. Pfeiffer and K.W. West, Phys. Rev. Lett. **64**, 1793 (1990).

5 J.P. Eisenstein, G.S. Boebinger, L.N. Pfeiffer, K.W. West and S. He, Phys. Rev. Lett. **68**, 1383 (1992).

6 S.Q. Murphy, J.P. Eisenstein, G.S. Boebinger, L.N. Pfeiffer and K.W. West, Phys. Rev. Lett. **72**, 728 (1994).

7 B.Y.K. Hu, Phys. Scr. T 69, 170 (1997).

8 F. von Oppen, S.H. Simon and A. Stern, Phys. Rev. Lett. 87, 106803 (2001).

9 L.J. van der Pauw, Philips Res. Rep. **13**, 1 (1958).

10 I.B. Spielman, J.P. Eisenstein, L.N. Pfeiffer and K.W. West, Phys. Rev. Lett. **84**, 5808 (2000).

11 These represent the state-of-the-art tunneling results, not published, done by Ian Spielman.

12 I.B. Spielman, J.P. Eisenstein, L.N. Pfeiffer and K.W. West, Phys. Rev. Lett. **87**, 036803 (2001).

13 S.R. Renn, Phys. Rev. Lett. **68**, 658 (1992).

14 K. Moon, *et al.*, Phys. Rev. B **51**, 5138 (1995).

15 J.M Duan, Europhys. Lett. **29**, 489 (1995).

16 K. Yang, Phys. Rev. B **58**, 4246 (1998).

17 K. Yang and A.H. MacDonald, Phys. Rev. B **63**, 073301 (2001).

18 Y.B. Kim, *et al.*, Phys. Rev. B **63**, 205315 (2001).

19 A.H. MacDonald, Physica B **298**, 129 (2001).

Chapter 6: Phase Boundary

So far, the system at $\nu_T = 1$ has been primarily studied in the case where the layers are sufficiently close together, and the interlayer Coulomb interactions sufficiently strong, such that the (111) state is evidenced. In this chapter, the transition out of the (111) state is explored as the layer separation (or the "effective layer separation" actually) is increased. Increasing the effective layer separation reduces the effects of the interlayer interactions until the electrons in the different layers are no longer highly correlated with each other. Under this condition, the layers behave fairly independently, and the layers are said to be "weakly coupled."

Whether the system behaves as two weakly coupled individual layers, each at $\nu = \frac{1}{2}$, or as a strongly coupled entity better described by the total filling factor $\nu_T = \frac{1}{2} + \frac{1}{2} = 1$, depends on the interlayer coupling strength. The coupling strength in turn depends on two parameters: the symmetric-antisymmetric tunneling gap energy Δ_{SAS} and the effective layer separation d / ℓ, these are discussed in Section 4.4. As our samples have very small tunneling gap energies ($\Delta_{SAS} \approx 90\mu\mathrm{K}$), the interlayer coupling strength will be largely determined by the interlayer Coulomb coupling. In a single sample, d is of course fixed, but we can modify the effective layer separation by changing the electron density, which at constant filling factor, changes ℓ.

This phase transition has been the subject of much speculation [1-8]. Unknown is the order of the phase transition or even the number of phases involved. In addition to the weakly coupled phase and the (111) phase, there may be one or more additional phases intermediate to the two, such as a paired quantum Hall state [3, 4] or bilayer charge density striped phase [7].

As Coulomb drag is a direct probe of interlayer Coulomb interactions – and interlayer Coulomb interactions are the primary mechanism for the interlayer coupling, Coulomb drag promises to be an important experimental probe of this phase transition.

6.1 COULOMB DRAG ACROSS THE PHASE BOUNDARY

These measurements were made on samples 'N' and 'R', discussed in Sec. 5.1. For these data, currents of 1 nA and 5 Hz were typically used. The Coulomb drag setup can be found in Appendix C.

Figure 6.1 shows both the longitudinal and the Hall drag resistance in the vicinity of $\nu_T = 1$ for some representative values of the effective layer separation d/ℓ at $T = 30$ mK. Plotted against $\nu_T^{-1} = eB/hn_T$ (the density n_T is held constant and the magnetic field B is changed), the top panels shows the drag at $d/\ell = 1.60$ when the system is in the strongly coupled interlayer coherent phase. On the left side is the Hall drag resistance. As shown in Sec. 5.2, when the system is in the strongly coupled phase, the drag layer exhibits a quantized Hall resistance relative to the current in the drive layer.

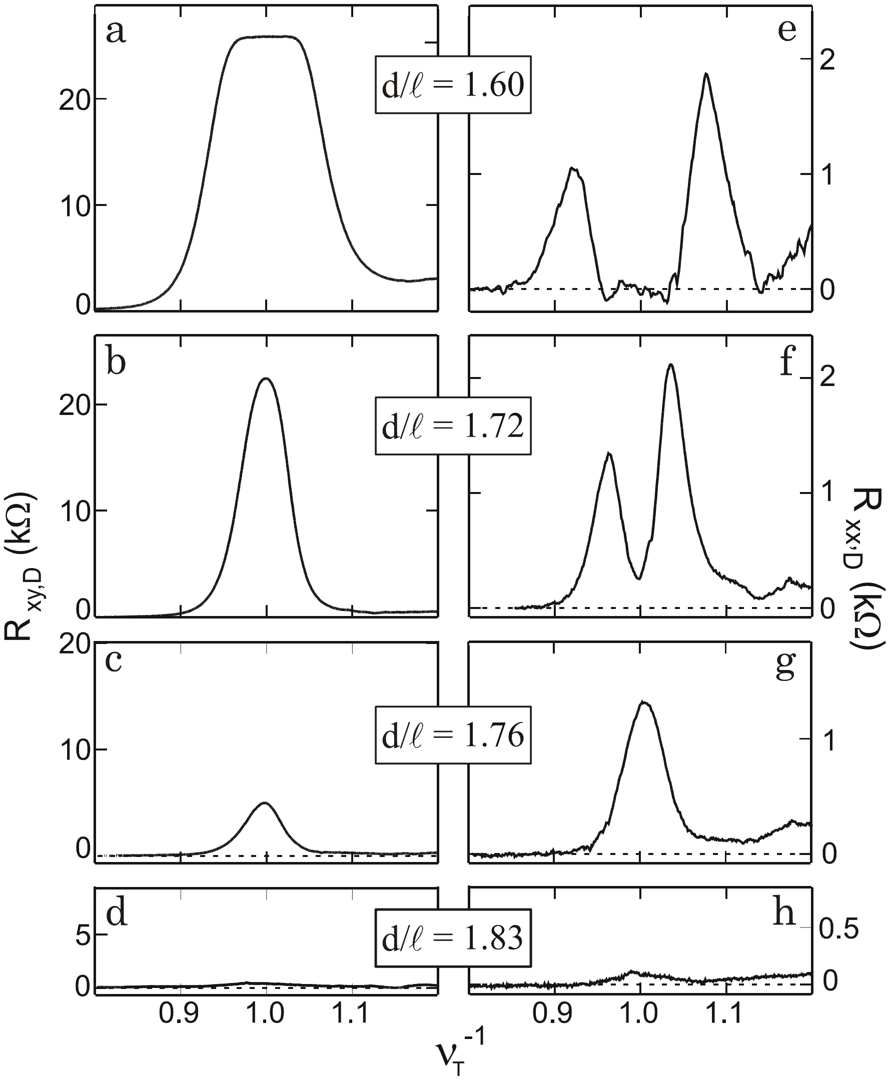

Figure 6.1: Coulomb drag versus ν_T^{-1} for four values of effective layer separation d/ℓ. Hall drag is on the left; longitudinal drag on the right. $T = 30$ mK. Sample 'N'.

On the right is the longitudinal drag, which goes to zero across the same $\Delta\nu_T^{-1}$ for which the Hall drag is quantized. On either side of the minimum in Fig. 6.1e there are large peaks almost 2 kΩ high. This is a tremendously large value for the longitudinal drag – it is roughly half as large as the single layer resistance of this sample.

In the subsequent panels of Fig. 6.1 the behavior of both the longitudinal and Hall drag resistance is shown as the interlayer coupling strength is decreased (d/ℓ is increased) while the temperature remains at $T = 30$ mK. The second row shows the drag at d/ℓ=1.72. In Fig. 6.1b, there is still a large feature in the Hall drag but it is no longer quantized. In Fig. 6.1f, the broad minimum characteristic of the interlayer coherent phase has narrowed; it no longer goes all the way to zero and the large flanking peaks have moved in toward $\nu_T = 1$. By d/ℓ=1.76 (Figs. 6.1c and 6.1g), the Hall drag reaches just about one-fifth of its quantized value and the flanking peaks in the longitudinal drag have merged to form a local maximum at $\nu_T = 1$. In the bottom panel, at d/ℓ=1.83 and the Hall drag has nearly disappeared, while the local maximum in the longitudinal drag has shrunk considerably. These data were taken on sample ‘N’.

In Figure 6.2 the same phase transition is plotted in a different manner. This time just the data points at $\nu_T = 1$ are plotted as a function of d/ℓ. This data was taken with sample ‘R’ at $T = 50$ mK. The open circles show the Hall drag: at low d/ℓ the system is in the interlayer coherent state and the Hall drag is quantized. At high d/ℓ, the system is in the weakly coupled phase and the Hall Drag is nearly zero. The transition between these two regimes is seen to be simple and monotonic.

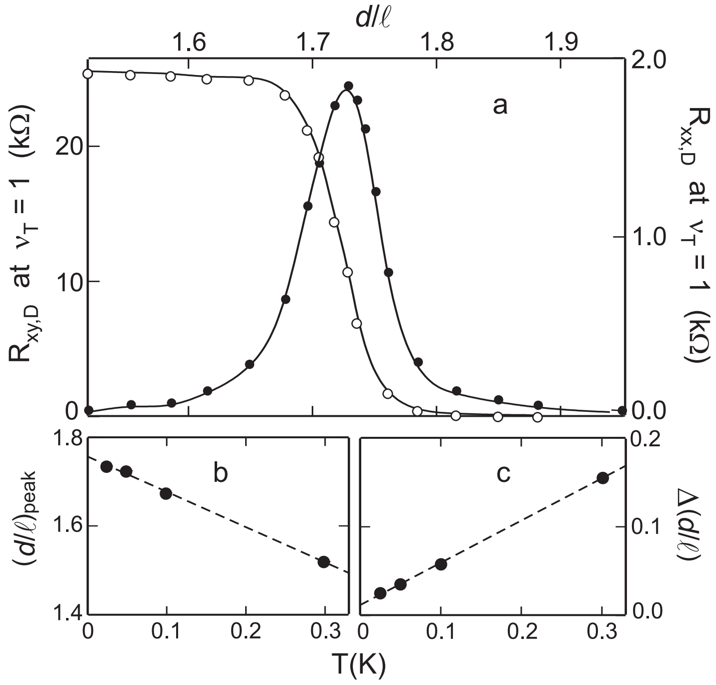

Figure 6.2: Coulomb drag at $\nu_T = 1$ versus d/ℓ. In a) open circles show Hall drag $R_{xy,D}$ and closed circles show longitudinal drag $R_{xx,D}$ at $T = 50$ mK. Panel b) shows the location, and panel c) the half-width, of the peak in longitudinal drag versus temperature. Lines are guides to the eye. Sample 'R'.

This cannot be said for the longitudinal drag, represented by the solid circles. In the interlayer coherent phase the longitudinal drag at $\nu_T = 1$ is near zero. In the weakly coupled phase, the longitudinal drag is also extremely small (see Sec. 6.3 for discussion on longitudinal drag in the weakly coupled regime); so one might expect that the longitudinal drag would remain small in the transition region between the two phases. Instead, the drag becomes progressively larger as the midway point of the phase transition is approached, reaching an impressive maximum height of 1.8 kΩ at d/ℓ = 1.73. This behavior was entirely unexpected.

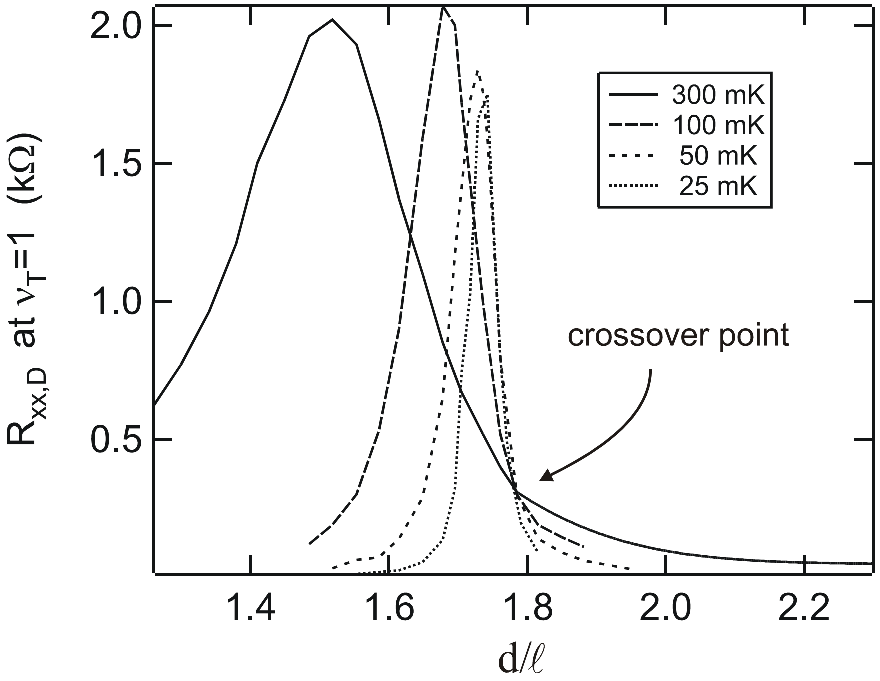

Figure 6.3: Longitudinal drag at $\nu_T = 1$ versus d/ℓ for 4 temperatures: 25 (dotted line), 50 (short-dash line), 100 (long-dash line) and 300 (solid line) mK. Sample 'R'.

The width and location of this peak in the longitudinal drag depend on the temperature. Figure 6.3 shows just the longitudinal drag, now at four temperatures: 25, 50, 100 and 300 mK. The peaks move to lower d/ℓ as the temperature is increased. Figure 6.2b shows the peak location $(d/\ell)_{peak}$ versus temperature. Simple extrapolation puts the zero temperature peak at $(d/\ell)_{peak,T=0} \approx 1.758$ indicating the location of the quantum critical point. The temperature-independence of the drag resistivity at $d/\ell \approx 1.785$ is another indicator the location of the quantum critical point [9].

The peak also becomes broader as the temperature is raised. Figure 6.2c shows the full width at half maximum $\Delta\left(d/\ell\right)$ versus temperature. Notice, though, that the height of the peak remains relatively constant over the temperature range spanned.

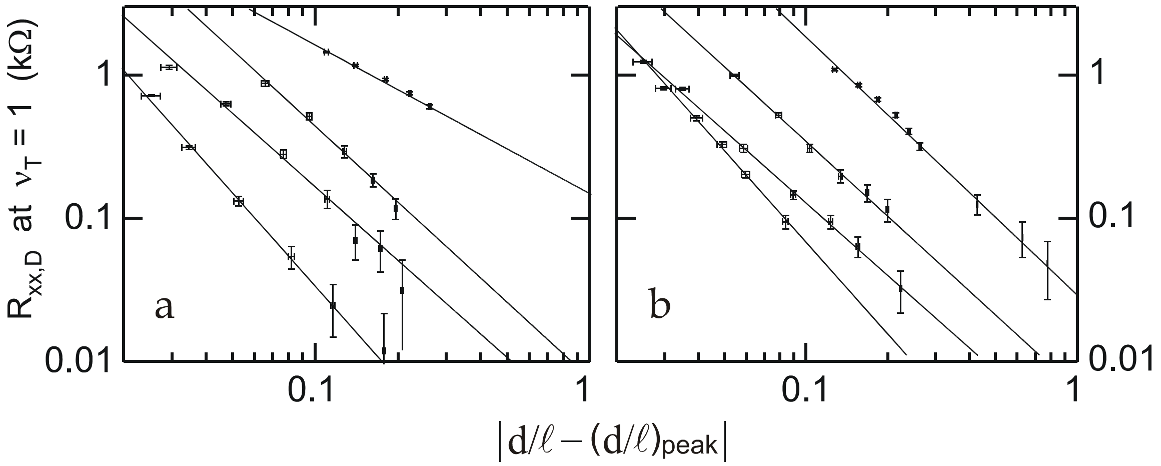

Figure 6.4: Longitudinal drag at $\nu_T = 1$ versus $\left|d/\ell - (d/\ell)_{peak}\right|$ for four different temperatures: 300, 100, 50 and 25 mK from top to bottom. For clarity, the data from the low d/ℓ side of the peak is shown in panel a, and the high side in panel b. Lines are fits to $R_{xx,D} \propto \left|d/\ell - (d/\ell)_{peak}\right|^{-y}$. Sample ‘R’.

At all four temperatures the longitudinal drag is notably symmetric about the peaks – beyond a $\Delta(d/\ell) \approx (0.02,\ 0.02,\ 0.06,\ 0.1)$ of the peak location for (25, 50, 100, 300) mK the longitudinal drag is well fit by a power law. Fig. 6.4a shows the low d/ℓ side of the data at the four different temperatures and Fig. 6.4b the high d/ℓ side, plotted in a log-log style. The lines through the data show the least squares best fit for each temperature. The slope of the line yields the value of the exponent y in the relation $R_{xx,D} \propto \left|d/\ell - (d/\ell)_{peak}\right|^{-y}$. For T = (25, 50, 100, 300) mK, y is observed to be (2.18, 1.72, 1.78, 1.85) for panel a, and (2.18, 1.72, 1.78, 1.05) for panel b. For the 300 mK data in panel (a) we must go to extremely low densities (as low as $n = 1.6\times10^{10}\ \mathrm{cm}^{-2}$) to obtain the low d/ℓ data because the 300 mK peak is located at an already low $(d/\ell)_{peak} = 1.52$. The anomalous value ($y = 1.05$) for the low d/ℓ side 300 mK data, may be related to working at these anomalously low densities.

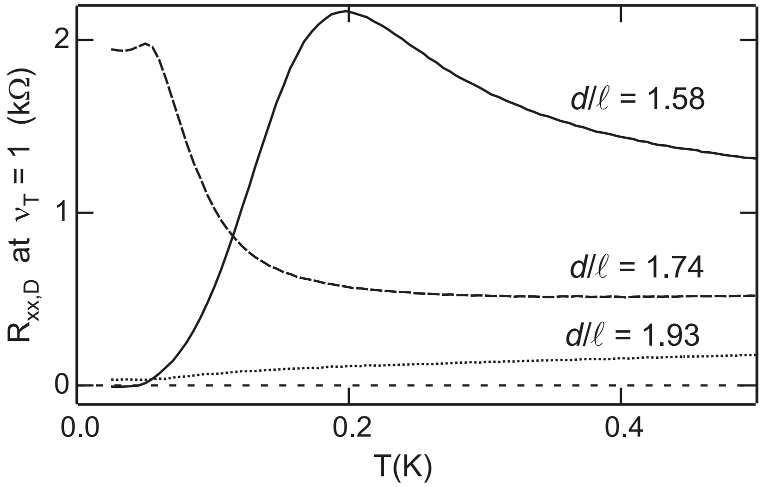

Figure 6.5: Temperature dependence of longitudinal drag measured at $\nu_T = 1$ for three different d/ℓ. Sample 'R'.

Figure 6.5 shows the temperature dependence of the longitudinal drag at three different d/ℓ values, representing the three main regimes of the phase transition. Below $T \approx 50$ mK, d/ℓ=1.58 is well into the bilayer quantum Hall phase – the longitudinal drag at $\nu_T = 1$ is near zero. When the temperature is increased we observe the thermal activation of the energy gap. The activation energy is observed to be $\Delta \approx 0.7$ K, defined such that

$R_{xx,D} \propto e^{-\Delta/2T}$. Notice that this agrees well with the activation energy observed in the drag resistance in sample 'R' shown in Fig. 5.6. At d/ℓ=1.93 the system is in the weakly coupled regime; the drag is very small and increases with temperature. This is the typical temperature dependence of longitudinal drag, which until recently had only been observed in the weakly coupled regime [10]. This is because increasing the temperature increases the phase space available for momentum transfer (via interlayer composite fermion scattering) and leads to a larger drag resistance [11, 12, 13], as is seen at $B = 0$.

At d/ℓ=1.74, again at low temperature, the longitudinal drag is midway through the transition region and exhibits a large local maximum. The striking temperature dependence of this data – it is nearly constant up to about 60 mK and then drops precipitously with temperature from 60 mK to 100 mK – is uncharacteristic behavior. This is the opposite dependence that is observed in either the interlayer coherent phase or the weakly coupled phase and is unique to the transition region between them. Such an inverted temperature dependence is, however, predicted to occur in the vicinity of a phase boundary as a result of fluctuations [2, 5, 14, 15]. The d/ℓ=1.58 curve also shows the same inverted dependence, though less dramatically, at temperatures above its phase boundary at $T \approx 0.2$ K.

Stern and Halperin [5] modeled the effects of density fluctuations in the transition region between the weakly coupled and the interlayer coherent phases and correctly accounted for the temperature dependence of the longitudinal drag in this region, as well as a number of other features of our data. They begin with the supposition that the behavior of the drag in the transition region is due to the inevitable density inhomogeneities found in any real bilayer electron system. In their model, puddles of the interlayer coherent phase form in the predominantly weakly coupled system as the phase boundary is approached from the high d/ℓ side. The mixture of the two states produces an increasingly large longitudinal drag dissipation as d/ℓ is lowered and a greater fraction f of the sample is occupied by the interlayer coherent puddles. Once $f \approx \frac{1}{2}$ the phase will percolate and the system will behave as interlayer coherent and the longitudinal drag will be zero (unless thermally activated). Shortly before this happens, at $f \approx 0.475$ for our sample [16], the longitudinal drag is predicted to reach its maximum value, a value calculated to be close to $\frac{1}{2}(h/e^2)$. This is consistent with our observation of a maximum longitudinal drag resistance of ~2kΩ measured across roughly $(4.5)^{-1}$ of a square [17].

This model can account for the inverted temperature dependence observed in Fig. 6.5 when the authors make the not-unreasonable assumption that f decreases with increasing temperature. So, by this rationale, when d/ℓ=1.74 and $T \leq 0.06$ K, the fraction of the sample occupied by the interlayer coherent puddles must be $f \approx 0.475$, as the drag is at its maximal value. Increasing the temperature further will then reduce f, and reduce the drag. For d/ℓ=1.58, $f \geq \frac{1}{2}$ when $T \leq 0.2$ K, and we see the thermally activated gap behavior. The maximum at $T \approx 0.2$ K locates $f \approx 0.475$ and temperature increases beyond that reduce f, and so reduce the drag. Their model also accounts for the large flanking peaks seen on either side of the $\nu_T = 1$ minimum in Fig. 6.1e and 6.1f, by making a similar assumption that f decreases as the filling factor deviates from

$\nu_T = 1$. Although their model can account for many of the features in our data, it does not account for all of them. For instance, it cannot explain the remarkable symmetry observed in the longitudinal drag at $\nu_T = 1$ as a function of d/ℓ.

Stern and Halperin are only two of the many theorists to have contemplated this phase transition. Schliemann *et al.* [1] start with the assumption that there are only two phases: the interlayer coherent phase and the weakly coupled phase. Through numerical modeling they find that the phase transition in d/ℓ will be first order. The broad transition regions observed in Fig. 6.3, however, make it seem unlikely that this is a first order phase transition.

Simon *et al.* [8] theorize that the transition region is composed of interpenetrating composite fermion and composite boson fluids. This model makes similar predictions to the Stern and Halperin model.

Bonesteel *et al.* [3] make no a priori assumptions on the number of phases, and find that under ideal conditions the system should transition from the incompressible interlayer coherent state directly into another incompressible state (a “paired quantum Hall state”) as d/ℓ is increased. At zero temperature, in an ideal system with no disorder, no tunneling, and no density imbalance, there exists an instability to pairings between the composite fermions in the different layers, no matter how far apart the layers are. In real systems, eventually, at some d/ℓ, less than ideal conditions will presumably predominate, and the system will transition to the weakly coupled state.

Zhou and Kim [2] studied the transition from the weakly coupled state to the paired quantum Hall state specifically in regard to its signature in Coulomb drag and predicted the inverted temperature dependence of the drag when near the phase boundary. Also predicting more than one phase transition are Kim *et al.* [4]. They anticipate a progression through three, possibly four, different phases as the system goes from the (111) state at low d/ℓ, to the (33-1) state at intermediate d/ℓ and finally to the weakly coupled compressible phase at high d/ℓ. A fourth state is postulated to exist between the (111) and (33-1) states, which would either be a strong pairing state or a descendent of the (33-1) state.

6.2 EFFECT OF DENSITY IMBALANCE ON PHASE BOUNDARY

In this section layer density imbalance, $\frac{\Delta n}{n_T} \equiv \frac{n_{drag} - n_{drive}}{n_{drag} + n_{drive}} \neq 0$, where $n_{drag(drive)}$ is the electron density in the drag (drive) layer, is studied for its effect on the location of the phase boundary. Thus, we are effectively mapping the location of the phase boundary in the $\Delta_{SAS} \to 0$; d/ℓ – $\Delta n/n_T$ plane. As Hall drag is the only probe of the interlayer coherent phase that achieves a universal value in the $\nu_T = 1$ state, and with the phase boundary defined as half of this universal value (in Fig. 6.2, $(d/\ell)_c$ determined by this method agrees with that determined by the location of the peak in the longitudinal drag to within 0.25%), it is the only probe that has a universal value at the phase boundary. This makes it an especially robust measurement of the location of the phase boundary, and this is why we use it here.

Figure 6.6 shows the Hall drag at $\nu_T = 1$ versus d/ℓ at $T = 50$ mK. The closed squares show the balanced case $\Delta n / n_T = 0$. This curve is very similar to the Hall drag shown in Fig. 6.2, even though these two data were taken in different samples (although from the same wafer) with different mesa geometries. The phase boundary, as defined above, falls at $d/\ell = 1.714$ (we use linear interpolation to find $R_{xy,D} = \frac{1}{2} h/e^2$).

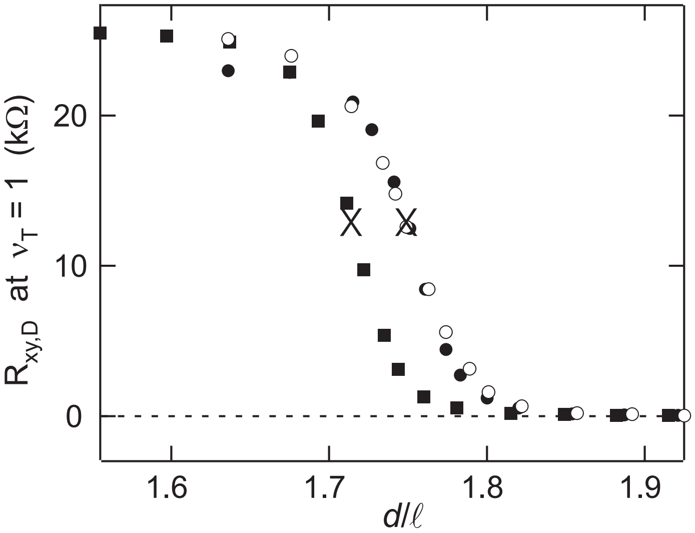

Figure 6.6: Hall drag at $\nu_T = 1$ versus d/ℓ at $T = 50$ mK. Phase boundary is defined as the d/ℓ where $R_{xy,D} = \frac{1}{2}(h/e^2)$ and is marked with 'X's. Closed squares represent $\Delta n / n_T = 0$, open and closed circles represent $\Delta n / n_T = +0.1$, -0.1 respectively. Sample 'Y'.

When the layers are imbalanced, shown as open (closed) circles for $\Delta n / n_T = +0.1(-0.1)$, there is a clear shift of the phase boundary to higher d/ℓ. The amount of shift appears to be independent of the sign of the density imbalance. From similar data at additional values of $\Delta n / n_T$ we can construct the phase boundary in the $d/\ell - \Delta n / n_T$ plane as shown in Fig. 6.7.

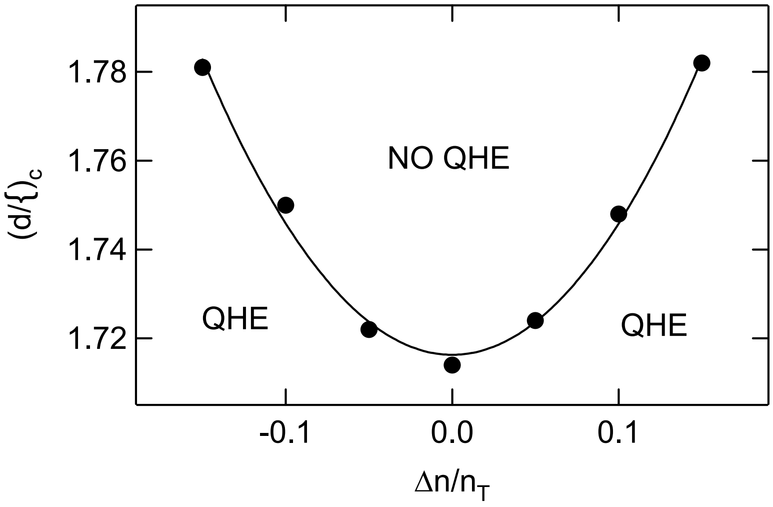

Figure 6.7: Location of phase boundary $(d/\ell)_c$, as determined by Hall drag, versus density imbalance $\Delta n / n_T$. Line is least squares parabolic fit. Sample 'Y'.

The phase boundary appears symmetric with $\Delta n / n_T$, and is well fit to a parabola, at least out to $\Delta n / n_T = \pm 0.15$. This parabolic phase boundary has also been seen in tunneling measurements done in a sample from the same wafer [18].

This dependence of the phase boundary on the density imbalance is somewhat surprising. A density imbalance tips the pseudospins out of the XY plane, which naively, would reduce the pseudospin stiffness which is related to the XY component of the pseudospins [19, 20]. Then to compensate for this, the phase boundary would be expected to move to smaller values of d/ℓ, as the pseudospin stiffness is inversely dependent on d/ℓ.

However, Joglekar and MacDonald predicted this counterintuitive result based on Hartree-Fock calculations specifically for the case of interlayer bias voltage [21]. They found that the magneto-roton minimum in the collective mode spectrum plays an important role in the transition out of the interlayer coherent phase as d/ℓ is increased. When the magneto-roton minimum goes to zero, a new gapless mode exists, and this destroys the superfluid phase. Imbalancing the layers raises this minimum, and the phase boundary instead increases. They also predicted that the increase to be quadratic in $\Delta n/n_T$, as observed.

6.3 LONGITUDINAL COULOMB DRAG AT LARGE d/ℓ

Longitudinal Coulomb drag at $\nu_T = 1$ was originally studied only at high d/ℓ due to practical constraints: low d/ℓ requires low d as well as low density $\ell \propto n^{-1/2}$. Although the barrier widths were already made small enough, the as-grown density in the first study of drag at $\nu_T = 1$ [10] was more than twice the density in our sample, and 8 times larger than our lowest gated density.

At large effective layer separation the system can be modeled as two weakly coupled composite fermion liquids [11, 12, 13], better described as two individual layers at $\nu = \frac{1}{2}$ rather than as a composite system at $\nu_T = 1$. The slow decay of density fluctuations in the individual layers explains the dramatic 10^3 to 10^4 -fold increase observed in the magnitude of the drag over its zero field value [11], but there is nothing special predicted to occur at filling factor $\nu_T = \frac{1}{2} + \frac{1}{2} = 1$ in this model, and indeed there was nothing special seen in the early observations of longitudinal drag at $d/\ell = 3.95$ [10].

With the low density samples available for this work, along with *in situ* density tuning with our metallic Schottky gates above and below the 2DES, we are able to probe a large range of effective layer separations both above and below the phase boundary, from $d/\ell \approx 1.3$ deep in the excitonic quantum Hall state, to $d/\ell \approx 2.7$ far into the weakly coupled composite fermion regime, in as fine of steps as we wish – an unprecedented exploration of the phase boundary.

One of the surprising discoveries in this exploration at the high d/ℓ end of the range was that a feature appears at $\nu_T = 1$ when the system is well into the weakly coupled state, approximately $\Delta(d/\ell) \approx 1.0$ away from the phase boundary. A local maximum in the longitudinal drag in the weakly coupled phase appears at values of d/ℓ as large as 2.59. Figure 6.8 shows the longitudinal drag resistivity versus magnetic field at the highest d/ℓ at which a local maximum can be observed at $\nu_T = 1$ for data taken at $T = 0.3$ K. Here we used sample 'K', which has a 10-square long mesa, in order to boost the signal-to-noise ratio, though we have confirmed these results with sample 'R'.

From Sec. 6.1, the phase boundary is located at $\left(d/\ell\right)_{peak} \approx 1.52$ at $T = 0.3$ K. Yet at d/ℓ=2.59, which is shown in the figure, a local maximum can be seen at $\nu_T = 1$. The region around $\nu_T = 1$ is magnified in the inset to better display the residual feature. Longitudinal drag observed above this d/ℓ value has just a simple shallow minimum in the region around $\nu_T = 1$ [10].

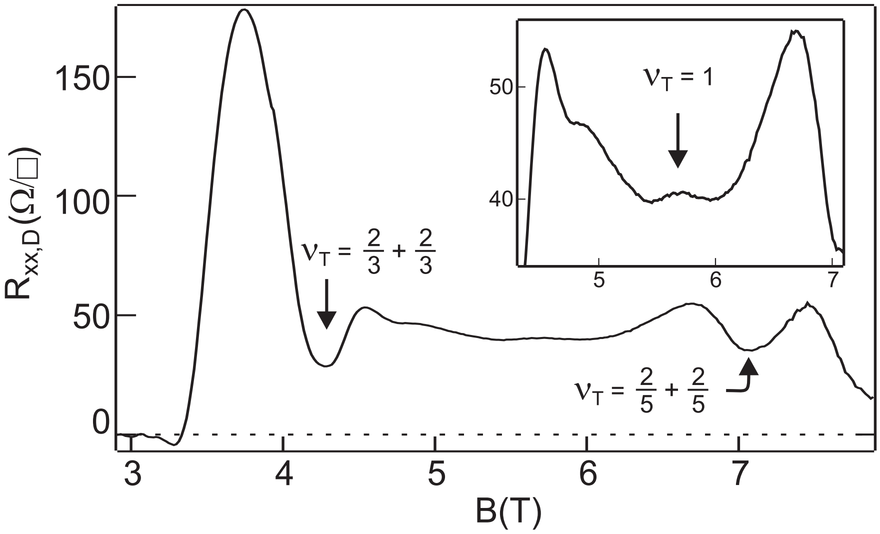

Figure 6.8: Longitudinal drag at relatively high effective layer separation $d/\ell = 2.56$ ($n = 6.9\times10^{10}$ cm^{-2}) at $T = 300$ mK. Inset shows that there is already a small bump at $\nu_T = 1$. Sample 'K'.

Whether this feature is related to residual fluctuations of the main phase transition, or if it is revealing the existence of one of the additional hypothetical phases is unknown. Because this bump occurs in a compressible phase, perhaps this is indicating that there is more than one compressible phase. Interestingly, neither the Hall drag, nor the tunneling conductance, show anomalies at $\nu_T = 1$ at this d/ℓ.

As the effective layer separation is reduced, this small local maximum, or bump, in the longitudinal drag at $\nu_T = 1$ becomes more and more prominent. Figure 6.9 shows this progression, starting with the same data shown in Fig. 6.8, which is the bottommost curve. The curves above it have lower and lower effective layer separations.

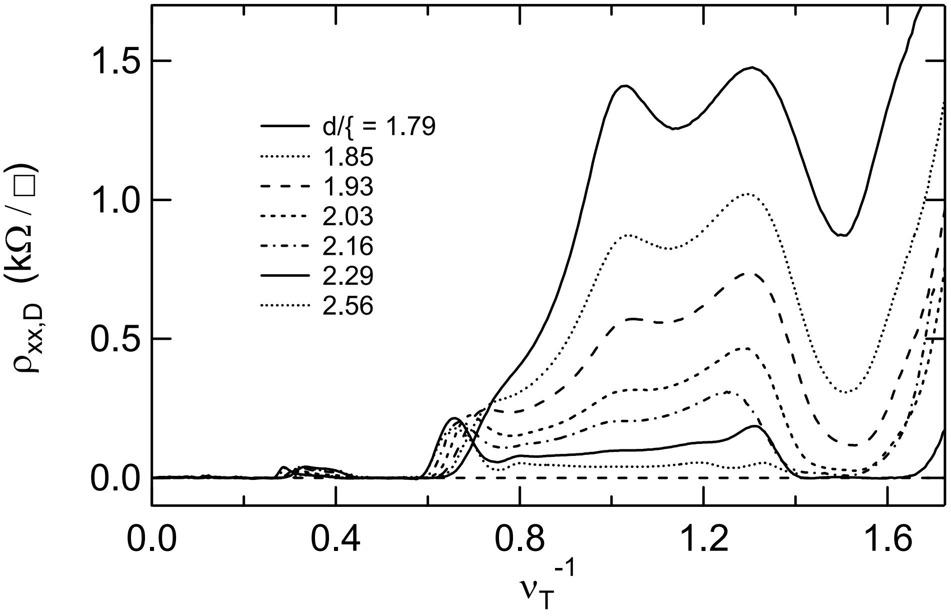

Figure 6.9: Longitudinal drag versus inverse total layer filling factor ν_T^{-1} at $T = 0.3$ K for seven effective layer separations: $d/\ell = 2.56,\ 2.29,\ 2.16,\ 2.03,\ 1.93,\ 1.85,\ 1.79$ going from bottom to top. Notice that the bump at $\nu_T = 1$ gets more pronounced as d/ℓ is decreased. Sample 'K'.

Reducing d/ℓ tends to increase the overall drag, mainly at high magnetic fields. In addition to this overall increase in the drag as d/ℓ is lowered, there is also an increase in the local enhancement of the drag at $\nu_T = 1$. This local enhancement continues to increase as the phase boundary is approached, as shown in the 300 mK curve in Fig. 6.3. In fact, even though this data is from a different sample with a different mesa geometry, it can be mapped very well to the 300 mK data points shown in Fig 6.3. This would make it seem that this small bump seen at high d/ℓ is just a remnant of the main phase transition that peaks at $d/\ell = 1.52$.

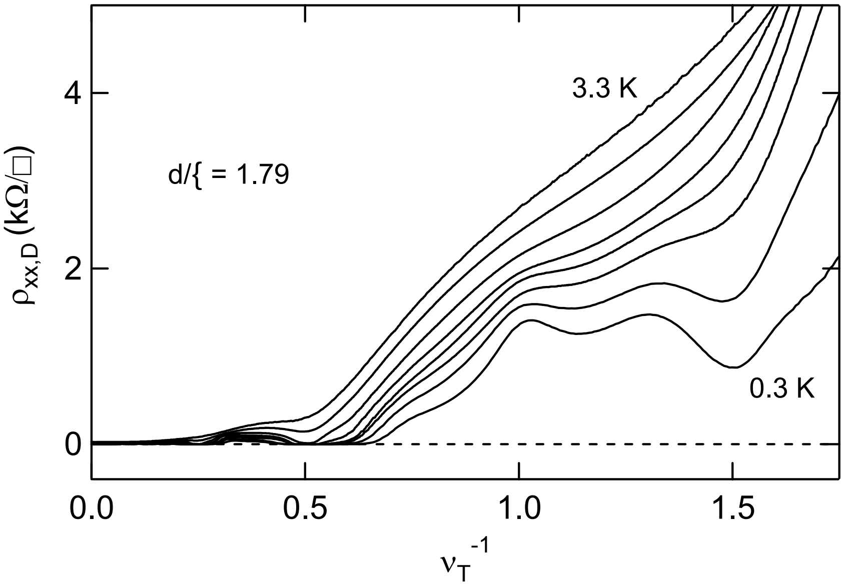

Figure 6.10: Longitudinal drag versus inverse total layer filling factor ν_T^{-1} for $d/\ell = 1.79$ at eight temperatures: $T = 0.3$, 0.4, 0.6, 0.7, 0.9, 1.3, 2.3, 3.3 K from bottom to top. The bump at $\nu_T = 1$ gets less pronounced as the temperature is raised. Sample 'K'.

Figure 6.10 shows the temperature dependence of one of these bumps on the high d/ℓ side of the phase boundary. Shown is the longitudinal drag resistivity versus the magnetic field, in units of the single layer inverse filling factor, for $d/\ell = 1.79$, which has the lowest d/ℓ and the largest bump of the series shown in Figure 6.9. At $T = 0.3$ K, the bump at $\nu_T = 1$ is marked. As the temperature is increased, the drag resistivity increases overall, due to an increase in the phase space available for scattering [11, 12, 13]. But notice that the size of the bump is *decreasing* with increasing temperature. By $T = 0.4$ K it is already notably smaller, and by $T = 1.3$ K it can no longer be distinguished from the background.

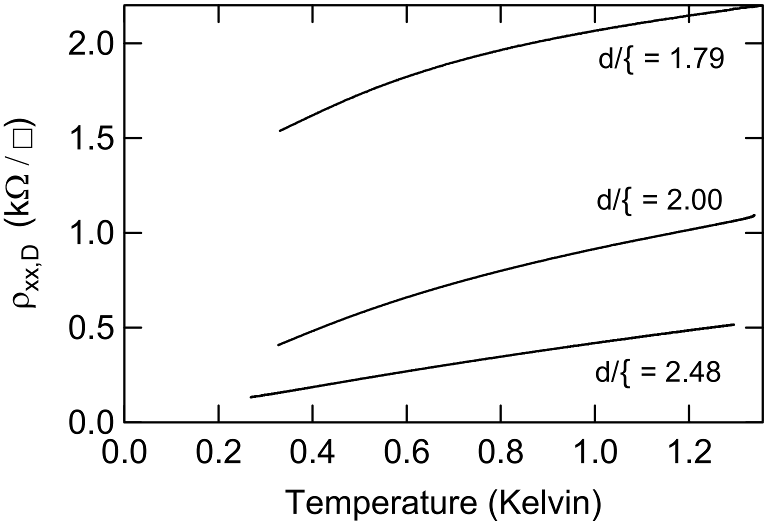

Figure 6.11: Longitudinal drag at $\nu_T = 1$ versus temperature for three effective layer separations: $d/\ell = 1.79,\ 2.00,\ 2.48$ from top to bottom. Sample 'K' $(d/\ell = 1.79,\ 2.00)$ and 'H' $(d/\ell = 2.48)$.

Figure 6.11 shows the drag resistivity at $\nu_T = 1$ versus temperature for 3 different values of effective layer separation. The $d/\ell = 1.79$ curve corresponds to the data in Fig. 6.8. Also shown are the curves for $d/\ell = 2.00$ and 2.48. Notice that all of them have a sublinear temperature dependence.

The $d/\ell = 2.48$ curve, which has a minimal bump contribution, and so may be thought to represent the more general 'background' drag temperature dependence, is extremely well fit (so well that there's no point in showing it in the graph, as it lies completely on the data, and can't be distinguished from it) to a power law curve that intersects the origin. The exponent of the fit, $\rho_{xx,D} = 0.415 \times T^{0.867}$ is contrary to theoretical predictions based on the composite fermion model, which predicts a $T^{4/3}$ dependence [11, 12, 13].

6.4 DENSITY IMBALANCE AT HIGH d/ℓ

This shifting of the phase boundary to higher d/ℓ with density imbalance is also observed in longitudinal drag at high d/ℓ. At high d/ℓ, a small bump is observed at $\nu_T = 1$ in the longitudinal drag (see Sec. 6.3). At such high d/ℓ we are probing the phase transition well into the 'NO QHE' side of the phase boundary. The small bump we observe is thought to be the tail of the quantum critical fluctuations of the interlayer coherent state. As d/ℓ is reduced this bump grows larger. In this section we show that as we imbalance the layer densities by applying a bias voltage between the layers while staying at constant d/ℓ, we also observe this bump becoming larger, indicating that the sample is being pushed closer to the phase boundary (or rather, the phase boundary is moving closer to the sample's effective layer separation).

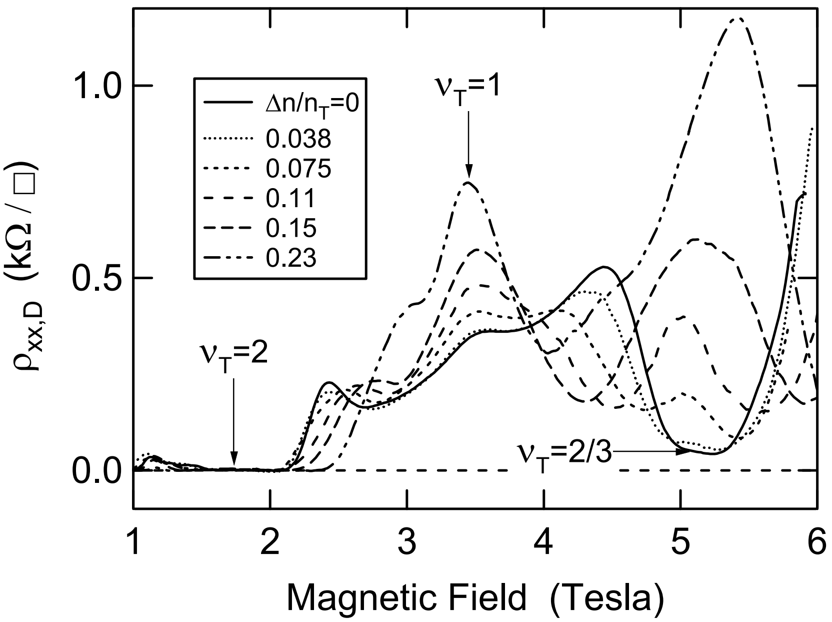

Figure 6.12: Longitudinal drag resistivity versus magnetic field for $d/\ell = 2.00$. Solid line shows balanced layer density case, and the remaining curves are for imbalanced layer densities. 'Bump' at $\nu_T = 1$ appears to grow larger with increasing density imbalance. Sample 'K'.

Figure 6.12 shows this for constant $d/\ell = 2.00$. The solid line shows the longitudinal drag resistivity when each layer has the same density $n = 4.06\times10^{10}\,\mathrm{cm}^{-2}$. There is a small bump visible at $\nu_T = 1$. As the layers become increasingly unbalanced (dotted, short-dashed, medium-dashed, long-dashed, and dot-dashed lines), this bump is observed to get larger and larger. For clarity, only the positive imbalance case is shown, but negative imbalance produces similar results.

Contrasting this behavior is the feature at $\nu_T = 2/3$ in the balanced drag. The deep minimum observed around 5¼ Tesla is due to the fractional quantum Hall state that exists at $\nu = 1/3$ in each layer. The many-body energy gap that forms at this filling fraction inhibits drag scattering and the drag resistivity is observed to go towards zero. As the layers are unbalanced, it is revealed that this is a single-layer effect. The $\nu = 1/3$ minima in each layer are translated, one to higher magnetic field, the other to lower, in concert with the density changes in each layer. This is observed as the splitting of the $\nu_T = 2/3$ minimum as the density imbalance is increased. However the feature at $\nu_T = 1$ does not split with layer density imbalance – this is truly a bilayer effect. It is not the $\nu = 1/2$ in each layer that is responsible for this feature, but rather the total filling factor in both layers adding up to unity.

This intensification of the $\nu_T = 1$ feature with density imbalance so far above the phase boundary in d/ℓ indicates that this feature is likely a remnant of the same phase transition discussed in Section 6.1. This bump at $\nu_T = 1$ is likely due to quantum critical fluctuations and does not represent a new phase.

* * *

---

1 J. Schliemann, S.M. Girvin and A.H. MacDonald, Phys. Rev. Lett. **86**, 1849 (2001).

2 F. Zhou and Y.B. Kim, Phys. Rev. B **59**, 7825 (1999).

3 N.E. Bonesteel, I.A. McDonald and C. Nayak, Phys. Rev. Lett. **77**, 3009 (1996).

4 Y.B. Kim, C. Nayak, E. Demler, N. Read and S. Das Sarma, Phys. Rev. B **63**, 205315 (2001).

5 A. Stern and B.I. Halperin, Phys. Rev. Lett. **88**, 106801 (2002).

6 S. He, S. Das Sarma and X.C. Xie, Phys. Rev. B **47**, 4394 (1993).

7 E. Papa, J. Schliemann, A.H. MacDonald and M.P.A. Fisher, Phys. Rev. B **61**, 115330 (2003).

8 S.H. Simon, E.H. Rezayi and M.V. Milovanovic, Phys. Rev. Lett. 91, 046803 (2003).

9 S.L. Sondhi, S.M. Girvin, J.P. Carini and D. Shahar, Rev. Mod. Phys. **69**, 315 (1997).

10 M.P. Lilly, J.P. Eisenstein, L.N. Pfeiffer and K.W. West, Phys. Rev. Lett. **80**, 1714 (1998).

11 I. Ussishkin and A. Stern, Phys. Rev. B **56**, 4013 (1997).

12 S. Sakhi, Phys. Rev. B **56**, 4098 (1997).

13 Y.B. Kim and A.J. Millis, Physica E **4**, 171 (1999).

14 B.N Narozhny, I.L. Aleiner and A. Stern, Phys. Rev. Lett. **86**, 3610 (2001).

15 I. Ussishkin and A. Stern, Phys. Rev. Lett. **81**, 3932 (1998).

16 At $d/\ell \approx 1.74$, $\varepsilon \equiv (k_F l_{tr})^{-1} \approx 0.1$ for our sample. k_F is the Fermi wavevector and l_{tr} is the transport mean free path.

17 Assuming we can apply van der Pauw formalism to Coulomb drag, the resistance along one side of the square sample measures $\sim \ln 2/\pi$ of a square.

18 I.B. Spielman, M. Kellogg, J.P. Eisenstein, L.N. Pfeiffer and K.W. West, cond-mat/0406067.

19 K. Yang, K. Moon, L. Zheng, A.H. MacDonald, S.M. Girvin, D. Yoshioka and S.C. Zhang, Phys. Rev. Lett. **72**, 732 (1994).

20 K. Moon, H. Mori, K. Yang, S.M. Girvin, A.H. MacDonald, L. Zheng, D. Yoshioka and S.C. Zhang, Phys. Rev. B **51**, 5138 (1995).

21 Y.N. Joglekar and A.H. MacDonald, Phys. Rev. B **65**, 235319 (2002).

Chapter 7: Counterflow Superfluidity

There are two different fundamental ways current can be sent through a bilayer system: equal currents can be sent through the two layers flowing in the same direction, or equal currents can be sent through the two layers but flowing in opposite directions. We call the first mode the parallel channel, and the second the counterflow channel. Any other current configuration is just a linear combination of these two channels.

The transport in each of these channels can be understood in terms of the two different models of the (111) state. For the parallel channel, the pseudospin ferromagnet model discussed in Section 4.6 offers an intuitive understanding of the transport mechanism responsible for current flow in this mode. In this model, the electrons are not localized in one layer or the other; they are in a superposition of the two layer eigenstates. This makes it impossible to localize the current to just one of the layers. A voltage applied across one layer will push on delocalized electrons and induce a current flow in both the layers, producing equal currents flowing in the two layers in the same direction: the parallel current mode.

Current flow in the counterflow channel can best be thought of using the excitonic condensate model discussed in Section 4.7. In this model, holes in one layer are bound to electrons in the other layer; these interlayer excitons are in the same quantum state and constitute a Bose-Einstein condensate. Current in the counterflow channel is then due to a superfluid flow of these excitons – as the excitons move in one direction, currents of opposite direction will be produced in the individual layers. According to this model, this counterflow current should be dissipationless and as excitons are charge-neutral, it should be unaffected by the magnetic field.

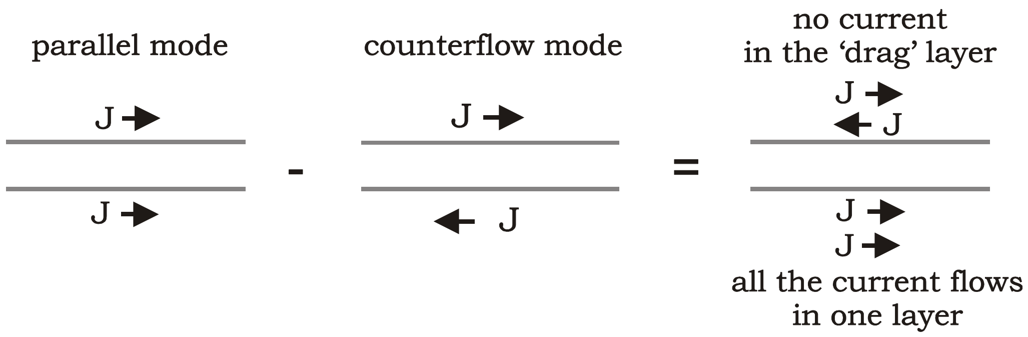

Figure 7.1: The Coulomb drag measurement is a linear combination of equal measures of the parallel and counterflow current channels.

The Coulomb drag measurement studied in the previous chapters is a straightforward linear combination of these two fundamental current configuration modes (see Fig. 7.1). An equal measure of each of these currents meets the boundary requirements for Coulomb drag: no net current in the drag layer and all the current flowing in the drive layer. Though Coulomb drag is an excellent probe of the phase boundary – the longitudinal drag signal is the only one sensitive enough to show the incipient phase transition as far away from the phase boundary as $d/\ell-(d/\ell)_c \approx 1.1$ (Sec. 6.3) – it is only an indirect measure of the anticipated superfluid mode that exists in the counterflow channel [1, 2, 3, 4].

In this chapter a purely counterflow current is set up in order to directly detect the superfluid mode, which should manifest as oppositely directed dissipationless currents having infinite conductivity.

7.1 SAMPLE: ‘Y’

The data shown in this chapter was obtained from sample piece ‘Y’, taken from the same wafer used for all the experiments shown in this thesis and discussed in detail in Chapter 1. Sample ‘Y’ is a 5 mm x 5 mm piece from the center of the wafer. Standard photolithographic techniques with AuNiGe contacts were employed [5]. The sample was thinned to 49 μm with a Bromine-methanol etch. The central region of the mesa is 160 μm x 320 μm with 7 arms extending out of it for electrical contact (see Fig. 7.2 for photo of sample).

The four arms configured as two ‘Y’-shaped projections coming out at the top and bottom of the mesa in Fig. 7.2 are used for injecting current symmetrically into the layers (detailed considerations that went into this sample design can be found in Appendix B). The remaining three arms extending out of the sides of the mesa are used for measuring the longitudinal and Hall voltages. These arms have both top and bottom gates so that we can measure the voltage in either the top or bottom layer (or both). The longitudinal voltage probes are spaced one square apart. The nominal density in each well is 5.4 x 10^{10} cm^{-2}, the mobility 1 x 10^{6} cm^2/Vs and the tunneling resistance at resonance $R \approx 100\ \text{M}\Omega$. The density in the central mesa region was controlled by electrostatic gates above and below the central bar. We could achieve densities as low as 1.7 x 10^{10} cm^{-2} per layer by applying voltages to these gates. The densities in the two layers were balanced by matching the plateaus in, and slopes of, the Hall resistivity in each layer while the sample was in the counterflow current configuration.

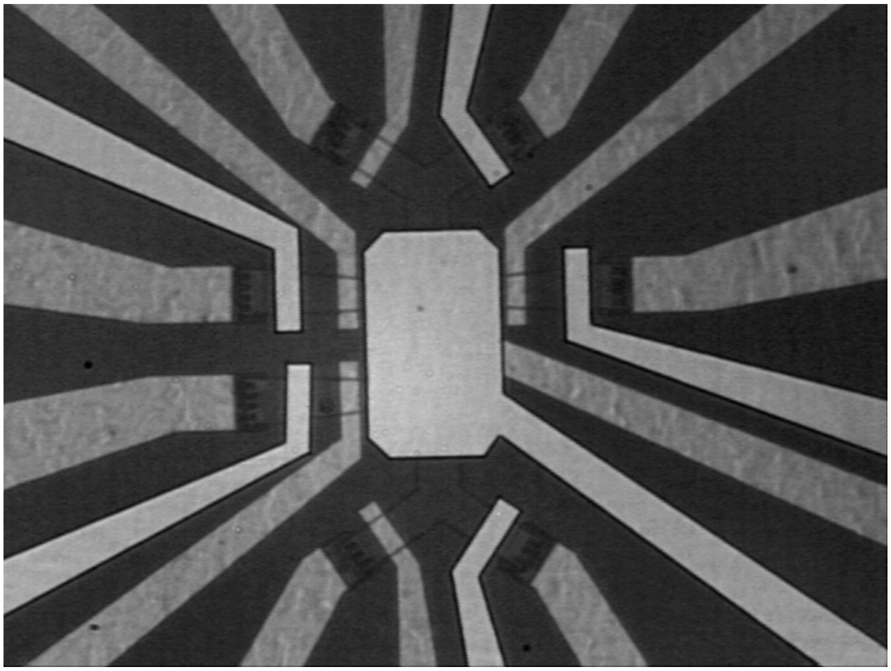

Figure 7.2: Infrared photo of sample 'Y'. Back gates appear lightest; top gates are medium gray. The mesa arms can be seen in outline, the main mesa region is obscured by the large central back gate. Field is ~1.5 mm across.

7.2 COUNTERFLOW AND PARALLEL DEFINITIONS

For the counterflow measurement a current is sent into one of the layers, extracted from that layer, and the sent into the second layer going in the opposite direction (see Fig. 7.3). The current can be measured before it is redirected into the second layer by sending it through a resistor (shown at the right side of the schematic in the figure), and measuring the voltage across that resistor. The Hall V_y or the longitudinal V_x voltage is then measured in one of the layers. V_y (V_x) divided by the injected current I_x, yields the Hall (longitudinal) counterflow resistance R_{xy}^{CF} (R_{xx}^{CF}). See Appendix D for a detailed counterflow setup.

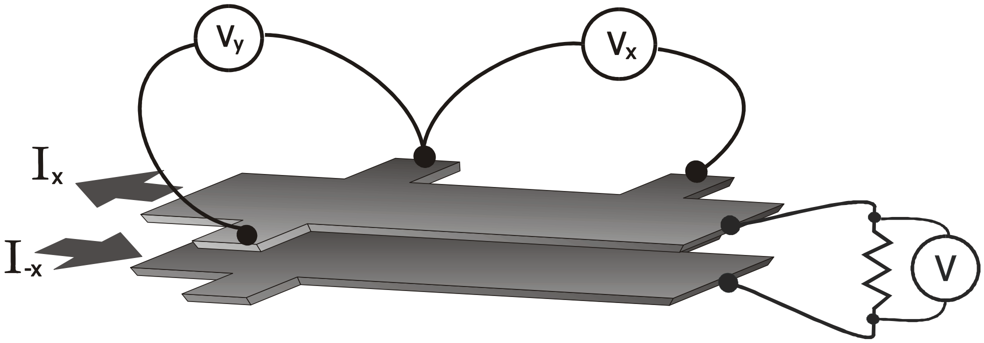

Figure 7.3: Schematic of counterflow measurement setup. Current is sent into the bottom layer, removed from the bottom layer, sent through an external resistor (sometimes) to measure it, and redirected into the top layer going in the opposite direction. This sets up equal but oppositely directed currents in the two layers. Voltages are then measured in just one of the layers.

For the parallel mode configuration, the current is redirected into the second layer going in the same direction as the current in the first layer (see Fig. 7.4). Now V_y (V_x) divided by the injected current I_x, yields the Hall (longitudinal) parallel resistance $R_{xy}^{\parallel}$ ($R_{xx}^{\parallel}$).

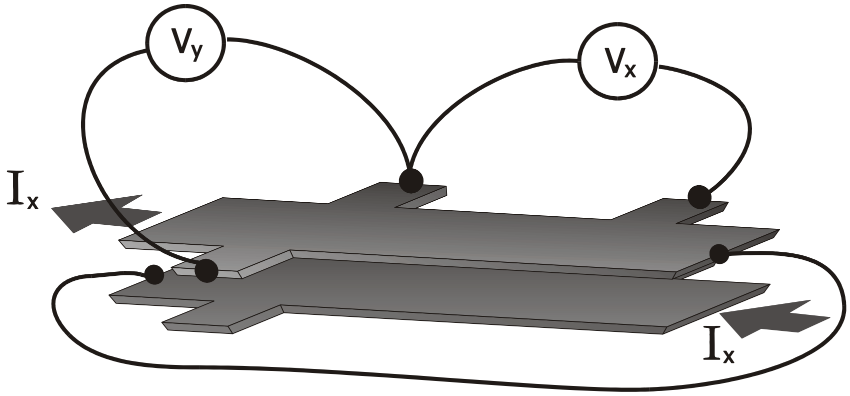

Figure 7.4: Schematic of parallel configuration. Current is sent into the bottom layer, removed from the bottom layer, and redirected into the top layer going in the same direction. Voltages are then measured in just one of the layers.

It is important to be able to monitor the current before it is redirected into the second layer, as the $\nu_T = 1$ state exhibits enhanced tunneling [6] between the layers and this will cause some current leakage between the layers when the system is in the (111) state. This leakage is detected by measuring the current before it enters the first layer and then again after it has left the first layer but before entering the second layer, the difference between the two indicates the tunneling current. We measure a ≈ 5 pA difference between the two currents when the system is at $\nu_T = 1$. In the parallel configuration this will create a ~1% mismatch in the magnitudes of the currents that are in each layer for our typical 0.5 nA drive currents. However, in the much more important counterflow configuration, this will not affect the relative magnitudes of the currents.

7.3 HALL AND LONGITUDINAL RESISTANCE VERSUS MAGNETIC FIELD

Figure 7.5 shows the primary result of this thesis. The main figure shows the Hall resistance for constant density $n = 2.46 \times 10^{10}\,\mathrm{cm}^{-2}$ per layer, as the magnetic field is ramped from zero to 2.4 Tesla, at $T = 30$ mK for both the parallel (dotted line) and counterflow (solid line) configurations. This density corresponds to $d/\ell = 1.55$, when calculated at $\nu_T = 1$, where $\ell = \sqrt{\hbar / eB}$ is the magnetic length. Up to about 1.8 Tesla the layers behave independently and we see the usual quantum Hall effect as though the second layer were non-existent. The direction of the current in the second layer is irrelevant and so $R_{xy}^{\|} = R_{xy}^{CF}$. But as the system enters the highly correlated bilayer quantum Hall state at $\nu_T = 1$, centered around 2 Tesla, the direction of the current in the second layer splits the data: $R_{xy}^{\|}$ goes up to form a quantized plateau at $2h/e^2$ while R_{xy}^{CF} drops to zero.

The vanishing Hall resistance in the counterflow configuration R_{xy}^{CF} is a remarkable observation. Current is confirmed to be flowing in the layer – it is measured prior to being redirected into, and after exiting, the layer in which the Hall voltage is measured – and yet it produces no Hall voltage. This is not an effect of the two layers being shorted together at the voltage contacts causing the opposing Hall voltages in each layer to cancel each other out. The voltage probes are only connected to one of the layers, if they were contacting both layers then the current would shunt through the voltage contacts, and this loss would be detected in the external resistor, which measures the current prior to redirection.

This vanishing Hall resistance is a startling indicator that the counterflow current is being carried not by individual electrons in each of the layers, but by charge-neutral interlayer excitons capable of flowing in the presence of a 2 Tesla magnetic field without being affected by it.

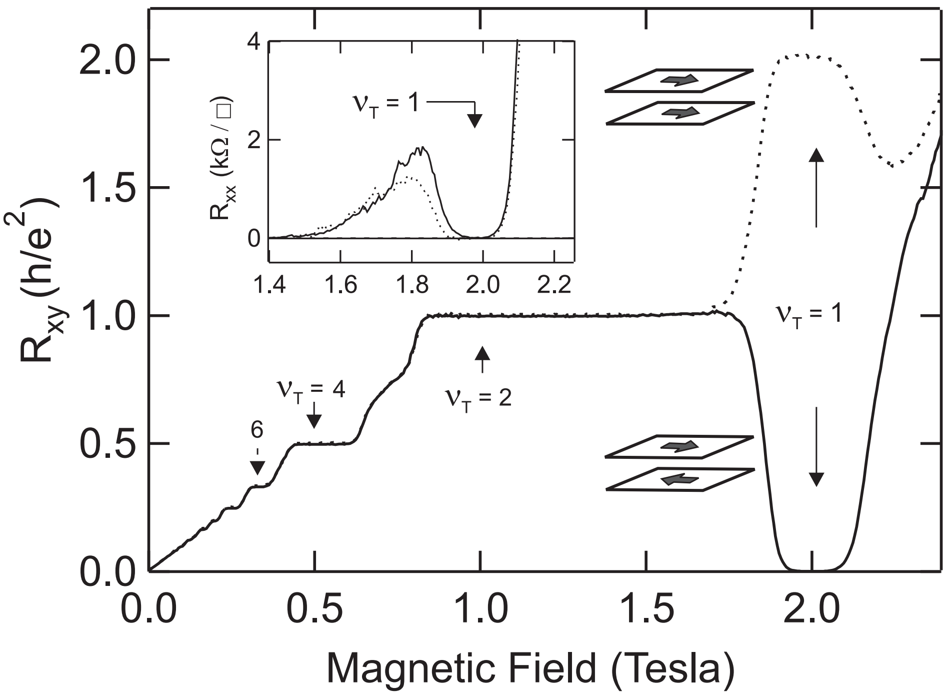

Figure 7.5: Main figure shows the Hall resistivity versus magnetic field in the parallel (dotted line) and counterflow (solid line) configuration for $n = 2.46\times10^{10}\,\mathrm{cm}^{-2}$ and $T = 30$ mK. The inset shows the longitudinal voltages. Voltages are measured in one layer only.

Notice that the plateau in the parallel configuration is at twice the expected value for total filling factor one. This is because we define the resistance as the voltage divided by the current in a single layer, not the net current flowing through the bilayer.

The second test for excitonic superfluitiy in the counterflow channel is to see if the exciton current observed in the counterflow Hall resistance is flowing without dissipation. The dissipation is measured by measuring the longitudinal resistance.

The inset of Fig. 7.5 shows the longitudinal resistances $R_{xx}^{\|}$ and R_{xx}^{CF} under the same conditions, focusing on the region near $\nu_T = 1$. Although not shown, the two are again identical at low fields. And unlike the Hall resistance, they are also nearly identical in the interlayer coherent state at $\nu_T = 1$. R_{xx}^{CF} (solid line) is a little larger than $R_{xx}^{\|}$ (dotted line) around 1.8 Tesla, which is where the sample is transitioning into the $\nu_T = 1$ state. This is because of the strong interlayer Coulomb drag that occurs in the transition region [7]. When the sample is in the counterflow configuration, the two oppositely directed currents will exert a strong dragging force on one another that does not exist in the parallel configuration, and so R_{xx}^{CF} will be increased over the parallel value $R_{xx}^{\|}$. As both $R_{xx}^{\|}$ and R_{xx}^{CF} go to zero at $\nu_T = 1$, this indicates that the $\nu_T = 1$ state is dissipationless in both the parallel and counterflow configurations. Thus the exciton current is flowing with vanishing dissipation.

7.4 TEMPERATURE DEPENDENCE AT $\nu_T = 1$

Focusing on the resistances at $\nu_T = 1$ only, Figure 7.6 shows the temperature dependence of the Hall and longitudinal resistances in both the parallel and counterflow configurations when the system is in the interlayer coherent state. Panel a shows $R_{xx}^{\|}$ (open circles) and $R_{xy}^{\|}$ (closed squares) for $d/\ell = 1.48$ for temperatures ranging from 35 mK to 400 mK. The Hall resistance never strays far from its quantized value $2h/e^2$, while the longitudinal resistance drops almost three orders of magnitude over this temperature range, exhibiting straight line activated behavior $R_{xx}^{\|} = R_0 e^{-\Delta/2T}$ with energy gap $\Delta \approx 0.5$ K.

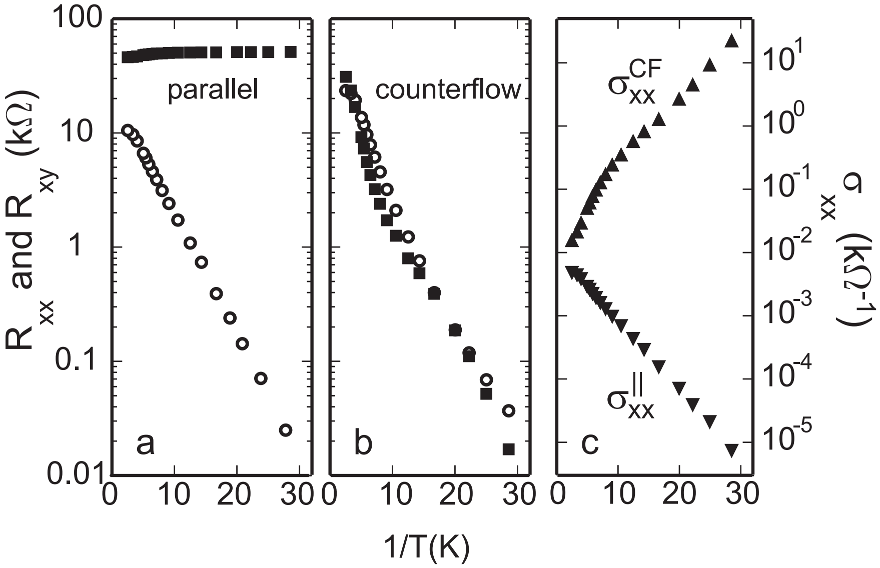

Figure 7.6: Temperature dependence of the resistances (panels a and b) and conductivity (panel c) at $\nu_T = 1$ for both parallel and counterflow configurations at $d/\ell = 1.48$. In a) open circles represent $R_{xx}^{\|}$, closed squares $R_{xy}^{\|}$; in b) open circles represent R_{xx}^{CF}, closed squares R_{xy}^{CF}. c) shows the counterflow and parallel longitudinal conductivities, σ_{xx}^{CF} and $\sigma_{xx}^{\|}$, respectively.

Panel b shows the same for the counterflow resistances, R_{xx}^{CF} (open circles) and R_{xy}^{CF} (closed squares). R_{xx}^{CF} is very similar to $R_{xx}^{\|}$; showing the same activated behavior with the same energy gap of 0.5 K. But here R_{xy}^{CF} also drops precipitously as the temperature is lowered, and at a very similar rate to both the R_{xx} data, though it does not form a straight line as the others do.

More illuminating is the same data plotted as longitudinal conductivity:

$$\sigma_{xx} = \frac{\rho_{xx}}{(\rho_{xx}^2 + \rho_{xy}^2)}, \tag{7.1}$$

where we take $\rho \approx R$, as our longitudinal voltage probes are spaced one square apart. This is shown in panel c. Here the transport properties of the two different current configurations clearly and radically diverge as the temperature is lowered. The upward pointing triangles in the top half of panel c indicate the longitudinal conductivity in the counterflow configuration σ_{xx}^{CF}; and the downward triangles in the bottom half represent $\sigma_{xx}^{\|}$. $\sigma_{xx}^{\|}$ goes to zero as the temperature goes to zero, again, in an activated fashion. This is precisely the behavior expected for any ordinary quantum Hall state. On the other hand, σ_{xx}^{CF} becomes dramatically larger as the temperature is lowered. By 35 mK there is more than six orders of magnitude difference in the conductivities of the two current configurations. The behavior of σ_{xx}^{CF} has never been seen before in quantum Hall systems. Current is just slipping through this system with barely any forces on it. It is quite remarkable.

7.5 DEPENDENCE ON EFFECTIVE LAYER SEPARATION

The dependence on the effective layer separation d/ℓ is shown in Fig. 7.7; using just R_{xy}^{CF} as the indicator of the onset of the bilayer quantum Hall state. The quantum phase transition as the effective layer separation is reduced has been observed to occur around $d/\ell = 1.73$ in the Coulomb drag [7] measured in a sample from the same wafer.

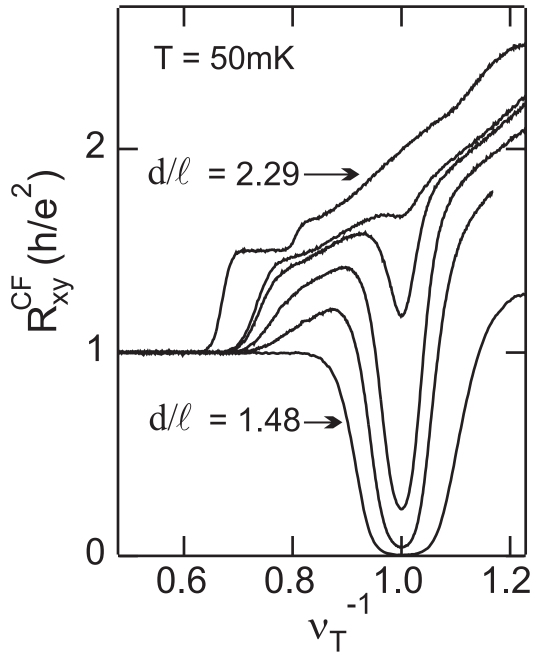

Figure 7.7: Sample enters excitonic superfluid state as evidenced by R_{xy}^{CF} dropping to zero as the effective layer separation d/ℓ is reduced. Figure shows R_{xy}^{CF} versus inverse filling factor ν_T^{-1} for $d/\ell = 2.29, 1.75, 1.71, 1.66, 1.59, 1.48$, all at $T = 50$ mK.

Figure 7.7 shows R_{xy}^{CF} versus the inverse of the total filling factor $\nu_T^{-1} = eB/hn_T$ (for easier comparison of data with different d/ℓ) taken at $T = 50$ mK. The topmost curve, with $d/\ell = 2.29$, shows the sample to be well out of the interlayer coherent state. The behavior seen is typical of the Hall resistance in a single layer 2DES, with no distortion or feature at $\nu_T = 1$, indicating a lack of correlation with the second layer. As d/ℓ is reduced, a dip begins to form at $\nu_T = 1$, becoming deeper and more fully developed as the layers are brought (effectively) closer together. By $d/\ell = 1.48$ there is a broad minimum that goes nearly to zero, signaling that the sample is now well within the bilayer quantum Hall state. By interpolation, the minimum reaches half its uncorrelated value at $d/\ell = 1.70$, which may be thought of roughly as the location of the transition point, fairly consistent with the Coulomb drag observations in Section 6.1.

7.6 DISCUSSION

These data support the model of this state as a Bose-Einstein condensate of interlayer excitons discussed in Section 4.7. In this view one of the half-filled Landau levels in the individual layers can be viewed as a full Landau level that is half-filled with holes [8]. Then the bilayer system can be regarded as one layer of electrons and one layer of holes. Because they are oppositely charged, the electrons and holes bind together to form composite particles called excitons. As the electrons and holes directly across from one another in the layers have opposite k quantum numbers (see Section 4.1), when they combine together as excitons, all the excitons will be in the $k = 0$ state, and so this will constitute a Bose-Einstein condensation of excitons. Figure 7.8 shows a schematic of these interlayer excitons.

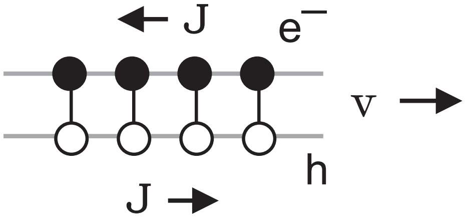

Figure 7.8: Schematic showing how interlayer excitons can create counterflowing currents in the two layers. Electrons e^- in one layer bind to conduction band holes h in the other layer, and the resulting excitons condense into a superfluid. Dissipationless flow in one direction produces equal but oppositely directed dissipationless currents **J** in the layers.

If this excitonic condensate were to flow in one direction, equal but oppositely directed currents would be set up in the two layers. This is precisely the current configuration that is set up in the counterflow measurement. As excitons are charge neutral, they can flow in the presence of a magnetic field without producing a Hall voltage. Our vanishing Hall resistance R_{xy}^{CF} in the counterflow configuration at $\nu_T = 1$ shown in Fig. 7.5 supports this model of current flow via charge-neutral excitons.

The vanishing longitudinal resistance R_{xx}^{CF} in the counterflow configuration at $\nu_T = 1$, shown in the same figure, indicates that these excitons are flowing with very little dissipation. Figure 7.6 suggests that the dissipation goes to zero as the temperature goes to zero, and that in the zero temperature limit, this excitonic condensate is a superfluid, as predicted by Wen and Zee [1] and others [2, 3, 4].

However, as Fig. 7.6 also shows, both the dissipation R_{xx}^{CF} and Hall resistivity R_{xy}^{CF} in the counterflow configuration remain finite at finite temperatures. In the ideal case, both of these quantities should drop to zero for $T < T_{KT}$ where T_{KT} is the Kosterlitz-Thouless temperature [9]. Instead we are seeing activated behavior. One reason for seeing this activated behavior is because the critical current for this superfluid is zero [3, 10], so the act of making a resistance measurement at all is expected to impart an energy gap to the system. However, this energy gap should be dependent on the magnitude of the current. Our observed energy gap of $\Delta \approx 0.5$ K persists even when we use different drive currents (from 20 pA to 1 nA – currents above 1 nA caused sample heating).

The presence of interlayer tunneling in the sample, even though extremely small, also disturbs the state. The binding of neutral vortex-antivortex excitations is a crucial element of the Kosterlitz-Thouless phase transition discussed in Section 4.6, but tunneling alters this binding mechanism.

Tunneling destroys the symmetry of the (111) state. With a finite tunneling gap energy, the order parameter φ is no longer degenerate for all angles $0 \le \varphi < 2\pi$; instead the energy will have a minimum at $\varphi = 0$. In the pseudospin representation this corresponds to pseudospins pointing in the x-direction. Since the pseudospins will prefer to lie in the x-direction the meron-antimeron pairs will bind along the y-direction, held together by the so-called “domain strings” as shown in Fig. 7.9. These domain lines have a fixed energy per unit length, and thus bind the merons as fixed tension strings of arbitrary length. At some length this tension will exceed the electrostatic repulsion of like-charged merons and they will be able to bind together. An energy gap will be created for these new charged excitations [11]. However, domain string binding is only expected to occur for tunneling gap energies $\Delta_{SAS}/(e^2/\varepsilon\ell) > 5\times10^{-4}$ [11], our tunneling gap energy is roughly $\Delta_{SAS}/(e^2/\varepsilon\ell) \approx 10^{-6}$.

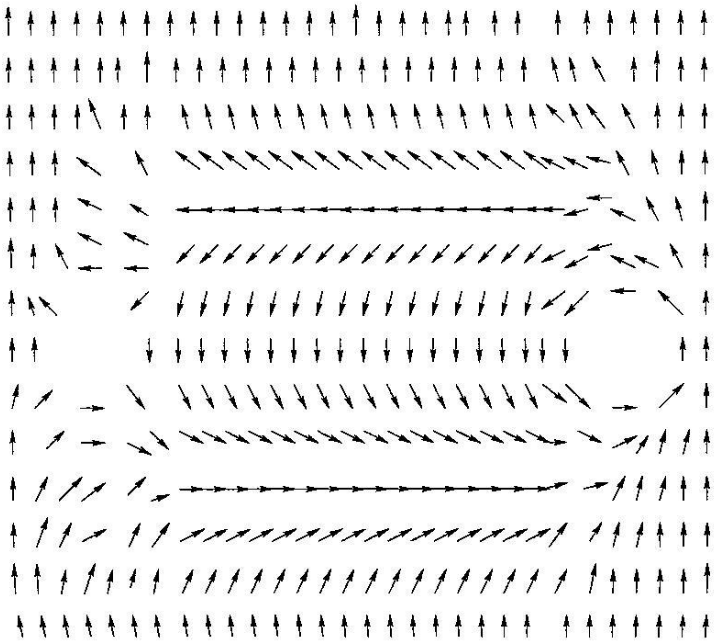

Figure 7.9: Bound pair of opposite vorticity merons that have the same charge. The like-charges are held together by the domain string between them shown in this pseudospin representation of a bilayer system with significant interlayer tunneling. In the presence of tunneling the pseudospins will want to lie in the x-direction (towards the top in this depiction). Taken from Ref. 11.

It is most likely that this energy gap is due to disorder in the system. The sample is going insulating at magnetic fields just above $\nu_T = 1$ (see inset of Fig. 7.5). Thus we are working in a regime where disorder effects are strong. Disorder creates, and pins, single merons even in the absence of current. The energy gap observed may be due to an array of disorder sites, and the hopping energy as merons jump from site to site [10].

Additionally, Fertig and Straley [12] show that the combination of finite tunneling and a strong enough disorder potential can create strings of overturned spins with free vortices at either end, with possible low energy excitations of the vortices and new 'string glass' states.

Although the mechanism responsible for the observed energy gap is not certain, the data remains consistent with the proposed excitonic condensate ground state. These results were confirmed by another group after our data was disseminated. Tutuc *et al.* measured vanishing Hall and longitudinal resistances in counterflow current configuration in a hole-hole bilayer system [13].

We believe that our data supports the achievement of the Bose-Einstein condensation of excitons, as evidenced by superfluid-like counterflowing currents in a bilayer two-dimensional electron system at $\nu_T = 1$.

* * *

---

1 X.G. Wen and A. Zee, Phys. Rev. Lett. **69**, 1811 (1992).

2 Z.F. Ezawa and A. Iwazaki, Phys. Rev. B **47**, 7295 (1993).

3 K. Moon, *et al.*, Phys. Rev. B **51**, 5138 (1995).

4 A.H. MacDonald, Physica B **298**, 129 (2001).

5 See Appendix A for detailed processing steps.

6 I.B. Spielman, J.P. Eisenstein, L.N. Pfeiffer and K.W. West, Phys. Rev. Lett. **84**, 5808 (2000) and Phys. Rev. Lett. **87**, 036803 (2001).

7 See Section 6.1.

8 A.H. MacDonald, Physica B **298**, 129 (2001).

9 J.M. Kosterlitz and D.J. Thouless, J. Phys. C **6**, 1181 (1973).

10 M. Abolfath, A.H. MacDonald and L. Radzihovsky, Phys. Rev. B **68**, 155318 (2003).

11 S. Das Sarma and A. Pinczuk, *Perspectives in Quantum Hall Effects* (John Wiley & Sons, Inc., New York 1997). See chapter by S.M. Girvin and A.H. MacDonald.

12 H.A. Fertig and J.P. Straley, Phys. Rev. Lett. **91**, 046806 (2003).

13 E. Tutuc, M. Shayegan and D.A. Huse, cond-mat/0402186.

Appendix A

DETAILED SAMPLE PROCESSING STEPS

Sample processing is something of a matter of faith – when you find a series of steps that works, you don't question why. The following steps gave me a 100% success rate (all the contacts had a low contact resistance to both layers, and the metal structures and mesa geometry had clean smooth edges):

1. Cleave off a 5 mm x 5 mm piece of the sample from the parent wafer.
2. Clean sample, on the spinner, first with acetone, then with methanol. Blow dry with dry N_2 while spinning.
3. Spin on Shipley S1813 photoresist for 30 seconds at 5krpm.
4. Bake for 25 minutes at 90°C.
5. Align mesa pattern in mask aligner (we use a Karl Suss mask aligner, model MJB3 with a 200W Hg lamp), being sure that the mesa pattern avoids any defects in the crystal. Expose for 5 seconds (at ~14 mW/cm^2).
6. Develop in a 50:50 mixture of Shipley 351 developer and deionized water (I used 20mL of each) for about 1 minute. Then rinse in a stream of deionized water for about 2 minutes.
7. Carefully take the edge of a folded up lint-free clean room towelette in which the edge has been soaked in acetone, and remove any photoresist that has remained at the edges of the sample. Then quickly dunk the sample in the developer solution again and rinse again under the deionized water stream. Blow dry well with dry N_2.
8. Bake the sample for 30 minutes at 90°C.

9. About 6 minutes before the baking is done, mix together the etch solution:
    - o 100 mL deionized water (≳ 11 MΩ-cm)
    - o 10 mL phosphoric acid
    - o 2 mL 30% hydrogen peroxide
10. Stir (with magnetic stirrer) for approximately 4 minutes (put watch glass on top of beaker to prevent evaporation).
11. Fill a small Kimex dish with the acid etch solution, and then put the sample into the dish and leave it there for 8 minutes. (The acid etches at a rate of ~ 1000 Å/min.)
12. Have two Kimex dishes nearby, filled with deionized water. To stop the etch, remove the sample from the acid solution and plunge it into one of the dishes of deionized water, and then into the other. Then let it sit in a dish of acetone to remove the remaining photoresist.
13. Clean well on the spinner, first with acetone, then methanol, and then with deionized water. Then dry with N_2 while still spinning.
14. Spin on AZ5214 photoresist for 30 seconds at 5krpm.
15. Bake on top of a hotplate set to 100°C for 45 seconds.
16. Align the mask with the contact pattern in the mask aligner, expose for 15 seconds.
17. Develop in a 4:1 solution of deionized water and AZ400K developer (I used 24mL of water and 6mL of developer). It takes approximately 20-30 seconds to develop.
18. Clean on spinner with a stream of deionized water for 2 minutes. Then blow dry with N_2 for another 2 minutes while still spinning.
19. Put the sample in the evaporator along with two boats. In a tungsten boat (R. D. Mathis # S3-.015W) put 3 slugs of Nickel (99.995% pure), and in a tungsten boat that has an aluminum oxide barrier (R. D. Mathis # S35-A0-W), which we mounted on copper stilts (~ 3 inches tall) to bring the boat closer to the sample so we would not waste as much Gold, put in two nuggets of a eutectic mixture (88:12) of Gold and Germanium (99.85% pure).
20. First evaporate 300 Å of Nickel (at a rate of ~ 8 Å /sec), and then evaporate 1350 Å of Gold-Germanium (at ~ 20 Å /sec).

21. Set sample in acetone for 5 to 10 minutes until metal lifts off; squirting the sample with an acetone stream will hasten this process.
22. Clean and dry sample on spinner, first with acetone, then methanol and finally dry N_2 gas.
23. Anneal contacts on a heater strip in a sealed box that has had forming gas (15% H_2, 85% N_2) flowing through it for at least 5 minutes (to displace all the air). Anneal at 440°C for 10 minutes.
24. Clean and dry sample on spinner again (as in step 13).
25. Spin on AZ5214 for 30 seconds at 5krpm.
26. Bake on top of a hotplate set to 100°C for 45 seconds.
27. Align mask with pattern of top gates and contact leads in mask aligner, expose for 15 seconds.
28. Develop in a 4:1 solution of deionized water and AZ400K developer (I use 24mL of water and 6mL of developer). It takes approximately 20-30 seconds to develop.
29. Rinse in stream of deionized water for about 1 minute, and blow dry with N_2.
30. Then clean on the spinner, two minutes with a deionized water stream, and two minutes blowing dry with N_2.
31. Evaporate on a 1600 Å layer of Aluminum (99.999% pure).
32. Put sample in acetone to soak for about 30 minutes; then remove Aluminum by squirting sample with a stream of acetone. Clean and dry sample with acetone, methanol and dry N_2.
33. Cleave off three 5 mm x 5 mm chips from a piece of scrap GaAs. Clean and dry them well.
34. Clean a quartz disk (1.50” diameter, 0.130” thick) with an acetone soaked clean room towelette. Then place the disk on the spinner and clean with acetone, then methanol, and then dry with N_2.
35. Put the disk on a hotplate set to 170°C and let it get hot.
36. Chip off small pieces (about the sizes of large grains of salt) of clear mounting wax (South Bay Technology, Inc., www.southbaytech.com, product #MWH135 – aka

"Quickstick 135") with a razor blade. Set three of these pieces in a large triangle pattern so that the wax pieces are about 5 mm from the edge, spaced 120° apart.

37. Once the wax melts, put the scrap pieces of GaAs on top of the wax droplets, and push them into the wax using the end of a wooden stick. Push them straight down, try not to let them move laterally. Push down very hard. The aim is to thin out the wax layer beneath the GaAs chip.
38. Remove the disk from the hotplate, and let cool a bit. Then spray the disk with acetone to remove any wax residue around the chips. Rinse with methanol, dry with N_2 and return disk to heater.
39. Put a small piece of wax on the center of the disk. Once it melts, put your sample piece, top side down, on the wax droplet. Push down hard with the wooden stick. Remove the disk from the heater, cool, and again rinse away any residue with a stream of acetone, and then methanol. Dry disk with N_2. Set aside.
40. Clean a glass plate (about 6" x 6" x ¼") with acetone soaked towelettes, then rinse well with methanol and dry. Wrap the plate in a large sheet of dextalose paper (or a large filter paper) as though wrapping a gift, and secure it with masking tape. One side of the plate should be tape-free and covered with just one smooth layer of paper, set this side up in a plastic tray (slightly bigger than the plate, with a lip at least ½" high).
41. Put the quartz disk with the sample on it in a cylindrical Teflon chuck that has the following dimensions: height = 2", OD = 2.00", ID = 0.275". At each end there will be a socket that will hold the quartz disk, with dimensions at one end: socket depth = 0.150", socket diameter = 1.50"; and at the other end: socket depth = 0.130", socket diameter = 1.50". Put the disk in the deeper socket, with the sample side facing out of the socket. Use a drop of water for adhesion.
42. Mix bromine-methanol etch. Bromine is highly corrosive, and highly reactive with acetone (with which it produces a tear gas). So wear a face shield, gloves and lab coat when handling bromine, and work under a fume hood. Do not have any acetone near the workspace. Put 25mL of methanol in a graduated cylinder. Add

4mL of bromine. Pour this mixture into a 30mL beaker. Rinse out the cylinder with water and put away.

43. Soak top side of dextalose paper covered glass plate with methanol. Pour a small amount of the bromine-methanol solution on the center of the plate. Grab hold of the Teflon chuck, holding the sample side down.
44. Because the bromine-methanol can etch roughly if it is allowed to stagnate on the sample surface, the sample must always be kept moving. Gingerly set the chuck on the glass plate so that the sample contacts the bromine-methanol solution. Immediately begin making 'figure-8' motions along the plate with the chuck – this will keep the solution moving across the sample and the etching will proceed smoothly. Make 100 'figure-8's and then just as gingerly slide the chuck off of the plate laterally (rather than pulling it up off the paper). Rinse the sample and chuck with methanol and dry with N_2.
45. After every 100 'figure-8's the thickness should be measured. We use an Ono Sokki gauge (stand model: ST-022, gauge model: EG-225) to measure the sample height.
46. Pour some more bromine-methanol in the center of the plate and repeat the process – making another 100 'figure-8's. Clean off the sample and chuck, and measure the sample height.
47. Continue this until the sample thickness reaches about 170 μm. The sample can only be thinned to about 170 μm in the deep socket, so once it reaches this thickness, the disk must be removed from the deep socket and put into the shallow socket at the other end of the chuck.
48. Continue this process with the disk now in the shallow socket, but start making fewer 'figure-8's between measurements, as the etch process will proceed more quickly with the disk at this end. As the target thickness of 50 μm is approached, make only a few 'figure-8's between measurements, so that the sample does not become accidentally over-thinned.
49. Once the sample is thinned to 50 μm, remove the disk from the chuck. Clean disk in methanol, and dry with N_2. Pour any remaining bromine-methanol into a

container filled with sodium thiosulfate powder, this will neutralize the bromine. Rinse out the paper with water, and throw away. Clean the glass plate with methanol and dry with towelettes. Rinse off the plastic tray.

50. Remove the scrap GaAs chips at the edges of the disk by scraping them with a clean razor blade.
51. With the sample still firmly attached to the disk, clean the ensemble on the spinner, sample side up, first with acetone, then methanol, then deionized water. Blow dry for 2 minutes with N_2 stream while still spinning.
52. Spin on AZ5214 for 30 seconds at 5krpm. Put on enough AZ5214 before spinning so that the whole disk is covered after it is spun.
53. Set disk in kimax dish cover, and put in oven to bake for 30 minutes at 80°C.
54. Set disk/sample in mask aligner, dial it all the way down, in contact mode, so that it will fit, and align the back gates. This step requires an infrared camera, so that the structures on the top side will be visible for the alignment process (GaAs is transparent in the infrared).
55. Expose for 15 seconds.
56. Develop in a 4:1 solution of deionized water and AZ400K developer (I use 60mL of water and 15mL of developer). It takes approximately 30-40 seconds to develop. Rinse under a stream of deionized water for about 1 minute, and blow dry with N_2.
57. Put disk/sample on spinner, and clean with a stream of deionized water for 2 minutes, while spinning. Then blow dry with N_2 for another 2 minutes, while spinning.
58. Evaporate on 1500 Å of Aluminum (99.999% pure).
59. Soak disk/sample in a dish of acetone for a few minutes for the Aluminum liftoff.
60. Clean the sample with a stream of acetone, and set the disk/sample in a kimax dish with a round filter paper (Whatman #1001055) on the bottom, and filled with clean acetone. Set it sample side down, supported at one edge by a small magnet stirrer. It will take a few to several hours for the acetone to dissolve the wax that is holding the sample to the disk so that the sample will fall off and settle on the filter paper.

61. Remove the disk and magnet stirrer. Cover the sample with a second filter paper, and carefully remove the filter paper/sample sandwich from the acetone bath with a pair of tweezers. It will be easier to handle this if a fold is put near the edge of the papers.
62. Keeping the sample always between two filter papers (they can be replaced by clean ones as desired), squirt methanol on the papers/sample to remove acetone residue. Allow to dry naturally.
63. Bring the sample, like this, over to the wire-up station. A custom chuck must be made out of Teflon, with very small holes drilled in the center, so that the vacuum that will hold the sample to the surface will be very gentle. Slide the sample off of the filter paper, top side up, onto the center of this Teflon chuck. If necessary, use a sharpened wooden stick to push the sample to where it needs to go. Turn the vacuum on.
64. Solder 1 mil gold wire to the contact pads around the perimeter of the design using Indium (99.999% pure) as the solder. We use an Oryx model 54204-T-20VA miniature soldering iron with Oryx isotip # 7258.
65. To secure the sample for the wire up of the back gates, remove the sample from the chuck, and flip it over onto a glass microscope slide. The sample will be suspended above the slide, supported by the gold wires. Solder a few of these gold wires to the glass slide to secure the sample. Set this ensemble onto a standard vacuum chuck.
66. Use conducting epoxy (epo-tek H20E from Epoxy Technology, Inc.) to attach 1 mil gold wires to the backside contact pads. Mix the epoxy extremely well (stir with a wooden stick for about 10 minutes). First put blobs of this epoxy onto the contact pads (with a sharpened wooden stick), and then poke the ends of the gold wires into the blob. Put the slide and sample in to bake at 125°C for 1 hour to harden the epoxy. Unsolder the wires from the glass plate, and the sample is now ready to be wired up to the pins of a DIP header or custom sample mount.

* * *

Appendix B

MASK DESIGN

We design the masks used in the photolithography that defines the mesa geometry, contact location and the gating/contact lead structure. For my early data, I used masks already in existence that had been designed by other members of the group. But for my counterflow work, there were no preexisting mask designs that would allow for a counterflow current configuration, so this mask I designed myself.

The foremost issue in my design for the counterflow mask was to include enough contact leads so that separate currents could be sent to the different layers. This requires a minimum of four current leads (if the interlayer current is to also be monitored). In single layer systems this number of contacts would not be a problem, but for double layers each contact needs a set of arm gates for separate layer contacting [1], this requires up to three wires for each contact. Our sample mounts can accommodate at most 18 wires, so for compatibility with all the existing cryostats, I was limited to this number of contacts and gates. Even so the fewest number of contacts and gates I could manage was 19 (see Fig. B.1); and two of the arm gates had to be wired to the same sample mount pin (the two back arm gates of the longitudinal voltage probes), which however never limited the measurement configurations I could set up.

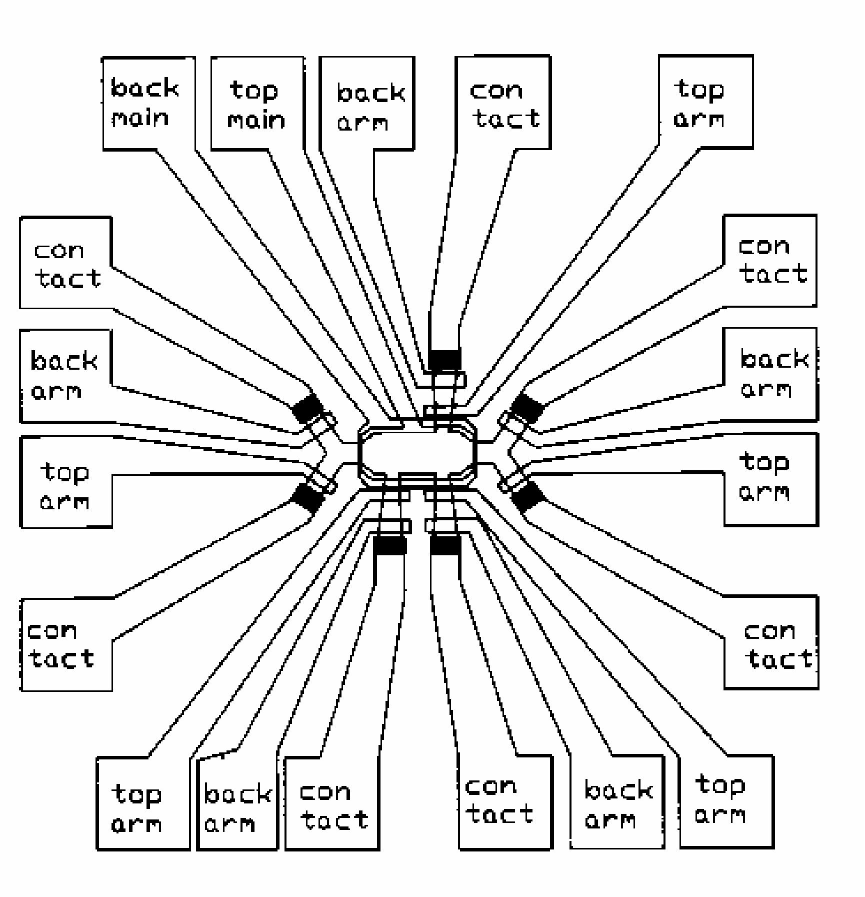
back
main
top
main
back
arm
con
tact
top
arm
con
tact
con
tact
back
arm
back
arm
top
arm
top
arm
con
tact
con
tact
top
arm
back
arm
con
tact
con
tact
back
arm
top
arm

Figure B.1: Mesa and gating design for sample 'Y' used for counterflow experiments. The entire structure is 3mm x 3mm. Figures 1.4 and 7.2 show a crystal processed with this mask.

I also wanted the current distribution to be uniform through the central electron region. For the counterflow experiment, the current density should be equal but opposite in the two layers. To ensure this I settled on the 'Y'-shaped design for my current contacts; the narrow constriction before the current enters the central region means that the current distribution will only have a small dependence on which contact it originates from. To test the current uniformity I modeled the current flow in the mesa geometry using the partial differential equation solver toolbox in MATLAB [2]. By solving the Laplace equation

($\nabla^2\Phi = 0$, where Φ is the electrostatic potential) with the following boundary conditions: $\Phi = \text{constant}$ along the end of the lower left arm of the 'Y' contact, $\Phi = 0$ at the end of the right contact and $\frac{\partial\Phi}{\partial n} = 0$ (where $\frac{\partial}{\partial n}$ is the normal derivative) along the remaining edges of the mesa; and then plotting $-\nabla\Phi$, I can produce a vector representation of the current distribution in my mesa geometry (see Fig B.2).

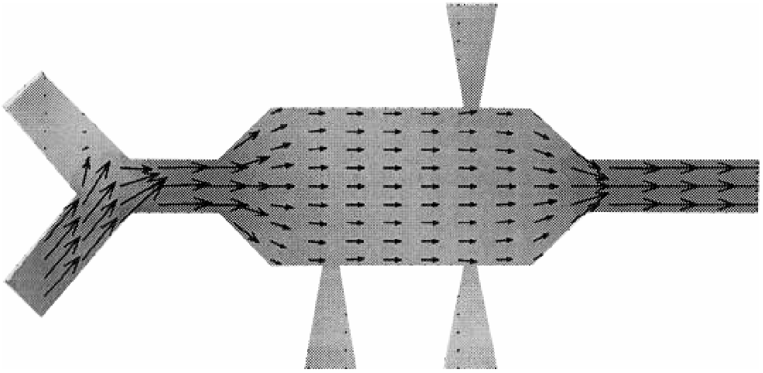

Figure B.2: Numerical calculation of classical current distribution in counterflow mesa.

Also at issue in the mesa design is the number of total squares that the current will flow through, as well as the number of squares that we are measuring along. A square is the two-dimensional analogue to the length of the sample that the current flows through. It is defined as the length *L* divided by the width *W* of the sample: *L/W*.

At the low densities at which we work, the layer resistivity can become very large even at moderate magnetic field strengths and the total resistance of the sample can become so large that it changes the entire measurement circuit dynamics. Usually this shows up as a phase shift of the drive current in the sample. So I made an effort to keep the total number of squares the current would pass through less than about 10 squares per layer.

Additionally, it has been empirically noted that the number of squares measured across has an effect on the quality of the data taken at very low temperature and density (thus in the bilayer quantum Hall regime). Some of our nicest data has come from square central regions (samples ‘N’ and ‘R’) where we were measuring approximately $ln2/\pi$ squares (assuming van der Pauw current distribution [3]), and some of the least-nice data has come from a rectangle ten squares long (sample ‘K’). So for this design I went in between the two and chose a one square long measurement region. This way, the resistance that we measure, will be approximating the resistivity (the resistance per square).

Also to be considered is that the mesa region needs to be small enough so that the inevitable Gallium “bullet” defects [4] in the crystal can be avoided when aligning the pattern onto the sample. And the front and back gates should not lie above or below each other, because of the concern of shorts developing between the two. All these requirements were met in the design shown in Fig. B.1.

* * *

---

1 J.P. Eisenstein, L.N. Pfeiffer and K.W. West, Appl. Phys. Lett. **57**, 2324 (1990).

2 See Appendix E for detailed information on how to use the PDEtool in MATLAB for this kind of calculation.

3 L.J. van der Pauw, Philips Res. Rep. **13**, 1 (1958).

4 Inevitably, small blobs of gallium will get sputtered onto the crystal during the molecular beam epitaxy process. These "bullets" of gallium can short together the two electron layers, and so they must be avoided during the photolithography alignment process. They are easily visible under the mask aligner microscope.

Appendix C

COULOMB DRAG SETUP

Measurements such as Coulomb drag, counterflow and tunneling can only be done because we are able to make electrical contact to the layers individually. We do this by a technique called "selective depletion" which was invented by Eisenstein *et al.* [1]. By applying negative voltages to the gates that lie above and below the contact arms, we deplete the electrons in a region that cuts across the arm in the layer closest to the gate. This makes one layer in the arm highly resistive to the flow of current and virtually all of the current will flow in the other layer. We test and calibrate these arm gates by running "gate characteristic" measurements [2]. The gate characteristic information is used to set up the measurements requiring individual layer contact, such as Coulomb drag.

In the Coulomb drag measurement, current is driven through just one of the layers, and the voltage is measured along the other, open-circuited layer. It is very important that the layer in which the current flows is at or near ac ground, as alternating common mode voltages on this layer will cause a current to flow between the layers (either by tunneling or by capacitive coupling) and this can result in a spurious drag signal. The simplest way to prevent this is to connect the two layers together at one of the contact points and then to ground this contact. Then both the layers will be at both ac and dc ground. Coulomb drag measurements that require a dc bias voltage between the layers (for the suppression of tunneling or for layer density imbalance measurements), will call for a more complicated circuit.

C.1 SETUP WITHOUT INTERLAYER BIAS

For the simpler Coulomb drag measurement, I will give as an example an actual setup I used for sample 'Y'. This is a standard Coulomb drag setup.

Put a 10k/100 Ω voltage divider on the EG&G/Princeton Applied Research model 124A lock-in amplifier's output, set the output to 2 V RMS and the frequency to 23 Hz. Put a 10 MΩ resistor in series with the voltage divider, followed by a precision 10 kΩ resistor, which will be used to sense the current being sent into the sample. The voltage across this resistor will be measured by a second lock-in that has been synchronized to the first lock-in. Send the current into arm 18 (see sample map in Fig. C.1). Cut off arm 11 by putting -2 V on gate 10, ground contact 11. Put -0.45V on gate 16 to force the current to only go through the bottom layer in arm 18. Keep contacts 8 and 17 open and put -43 V on gates 5, 6 and 15. This will nullify contacts 8 and 17, and allow arms 1 and 2 to be used to probe the voltage in the top layer. Attach a pair of twisted coaxial cables from contacts 1 and 2 directly to the first lock-in's differential amplifier (model 116) set to direct mode. Ground contact 7, and ground all gates not in use. The layers will be connected through contact 7.

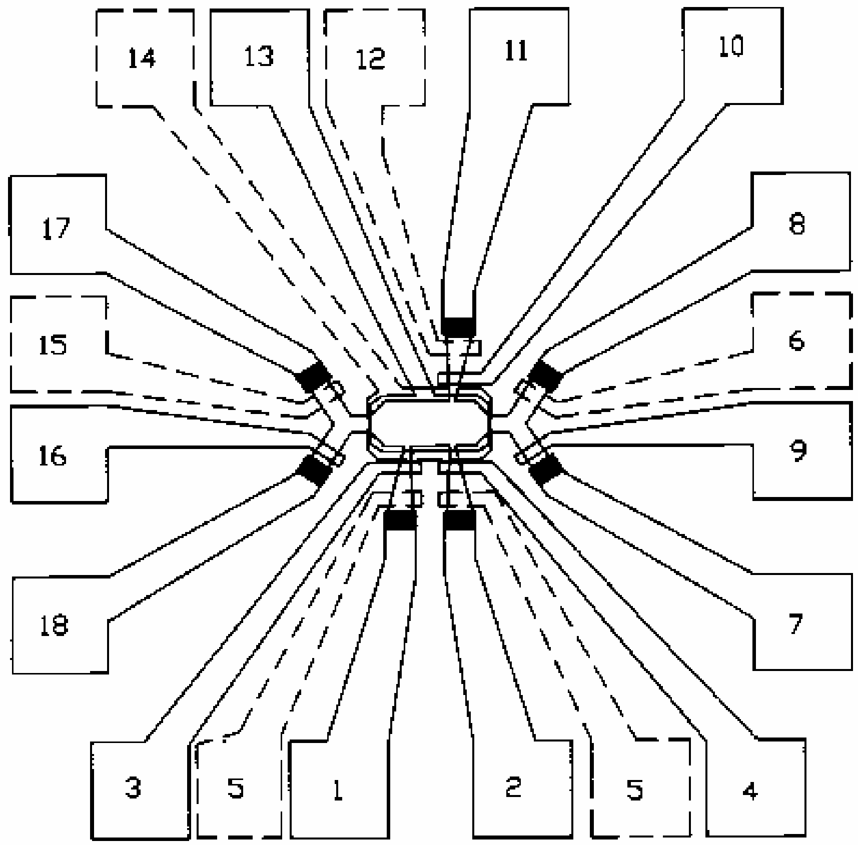

Figure C.1: The map for sample 'Y'. Black rectangles are the contacts. The dashed lines indicate back gates.

C.2 SETUP WITH INTERLAYER BIAS

If the layers cannot be at the same dc voltage, in the case of interlayer bias dependent measurements for example, then the Coulomb drag circuit must be setup the following way (Fig C.2).

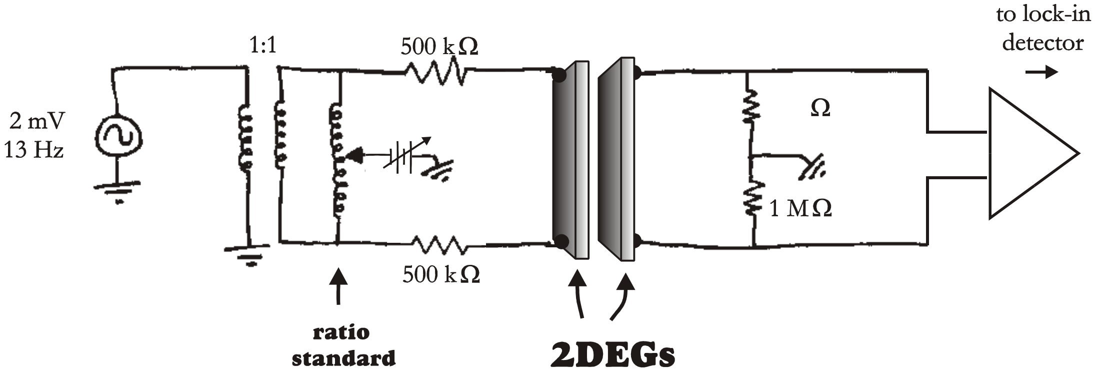

Figure C.2: The Coulomb drag circuit with interlayer bias.

Again, I will use as an example an actual setup used with sample 'K'. Put a 10k/100 Ω voltage divider on the lock-in amplifier's output, set the output to 0.2 V RMS and the frequency to 13 Hz. Connect this to the top right input of a 1:1 Gertsch model ST-200 transformer. Connect "T"-connectors to the two transformer outputs. Connect one arm of one "T" to the input of a Gertsch AC model 1011 Ratio Standard. Connect one arm of the other "T" to the ratio standard's common. Put 500 kΩ resistors in series with the remaining arms of the "T"'s with a 10 kΩ resistor in series with one of these – use this as the current sense resistor – the voltage across this resistor is measured by a second, synchronized lock-in detector. Connect one of these leads to arm 12 and the other to arm 14 (see sample map, Fig. C.3). Put -0.6 V on gates 13, this will force the current to flow only in the bottom 2DEG layer. Cut off arm 9 with -2 V on gate 10, ground contact 9.

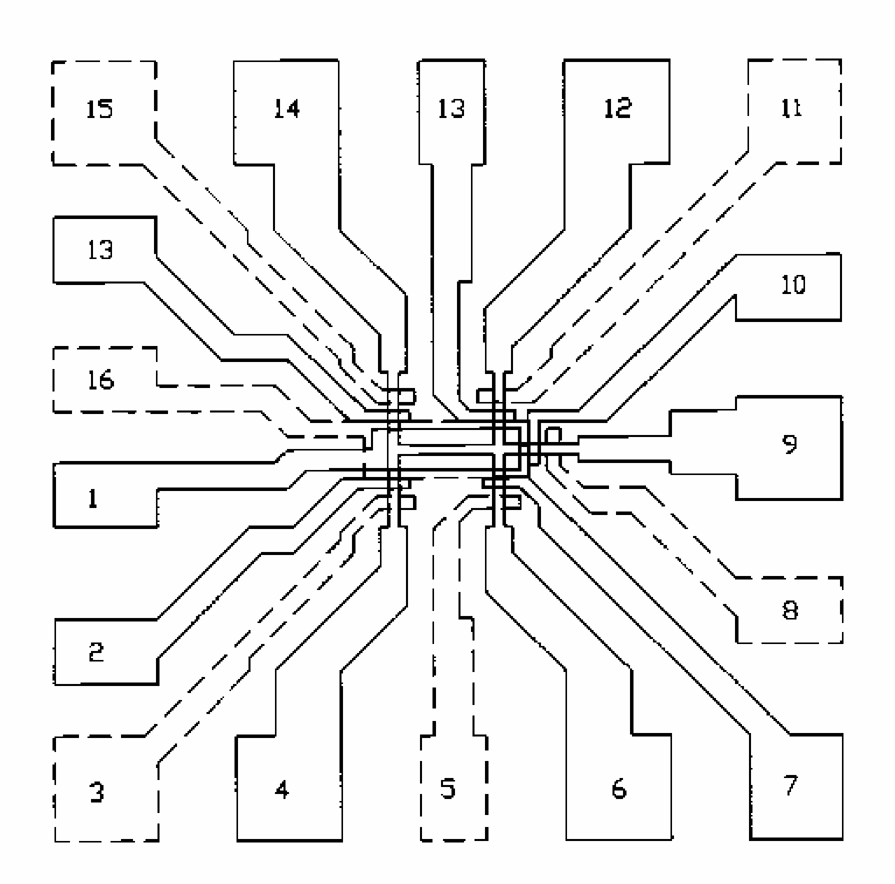

Figure C.3: The map for sample 'K'. The dashed lines indicate back gates.

Connect arms 4 and 6 to the lock-in's differential preamplifier (model 116), in direct mode, and connect the two leads together with two high-accuracy 1 MΩ resistors in series with a connection to ground in between them (see Fig C.2). Put -39 V on gates 3 and 5, this will connect the voltage probes to the top 2DEG layer only.

The ground between the two 1 MΩ resistors sets a virtual ground in the center of the drag layer, so long as the two 1 MΩ resistors plus the resistances in arms 4 and 6 are precisely matched.

C.3 CALIBRATING THE RATIO STANDARD

The output of the ratio standard can either be grounded or connected to a dc voltage source, either way this will set a virtual ac ground in the drive layer. The ratio standard allows for this ac ground to be moved around the circuit, so that it can be tuned to lie in the 2DEG itself. This can best be done by looking at the 90° phase common mode voltage signal on the drag layer during the drag measurement while varying the ratio standard setting. Switch the preamplifier mode from 'A-B' (measuring the differential voltage) to 'A' or 'B' (measuring the absolute voltage on input 'A' or 'B') and change the lock-in's phase setting to 90°. When the ac ground is not centered in the 2DEG, the oscillating drive current will induce an oscillating common mode voltage on the layer. The further away ac ground is

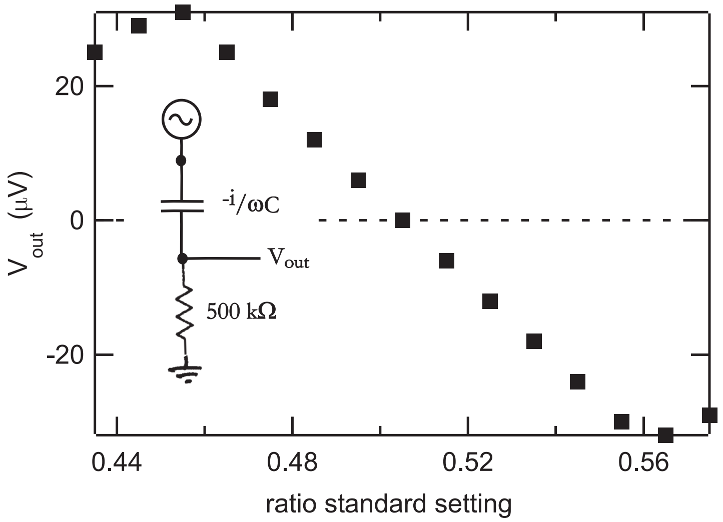

Figure C.4: The 90° phase common mode voltage on the drag 2DEG as a function of the ratio standard setting. In this measurement, the Coulomb drag circuit shown in Fig. C.2 is reduced to the voltage divider shown in the inset.

from the 2DEG, the larger this signal will be. The 2DEG layers will act as a parallel plate capacitor and this signal will induce a 90° phase current to flow through the layers and into the ground between the two 1 MΩ resistors (now effectively 500 kΩ, as they are in parallel). The Coulomb drag circuit is reduced to the voltage divider shown as the inset to Figure C.4, where the effective applied ac common mode signal is easily shown to be linearly proportional to the ratio standard setting. The capacitance, C, of the two 2DEG layers is of order 100 pF for my mesa geometries.

Figure C.4 shows the results of this measurement on sample 'K' at 300mK with a 13 Hz, 100 nA drive current. The ratio standard setting is ranged from 0.435 to 0.575 at 0.01 increments. The linear response observed over most of this range indicates how fittingly the circuit reduces to a simple voltage divider, as well as the linearity of the applied ac common mode voltage with the ratio standard setting. This linear behavior stops below 0.455 and above 0.565, when the amplitude of the common mode voltage becomes too large to maintain the integrity of the selective depletion scheme for maintaining separate layer contact, thus current starts flowing into both layers, and the voltage divider circuit is no longer valid.

When the ac ground is centered in the 2DEG, the common mode voltage is zero and no current flows between the layers: V_{out} will read zero – this yields the proper ratio standard setting. For the data shown in Figure C.4, the proper setting is 0.505.

C.4 SETTING THE PHASE

Also to be considered in setting up the Coulomb drag measurement is the proper adjustment to the lock-in's phase setting. The phase of the signal coming out of the lock-in detector's output will get shifted slightly as it goes through the circuit before it reaches the 2DEG. Working at these low frequencies, including the transformers in the circuit tends to shift the phase, as do the large resistances that we use in a circuit along with the inevitable capacitances to ground through the wires in the cryostat (a few nF). The proper phase setting will be the one in which the current actually flowing in the bottom layer of the 2DEG is defined as being purely real.

The best way to set the phase, is to actually probe the current at a point in the circuit that is very close to the 2DEG. In the above setup, the 10 kΩ resistor in series with one of the 500 kΩ in the drive layer side of the circuit should be placed nearest to the 2DEG and this can be used to set the phase. In the simpler Coulomb drag setup discussed earlier (in Section C.1), it is best to temporarily insert a sense resistor between the 2DEG and ground (in between contact 7 and ground in the example used) and set the phase by this current, then remove the resistor. The phase is set correctly when the 0° signal is frequency independent and any 90° signal is strongly frequency dependent; and I have found that this method ensures that.

* * *

---

1 J.P. Eisenstein, L.N. Pfeiffer and K.W. West, Appl. Phys. Lett. **57**, 2324 (1990).

2 See Appendix F for detailed information on how to take and interpret gate characteristics.

Appendix D

COUNTERFLOW MEASUREMENT SETUP

As an example of the counterflow setup, I will describe the setup used for the counterflow Hall data shown in Figure 7.5. This is a standard counterflow setup.

Put a 10k/100 Ω voltage divider on the EG&G/Princeton Applied Research model 124A lock-in amplifier's output, set the output to 5 V RMS and the frequency to 5.1 Hz. Put a 10 MΩ resistor in series with the voltage divider. Cut off arm 1 by putting -2 V on gate 3; ground contact 1 (see sample map in Fig. D.1). Put -43V on gates 6 and 15 to force the current to only go through the bottom layers in arms 8 and 17. Send the current into arm 8, extract current from arm 17, and then send through a precision 10 kΩ resistor for sensing the current. Measure the voltage across this resistor using a second lock-in that has been synchronized to the first lock-in. The phase can be set by this current. Put -0.45V on gates 9 and 16 to force the current to only go through the top layers in arms 7 and 18. Redirect the current into arm 18 and then ground arm 7. Attach a pair of twisted coaxial cables to arms 2 and 11 for measuring the Hall voltage and connect these to the first lock-in's differential amplifier (model 116) set to direct mode. Put -43V on gates 5 and 6 so that these arms only probe the top layer. For parallel configuration, the setup would be the same except that the roles of arms 8 and 17 would be reversed: the current would first be sent into arm 17 and then be extracted from arm 8.

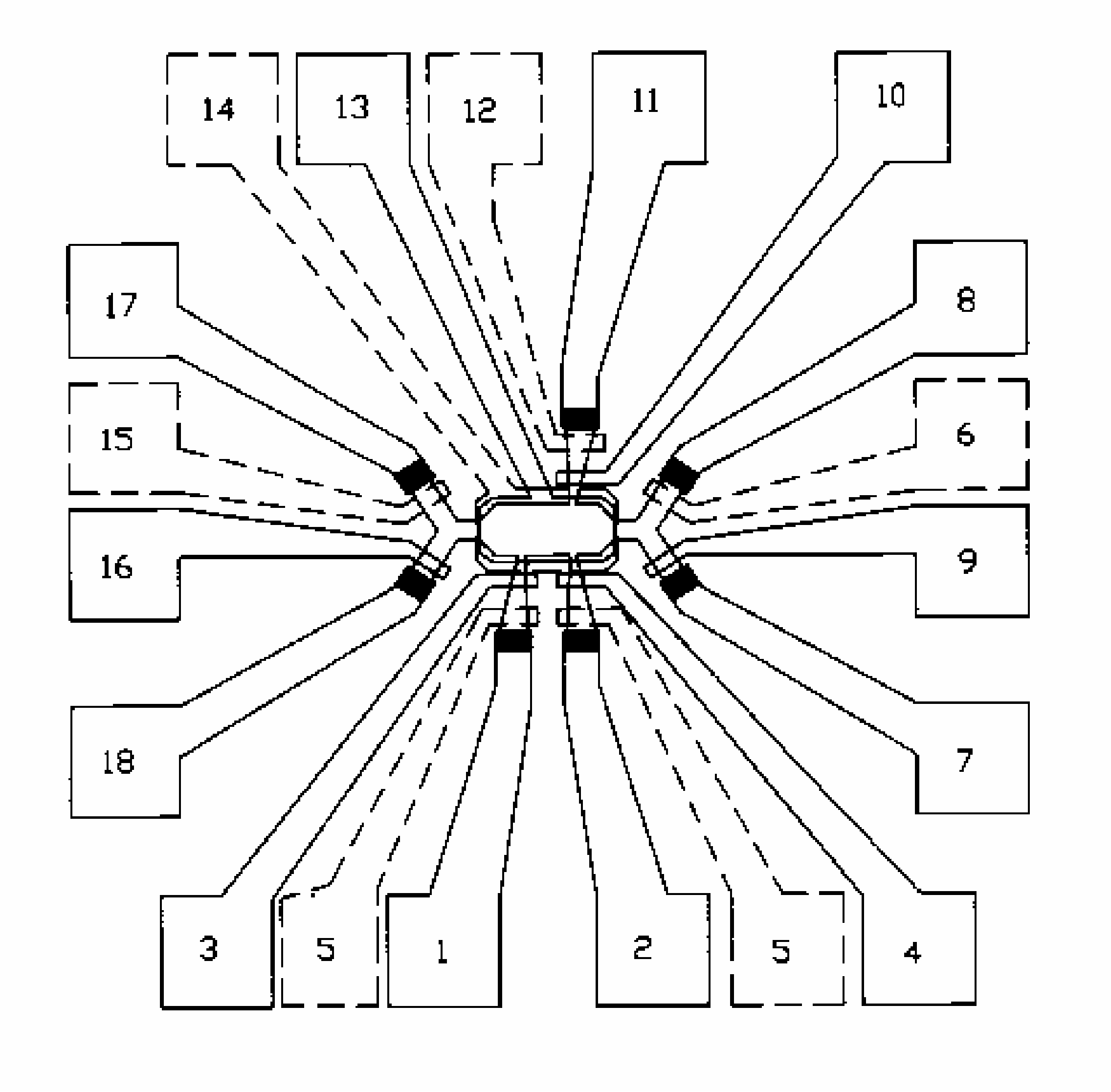
14
13
12
11
10
17
8
15
6
16
9
18
7
3
5
1
2
5
4

Figure D.1: The map for sample 'Y'. The dashed lines indicate back gates.

* * *

Appendix E

MODELING CURRENT FLOW WITH PDETOOL IN MATLAB

The Partial Differential Equation Toolbox in MATLAB can be used to solve the LaPlace equation ($\nabla^2 \Phi = 0$) for an arbitrary two-dimensional shape. The following instructions are a modified version of instructions given to me by Ken Cooper.

1. Start up MATLAB.
2. To open the Partial Differential Equation Toolbox, type
   >>**pdetool**
   at the prompt, and then hit **return**.
3. This will open up the PDE Toolbox window. Press the **moon** shape button to draw a shape in the blank space below the menu bar. Click the mouse to define the vertices. When you return to your starting point, the shape will close itself automatically.
4. Press the **dΩ** button to set up the boundary conditions for your shape. Select one or more sides of your shape by clicking them with the mouse (Shift-click for multiple selections). Then under the **Boundary** menu, select **Specify Boundary Conditions**. Choose **Dirichlet** conditions to set a constant voltage (set h=1, r to the voltage, e.g. r=0 or r=1). Choose **von Neumann** for the condition that no current flows across the boundary (set g=0 and q=0). Do this for all sides of your shape.

5. Press the **PDE** button. This will bring up a box with generic differential equations to choose from. For the LaPlace equation, choose **elliptical** and set c=1, a=0, and f=0.

6. This program will solve for the potential using the **finite element method**. This method breaks up the shape into a mesh, to initiate this mesh, press the **triangle** button.

7. You can then refine this mesh by pressing the **triangle-within-a-triangle** button. Pressing this twice is usually sufficient.

8. Press the **"="** button to solve the equation for your shape. This will display the solution as a color gradient in your shape, where each color represents an equipotential.

9. For other display options, press the **plot** button. Choose **arrow** and "**- grad u**" and **proportional** to display the current as a vector field (Fig. E.1).

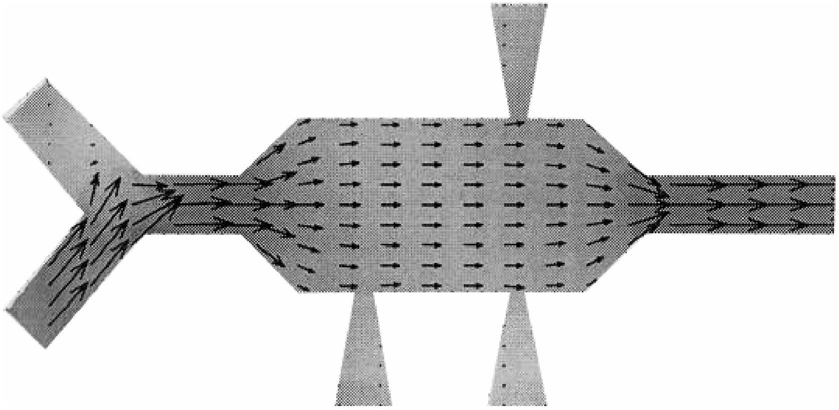

Figure E.1: Numerical calculation of current distribution in counterflow mesa.

10. To further manipulate the data, you must export it out of PDE Tool into the main MATLAB program. To do this select **Boundary:Export Boundary**, **PDE:Export PDE Coefficients**, **Mesh:Export Mesh**, and **Solve:Export Solution**. PDE Tool

will automatically assign variable names to these data arrays. ‘u’ is the calculated potential, ‘p’ and ‘t’ are the mesh coordinates, etc.

11. Back in the main MATLAB window, here are some commands you can use to display and manipulate the PDE Tool data:

```
>>pdesurf(p,t,u)     {displays a 3D view of the solution, click the mouse in the
                      figure window to change the display angle}

>>help pdesurf       {use the help command for more information on a command}

>>[jxt,jyt]=pdecgrad(p,t,c,u)       {this takes the gradient of u in the x and y
                      directions and names the output ‘jxt’ and ‘jyt’}

>>jxn=pdeprtni(p,t,jxt)       {this converts the triangle mesh data into node data}

>>jyn=pdeprtni(p,t,jyt)       {this does the same for the y-component data}

>>x=-1.5:0.01:1.5

>>y=-1.0:0.01:1.0    {these create an x-y grid for plotting the node data}

>>jxgrid=tri2grid(p,t,jxn,x,y)     {this maps the x-component current node data
                                    to the grid}

>>jygrid=tri2grid(p,t,jyn,x,y)     {and the y-component node data}

>>contour(jxgrid)    {makes a contour plot of the x-component of the current}

>>jxcs=jxgrid(:,200)    {takes line x=200 from ‘jxgrid’ and saves it as a 1D array
                        called ‘jxcs’}

>>plot(jxcs)               {plots the 1D array}
```

* * *

Appendix F

HOW TO TAKE GATE CHARACTERISTICS

This measurement tests the diffusive contact resistance to each layer, as well as calibrates the arm gate voltages needed to establish separate layer contact.

Put a 511/1 Ω voltage divider on the EG&G/Princeton Applied Research model 124A lock-in amplifier's output; along with the 600 Ω output impedance of the lock-in, this will serve as a 1000:1 voltage divider. Set the output voltage knob to 1 V RMS, thus applying an approximately 1 mV signal to the 2D electron gas. Send this signal across a resistor (we usually use one of our variable resistor boxes) and then into the contact arm you wish to check; ground all the other contacts.

Measure the voltage across the resistor using the lock-in's differential preamplifier (model 116) while applying a steadily decreasing voltage to the arm gate you wish to test (all other gates should be grounded). The value you choose for the resistor should be one that is comparable to the contact's resistance (1 kΩ is good, unless there are other resistances in series with the contact arm, and then include those). The voltage across the resistor approximates the conductance of the contacts. Figure F.1 shows typical gate characteristic measurements.

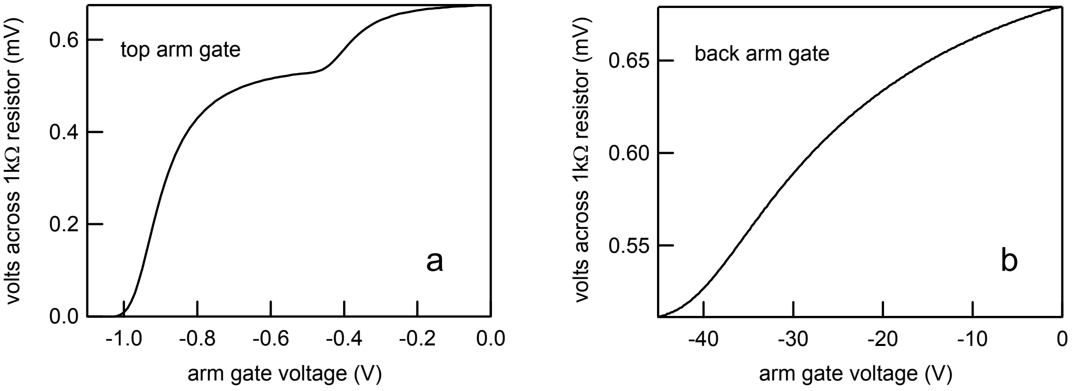

Figure F.1: Typical gate characteristics for the top (a) and back (b) gates of one of the contact arms. Taken at 4 K with a 1 mV excitation signal.

As the gate voltage decreases from zero on the top arm gate (Fig F.1a), the electrons begin being depleted underneath the arm gate in the top layer. At first this has little effect on the conductance of the arm; but as the electrons near total depletion, the conductance in the depleted layer falls dramatically until the layer no longer supports current flow – this creates the step observed around -0.4 V. Once the top layer is depleted, the region underneath the gate in the bottom layer starts losing electrons. Again, this has little effect on the conductivity until the gate voltage reaches around -0.8V, and then the conductivity drops quickly to zero as the last electrons are depleted at just below -1 V.

For the back arm gate characteristics, we only deplete the bottom layer since the large voltages that would be required to deplete both layers (around -80 V) may cause electrical breakdown in the sample. The depletion of the bottom layer is completed around the inflection point seen around -42 V in Fig F.1b.

The contact resistance can be backed out of these measurements by solving the voltage divider equation (F.1)

$$R_{contacts}(k\Omega) = \frac{1 - V_{out}(mV)}{V_{out}(mV)} \tag{F.1}$$

for the measurement setup (Fig F.2).

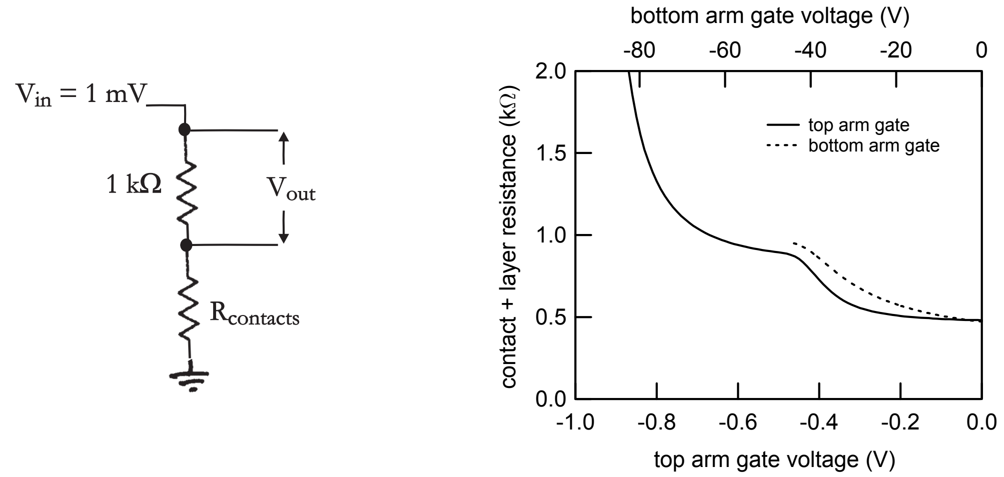

Figure F.2: On the left is the gate characteristic measurement circuit – a simple voltage divider. And on the right, the resistances inferred from the gate characteristic measurements in Fig F.1.

Applying this equation to the data in Fig F.1 gives the resistance of each layer alone as well as the two combined (Fig F.2).

* * *

Appendix G

LAYER DENSITY BALANCING BY COULOMB DRAG

There are two methods in general use for balancing the densities of the two layers. If there is a reasonable tunneling signal, tunneling is an excellent method for matching the densities in the two layers. For this work, samples were chosen for their exceedingly low tunneling, and consequently I did not have sufficient tunneling signal to use this method to balance the layers.

The second method for balancing the layers is to take conventional transport measurements of the layers individually – the location of the QHE minima with respect to the magnetic field depends on the layer's density. This technique is just a matter of getting the minima in the magneto-transport data traces in each layer to line up.

Since the transport measurement I used most regularly was Coulomb drag, I found what was for me a simpler method for balancing the layers – balancing by Coulomb drag. This proved to be equally precise as the other methods, and gave similar balancing gate voltages to within this precision. This also had the added advantage that I was balancing in the configuration that I would be taking the data in, incase the configuration has subtle influences on the density, the homogeneity, or more directly – the regions probed in the density balancing measurements. However, slight mismatches in density have very little impact on the drag (a ±5 mV change in the top gate voltage, results in a ~ 1.5% change in the value of the drag), so balancing by Coulomb drag was favored mainly for its convenience.

It is possible to balance the two layers by Coulomb drag because the drag in the high Landau levels goes negative when the layers are out of balance [1]. So I would simply take Coulomb drag measurements up to the fifth Landau level or so at different gating voltages,

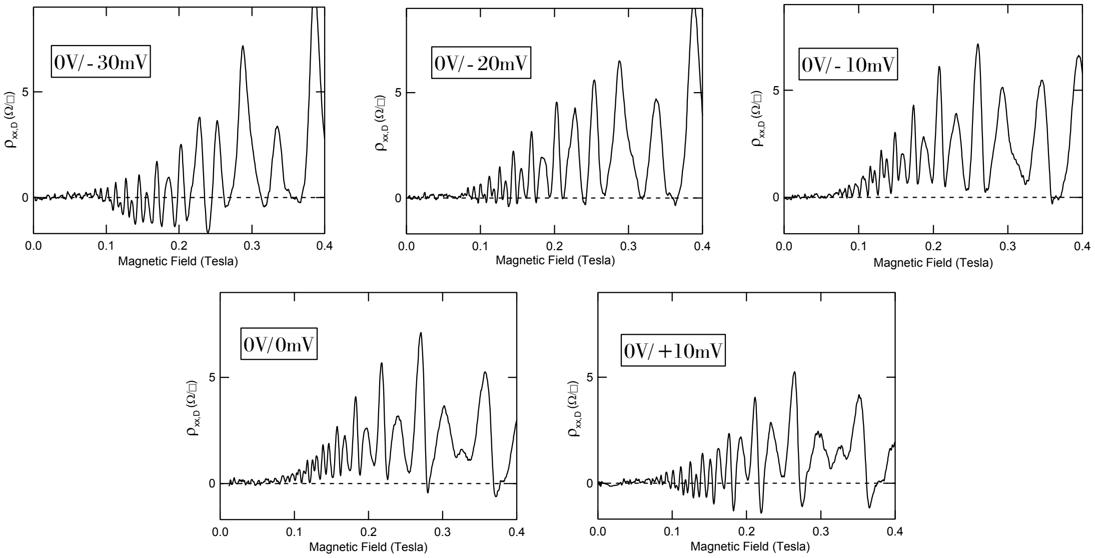

Figure G.1: Coulomb drag measurements from sample 'K' taken September 21, 2000 is used to find the top gate voltage that balances the ungated bottom layer. 0V/-10mV was chosen as the balanced gating configuration.

and select the one that showed the drag to be positive over the largest range (see Figure G.1). This method was confirmed by checking how well the locations of the QHE minima in magnetic field were linearly fit to the inverse filling factors of these minima (by the relation $B = \frac{nh}{\nu e}$, where ν is the Landau level filling factor); a smaller standard deviation to the fit should indicate that the minima are well defined by a single density n (the same density that is in each layer). The drag I chose as balanced by eye, always had the smallest standard deviation in the fit, confirming my choice.

* * *

---

1 J.G.S. Lok, S. Kraus, M. Pohlt, K. Güven, W. Dietsche, K. von Klitzing, W. Wegscheider and M. Bichler, Physica B **298**, 135 (2001).

Appendix H

HOW TO DETERMINE DENSITY AND MOBILITY

We measure the density by comparing the locations (in magnetic field) of the minima in the Shubnikov-de Haas oscillations with their Landau level filling factor ν. The two are related by

$$B_{\min} = \frac{hn}{e\nu}. \tag{H.1}$$

Plotting $B_{\min}$ versus ν^{-1} should yield a straight line, the slope of which is directly proportional to the density n. This will work with the Shubnikov-de Haas oscillations in Coulomb drag, tunneling and other measurements, but here I will go through an example where the density is calculated using conventional transport through both layers (this is the standard method used in our lab).

Conventional transport through both layers has a very simple setup: Put a 10k/100 Ω voltage divider on the EG&G/Princeton Applied Research model 124A lock-in amplifier's output, set the output to ~ 5 V_{RMS} (for an ~ 5 nA current, though I go as high as 20 nA for these measurements). Put a 10 MΩ resistor in series with the voltage divider, followed by a precision 10 kΩ resistor, which will be used to sense the current being sent into the sample; the voltage across this resistor will be measured by a second lock-in that has been synchronized to the first lock-in. Send the current into one the contacts and ground another; the current will flow between these two contacts. Attach a pair of twisted coaxial cables to two of the remaining contacts to measure the longitudinal resistivity. Open all the remaining contacts; ground all of the gates.

Figure H.1 shows the typical result of such a measurement done at $T = 0.05K$ for sample 'Y' at nominal density, versus magnetic field. Shubnikov-de Haas oscillations can be identified up to $\nu = 30$ in this sample at this temperature – I have labeled a few of them in the figure.

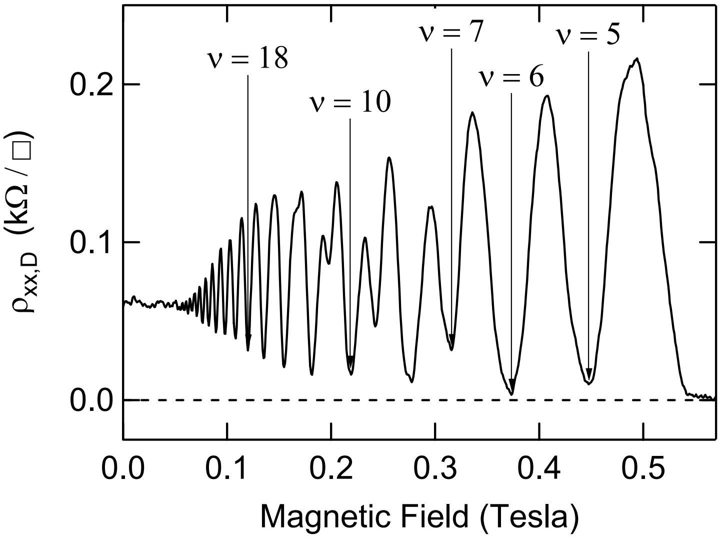

Figure H.1: Conventional transport measurement on sample 'Y' at nominal density. The locations of the minima can be used to determine the density of the sample. Some of the filling factors are identified. The odd filling factors correspond to spin-split Landau levels and have a smaller energy gap than the even filling factors, this is why they disappear above $\nu = 11$, where the thermal energy is comparable to the energy gap, but the even ones remain.

When the minima in magnetic field from Fig. H.1 are plotted against the inverse of the filling factor, a straight line results (see Figure H.2). If a straight line is not obtained, then the filling factors have been counted wrong.

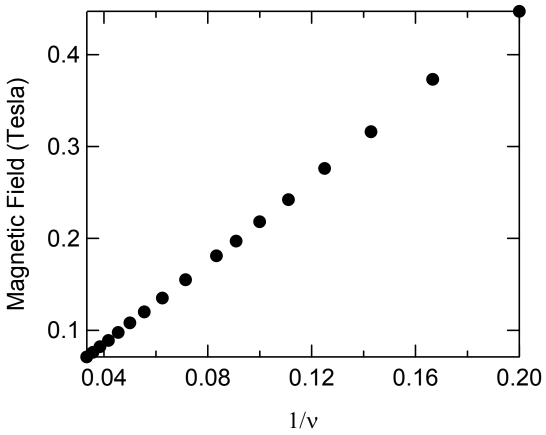

Figure H.2: The location of the minima in magnetic field taken from Figure H.1 are plotted versus the inverse of the filling factor. The slope of this line is directly proportional to the electron density.

The line shown in Fig. H.2 is fit by the function $B(T) = -0.0056T + 2.255\frac{1}{\nu}$. The offset comes from the fact that in our transport measurements we are ramping the current in the magnet, creating a small $\frac{dI}{dt}$ voltage which diverts some of the current through the shunt, and leads to an offset between the measured current and the actual magnetic field that's generated.

Comparing the slope of this line to the more useful version of equation (H.1):

$$B_{\min}(T) = 0.414 \times n(10^{10}\,\mathrm{cm}^{-2}) \times \frac{1}{\nu}, \tag{H.2}$$

and the density is found to be $n = 5.45 \times 10^{10}\,\text{cm}^{-2}$. Note that this is slightly higher than the nominal density for sample ‘Y’ quoted in this thesis, because this is the unbalanced nominal density, and we quoted the balanced nominal density.

The mobility is defined as $\mu = \frac{e\tau}{m^*}$ and is thus a direct measure of the momentum relaxation time τ. The mobility can be obtained by combining the electron density and the sample resistivity at zero magnetic field, which is $\rho_{xx} = 64\ \Omega/\square$ from Figure H.1, using the relation:

$$\mu\left(\frac{\text{cm}^2}{V \cdot s}\right) = \frac{1}{\rho_{xx}\left(\Omega/\square\right) e(C) n(\text{cm}^{-2})} \tag{H.3}$$

For this example the mobility is $\mu = 896{,}000\ \frac{\text{cm}^2}{V \cdot s}$.

* * *

Appendix I

HOW TO DETERMINE DENSITY IMBALANCE

Applying a bias voltage between the layers shifts charge from one layer to the other. The amount of charge that is transferred can be estimated by treating the two layers as a parallel plate capacitor with capacitance $C = \frac{A\varepsilon_0\kappa}{d}$, where ε_0 is the permittivity of free space, κ is the dielectric constant ($\kappa \sim 12.8$ in GaAs) and A is the layer area. Then

$$\Delta n \equiv n_1 - n_2 = \frac{Q}{eA} - \frac{-Q}{eA} = \frac{2Q}{eA} \tag{I.1}$$

where Q is the excess charge in the layer; this can be solved for using the basic capacitor formula $Q = CV$:

$$\Delta n = \frac{2Q}{eA} = \frac{2CV}{eA} = \frac{2A\varepsilon_0\kappa V}{deA} = \left(\frac{2\varepsilon_0\kappa}{de}\right)V \tag{I.2}$$

which gives a relationship between the bias voltage applied V and the resulting change in absolute density Δn. However, rather than relying on this equation, we can also measure this relation directly. This is how I determined $\frac{\Delta n}{n_T}$ for the data shown in this thesis.

Again we use the fact that the drag goes negative in the high Landau levels when the layers are imbalanced [1]. Specifically, it goes negative when the Landua level filling factor difference between the layers $\Delta\nu = \nu_1 - \nu_2$ is odd.

If a bias voltage is applied along with a small perpendicular magnetic field such that the drag is in a regime where the high Landau level Shubnikov-de Haas oscillations are strong, then $\Delta\nu$ can be determined by observing the oscillations as it changes from odd to even and back again, and then Δn can be inferred by the relation:

$$\frac{\Delta n}{n_T} = \frac{\Delta\nu}{\nu_1 + \nu_2}. \tag{I.3}$$

As an example, Figure I.1 shows data taken on sample 'K' at nominal (balanced) density in a perpendicular magnetic field $B = 0.129T$. When the bias voltage is zero, the Coulomb drag is in a Shubnikov-de Haas minimum with $\nu = 16$ in each layer. As an interlayer bias is applied, this minimum will go negative as $\Delta\nu$ approaches an odd number and will rise back up as $\Delta\nu$ becomes even. The peaks in Figure I.1 correspond to these even $\Delta\nu$. By noting the bias voltage separating the peaks and utilizing equation I.3, it can be found that $\frac{\Delta n}{n_T} = 0.050 \times \text{bias}(mV)$ for this density. This corresponds to a value of $d = 277\,\text{Å}$ in equation I.2, very close to our center-to-center well separation of $d = 280\,\text{Å}$.

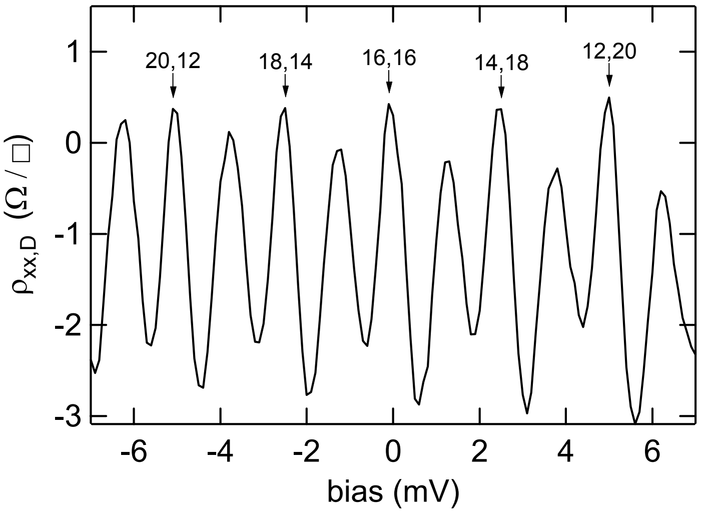

Figure I.1: Longitudinal drag resistivity versus interlayer bias at $n = 5.1\times10^{10}\,\mathrm{cm}^{-2}$ with $B = 0.129\ T$ taken at 0.3 K. The peaks occur when the filling factor in each layer differ by an even integer, the number pairs indicate the filling factor in each layer.

The same measurement can be done for the other densities, allowing us to convert from bias voltage to density imbalance at any density.

* * *

---

1 J.G.S. Lok, S. Kraus, M. Pohlt, K. Güven, W. Dietsche, K. von Klitzing, W. Wegscheider and M. Bichler, Physica B **298**, 135 (2001).

Appendix J

CHRONOLOGICAL LIST OF ALL 2D-2D COULOMB DRAG EXPERIMENT PAPERS PUBLISHED AS OF JUNE 15, 2004

1. T.J. Gramila, J.P. Eisenstein, A.H. MacDonald, L.N. Pfeiffer and K.W. West, "Mutual Friction between Parallel Two-Dimensional Systems," Phys. Rev. Lett. **66**, 1216 (March 4, 1991).
2. T.J. Gramila, J.P. Eisenstein, A.H. MacDonald, L.N. Pfeiffer and K.W. West, "Electron-Electron Scattering between Parallel 2-Dimensional Electron Gases," Surf. Sci. **263**, 446 (February 19, 1992).
3. U. Sivan, P.M. Solomon and H. Shtrikman, "Coupled Electron-Hole Transport," Phys. Rev. Lett. **68**, 1196 (February 24, 1992).
4. J.P.Eisenstein, "New Transport Phenomena in Coupled Quantum Wells," Superlattices and Microstructures **12**, 107 (September 1992).
5. T.J. Gramila, J.P. Eisenstein, A.H. MacDonald, L.N. Pfeiffer and K.W. West, "Evidence for Virtual-Phonon Exchange in Semiconductor Heterostructures," Phys. Rev. B **47**, 12957 (May 15, 1993).
6. T.J. Gramila, J.P. Eisenstein, A.H. MacDonald, L.N. Pfeiffer and K.W. West, "Measuring Electron-Electron Scattering Rates through Mutual Friction," Physica B **197**, 442 (March 1994).
7. H. Rubel, E.H. Linfield, D.A. Ritchie, K.M. Brown, M. Pepper and G.A.C. Jones, "Study of the Carrier Density Dependence of the Frictional Drag between Closely Spaced Two-Dimensional Electron Gases," Semicond. Sci. Technol. **10**, 1229 (September 1995).
8. N.P.R. Hill, J.T. Nicholls, E.H. Linfield, M. Pepper, D.A. Ritchie, A.R. Hamilton and G.A.C. Jones, "Frictional Drag between Parallel Two-Dimensional Electron Gases in a Perpendicular Magnetic Field," J. Phys.: Condens. Matter **8**, L557 (September 23, 1996).
9. H. Rubel, A. Fischer, W. Dietsche, K. von Klitzing and K. Eberl, "Observation of Screening in the Magneto-Coulomb Drag between Coupled Two-Dimensional Electron Systems," Phys. Rev. Lett. **78**, 1763 (March 3, 1997).

10. N.K. Patel, E.H. Linfield, K.M. Brown, M. Pepper, D.A. Ritchie and G.A.C. Jones, "Magnetic Field Studies of Coulomb Drag in a Coupled Double Quantum Well System," Semiconductor Science and Technology **12**, 309 (March 1997).
11. N.P.R. Hill, J.T. Nicholls, E.H. Linfield, M. Pepper, D.A. Ritchie, G.A.C. Jones, B.Y.K. Hu and K. Flensberg, "Correlation Effects on the Coupled Plasmon Modes of a Double Quantum Well," Phys. Rev. Lett. **78**, 2204 (March 17, 1997).
12. H. Rubel, A. Fischer, W. Dietsche, C. Jorger, K. von Klitzing and K. Eberl, "Magnetic Field Studies of the Frictional Drag between Two-Dimensional Electronic Systems - Coulomb versus Phonon Coupling," Physica E **1**, 160 (December 1997).
13. M.P. Lilly, J.P. Eisenstein, L.N. Pfeiffer and K.W. West, "Coulomb Drag in the Extreme Quantum Limit," Phys. Rev. Lett. **80**, 1714 (February 23, 1998).
14. H. Rubel, A. Fischer, W. Dietsche, C. Jorger, K. von Klitzing and K. Eberl, "The Frictional Drag between Coupled Two-Dimensional Electronic Systems in Magnetic Fields," Physica B **251**, 859 (June 1998).
15. N.P.R. Hill, J.T. Nicholls, E.H. Linfield, M. Pepper, D.A. Ritchie, B.Y.K. Hu and K. Flensberg, "Electron-Electron Scattering between Closely Spaced Two-Dimensional Electron Gases," Physica B **251**, 868 (June 1998).
16. X.G. Feng, S. Zelakiewicz, H. Noh, T.J. Ragucci, T.J. Gramila, L.N. Pfeiffer and K.W. West, "Negative Electron Drag and Holelike Behavior in the Integer Quantum Hall Regime," Phys. Rev. Lett. **81**, 3219 (October 12, 1998).
17. H. Noh, S. Zelakiewicz, X.G. Feng, T.J. Gramila, L.N. Pfeiffer and K.W. West, "Many-body Correlations Probed by Plasmon-Enhanced Drag Measurements in Double-Quantum-Well Structures," Phys. Rev. B **58**, 12621 (November 15, 1998).
18. C.H.W. Barnes, A.G. Davies, K.R. Zolleis, M.Y. Simmons and D.A. Ritchie, "Intrinsic Coupling Mechanisms between Two-Dimensional Electron Systems in Double Quantum Well Structures," Phys. Rev. B **59**, 7669 (March 15, 1999).
19. H. Noh, S. Zelakiewicz, T.J. Gramila, L.N. Pfeiffer and K.W. West, "Phonon-mediated Drag in Double Layer Two-Dimensional Electron Systems," Phys. Rev. B **59**, 13114 (May 15, 1999).
20. C. Jorger, S.J. Cheng, W. Dietsche, R. Gerhardts, P. Specht, K. Eberl and K. von Klitzing, "Frictional Drag between Coupled 2D Hole Gases in GaAs/AlGaAs Heterostructures," Physica E **6**, 598 (February 2000).
21. C. Jorger, S.J. Cheng, H. Rubel, W. Dietsche, R. Gerhardts, P. Specht, K. Eberl and K. von Klitzing, "Frictional Drag between Coupled Two-Dimensional Hole Gases in GaAs/Al0.3Ga0.7As Heterostructures," Phys. Rev. B **62**, 1572 (July 15, 2000).
22. S. Zelakiewicz, H. Noh, T.J. Gramila, L.N. Pfeiffer and K.W. West, "Missing $2k_F$ Response for Composite Fermions in Phonon Drag," Phys. Rev. Lett. **85**, 1942 (August 28, 2000).

23. J.G.S. Lok, S. Kraus, M. Pohlt, W. Dietsche, K. vonKlitzing, W. Wegscheider and M. Bichler, “Spin Effects in the Magnetodrag between Double Quantum Wells,” Phys. Rev. B **63**, 041305 (January 15, 2001).

24. J.G.S. Lok, S. Kraus, M. Pohlt, K. Guven, W. Dietsche, K. vonKlitzing, W. Wegscheider and M. Bichler, “Spin Anomalies in the Magneto-Drag between Double Layer 2DEGs,” Physica B **298**, 135 (April 2001).

25. J.G.S. Lok, S. Kraus, W. Dietsche, K. vonKlitzing, F. Schwerdt, M. Hauser, W. Wegscheider and M. Bichler, “Negative Magneto-drag of Double Layer 2DEGs,” Physica E **12**, 119 (January 2002).

26. M. Kellogg, I.B. Spielman, J.P. Eisenstein, L.N. Pfeiffer and K.W. West, “Observation of Quantized Hall Drag in a Strongly Correlated Bilayer Electron System,” Phys. Rev. Lett. **88**, 126804 (March 25, 2002).

27. R. Pillarisetty, H. Noh, D.C. Tsui, E.P. de Poortere, E. Tutuc and M. Shayegan, "Frictional Drag between Two Dilute Two-Dimensional Hole Layers,” Phys. Rev. Lett. **89**, 016805 (July 1, 2002).

28. M. Kellogg, J.P. Eisenstein, L.N. Pfeiffer and K.W. West, "Evidence for $2k_F$ Electron-Electron Scattering Processes in Coulomb Drag,” Solid State Communications **123**, 515 (October 7, 2002).

29. R. Pillarisetty, H. Noh, E. Tutuc, E.P. de Poortere, D.C. Tsui and M. Shayegan, “In-Plane Magnetodrag between Dilute Two-Dimensional Systems,” Phys. Rev. Lett. **90**, 226801 (June 6, 2003).

30. M. Kellogg, J.P. Eisenstein, L.N. Pfeiffer and K.W. West, "Bilayer Quantum Hall Systems at $\nu_T=1$: Coulomb Drag and the Transition from Weak to Strong Interlayer Coupling,” Phys. Rev. Lett. **90**, 246801 (June 20, 2003).

31. R. Pillarisetty, H. Noh, E. Tutuc, E.P. Poortere, D.C. Tsui and M. Shayegan, “Frictional Drag between Dilute Two-Dimensional Hole Systems,” Physica E **22**, 300 (April 2004).

32. K. Muraki, J.G.S. Lok, S. Kraus, W. Dietsche, K. von Klitzing, D. Schuh, M. Bichler and W. Wegscheider, “Coulomb Drag as a Probe of the Nature of Compressible States in a Magnetic Field,” Phys. Rev. Lett. **92**, 246801 (June 15, 2004).

* * *

Appendix K

FORTRAN CODE

There are 4 Fortran programs in this appendix*:

CoulombDragforCosineWells is the most basic program, it calculates the drag for GaAs electrons (m* = 0.067), assuming their wavefunctions take on a cosine shape in the wells (this is a pretty good assumption). This program numerically integrates equation 2.29 for layer separation d, well width w, density in layer 1 n_1, density in layer 2 n_2, and temperature T as input by the user.

CoulombDragusingFormFactors is the same as "CoulombDragforCosineWells," except that instead of assuming a cosine wavefunction, this program uses the form factors (see Jauho & Smith [1] for discussion of form factors) specific to the DQW system. Before running this program, the program "dqwbiasandform" must be run first.

dqwbiasandform is a program written by Jim Eisenstein which calculates the electronic wavefunction for user-specified DQW parameters. I have modified this program so that it also computes the form factors and outputs them into two files named 'g11' and 'g12'. "CoulombDragusingFormFactors" will need to read these files in order to run. The form factors are dependent upon the *average* density of the system. So, it is important to run "dqwbiasandform" for each new *average* density calculated.

---

* These programs can be obtained at my website: http://www.its.caltech.edu/~mk/Coulomb_Drag.html.

HoleDragforCosineWells this program is the same as “CoulombDragforCosineWells,” except that it allows the user to choose the effective mass of the electron (or hole). This greater freedom makes for a slightly less user-friendly program though.

KNOWN PROBLEMS AND ISSUES:

1. Sometimes the integration algorithm will produce a 'bad' data point or two. This will be obvious when the data is plotted, as these bad points are off by a large amount! You will notice that these bad points are often calculated much faster than the neighboring data points. The only way to correct for this problem is to run the program again, just for that one point, at a much higher precision (this option is given to you when you run the program). You must then replace the bad data point with the new one.

2. These programs need to be linked to "smaths.lib" and "smathd.lib" in order to run. You must add these links to the workspace that you run the program from. Add these links under Project:Settings:Link.

* * *

---

1 A.P. Jauho and H. Smith, Phys. Rev. B **47**, 4420 (1993).

Program #1: <u>CoulombDragforCosineWells</u>

```
*
*  PROGRAM CoulombDragforCosineWells.f
*
*  Integrates 4D boltzmann formulation for the drag, as given in
*  a paper by Jauho & Smith PRB 47,4420, assuming the electron
*  wavefunction is a cosine (as is used in the paper).
*  This program will output either CD vs. T, or CD vs. delta(n)/<n>
*  for a given <n> (density per layer), d (center-to-center layer
*  separation), w (well width), and in T (temperature).
*
*  This program only calculates the drag for electrons with
*  m* = 0.067m_0  - the effective mass of electrons in GaAs.
*  And kappa is set to 12.8.
*
    INTEGER MAXFCN,N,I,J,dragtype,loop
    real time1,time2
    character filename*25,fdt1*56,fdt2*23,temp*3,header*80,stime*8
    character precisionvariable*12, dragtypename*21
    double precision
    A(4),B(4),RESULT,F,ERREST1,ERRABS,ERRREL,RESULT1
    double precision L,ERREST2,deltat,tend,n1r,n2r,kf1,kf2,kfmax
    double precision nave,deltanend,errnumber,deltan,dr,wr,pi
    double precision tf1,tf2,tfmax
    double precision n1,n2,w,d,t
    EXTERNAL F,DQAND
    common n1,n2,w,d,t

    pi=3.1415927
    N = 4
    MAXFCN = 2100000000
    ERRABS=0.0

*  choose 'CD vs. T' or 'CD vs. delta n' option
    PRINT *,"
10  PRINT *,'Enter the number "0" if you wish to calculate Drag vs. T;'
    PRINT *,'or "1" if you wish to calculate Drag vs. delta(n)/<n>:'
    PRINT *, "
    READ *,dragtype

     IF (dragtype == 0) THEN
     dragtypename = 'Drag vs. T'
     ELSE IF (dragtype == 1) THEN
```

```
       dragtypename = 'Drag vs. delta(n)/<n>'
       ELSE
       PRINT *, "
       PRINT *, 'You must choose either 0 or 1, please try again.'
       PRINT *, "
       GOTO 10
       END IF

      PRINT *, "
      PRINT *, 'You have chosen:'
      PRINT 44, dragtypename
44    FORMAT (A40)
      PRINT *,""
*  get n,d,w,T etc. as needed, and automatically set errrel from these - allow
*  the option of autochoose errrel or choose it manually.  Then it's up to the user to
*  understand how to choose them.

       IF (dragtype == 0) THEN
               PRINT *,"
               PRINT *,'Start temperature in K:'
               PRINT *, "
               READ *,t
               PRINT *,"
               PRINT *,'Temperature steps in delta K:'
               PRINT *, "
               READ *,deltat
               PRINT *,"
               PRINT *,'End temperature in K:'
               PRINT *, "
               READ *,tend
               PRINT *,"
               PRINT *,'Density in layer 1 (in units of 10^10 cm^-2):'
               PRINT *, "
               READ *,n1r
               PRINT *,"
               PRINT *,'Density in layer 2 (in units of 10^10 cm^-2):'
               PRINT *, "
               READ *,n2r
       ELSE
               PRINT *,"
               PRINT *,'Average density per layer <n> (x10^10 cm^-2):'
               PRINT *, "
               READ *,nave
               PRINT *,"
               PRINT *,'delta(n) per layer steps (in units of 10^10 cm^-2):'
```

```
              PRINT *, ''
              READ *,deltan
              PRINT *,''
              PRINT *,'delta(n)/<n> max (e.g., 0.6):'
              PRINT *, ''
              READ *,deltanend
              PRINT *,''
              PRINT *,'Temperature in K:'
              PRINT *, ''
              READ *,t
       END IF

      PRINT *,''
      PRINT *,'center-to-center layer separation, d, (in Angstroms):'
      PRINT *, ''
      READ *,dr
      PRINT *,''
      PRINT *,'well width, w, (in Angstroms):'
      PRINT *, ''
      READ *,wr

      IF (dragtype == 0) THEN
              ERRREL = 0.02
      ELSE
              ERRREL = 0.01
      ENDIF

* set parameters to their MKS units
      d = dr*1D-10
      w = wr*1D-10
      IF (dragtype == 0) THEN
       n1 = n1r*1D14
       n2 = n2r*1D14
      ELSE
       n1 = nave*1D14
       n2 = nave*1D14
      ENDIF

* and determine k_fermi and T_fermi for setting L:
      kf1 = sqrt(2*pi*n1)
      kf2 = sqrt(2*pi*n2)
      kfmax = max(kf1,kf2)
      tf1 = 4.15D-14*n1
      tf2 = 4.15D-14*n2
      tfmax = max(tf1,tf2)
```

```
*  Now choose to have 'ERRREL' set automatically or by hand:
     PRINT *,"
     PRINT *,'If you wish to set the precision of the calcualtion'
     PRINT *,'yourself, type in "man".  Type in anything else and'
     PRINT *,'the precision will be assigned automatically.'
     PRINT *, "
     READ *,precisionvariable
      IF (precisionvariable == 'man') THEN
                PRINT *,"
                PRINT *,'For ', dragtypename, ' the error variable "ERRREL" '
                PRINT 46,'is set to', ERRREL,'.  For higher precision (but'
46              FORMAT (A10,F6.2,A28)
                PRINT *,'longer computation time) type in a SMALLER number.'
                PRINT *, 'For less precision, but faster computation time'
                PRINT *,'type in a LARGER number (but keep it < 1).'
                PRINT *,'(to learn more about "ERRREL", see "DQAND" '
                PRINT *,'in IMSL library).  Enter error precision now:'
                PRINT *, "
                READ *,ERRREL
      ELSE
      ENDIF

     PRINT *,"
45   FORMAT (A19,F8.3)
     PRINT 45,'ERRREL is set to: ', ERRREL
     PRINT *,"


*  get filename
     PRINT *,"
     PRINT *,'This program will put the results of the calculations'
     PRINT *,'in a subdirectory of your current folder.  The'
     PRINT *,'subdirectory will be called "output" (you may need to'
     PRINT *,'create this yourself).  You must choose a file name'
     PRINT *,'for each run of this program.'
     PRINT *,"
     PRINT *,'What filename do you wish to use?'
     PRINT *,"
     READ *,filename
     fdt2 = 'output\'//filename
     open(2,FILE=fdt2)

*  write header information to file
```

```
      WRITE (2,33),dragtypename
33  FORMAT (",A36)
      WRITE (2,'(A20)') (")
      WRITE (2,'(A42)') 'For GaAs electrons (m*=0.067, kappa=12.8),'
      WRITE (2,34) 'd =',dr,'A, w =',wr,'A.  Cosine wavefunction.'
34  FORMAT (A3,F6.1,A8,F6.1,A25)
      IF (dragtype == 0) THEN
      WRITE (2,36) 'n1 =',n1r,', n2 =',n2r,' x 10^10 cm^(-2)'
36  FORMAT (A4,F5.2,A6,F5.2,A16)
      ELSE
      WRITE (2,37) 'T =',t,'K.  n1, n2 are in MKS units (m^-2).'
37  FORMAT (A3,F6.2,A35)
      ENDIF


*  this calculates the number of times to run the do loop
      IF (dragtype == 0) THEN
       loop = nint((tend -t)/deltat)+1
      ELSE
       loop = nint((deltanend*nave)/(2*deltan))+1
      ENDIF


      PRINT *,"
      CALL TIME(stime)
      PRINT *,'start time: ',stime
      PRINT *,"
      PRINT 47, 'd =',dr,' Angstroms'
47  FORMAT (A4,F6.1,A10)
      PRINT 47, 'w =',wr,' Angstroms'
      IF (dragtype == 0) THEN
       PRINT 48, 'n1 =',n1r,' x 10^10 cm^-2'
       PRINT 48, 'n2 =',n2r,' x 10^10 cm^-2'
48   FORMAT (A5,F6.2,A14)
       PRINT *,'  K','       Ohms    ','error   ','elapsed seconds'
       WRITE (2,'(A20)') (")
       WRITE (2,'(A42)'),' K       Ohms           error        sec'
      ELSE
       PRINT 49, 'T =',t,'K'
49   FORMAT (A4,F6.2,A2)
       PRINT 445,'n1        n2','Ohms','error','seconds'
445 FORMAT (",A14,A14,A11,A15)
       WRITE (2,'(A20)') (")
450 FORMAT (",A7,A10,A12,A16,A12,A7)
       WRITE (2,450),'n1','n2','ohms','error','sec','deltan'
      ENDIF


      DO 7, I=1,loop

*  This sets the integration limits, and calls the integration
*  program (DQAND) from the IMSL library, and solves the integral
*
* SET APPROPRIATE LIMITS (L) FOR THE TEMPERATURE
      IF (t .LE. tfmax/10) THEN
      L = 2*kfmax
      ELSE IF (tfmax/10 .LT. t .LE. tfmax/6.5) THEN
      L = 3*kfmax
      ELSE IF (tfmax/6.5 .LT. t .LE. tfmax/4.5) THEN
      L = 4*kfmax
      ELSE
      L = 5*kfmax
      END IF

      A = (/0.0D8,0.0D8,-L,0.0D8/)
      B = (/L,L,0.0D8,L/)

      CALL CPU_TIME(time1)
      CALL DQAND(F,N,A,B,ERRABS,ERRREL,MAXFCN,RESULT,ERREST1)
      RESULT1 = RESULT

      A = (/0.0,0.0,0.0,0.0/)
      B = (/L,L,L,L/)

      CALL DQAND(F,N,A,B,ERRABS,ERRREL,MAXFCN,RESULT,ERREST2)
      CALL CPU_TIME(time2)

       IF (dragtype == 0) THEN
      PRINT
      100,t,RESULT+RESULT1,SQRT(ERREST1**2+ERREST2**2),time2-time1
100FORMAT      (",F5.1,F11.4,E14.4,F8.1)
      WRITE (2, 20),t,RESULT+RESULT1,SQRT(ERREST1**2+ERREST2**2),
     &time2-time1
20  FORMAT (F5.1,E15.4,E14.4,F9.1)
       ELSE
      PRINT 101,n1,n2,RESULT+RESULT1,SQRT(ERREST1**2+ERREST2**2),
     &time2-time1
101FORMAT      (",2E9.2,F11.4,E14.4,F9.1)
      WRITE (2,
      21),n1,n2,RESULT+RESULT1,SQRT(ERREST1**2+ERREST2**2),
     &time2-time1,(2*(n1-n2)/(n1+n2))
21   FORMAT (E10.3,E10.3,E13.6,E14.4,F10.1,F8.5)
      ENDIF

* increment the temperature or the delta n
     IF (dragtype == 0) THEN
     t = t + deltat
     ELSE
     n1 = n1 + deltan*1D14
     n2 = n2 - deltan*1D14
     ENDIF

    7CONTINUE

     END


     double precision FUNCTION F(N,X)
     integer N
     double precision X(N),qtf,kb,tf1,tf2,k
     double precision a,kappa,Const,pi,m,Const2
     double precision n1,n2,w,d,t
     common n1,n2,w,d,t


     tf1 = 4.15D-14*n1
     tf2 = 4.15D-14*n2
     kappa = 12.8
     qtf = 1.977D8
     pi = 3.1415927
     m = (1/(4*pi*pi)-1/3.0+1/(pi*pi))
     kb = 1.381D-23
*  a is m* e^2/pi^2 kb h_bar qtf^4 (4 pi epsilon)^2
     a = 5.76361D-27
*  k is (h_bar)^2/2 m*
     k = 9.1187D-38


     Const = a / (kappa*kappa*n1*n2*t)
     Const2 = qtf*qtf*Const

*  Here is the integrand (X{} = k1y,k1'x,k1'y,k2perp):
     IF (sqrt(X(2)**2+(X(3)-X(1))**2) .GE. 0.0) THEN

     F= Const*X(1)*(sqrt(X(2)**2+(X(3)-X(1))**2))**3*(EXP((k*(X(1)**2)
&-kb*tf1)/(kb*t))+1)**(-1)*(1-(EXP((k*(X(2)**2+X(3)**2)-kb*tf1)
&/(kb*t))+1)**(-1))*(EXP((k*(X(4)**2+(X(2)**2+(X(3)-X(1))**2)
&/4+((X(1)**2-X(2)**2-X(3)**2)**2/(4*(X(2)**2+(X(3)-X(1))**2))
&-(X(1)**2-X(2)**2-X(3)**2)/2))-kb*tf2)/(kb*t))+1)**
&(-1)*(1-(EXP((k*(X(4)**2+(X(2)**2+(X(3)-X(1))**2)/4+(X(1)**2
&-X(2)**2-X(3)**2)/2+(X(1)**2-X(2)**2-X(3)**2)**2/(4*(X(2)**2
&+(X(3)-X(1))**2)))-kb*tf2)/(kb*t))+1)**(-1))*(EXP
&(sqrt(X(2)**2+(X(3)-X(1))**2)*d)*(sinh(sqrt(X(2)
&**2+(X(3)-X(1))**2)*w/2))**(-2)*(8*pi*pi/(sqrt(X(2)**2+(X(3)-X(1))
&**2)*w*(4*pi*pi+(X(2)**2+(X(3)-X(1))**2)*w*w)))**(-2)
&*((2/(sqrt(X(2)**2+(X(3)-
&X(1))**2)*w)-EXP(-sqrt(X(2)**2+(X(3)-X(1))**2)*w/2)*
&sinh(sqrt(X(2)**2+(X(3)-X(1))**2)*w/2)*(8*pi*pi/
&(sqrt(X(2)**2+(X(3)-X(1))**2)*w*(4*pi*pi+(X(2)**2+(X(3)-X(1))**2)
&*w*w)))**2+sqrt(X(2)**2+(X(3)-X(1))**2)*w/(4*pi*pi+
&(X(2)**2+(X(3)-X(1))**2)*w*w))+sqrt(X(2)**2+(X(3)-X(1))**2)
&/qtf)**2-EXP(-d*sqrt(X(2)**2+(X(3)-X(1))**2))*(sinh(sqrt(X(2)
&**2+(X(3)-X(1))**2)*w/2))**2*(8*pi*pi/(sqrt(X(2)**2+(X(3)-X(1))
&**2)*w*(4*pi*pi+(X(2)**2+(X(3)-X(1))**2)*w*w)))**2)**(-2)

 ELSE

 F= Const2*X(1)*(sqrt(X(2)**2+(X(3)-X(1))**2))*(EXP((k*(X(1)**2)
&-kb*tf1)/(kb*t))+1)**(-1)*(1-(EXP((k*(X(2)**2+X(3)**2)-kb*tf1)
&/(kb*t))+1)**(-1))*(EXP((k*(X(4)**2+(X(2)**2+(X(3)-X(1))**2)
&/4+((X(1)**2-X(2)**2-X(3)**2)**2/(4*(X(2)**2+(X(3)-X(1))**2))
&-(X(1)**2-X(2)**2-X(3)**2)/2))-kb*tf2)/(kb*t))+1)**
&(-1)*(1-(EXP((k*(X(4)**2+(X(2)**2+(X(3)-X(1))**2)/4+(X(1)**2
&-X(2)**2-X(3)**2)/2+(X(1)**2-X(2)**2-X(3)**2)**2/(4*(X(2)**2
&+(X(3)-X(1))**2)))-kb*tf2)/(kb*t))+1)**(-1))*(2*d*qtf+2*w*qtf*m
&*(1+sqrt(X(2)**2+(X(3)-X(1))**2)*d+sqrt(X(2)**2+(X(3)-X(1))**2)
&/qtf)+2+2*sqrt(X(2)**2+(X(3)-X(1))**2)*d+sqrt(X(2)**2+(X(3)-X(1)
&)**2)/qtf+sqrt(X(2)**2+(X(3)-X(1))**2)*qtf*w*w*m*m)**(-2)
 ENDIF

 RETURN
 END
```

Program #2: CoulombDragusingFormFactors

```
*
*  PROGRAM CoulombDragusingFormFactors.f
*
*  Integrates 4D boltzmann formulation for the drag, as given in
*  a paper by Jauho & Smith PRB 47,4420, using form factors calculated
*  for our wells (this is discussed in the paper).  You must run the
*  program 'dqwbiasandform' to generate the form factor files.
*  This program will output either CD vs. T, or CD vs. delta(n)/<n>.
*
*  This program only calculates the drag for electrons with
*  m* = 0.067m_0  - the effective mass of electrons in GaAs.
*  And kappa is set to 12.8.
*
      INTEGER MAXFCN,N,I,J,dragtype,loop,k
      real time1,time2
      character filename*25,fdt1*56,fdt2*23,temp*3,header*80(7),stime*8
      character precisionvariable*12, dragtypename*21
      double precision A(4),B(4),RESULT,F,ERREST1,ERRABS,ERRREL,RESULT1
      double precision L,ERREST2,deltat,tend,n1r,n2r,kf1,kf2,kfmax
      double precision nave,deltanend,errnumber,deltan,pi
      double precision tf1,tf2,tfmax
      double precision n1,n2,t, g11(2000),g12(2000)
      EXTERNAL F,DQAND
      common n1,n2,t,g11,g12

      pi=3.1415927
      N = 4
      MAXFCN = 2100000000
      ERRABS=0.0

*  inform user that they must run 'dqwbiasandform' first
      PRINT *,'Please note:'
      PRINT *,'You must run the program "dqwbiasandform" before'
      PRINT *,'running this program.  "dqwbiasandform" is a program'
      PRINT *,'Jim wrote which calculates the electron wavefunction'
      PRINT *,'for a specified DQW system.  Mindy has modified this'
      PRINT *,'program so that it will create files that contain'
      PRINT *,'the form factors g11 and g12 (see Jauho & Smith, PRB'
      PRINT *,'47, 4420 for more information on form factors).  This'
      PRINT *,'program will need to read those files.  The form factors'
      PRINT *,'are dependent on the average electron density, so new'
      PRINT *,'files must be generated when you wish to run the program'
```

```
     PRINT *,'for a new density.'
     PRINT *,''

*  choose 'CD vs. T' or 'CD vs. delta n' option
     PRINT *,''
10  PRINT *,'Enter the number "0" if you wish to calculate Drag vs. T;'
     PRINT *,'or "1" if you wish to calculate Drag vs. delta(n)/<n>:'
     PRINT *, ''
     READ *,dragtype

      IF (dragtype == 0) THEN
      dragtypename = 'Drag vs. T'
      ELSE IF (dragtype == 1) THEN
      dragtypename = 'Drag vs. delta(n)/<n>'
      ELSE
      PRINT *, ''
      PRINT *, 'You must choose either 0 or 1, please try again.'
      PRINT *, ''
      GOTO 10
      END IF

     PRINT *, ''
     PRINT *, 'You have chosen:'
     PRINT 44, dragtypename
44  FORMAT (A40)
     PRINT *,""

*  get n,d,w,T etc. as needed, and automatically set errrel from these - allow
*  the option of autochoose errrel or choose it manually.  Then it's up to the user to
*  understand how to choose them.

      IF (dragtype == 0) THEN
                PRINT *,''
                PRINT *,'Start temperature in K:'
                PRINT *, ''
                READ *,t
                PRINT *,''
                PRINT *,'Temperature steps in delta K:'
                PRINT *, ''
                READ *,deltat
                PRINT *,''
                PRINT *,'End temperature in K:'
                PRINT *, ''
                READ *,tend
                PRINT *,''
                PRINT *,'Density in layer 1 (in units of 10^10 cm^-2):'
                PRINT *, "
                READ *,n1r
                PRINT *,"
                PRINT *,'Density in layer 2 (in units of 10^10 cm^-2):'
                PRINT *, "
                READ *,n2r
       ELSE
                PRINT *,"
                PRINT *,'Average density per layer <n> (x10^10 cm^-2):'
                PRINT *, "
                READ *,nave
                PRINT *,"
                PRINT *,'delta(n) per layer steps (in units of 10^10 cm^-2):'
                PRINT *, "
                READ *,deltan
                PRINT *,"
                PRINT *,'delta(n)/<n> max (e.g., 0.6):'
                PRINT *, "
                READ *,deltanend
                PRINT *,"
                PRINT *,'Temperature in K:'
                PRINT *, "
                READ *,t
       END IF


      IF (dragtype == 0) THEN
                ERRREL = 0.02
      ELSE
                ERRREL = 0.01
      ENDIF

* set parameters to their MKS units
      IF (dragtype == 0) THEN
       n1 = n1r*1D14
       n2 = n2r*1D14
      ELSE
       n1 = nave*1D14
       n2 = nave*1D14
      ENDIF

* and determine k_fermi and T_fermi for setting L:
      kf1 = sqrt(2*pi*n1)
      kf2 = sqrt(2*pi*n2)
      kfmax = max(kf1,kf2)
      tf1 = 4.15D-14*n1
      tf2 = 4.15D-14*n2
      tfmax = max(tf1,tf2)


*  Now choose to have 'ERRREL' set automatically or by hand:
      PRINT *,"
      PRINT *,'If you wish to set the precision of the calcualtion'
      PRINT *,'yourself, type in "man".  Type in anything else and'
      PRINT *,'the precision will be assigned automatically.'
      PRINT *, "
      READ *,precisionvariable
       IF (precisionvariable == 'man') THEN
               PRINT *,"
               PRINT *,'For ', dragtypename, ' the error variable "ERRREL" '
               PRINT 46,'is set to', ERRREL,'.  For higher precision (but'
46             FORMAT (A10,F6.2,A28)
               PRINT *,'longer computation time) type in a SMALLER number.'
               PRINT *, 'For less precision, but faster computation time'
               PRINT *,'type in a LARGER number (but keep it < 1).'
               PRINT *,'(to learn more about "ERRREL", see "DQAND" '
               PRINT *,'in IMSL library).  Enter error precision now:'
               PRINT *, "
               READ *,ERRREL
       ELSE
       ENDIF

      PRINT *,"
45    FORMAT (A19,F8.3)
      PRINT 45,'ERRREL is set to: ', ERRREL
      PRINT *,"


*  get filename
      PRINT *,"
      PRINT *,'This program will put the results of the calculations'
      PRINT *,'in a subdirectory of your current folder.  The'
      PRINT *,'subdirectory will be called "output" (you may need to'
      PRINT *,'create this yourself).  You must choose a file name'
      PRINT *,'for each run of this program.'
      PRINT *,"
      PRINT *,'What filename do you wish to use?'
      PRINT *,"
      READ *,filename
```

```
     fdt2 = 'output\'//filename
     open(2,FILE=fdt2)

*  write header information to file
     WRITE (2,33),dragtypename
33  FORMAT ('',A36)
     WRITE (2,'(A20)') ('')
     WRITE (2,'(A42)') 'For GaAs electrons (m*=0.067, kappa=12.8),'
     WRITE (2,'(A46)') 'Form factors calculated from "dqwbiasandform":'
      open(96,FILE='header',FORM='formatted',STATUS='old')
      READ (96,'(A80)'), (header(i),i=1,7)
      close (96)
     DO 606  k=1,7
      WRITE (2,'(A80)') header(k)
606CONTINUE
     WRITE (2,'(A20)') ('')
     IF (dragtype == 0) THEN
     WRITE (2,36) 'n1 =',n1r,', n2 =',n2r,' x 10^10 cm^(-2)'
36  FORMAT (A4,F5.2,A6,F5.2,A16)
     ELSE
     WRITE (2,37) 'T =',t,'K.  n1, n2 are in MKS units (m^-2).'
37  FORMAT (A3,F6.2,A35)
     ENDIF


*  this calculates the number of times to run the do loop
     IF (dragtype == 0) THEN
      loop = nint((tend -t)/deltat)+1
     ELSE
      loop = nint((deltanend*nave)/(2*deltan))+1
     ENDIF


*  get the form factors loaded into arrays
     open(99,FILE='g12',FORM='formatted',STATUS='old')
     READ (99,140) (g12(i),i=1,2000)
     close (99)
     open(98,FILE='g11',FORM='formatted',STATUS='old')
     READ (98,140) (g11(i),i=1,2000)
     close (98)
140   FORMAT (2000(E12.6))

     PRINT *,''
     CALL TIME(stime)
     PRINT *,'start time: ',stime
```

```
      PRINT *,''

      IF (dragtype == 0) THEN
       PRINT 48, 'n1 =',n1r,' x 10^10 cm^-2'
       PRINT 48, 'n2 =',n2r,' x 10^10 cm^-2'
48     FORMAT (A5,F6.2,A14)
       PRINT *,'  K','       Ohms    ','error    ','elapsed seconds'
       WRITE (2,'(A20)') ('')
       WRITE (2,'(A42)'),' K       Ohms           error        sec'
      ELSE
       PRINT 49, 'T =',t,'K'
49     FORMAT (A4,F6.2,A2)
       PRINT 445,'n1       n2','Ohms','error','seconds'
445    FORMAT ('',A14,A14,A11,A15)
       WRITE (2,'(A20)') ('')
450    FORMAT ('',A7,A10,A12,A16,A12,A7)
       WRITE (2,450),'n1','n2','ohms','error','sec','deltan'
      ENDIF


      DO 7, I=1,loop

*  This sets the integration limits, and calls the integration
*  program (DQAND) from the IMSL library, and solves the integral
*
* SET APPROPRIATE LIMITS (L) FOR THE TEMPERATURE
      IF (t .LE. tfmax/10) THEN
      L = 2*kfmax
      ELSE IF (tfmax/10 .LT. t .LE. tfmax/6.5) THEN
      L = 3*kfmax
      ELSE IF (tfmax/6.5 .LT. t .LE. tfmax/4.5) THEN
      L = 4*kfmax
      ELSE
      L = 5*kfmax
      END IF

      A = (/0.0D8,0.0D8,-L,0.0D8/)
      B = (/L,L,0.0D8,L/)

      CALL CPU_TIME(time1)
      CALL DQAND(F,N,A,B,ERRABS,ERRREL,MAXFCN,RESULT,ERREST1)
      RESULT1 = RESULT

      A = (/0.0,0.0,0.0,0.0/)
      B = (/L,L,L,L/)
      CALL DQAND(F,N,A,B,ERRABS,ERRREL,MAXFCN,RESULT,ERREST2)
      CALL CPU_TIME(time2)

       IF (dragtype == 0) THEN
      PRINT 100,t,RESULT+RESULT1,SQRT(ERREST1**2+ERREST2**2),time2-time1
100   FORMAT      (",F5.1,F11.4,E14.4,F8.1)
      WRITE (2, 20),t,RESULT+RESULT1,SQRT(ERREST1**2+ERREST2**2),
     &time2-time1
20    FORMAT (F5.1,E15.4,E14.4,F9.1)
       ELSE
      PRINT 101,n1,n2,RESULT+RESULT1,SQRT(ERREST1**2+ERREST2**2),
     &time2-time1
101   FORMAT      (",2E9.2,F11.4,E14.4,F9.1)
      WRITE (2, 21),n1,n2,RESULT+RESULT1,SQRT(ERREST1**2+ERREST2**2),
     &time2-time1,(2*(n1-n2)/(n1+n2))
21    FORMAT (E10.3,E10.3,E13.6,E14.4,F10.1,F8.5)
       ENDIF

* increment the temperature or the delta n
      IF (dragtype == 0) THEN
      t = t + deltat
      ELSE
      n1 = n1 + deltan*1D14
      n2 = n2 - deltan*1D14
      ENDIF

    7CONTINUE

      END


      double precision FUNCTION F(N,X)
      integer N
      double precision X(N),qtf,kb,tf1,tf2,k
      double precision a,kappa,Const,pi,m,Const2
      double precision n1,n2,t,g11(2000),g12(2000)
      common n1,n2,t,g11,g12

      tf1 = 4.15D-14*n1
      tf2 = 4.15D-14*n2
      kappa = 12.8
      qtf = 1.977D8
      pi = 3.1415927
      kb = 1.381D-23
```

```
*  a is m* e^2/pi^2 kb h_bar qtf^4 (4 pi epsilon)^2
     a = 5.76361D-27
*  k is (h_bar)^2/2 m*
     k = 9.1187D-38

     Const = a / (kappa*kappa*n1*n2*t)


*  Here is the integrand (X{} = k1y,k1'x,k1'y,k2perp):
     F= Const*X(1)*(sqrt(X(2)**2+(X(3)-X(1))**2))**3*(EXP((k*(X(1)**2)
    &-kb*tf1)/(kb*t))+1)**(-1)*(1-(EXP((k*(X(2)**2+X(3)**2)-kb*tf1)
    &/(kb*t))+1)**(-1))*(EXP((k*(X(4)**2+(X(2)**2+(X(3)-X(1))**2)
    &/4+((X(1)**2-X(2)**2-X(3)**2)**2/(4*(X(2)**2+(X(3)-X(1))**2))
    &-(X(1)**2-X(2)**2-X(3)**2)/2))-kb*tf2)/(kb*t))+1)**
    &(-1)*(1-(EXP((k*(X(4)**2+(X(2)**2+(X(3)-X(1))**2)/4+(X(1)**2
    &-X(2)**2-X(3)**2)/2+(X(1)**2-X(2)**2-X(3)**2)**2/(4*(X(2)**2
    &+(X(3)-X(1))**2)))-kb*tf2)/(kb*t))+1)**(-1))*((g12(nint(2*sqrt
    &(X(2)**2+(X(3)-X(1))**2)/1D6)+1))**(-1)*(g11(nint(2*sqrt(X(2)**2
    &+(X(3)-X(1))**2)/1D6)+1)+sqrt(X(2)**2+(X(3)-X(1))**2)
    &/qtf)**2-g12(nint(2*sqrt(X(2)**2+(X(3)-X(1))**2)/1D6)+1))**(-2)

     RETURN
     END
```

Program #3: dqwbiasandform

```
c..
c.. ***************** PROGRAM DQWBIASANDFORM *************
c..
c.. This program does the same as DQWBIAS, but it also calculates
c.. the form factors g_11(q) and g_12(q).  q will range from 0 to
c.. 1x10^9 in 5x10^5 steps (units are 1/m^2).
c..
c.. Selfconsistent DQW solver allowing a finite bias voltage
c.. between the layers.
c..
c.. This program solves the Poisson and Schroedinger equations for
c.. DQW using the local density approximation for the
c.. exchange/correlation energy.
c..
      EXTERNAL FUNC
      real ynt(2),y(2,1000),x(1000),psi(1000),psisq(1000),psisql(1000)
      real psisqr(1000),g11(2000),g12(2000)
      real v(1000),vf(1000),vs(1000),vxc(1000)
      real zpsisq(1000),zzpsisq(1000)
      real ns,nd,nsr,nsl,ndl,ndr,nmean,mufr,mufl
      real zavl,zavr,zrmsl,zrmsr, dw
      double precision sum11,sum12,element11
      double precision element12
      real xx(100),slp(100),dd(100)
      integer i,j,q
      character filename*18,fdt*60,fg11*60,fg12*60
      common /blk2/a,b,h,v
      common /blk3/c1,c2
      common /blk4/npt
      pi=3.14159
c..
c.. For GaAs:     m=0.067, k=12.6
c..
c..   All energies in meV, all distances in angstroms, all
c..   sheet densities in units of 1e10 per cm^2.
c..
c..     c1 = 2*m/hbar^2 = 1.757e-5
c..     c2 = e^2/epsilon0/kappa = 0.01436
c..
c..     Bohr radius a0 = 99.63 angstroms
c..     Rydberg energy = ryd = 5.734 meV
c..
```

```
c..
      c1=1.757e-5
      c2=.01436
      a0=99.63
      c3=1e-6*(4*pi/3)*a0**3
      c5=a0*c2/4.
      ryd=5.734
      beta=1.2218
c..
c..
*     PRINT *,'Filename to store extraneous program output:'
*     READ *,filename
      fdt = 'header'
      open (unit=9,file=fdt)
      print *,'well width (A) ='
      read *,w
      write (9,151) w
151   format ('* well width (A)= ',f5.1)
      print *,'barrier width (A) ='
      read *,wb
       write (9,152) wb
152   format ('* barrier width (A)= ',f5.1)
      print *,'barrier height (meV) ='
      read *,vdisc1
      write (9,153) vdisc1
153   format ('* barrier height (meV)= ',f5.1)
      print *,'cladding barrier height (meV)='
      read *,vdisc2
      write (9,154) vdisc2
154   format ('* cladding barrier height (meV)= ',f5.1)
      print *,'Inclusion of LDA exchange/correlation (0 or 1) ='
      read *,xc
      write (9,155) xc
155   format ('* LDA exchange/correlation [1=on, 0=off] ',f2.0)
      print *,'right side donor density ndr ='
      read *,ndr
      write (9,156) ndr
156   format ('* right side donor density (10^10) = ',f5.2)
      print *,'left side donor density ndl='
      read *,ndl
      print *,'Interlayer bias voltage (mV) ='
      read *,vlr
      write (9,157) vlr
157   format('* interlayer bias voltage (mV)=',f6.3)
      print *,'Convergence diagnostics? (0 or 1)'
      read *,ndiag
*       write (9,160)
*       write (9,160)
*160   format ('*')
*       write (9,161)
*161   format ('*',1x,'ndl',6x,'nsl',6x,'nsr')
      nerr=0
      nsr=ndr
      nsl=ndl
c..
c..
      nmean=0.5*(ndr+ndl)
      delns=(ndr-ndl)/2
      dd(1)=delns
      ndelns=1
c..
c.. nw is the quantum well index, nw=1 is the left well, nw=2 the
c.. right.
9      do 466 nw=1,2
      psiprime0=1.
c..
c.. Donor and 2D areal charge concentrations, units of 10^10cm-2
c..
      nsl=nmean-delns
      nsr=nmean+delns
c..
c.. The effective donor density seen by either well includes both
c..  the actual donor density on that side plus the density of the
c..  donors on the other side compensated by the other layer of
c..  electrons.  This second component is due to the penetration
c..  effect itself.
c..
      nd=ndl-(ndr-nsr)
      ns=nsl
      if (nw .eq. 2) then
       nd=ndr-(ndl-nsl)
       ns=nsr
      endif
c..
c.. Square well appx. for ground state:
c..
      esqw=pi*pi/c1/w/w
c..
c.. Triangular Well Appx. for ground state:
c..
```

```
      etrw=5.1*(0.5*ns)**.6666
      e00=esqw
      if (etrw .lt. esqw) then
        e00=etrw
      endif
      es=e00
      de=0.2*es
c..
      tol=1e-6
      idm=2
      zmax=w+wb
      a=0.
      b=zmax
      h=1.
      nb=INT((b-a)/h)+1
c..
c.. make nb odd
c..
      if (2*int(nb/2) .lt. nb) go to 3
      nb=nb+1
c..
c.. Initialize distance, self-consistent potential and fixed charge
c..  potential.
c..
3     do 5 j=1,nb
      vbs=0
      x(j)=a+(j-1)*h
      xmx=x(j)
      if (x(j) .gt. w) then
        vbs=vdisc1
        xmx=w
        if (x(j-1) .le. w) then
          jw=j-1
        endif
      endif
      vf(j)=c2*nd*x(j)/2+vbs
      vs(j)=c2*ns*(1.-x(j)/w)*xmx/2
5     v(j)=vf(j)+vs(j)
      nct=0
      nsub=0
7     nnode=0
8     e=es
      iter=1
c..
c.. Decay const. in outer barrier
```

```
c..
10    alpha=sqrt(c1*(vdisc2-e))
c..
      psi0=psiprime0/alpha
      ynt(1)=psi0
      ynt(2)=psiprime0
      call KUTTA(FUNC,a,h,b,nb,ynt,y,e)
      nchs=0
      do 15 j=2,nb-1
      if (SIGN(1.,y(1,j)) .ne. SIGN(1.,y(1,j+1))) then
        nchs=nchs+1
        jnode=j
        xnode=x(j)
      endif
15    continue
      if (nchs .eq. nnode+1 .and. de .gt. 0.0) then
        de=-de/3.
      endif
      if (nchs .eq. nnode .and. de .lt. 0.) then
        de=-de/3.
      endif
      if (abs(de) .lt. e*tol .and. nchs .eq. nnode+1) goto 20
      e=e+de
      iter=iter+1
      if (iter .ge. 100 .and. nsub .eq. 0) then
         print *,'ground state non-convergent'
         nerr=1
         goto 1010
      endif
      if (iter .ge. 100 .and. nsub .eq. 1) then
         print *,'second subband non-convergent'
         nerr=1
         goto 1010
      endif
      go to 10
20    do 22 j=1,nb
      psi(j)=y(1,j)
      if (j .ge. jnode) then
        psi(j)=0.
      endif
22    psisq(j)=psi(j)*psi(j)
c..
c..
c.. Calculate norm of wavefunction, including barrier contrib.
c..
```

```
570   call inteq(nb,h,psisq,qint)
      delnorm=psi0*psi0/2/alpha
      psinorm=sqrt(qint+delnorm)
      delpct=delnorm/psinorm/psinorm
c..
c.. Normalize psi and psisq arrays
c..
      do 101 j=1,nb
      psi(j)=psi(j)/psinorm
      psisq(j)=psi(j)*psi(j)
101   zpsisq(j)=x(j)*psisq(j)
c..
c.. Get <z> for wavefunction, incl. barrier contrib.
c..
       zavb=-(psi0/2/alpha/psinorm)**2
       call inteq(nb,h,zpsisq,zav)
       zav=zav+zavb
c..
c.. Calculate self-consistent potential
c..
c..    evaluate at odd-numbered point 5 thru npt, then interpolate
c..    even-numbered point.
c..
108    do 110 j=5,nb,2
       call inteq(j,h,zpsisq,qa)
       qa=qa+zavb
       call inteq(j,h,psisq,qb)
       qb=qb+delpct
110    vs(j)=ns*c2*((qa-x(j)*qb)+x(j)/2.)
       vs(1)=0.
       vs(3)=0.5*vs(5)
       do 120 j=2,nb-1,2
120    vs(j)=(vs(j-1)+vs(j+1))/2.
c..
c..
c.. Calculate exchange-correlation energy
c..
      do 122 j=1,nb
      vxc(j)=0.
      if (psisq(j) .eq. 0.) goto 122
      rs=c3*ns*psisq(j)
      rs=rs**.333333
      rs=1/rs
      rsx=rs/21
c.. ax turns on or off correlation energy
```

```
      ax=1.
      vxc(j)=-ryd*beta*(1+.7734*ax*rsx*log(1+1/rsx))/rs
122   continue
c..
c..
1001  nct=nct+1
      if (nct .gt. 30) then
        nerr=1
        goto 1010
      endif
      etol=abs(e-es)/e
      if (etol .gt. .0001 .or. nct .lt. 8) go to 500
c..
c.. Done with ground state
c..
      e0=e-v(jw)
      zav0=zav
c..
c.. Get second moment, including barrier term
c..
      do 1080 j=1,nb
1080  zzpsisq(j)=x(j)*zpsisq(j)
      call inteq(nb,h,zzpsisq,zzav)
      zzavb=(psi0/2/alpha/psinorm)**2/alpha
      zzav=zzav+zzavb
      zrms=sqrt(zzav-zav0*zav0)
c..
c.. Find potential at middle of barrier, interpolate if necessary.
c..
63    xmidpt=a+w+wb/2.
      j=1
986   if (x(j) .eq. xmidpt) then
         vmid=v(j)
         goto 987
      endif
      if (x(j) .gt. xmidpt) then
         vmid=(v(j)+v(j-1))/2.
         goto 987
      endif
      j=j+1
      goto 986
c..
c.. evb is the energy of the conduction band
c.. edge at the center of the barrier relative to the band edge
c.. at the far interface of the well.
```

```
c..
c.. efl and efr are the left and right fermi levels relative to the
c.. band edge at the center of the barrier.
c..
c.. e0l and e0r are the subband energies relative to this same
c.. point.
c..
c..
987   evb=vmid+vdisc1-v(jw)
      efermi=ns*c5
      if (nw .eq. 1) then
         mufl=evb-e0-efermi
         e0l=evb-e0
      endif
      if (nw .eq. 2) then
         mufr=evb-e0-efermi
         e0r=evb-e0
      endif
      if (nw .eq. 1) then
       psisql=psisq
       zavl=zav
       zrmsl=zrms
      endif
      if (nw .eq. 2) then
       psisqr=psisq
       zavr=zav
       zrmsr=zrms
      endif
c..
c..
      goto 466
c..
c.. Make new potential
c..
500   ff=0.3
      do 1005 j=1,nb
      vold=v(j)
      vnew=vf(j)+vs(j)+vxc(j)*xc
1005  v(j)=vold+ff*(vnew-vold)
c..
c..
      de=0.5*(es-e)
      es=e
      goto 7
466   continue
```

```
c..
c.. Now I want to calculate the form factors g11(q) and g12(q) from the
c.. psisq for each well.  I am doing the double integration by creating a
c.. matrix representing the integrand and then summing all the elements.
c..
     dw=w+wb+w
     print *,'dw =',dw
     print *,'nb =',nb
     do 600 q=0,1999
      sum11=0
      sum12=0
      do 630 i=1,nb
               do 660 j=1,nb
      element12 = psisql(j)*psisqr(i)*exp(-q*0.00005*abs(i+j-dw-2))
               sum12 = sum12 + element12
      element11 = psisql(j)*psisql(i)*exp(-q*0.00005*abs(i-j))
               sum11 = sum11 + element11

660continue
630continue
               g11(q+1)=sum11
               g12(q+1)=sum12
600continue


c..
c.. Once here both wells have been calculated for a specific pair
c.. of densities nsl and nsr
c..
     efermir=c5*nsr
     efermil=c5*nsl
     xxtol=.001*(efermil+efermir)/2
     deltamu=mufl-mufr
     deltae0=e0l-e0r
     densdif=nsl-nsr
     xx(ndelns)=deltamu-vlr
     if (ndiag .ne. 1) goto 469
     print *,'Iteration ',ndelns
     print *,' nsl',nsl,' nsr=',nsr
     print *,' Delta mu=',deltamu
     print *,' Delta E0 =',deltae0
     print *,' Delta N=',densdif
     print *,'efermi-l=',efermil,' efermi-r=',efermir
     print *,' '
469   if (abs(xx(ndelns)) .lt. xxtol) goto 1010
```

```
      if (ndelns .eq. 1) goto 489
      slp(ndelns)=(xx(ndelns)-xx(ndelns-1))/(dd(ndelns)-dd(ndelns-1))
477   dd(ndelns+1)=dd(ndelns)-xx(ndelns)/slp(ndelns)
      delns=dd(ndelns+1)
      ndelns=ndelns+1
      goto 9
489   slp(1)=-c2*w
      goto 477
1010  if (nerr .eq. 1) goto 1020
      print *,'Interlayer bias (mV)=',vlr
      print *,'ndl=',ndl,' ndr=',ndr
      print *,'nsl=',nsl,' nsr=',nsr
      print *,'Subband mismatch=',deltae0
      print *,'Density difference=',densdif
      print *, 'zavl =', zavl, 'zavr =',zavr
      print *, 'zrmsl =',zrmsl,'zrmsr =', zrmsr
*       write(9,1015) ndl,nsl,nsr
*1015  format(f7.4,2x,f7.4,2x,f7.4)
*     write(9,901) zavl
*901          format ('zavl =',f10.4)
*     write(9,902) zavr
*902          format ('zavr =',f10.4)
*     write(9,903) zrmsl
*903          format ('zrmsl =',f10.4)
*     write(9,904) zrmsr
*904          format ('zrmsr =',f10.4)

c.. This prints the data to file.  Since the psisq data is (usually) longer
c.. than the g11 and g12 data (with it's standard 201 points, for a delta
c.. q of 10^6 1/m^2 between points), I need to first print all five arrays;
c.. then later print just three.
c..
*     do 800 j=1,2000
*      write(9,810) j-1,psisql(j),psisqr(j),g11(j),g12(j)
*810               format(I6,2E13.4,2E13.4)
*800          continue
c.. this makes special files of the form factors that can be read into
c.. one of the dqand_4Dsplitgg programs.  There is a single default name
c.. so if you want to save these, you need to change the filenames after
c.. running this program.
c..
      fg11 = 'g11'
      fg12 = 'g12'
      open (unit=11,file=fg11)
      open (unit=12,file=fg12)
      write (11,830) (g11(i),i=1,2000)
      write (12,830) (g12(i),i=1,2000)
830format (2000(E12.6))

1020  end
c..
c..
c..
c..
      subroutine KUTTA(FUNC,a,h,b,nb,ynt,y,e)
      EXTERNAL FUNC
      real ysv(2),f(2),w(4,2),ynt(2),y(2,500)
      idm=2
      eps=1.e-6
      x=a
      hh=h/2
      n=1
      do 30 i=1,idm
      ysv(i)=ynt(i)
30    y(i,1)=ynt(i)
40    xsv=x
      do 90 l=1,4
      call FUNC(ysv,x,f,e)
      do 50 i=1,idm
50    w(l,i)=h*f(i)
      go to (60,60,80,90), l
60    x=xsv+hh
      do 65 i=1,idm
65    ysv(i)=y(i,n)+w(l,i)*0.5
      go to 90
80    x=xsv+h
      do 85 i=1,idm
85    ysv(i)=y(i,n)+w(l,i)
90    continue
      np=n+1
      do 95 i=1,idm
      y(i,np)=y(i,n)+(w(1,i)+2.*(w(2,i)+w(3,i))+w(4,i))/6.
      if (abs(y(i,np)) .gt. 1.e6) then
        y(i,np)=y(i,n)
      endif
95    continue
      n=np
      if (n .ge. nb .or. x .gt. b-eps) go to 100
      do 98 i=1,idm
98    ysv(i)=y(i,np)
```

```
      go to 40
100   return
      end
c..
c..
      subroutine FUNC(ysv,x,f,e)
c..
c..   distances in angstroms
c..   energies in meV
c..
      real e,ysv(2),f(2),n,v(1000)
      common /blk2/a,b,h,v
      common /blk3/c1,c2
      n=(x-a)/h+1
      j=int(n)
      vpot=v(j)
      if (abs(n-j) .lt. 0.1) go to 50
      vpot=(v(j)+v(j+1))/2.
50    f(1)=ysv(2)
      f(2)=c1*(vpot-e)*ysv(1)
      return
      end
c..
c..
      subroutine inteq(n,h,y,qint)
      common /blk4/npt
      real y(npt)
      nint=n-1
      nn=nint/2
      qint=0.
      suma=0.
      sumb=0.
      do 20 j=1,nn
      jj=2*j
20    suma=suma+y(jj)
      do 25 j=1,nn-1
      jj=2*j-1
25    sumb=sumb+y(jj)
      qint=h*(y(1)+y(n)+4*suma+2*sumb)/3
      return
      end
```

Program #4: HoleDragforCosineWells

```
*
*  PROGRAM HoleDragforCosineWells.f
*
*  Integrates 4D boltzmann formulation for the drag, as given in
*  a paper by Jauho & Smith PRB 47,4420, assuming the electron/hole
*  wavefunction is a cosine (as is used in the paper).
*  This program will output either CD vs. T, or CD vs. delta(n)/<n>
*  for a given <n> (density per layer), d (center-to-center layer
*  separation), w (well width), and in T (temperature).
*
*  This program calculates the drag for any effective mass.
*  And kappa is set to 12.8.
*
     INTEGER MAXFCN,N,I,J,dragtype,loop
     real time1,time2
     character filename*25,fdt1*56,fdt2*23,temp*3,header*80,stime*8
     character precisionvariable*12, dragtypename*21
     double precision A(4),B(4),RESULT,F,ERREST1,ERRABS,ERRREL,RESULT1
     double precision L,ERREST2,deltat,tend,n1r,n2r,kf1,kf2,kfmax
     double precision nave,deltanend,errnumber,deltan,dr,wr,pi
     double precision tf1,tf2,tfmax,mas,Lraw
     double precision n1,n2,w,d,t,mass
     EXTERNAL F,DQAND
     common n1,n2,w,d,t,mass

     pi=3.1415927
     N = 4
     MAXFCN = 2100000000
     ERRABS=0.0

*  choose 'CD vs. T' or 'CD vs. delta n' option
     PRINT *,''
10   PRINT *,'Enter the number "0" if you wish to calculate Drag vs. T;'
     PRINT *,'or "1" if you wish to calculate Drag vs. delta(n)/<n>:'
     PRINT *, ''
     READ *,dragtype

      IF (dragtype == 0) THEN
      dragtypename = 'Drag vs. T'
      ELSE IF (dragtype == 1) THEN
      dragtypename = 'Drag vs. delta(n)/<n>'
      ELSE
```

```
       PRINT *, ''
       PRINT *, 'You must choose either 0 or 1, please try again.'
       PRINT *, ''
       GOTO 10
       END IF

      PRINT *, ''
      PRINT *, 'You have chosen:'
      PRINT 44, dragtypename
44    FORMAT (A40)
      PRINT *,''''
*  get n,d,w,T etc. as needed, and automatically set errrel from these - allow
*  the option of autochoose errrel or choose it manually.  Then it's up to the user to
*  understand how to choose them.

       IF (dragtype == 0) THEN
               PRINT *,''
               PRINT *,'Start temperature in K:'
               PRINT *, ''
               READ *,t
               PRINT *,''
               PRINT *,'Temperature steps in delta K:'
               PRINT *, ''
               READ *,deltat
               PRINT *,''
               PRINT *,'End temperature in K:'
               PRINT *, ''
               READ *,tend
               PRINT *,''
               PRINT *,'Density in layer 1 (in units of 10^10 cm^-2):'
               PRINT *, ''
               READ *,n1r
               PRINT *,''
               PRINT *,'Density in layer 2 (in units of 10^10 cm^-2):'
               PRINT *, ''
               READ *,n2r
       ELSE
               PRINT *,''
               PRINT *,'Average density per layer <n> (x10^10 cm^-2):'
               PRINT *, ''
               READ *,nave
               PRINT *,''
               PRINT *,'delta(n) per layer steps (in units of 10^10 cm^-2):'
               PRINT *, ''
               READ *,deltan
```

```
              PRINT *,"
              PRINT *,'delta(n)/<n> max (e.g., 0.6):'
              PRINT *, "
              READ *,deltanend
              PRINT *,"
              PRINT *,'Temperature in K:'
              PRINT *, "
              READ *,t
       END IF

      PRINT *,"
      PRINT *,'center-to-center layer separation, d, (in Angstroms):'
      PRINT *, "
      READ *,dr
      PRINT *,"
      PRINT *,'well width, w, (in Angstroms):'
      PRINT *, "
      READ *,wr
      PRINT *,"
      PRINT *,'effective mass (in units of m_e):'
      PRINT *, "
      READ *,mas

      IF (dragtype == 0) THEN
              ERRREL = 0.02
      ELSE
              ERRREL = 0.01
      ENDIF

* set parameters to their MKS units
      d = dr*1D-10
      w = wr*1D-10
      mass = mas/0.067

      IF (dragtype == 0) THEN
       n1 = n1r*1D14
       n2 = n2r*1D14
      ELSE
       n1 = nave*1D14
       n2 = nave*1D14
      ENDIF

* and determine k_fermi and T_fermi for setting L:
      kf1 = sqrt(2*pi*n1)
      kf2 = sqrt(2*pi*n2)
      kfmax = max(kf1,kf2)
      tf1 = 4.15D-14*n1/mass
      tf2 = 4.15D-14*n2/mass
      tfmax = max(tf1,tf2)


*  Now choose to have 'ERRREL' set automatically or by hand:
      PRINT *,"
      PRINT *,'If you wish to set the precision of the calcualtion'
      PRINT *,'yourself, type in "man".  Type in anything else and'
      PRINT *,'the precision will be assigned automatically.'
      PRINT *, "
      READ *,precisionvariable
       IF (precisionvariable == 'man') THEN
              PRINT *,"
              PRINT *,'For ', dragtypename, ' the error variable "ERRREL" '
              PRINT 46,'is set to', ERRREL,'.  For higher precision (but'
46            FORMAT (A10,F6.2,A28)
              PRINT *,'longer computation time) type in a SMALLER number.'
              PRINT *, 'For less precision, but faster computation time'
              PRINT *,'type in a LARGER number (but keep it < 1).'
              PRINT *,'(to learn more about "ERRREL", see "DQAND" '
              PRINT *,'in IMSL library).  Enter error precision now:'
              PRINT *, "
              READ *,ERRREL
       ELSE
       ENDIF

      PRINT *,"
45    FORMAT (A19,F8.3)
      PRINT 45,'ERRREL is set to: ', ERRREL
      PRINT *,"

*  this calculates the number of times to run the do loop
      IF (dragtype == 0) THEN
       loop = nint((tend -t)/deltat)+1
      ELSE
       loop = nint((deltanend*nave)/(2*deltan))+1
      ENDIF

* SET APPROPRIATE LIMITS (L) FOR THE TEMPERATURE
      PRINT *,"
      PRINT *,'You must set the integration limit for this'
      PRINT *,'program.  Ideally one integrates over the k'
      PRINT *,'momentum from 0 to infinity.  As the computer'
      PRINT *,'cannot integrate to infinity, you must pick'
      PRINT *,'a sufficiently large number so that all relevant'
      PRINT *,'processes are included in the integration.  You'
      PRINT *,'will know when your number is large enough, when'
      PRINT *,'increasing it no longer affects the outcome of'
      PRINT *,'the integration.  Typical range: 0.5 to 5 (x 10^8 m^-2).'
      PRINT *,"
      PRINT *,'Choose an integration limit (in units of 10^8 m^-2):'
      PRINT *, "
      READ *,Lraw

      L = Lraw * 1D8

*  get filename
      PRINT *,"
      PRINT *,'This program will put the results of the calculations'
      PRINT *,'in a subdirectory of your current folder.  The'
      PRINT *,'subdirectory will be called "output" (you may need to'
      PRINT *,'create this yourself).  You must choose a file name'
      PRINT *,'for each run of this program.'
      PRINT *,"
      PRINT *,'What filename do you wish to use?'
      PRINT *,"
      READ *,filename
      fdt2 = 'output\'//filename
      open(2,FILE=fdt2)

*  write header information to file
      WRITE (2,33),dragtypename
33  FORMAT (",A36)
      WRITE (2,'(A20)') (")
      WRITE (2,38) 'm* =',mas,'; kappa = 12.8; limit =',Lraw,'x10^8 m^-2.'
38  FORMAT (A4,F7.3,A23,F6.2,A11)
      WRITE (2,34) 'd =',dr,'A, w =',wr,'A.  Cosine wavefunction.'
34  FORMAT (A3,F6.1,A8,F6.1,A25)
      IF (dragtype == 0) THEN
      WRITE (2,36) 'n1 =',n1r,', n2 =',n2r,' x 10^10 cm^(-2)'
36  FORMAT (A4,F5.2,A6,F5.2,A16)
      ELSE
      WRITE (2,37) 'T =',t,'K.  n1, n2 are in MKS units (m^-2).'
37  FORMAT (A3,F6.2,A35)
      ENDIF


      PRINT *,"
```

```
     CALL TIME(stime)
     PRINT *,'start time: ',stime
     PRINT *,''
     PRINT 47, 'd =',dr,' Angstroms'
47   FORMAT (A4,F6.1,A10)
     PRINT 47, 'w =',wr,' Angstroms'
     IF (dragtype == 0) THEN
      PRINT 48, 'n1 =',n1r,' x 10^10 cm^-2'
      PRINT 48, 'n2 =',n2r,' x 10^10 cm^-2'
48    FORMAT (A5,F6.2,A14)
      PRINT *,'  K','      Ohms   ','error   ','elapsed seconds'
      WRITE (2,'(A20)') ('')
      WRITE (2,'(A42)'),' K      Ohms         error        sec'
     ELSE
      PRINT 49, 'T =',t,'K'
49    FORMAT (A4,F6.2,A2)
      PRINT 445,'n1       n2','Ohms','error','seconds'
445   FORMAT ('',A14,A14,A11,A15)
      WRITE (2,'(A20)') ('')
450  FORMAT ('',A7,A10,A12,A16,A12,A7)
      WRITE (2,450),'n1','n2','ohms','error','sec','deltan'
     ENDIF


     DO 7, I=1,loop

*  This sets the integration limits, and calls the integration
*  program (DQAND) from the IMSL library, and solves the integral


     A = (/0.0D8,0.0D8,-L,0.0D8/)
     B = (/L,L,0.0D8,L/)

     CALL CPU_TIME(time1)
     CALL DQAND(F,N,A,B,ERRABS,ERRREL,MAXFCN,RESULT,ERREST1)
     RESULT1 = RESULT

     A = (/0.0,0.0,0.0,0.0/)
     B = (/L,L,L,L/)

     CALL DQAND(F,N,A,B,ERRABS,ERRREL,MAXFCN,RESULT,ERREST2)
     CALL CPU_TIME(time2)

      IF (dragtype == 0) THEN
     PRINT 100,t,RESULT+RESULT1,SQRT(ERREST1**2+ERREST2**2),time2-time1
```

```
100FORMAT      (",F5.1,F11.4,E14.4,F8.1)
     WRITE (2, 20),t,RESULT+RESULT1,SQRT(ERREST1**2+ERREST2**2),
    &time2-time1
20  FORMAT (F5.1,E15.4,E14.4,F9.1)
      ELSE
     PRINT 101,n1,n2,RESULT+RESULT1,SQRT(ERREST1**2+ERREST2**2),
    &time2-time1
101FORMAT      (",2E9.2,F11.4,E14.4,F9.1)
     WRITE (2, 21),n1,n2,RESULT+RESULT1,SQRT(ERREST1**2+ERREST2**2),
    &time2-time1,(2*(n1-n2)/(n1+n2))
21  FORMAT (E10.3,E10.3,E13.6,E14.4,F10.1,F8.5)
      ENDIF

* increment the temperature or the delta n
     IF (dragtype == 0) THEN
     t = t + deltat
     ELSE
     n1 = n1 + deltan*1D14
     n2 = n2 - deltan*1D14
     ENDIF

    7CONTINUE

     END


     double precision FUNCTION F(N,X)
     integer N
     double precision X(N),qtf,kb,tf1,tf2,k
     double precision a,kappa,Const,pi,m,Const2
     double precision n1,n2,w,d,t,mass
     common n1,n2,w,d,t,mass

     tf1 = 4.15D-14*n1/mass
     tf2 = 4.15D-14*n2/mass
     kappa = 12.8
     qtf = 1.977D8*mass
     pi = 3.1415927
     m = (1/(4*pi*pi)-1/3.0+1/(pi*pi))
     kb = 1.381D-23
*  a is m* e^2/pi^2 kb h_bar qtf^4 (4 pi epsilon)^2
     a = 5.76361D-27/(mass)**3
*  k is (h_bar)^2/2 m*
     k = 9.1187D-38/mass
```

```
      Const = a / (kappa*kappa*n1*n2*t)
      Const2 = qtf*qtf*Const

*  Here is the integrand (X{} = k1y,k1'x,k1'y,k2perp):
      IF (sqrt(X(2)**2+(X(3)-X(1))**2) .GE. 0.0) THEN

      F= Const*X(1)*(sqrt(X(2)**2+(X(3)-X(1))**2))**3*(EXP((k*(X(1)**2)
     &-kb*tf1)/(kb*t))+1)**(-1)*(1-(EXP((k*(X(2)**2+X(3)**2)-kb*tf1)
     &/(kb*t))+1)**(-1))*(EXP((k*(X(4)**2+(X(2)**2+(X(3)-X(1))**2)
     &/4+((X(1)**2-X(2)**2-X(3)**2)**2/(4*(X(2)**2+(X(3)-X(1))**2))
     &-(X(1)**2-X(2)**2-X(3)**2)/2))-kb*tf2)/(kb*t))+1)**
     &(-1)*(1-(EXP((k*(X(4)**2+(X(2)**2+(X(3)-X(1))**2)/4+(X(1)**2
     &-X(2)**2-X(3)**2)/2+(X(1)**2-X(2)**2-X(3)**2)**2/(4*(X(2)**2
     &+(X(3)-X(1))**2)))-kb*tf2)/(kb*t))+1)**(-1))*(EXP
     &(sqrt(X(2)**2+(X(3)-X(1))**2)*d)*(sinh(sqrt(X(2)
     &**2+(X(3)-X(1))**2)*w/2))**(-2)*(8*pi*pi/(sqrt(X(2)**2+(X(3)-X(1))
     &**2)*w*(4*pi*pi+(X(2)**2+(X(3)-X(1))**2)*w*w)))**(-2)
     &*((2/(sqrt(X(2)**2+(X(3)-
     &X(1))**2)*w)-EXP(-sqrt(X(2)**2+(X(3)-X(1))**2)*w/2)*
     &sinh(sqrt(X(2)**2+(X(3)-X(1))**2)*w/2)*(8*pi*pi/
     &(sqrt(X(2)**2+(X(3)-X(1))**2)*w*(4*pi*pi+(X(2)**2+(X(3)-X(1))**2)
     &*w*w)))**2+sqrt(X(2)**2+(X(3)-X(1))**2)*w/(4*pi*pi+
     &(X(2)**2+(X(3)-X(1))**2)*w*w))+sqrt(X(2)**2+(X(3)-X(1))**2)
     &/qtf)**2-EXP(-d*sqrt(X(2)**2+(X(3)-X(1))**2))*(sinh(sqrt(X(2)
     &**2+(X(3)-X(1))**2)*w/2))**2*(8*pi*pi/(sqrt(X(2)**2+(X(3)-X(1))
     &**2)*w*(4*pi*pi+(X(2)**2+(X(3)-X(1))**2)*w*w)))**2)**(-2)

      ELSE

      F= Const2*X(1)*(sqrt(X(2)**2+(X(3)-X(1))**2))*(EXP((k*(X(1)**2)
     &-kb*tf1)/(kb*t))+1)**(-1)*(1-(EXP((k*(X(2)**2+X(3)**2)-kb*tf1)
     &/(kb*t))+1)**(-1))*(EXP((k*(X(4)**2+(X(2)**2+(X(3)-X(1))**2)
     &/4+((X(1)**2-X(2)**2-X(3)**2)**2/(4*(X(2)**2+(X(3)-X(1))**2))
     &-(X(1)**2-X(2)**2-X(3)**2)/2))-kb*tf2)/(kb*t))+1)**
     &(-1)*(1-(EXP((k*(X(4)**2+(X(2)**2+(X(3)-X(1))**2)/4+(X(1)**2
     &-X(2)**2-X(3)**2)/2+(X(1)**2-X(2)**2-X(3)**2)**2/(4*(X(2)**2
     &+(X(3)-X(1))**2)))-kb*tf2)/(kb*t))+1)**(-1))*(2*d*qtf+2*w*qtf*m
     &*(1+sqrt(X(2)**2+(X(3)-X(1))**2)*d+sqrt(X(2)**2+(X(3)-X(1))**2)
     &/qtf)+2+2*sqrt(X(2)**2+(X(3)-X(1))**2)*d+sqrt(X(2)**2+(X(3)-X(1)
     &)**2)/qtf+sqrt(X(2)**2+(X(3)-X(1))**2)*qtf*w*w*m*m)**(-2)
      ENDIF

      RETURN
      END
```